CONF-950846--MS

LA-13163-MS

UC-741
Issued: October 1996

Recent Papers from DX-1, Detonation Science and Technology

Compiled by
R. H. Warnes
S. A. Sheffield

Los Alamos
NATIONAL LABORATORY
Los Alamos, New Mexico 87545

TABLE OF CONTENTS

RECENT PAPERS FROM DX-1, DETONATION SCIENCE AND TECHNOLOGY

Compiled by

R. H. Warnes and S. A. Sheffield

ABSTRACT

Over the past year members of DX-1 have participated in several conferences where presentations were made and papers prepared for proceedings. There have also been several papers published in or submitted to refereed journals for publication. Rather than attach all these papers to the DX-1 Quarterly Report, we decided to put them in a Los Alamos report that could be distributed to those who get the quarterly, as well as others that have an interest in the work being done in DX-1 both inside and outside the Laboratory.

This compilation does not represent all the work reported during the year because some people have chosen not to include their work here. In particular, there were a number of papers relating to deflagration-to-detonation modeling that are not included. However, this group of papers does present a good picture of much of the unclassified equation of state and energetic materials work being done in DX-1. Several of the papers include co-authors from other groups or divisions at the Laboratory, providing an indication of the collaborations in which people in DX-1 are involved. The papers discuss the various subjects in less detail than if they were part of a quarterly report, but they are more complete in terms of describing the work done. In some cases, work in the areas is continuing, so the papers represent progress reports. In the case of papers in the refereed journals, they represent work that has been completed.

The papers are not ordered except that those given at meetings are first and the three journal articles are last. Because of space limitations established for the proceedings, the papers given at the American Physical Society Topical Conference on Shock Compression of Condensed Matter are all four pages in length. The format of each paper is the same as has been used in the paper submitted for publication.

In the case of the APS Meeting, papers with DX-1 people as authors or co-authors represent over 4% of all the papers given at the conference (15 out of about 350). Since this was an international meeting, this amount of participation illustrates the impact of our work on the shock and energetic materials community throughout the world.

I.

1995 APS TOPICAL CONFERENCE ON

"SHOCK COMPRESSION OF CONDENSED MATTER,"

AUGUST 13-18, 1995,

SEATTLE, WASHINGTON

DISCLAIMER

ISENTROPE ENERGY, HUGONIOT TEMPERATURE, AND THE MIE-GRUNEISEN EQUATION OF STATE

Charles A. Forest

Group DX-1, MS P952, Los Alamos National Laboratory, Los Alamos, NM 87545

Analytic expressions for both the isentrope energy and temperature along the Hugoniot curve may be expressed in terms of a single integral function for a Mie-Gruneisen equation of state with constant heat capacity c_v.

INTRODUCTION

The Mie-Gruneisen equation of state with a Hugoniot reference line is commonly used in calculations. The temperature on the Hugoniot and isentrope curves are at times desired. Calculation of the temperature along the Hugoniot was given by Walsh and Christian[1], the expression for which contains an integral function. This integral, for constant heat capacity c_v, and general Gruneisen parameter $\Gamma(v) = v(\partial p/\partial e)_v$, will be shown to be that integral which is necessary for the calculation of isentropic energy.

The calculation of temperature or the calculation of an arbitrary isentrope is often useful in fluid dynamic modeling. These properties are used in mixture equations of state that assume pressure equilibrium along with temperature equilibrium or isentropic behavior following a first shock. There is a convenience in having the single integral function $I(u)$ that facilitates both purposes.

BASIC FORMULATION

The Mie-Gruneisen equation of state using a first-shock Hugoniot reference line is written

$$p(v,e) = (\Gamma/v)(e - e_h(v)) + p_h(v) \qquad (1)$$

where v = specific volume, e = specific internal energy, $p_h(v)$ = Hugoniot pressure, $e_h(v) = \frac{1}{2}(p_h(v) + p_0)(v_0 - v) + e_0$, the Hugoniot relation.

The function $p_h(v)$ is calculated from two Rankine-Hugoniot relations (conservation of mass and momemtum) and the empirical $U_s(u)$ relation (the shock velocity into undisturbed material). These equations are, as functions of the shock particle velocity u, $v_h(u) = v_0(U_s(u) - u)/U_s(u)$, $p_h(u) = \rho_0 u U_s(u) + p_0$, and $U_s(u) = c + su + qu^2$.

Letting $u_h(v)$ be the inverse $v_h(u)$, then by composition $p_h(v) = p_h(u_h(v))$.

The empirical $U_s(u)$ relation is represented piecewise by a linear or quadratic over n segments, $u_1 < u_2 < \ldots < u_{n+1}$. A corresponding set of oppositely ordered volume segments are defined, $v_1 > v_2 > \ldots > v_{n+1}$ with $v_j = v_h(u_j)$. If $U_s(u) = c + su + qu^2$ on a segment, then $u_h(v)$ is obtained by solution of the quadratic equation

$$\left(\frac{qu_1(v)}{c}\right)u^2 - u + u_1(v) = 0 \quad \text{where}$$

$$u_1(v) = c(v_0 - v)/(v_0 - s(v_0 - v)).$$

If $q = 0$, then $u_h(v) = u_1(v)$.

If $q \neq 0$, the two roots for $u_h(v)$ are

$$u_a = 2u_1(v)/\left(1+\sqrt{1-4q\,u_1(v)^2/c}\right) \text{ and}$$

$$u_b = c/(qu_a).$$

The root u_a has the correct limit for $q = 0$ and has good numerical precision; and for $q \neq 0$, the u_b root has similar precision. Both are calculated using the fact that if the equation $ax^2 + bx + c = 0$ has roots x_1 and x_2, then $c = ax_1x_2$. The proper root must be selected to lie in the segment determined by v.

The derivatives of $p_h(v) = p_h(u_h(v))$ with respect to specific volume v, or of any other function parametrically given as a function of u, requires the derivative du_h/dv, which can be calculated implicitly from the mass equation

$$U_s(u_h(v))\, v = v_0\left[U_s(u_h(v)) - u_h(v)\right].$$

Differentiation gives

$$\frac{du_h}{dv} = \frac{U_s(u_h(v))}{\frac{dU_s}{du}(v_0 - v) - v_0}.$$

Using this result, with $u = u_h(v)$,

$$\frac{dp_h}{dv} = \rho_0\left[U_s + \frac{dU_s}{du}u\right]\frac{du_h}{dv}.$$

An expression for the Gruneisen gamma Γ in terms of c_v, T, β, and c^2 can be obtained from two thermodynamic equations related to Γ,

$$c_p = c_v(1 + \beta\,\Gamma\,T) \text{ and } c_p = \beta c^2/\Gamma, \text{ where}$$

$$c_p = (\partial e/\partial T)_p + p(\partial v/\partial T)_p,\ c_v = (\partial e/\partial T)_v$$

$$\beta = (\partial v/\partial T)_p/v, \text{ and } c^2 = (\partial p/\partial \rho)_s.$$

Equating the two c_p expressions and solving the resulting quadratic equation for Γ gives

$$\Gamma = \frac{2(\beta c^2/c_v)}{1 + [1 + 4(\beta c^2/c_v)\beta T]^{1/2}}.$$

ISENTROPE ENERGY AND MIE-GRUNEISEN EOS

From the thermodynamic equation, $Tds = de + pdv$ (with $ds \equiv 0$) and the equation of state,

$$\frac{de_i}{dv} = -p(v, e_i(v))$$

where $e_i(v)$ is the isentrope energy. The differential equation for e_i is then

$$\frac{de_i}{dv} + (\Gamma/v)e_i = (\Gamma/v)e_h(v) - p_h(v) \quad (2)$$

with initial value $e_i(v_1) = e_1$. Let now $g(v) = (\Gamma/v)$, and let $G(v) = \exp\{\int g(v)dv\}$ be the integrating factor.

For two special cases of (Γ/v), these functions are as follows:

1. If $\Gamma = \Gamma_0$, then $g(v) = (\Gamma/v)$ and $G(v) = v^{\Gamma}$.
2. If $\Gamma/v = \Gamma_0/v_0$, then $g(v) = \rho_0\Gamma_0$ and $G(v) = \exp\{\rho_0\Gamma_0 v\}$.

Now multiply equation (2) by G and integrate,

$$e_i(v)G(v) - e_1G(v_1) = \int_{v_1}^{v} G(v)[g(v)e_h(v) - p_h(v)]dv$$

Note that $\frac{dG}{dv} = G(v)g(v)$ and integrate by parts

$$\int_{v_1}^{v} G\, g\, e_h dv = [G\, e_h]_{v_1}^{v} - \int_{v_1}^{v} G \frac{de_h}{dv}\, dv.$$

Also note

$$\frac{de_h}{dv} + p_h = \tfrac{1}{2} \frac{dp_h}{dv}(v_0 - v) + \tfrac{1}{2}(p_h - p_0)$$

Finally then

$$e_i(v)G(v) - e_1 G(v_1) = G(v)\, e_h(v) - G(v_1) e_h(v_1)$$

$$-\int_{v_1}^{v} \frac{G(v)}{2}\left[\frac{dp_h}{dv}(v_0 - v) + p_h - p_0\right] dv$$

The remaining integral is not expressible in terms of elementary functions, and is not easily and accurately fit as a function of volume v because $p_h(v)$ has a singular point at $v = v_0(s-1)/s$ when $U_s = c + su$. Recall that the particle velocity has no such trouble and can be used for the integration change of variable. Thus let

$$I(v) = \int_{v_0}^{v} \frac{G}{2}\left[\frac{dp_h}{dv}(v_0 - v) + p_h - p_0\right] dv$$

(note lower limit of integration). Changing integration variable, let

$$v = v_h(u) \text{ and } dv = \frac{dv_h}{du}\, du.$$

This particular choice of variable change is advantageous because $p_h(v) = p_h(u_h(v))$ and

$$\frac{dp_h}{dv} = \frac{dp_h}{du}\,\frac{du_h}{dv} = \rho_0(U_s + u\frac{dU_s}{du})/\frac{dv_h}{du}$$

Also note

$$(v_0 - v) = v_0 u/U_s,\ p_h - p_0 = p_0 u U_s, \text{ and}$$

$$\frac{dv_h}{du} = \frac{v_0\left[u\frac{dU_s}{du} - U_s\right]}{U_s^2}.$$

Then

$$I(u) = \int_0^u \frac{G(v_h(u))}{2}\left[\frac{dp_h}{dv}\,\frac{dv_h}{du}(v_0 - v) + (p_h - p_0)\frac{dv_h}{du}\right] du, \text{ and finally,}$$

$$I(u) = \int_0^u \frac{G(v_h(u))\, u^2}{U_s(u)}\,\frac{dU_s}{du}\, du \qquad (3)$$

and

$$e_i(v)G(v) = e_1 G(v_1) + e_h(v)G(v) - e_h(v_1)G(v_1) - \left[I(u_h(v)) - I(u_h(v_1))\right]$$

Remark: $e_i(v)$ is the energy of the isentrope through the point $(v_1, e_1,)$, which may be any point in the domain of $p(v,e)$. A common usage is the case where $e_1 = e_h(v_1)$, that is the isentrope for a material element that has experienced a first shock.

The function $I(u)$ is represented on each (u_j, u_{j+1}) interval by the form $I(u) = a_1 + u^m(a_2 + a_3 u + a_4 u^2 + a_5 u^3 + a_6 u^4)$. In the neighborhood of $u = 0$, we let $m = 3$, and elsewhere let $m = 1$. For calculation of the derivative of $I(u)$, the exact expression

$$\frac{dI}{du} = G(v_h(u))\, u^2 \frac{dU_s}{du}/U_s(u) \text{ is used.}$$

The use of component equations of state in a equilibrium mixture equation of state requires not only an accurate function value but an accurate derivative so that the iterative equilibrium solution method will converge quickly. To that end, the function $I(u)$ is fitted by fitting the derivative of

$I(u)$ and $I(u)$ simultaneously. One need not use polynomials, any suitable analytically integrable basis function set would do.

TEMPERATURE AND HUGONIOT TEMPERATURE

The temperature as a function of (v,e) is

$$T(v,\ e) = \frac{(e - e_h(v))}{c_v} + T_h(v)$$

where $e_h(v)$ = Hugoniot energy and $T_h(v)$ = Hugoniot temperature, and c_v = constant heat capacity.

The temperature on the Hugoniot $T_h(v)$ is calculated via Walsh and Christian's method.[1]

They write on page 1554,

$$c_v \frac{dT_h}{dv} + \left(\frac{\partial p}{\partial T}\right)_v T_h = \frac{1}{2}\frac{dp_h}{dv}(v_0 - v) + \frac{1}{2}(p_h - p_0).$$

Changing variable to (v,e), $p(v,T) = p(v,\ e(v,T))$ and thus

$$\left(\frac{\partial p}{\partial T}\right)_v = \left(\frac{\partial p}{\partial e}\right)_v \left(\frac{\partial e}{\partial T}\right)_v = (\Gamma/v)\, c_v.$$

The differential equation is then

$$\frac{dT_h}{dv} + \frac{\Gamma}{v} T_h = \frac{1}{2c_v}\left\{\frac{dp_h}{dv}(v_0 - v) + p_h - p_0\right\}$$

with initial value $T_h(v_0) = T_0$. Using the same integrating factor and notation as in the integration of the isentrope energy equation,

$$T_h(v)\, G(v) - T_0 G(v_0) = \int_{v_0}^{v} \frac{G}{2c_v}\left\{\frac{dp_h}{dV}\ (v_0 - v) + p_h - p_0\right\} dv.$$

For c_v = constant, the integral is just $I(v)/c_v$, and thus

$$T_h(v)\, G(v) = T_0 G(v_0) + \frac{1}{c_v} I(u_h(v)).$$

ACKNOWLEDGEMENTS

I especially want to thank Genevieve Vigil and Larry Hill for their help in preparing this manuscript.

REFERENCES

1. J. M. Walsh and R. H. Christian, Equation of State of metals from Shock Wave Measurements, *The Physical Review*, **97**, No. 6, 1544-1556, March 15, 1955.

HUGONIOT AND SPALL DATA FROM THE LASER-DRIVEN MINIFLYER

R. H. Warnes, D. L. Paisley, and D. L. Tonks

Los Alamos National Laboratory, Los Alamos, NM 87545

The laser-driven miniflyer has been developed as a small-sized complement to the propellant- or gas-driven gun with which to make material property measurements. Flyer velocities typically range from 0.5 to 1.5 km/s, depending on the energy of the launching laser and the flyer dimensions. The 10–50 μm-thick flyers, 1–3 mm in diameter, and comparably small targets require very little material and are easy to recover for post-experiment analysis. To measure and improve the precision of our measurements, we are conducting an extensive series of experiments impacting well-characterized Cu, Al, and Au on several transparent, calibrated, windows (PMMA, LiF, and sapphire). Measurement of the impact and interface velocities with a high-time-resolution velocity interferometer (VISAR) gives us a point on the Hugoniot of the flyer material. These are then compared to published Hugoniot data taken with conventional techniques. In the spall experiments, a flyer strikes a somewhat thicker target of the same material and creates a spall in the target. Measuring the free-surface velocity of the target gives information on the compressive elastic-plastic response of the target to the impact, the tensile spall strength, and the strain rate at which the spall occurred. Volumetric strain rates at spall in these experiments are frequently in the 10^6–10^8 s^{-1} range, considerably higher than the 10^3–10^4 s^{-1} range obtainable from gas gun experiments.

INTRODUCTION

The Laser-driven Miniflyer has been developed over the last several years to measure the dynamic properties of materials under shock-wave conditions. A pulsed Nd:YAG laser is focused through a transparent substrate onto a thin multilayer that has been deposited on the substrate, Fig. 1. A thin foil (the flyer) is placed on the multilayer. The laser pulse is absorbed in the multilayer and creates a plasma, which in turn accelerates the flyer to its terminal velocity within three or four pulse widths of the laser. The nearly perfectly flat flyer then impacts a target and the response of the flyer and target after the impact are measured with a high-time-resolution laser velocity interferometer (VISAR) (1–2). Many of the material properties that are routinely determined with propellant- or gas-driven guns or explosives can be obtained with the Miniflyer.

Because the flyers and targets are very small (10-50 μm thick and 1 to 3 mm in diameter), recovery of the samples for post-shot analysis is straightforward. The amount of material needed for an experiment is also quite small—a definite advantage if the material being studied is toxic and/or expensive.

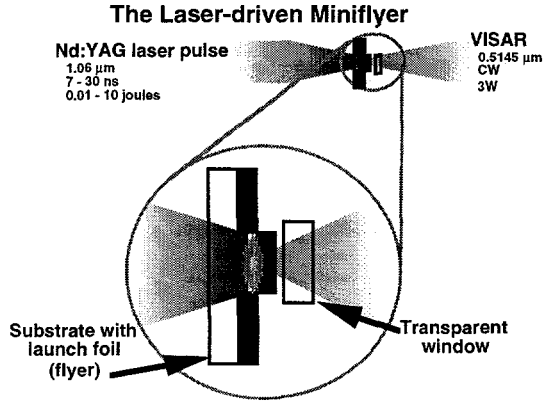

FIGURE 1. A schematic of the Laser-driven Miniflyer. The launching laser enters from the left, and the diagnostic laser enters from the right.

Some details of the Miniflyer launch and the direct optical recording of the VISAR data have been presented previously (3–4). The purpose of this paper is to describe the data analysis and to compare the results with data obtained by conventional techniques. The experiments discussed here are just the first few of many scheduled to determine if the assembly and alignment procedures and the precision of the measurements are adequate to determine accurate Hugoniots and spall-related properties. In addition we hope to determine the effect of scaling, if any, on the properties being measured.

HUGONIOT EXPERIMENTS

In these experiments the material to be studied, the "unknown", is the flyer—a 25-μm-thick foil of OFHC Cu in the as-received state of hardness. The target is one of several transparent window materials of known Hugoniot and calibrated for use with the VISAR in shock-wave experiments (5–6). PMMA, LiF, and sapphire are used. The VISAR is focused through the window and onto the flyer, Fig. 1. Before impact the velocity history of the flyer is recorded; after impact the flyer/target interface velocity is recorded, Fig. 2. From these two measurements, a point on the Hugoniot of the "unknown" flyer can be calculated.

Figure 3 shows graphically how a point on the flyer Hugoniot is determined from the impact and interface velocities. The measured impact velocity

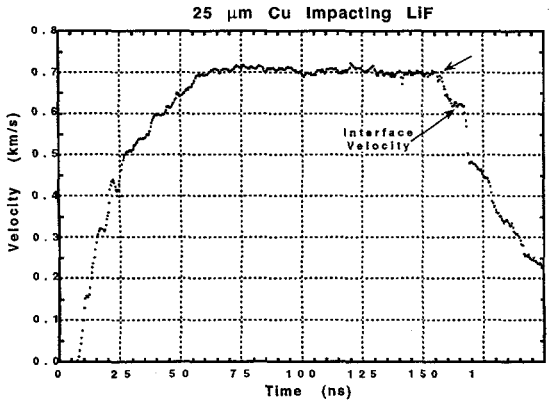

FIGURE 2. Velocity data from the VISAR. The data required are the impact and the flyer/window interface velocities.

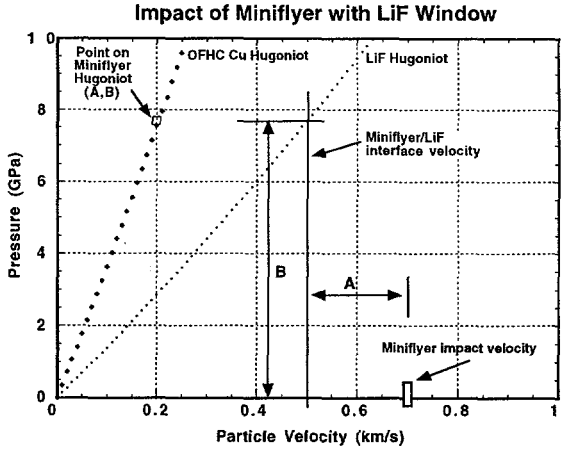

FIGURE 3. Graphical representation of the data analysis. From the flyer and interface velocities, a point on the flyer Hugoniot may be determined.

is shown as a rectangle on the particle velocity axis at 0.7 km/s. The measured interface velocity is corrected for the window effects (5–6) and then shown in Fig. 3 as the vertical line at a particle velocity of 0.5 km/s. The pressure at the flyer/target interface, B, is determined by the intersection of this vertical line and the window (in this case, LiF) Hugoniot. If the impact velocity minus the actual interface velocity is A, the coordinates of a point on the flyer Hugoniot are (A,B).

The measured Hugoniot of the flyer material is

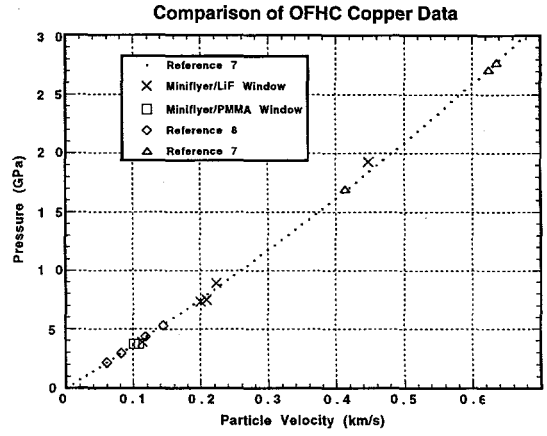

FIGURE 4. Comparison of Miniflyer data on OFHC copper with published data. LiF and PMMA windows were used in these experiments.

TABLE 1. Miniflyer Experiments, Calculations, and Comparisons

Experiment No.	Window Material	Impact Velocity (km/s)	Interface Velocity (km/s)	CTH Interface Velocity (km/s)	Measured Hugoniot u_p, P (km/s, GPa)	OFHC Cu Hugoniot u_p, P (km/s, GPa)	Difference in Pressure %
1	LiF	0.679	0.480	0.483	0.200, 7.341	0.200, 7.556	2.9
2	LiF	0.793	0.570	0.563	0.223, 8.907	0.223, 8.507	4.5
3	LiF	0.382	0.269	0.273	0.113, 3.918	0.113, 4.146	5.8
4	LiF	0.697	0.490	0.496	0.208, 7.511	0.208, 7.894	5.1
5	LiF	1.547	1.099	1.087	0.448, 19.25	0.448, 18.431	4.3
6	PMMA	0.930	0.821	0.827	0.109, 3.735	0.109, 3.993	6.9
7	PMMA	0.921	0.819	0.818	0.102, 3.724	0.102, 3.735	0.3

compared to published OFHC Hugoniot data in Fig. 4 (7–8). The parameters that can be varied to get a range of pressures and particle velocities on the Hugoniot of the flyer material are the impact velocity of the flyer (adjusted by changing the flyer thickness and the energy in the Nd:YAG laser pulse) and the impedance of the window used for the target.

The CTH code (9) has been used to model the flyer/target interaction. Table 1. gives some details of the small but representative set of experiments plotted in Fig. 4 and shows the agreement between the measured and calculated interface velocities.

SPALL ANALYSIS

The miniflyer wave profile data can be analyzed by wave code computer simulation. Information about the plasticity in the shock rise and release, as well as spall strength, can be extracted. To demonstrate this process, we present a simulation result of an early miniflyer experiment on aluminum.

Figure 5 shows the particle velocity data taken by a VISAR on the free surface of a sample foil of Reynolds aluminum nominally 50 μm thick. The flyer plate was launched from a substrate coated with a layer of vapor-deposited Al nominally 25 μm thick. The metallurgical properties of both foils are not well known.

Figure 5 also shows the result of a simulation using the characteristics wave code CHARADE (10). The materials modeling included the Johnson-Barker model for the plastic strain rate in the plastic rise (11), a backstress model for the reverse plastic flow in the release (12), and a pressure threshold spall model. The EOS used was a Mie-Grueneisen type with a pressure-dependent bulk modulus and constant Poisson's ratio (13). The equation of state material parameters used were roughly appropriate

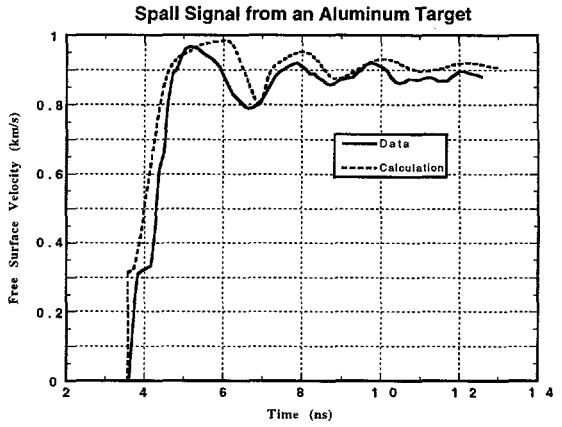

Figure 5. Comparison of free surface velocity data from a spalled aluminum target with a CHARADE wave code simulation.

for 6061-T6 Al. Using parameters for 2024 Al and 1100 Al produced little change in the calculated free surface velocity profile.

The volumetric tensile spall strength was found to be 1.8 GPa. This value, because it was obtained from a full hydro calculation in CHARADE, takes into account the wave evolution between the spall plane and the free surface. A calculated value of 2.8 GPa was found for a gas gun experiment on 6061-T6 Al (13).

In the calculation, the flyer plate impact velocity was taken to be the observed free surface peak particle velocity, since the impact velocity was not measured independently. This velocity produced a fairly good overall comparison with the free surface velocity data, as seen in Fig. 5. The fit of calculation to data was done only on a qualitative basis since the materials are not well characterized. The various materials models were adjusted to

demonstrate that the general features in the data are reproducible with CHARADE, as seen in the figure.

It is of interest to compare the materials parameters arrived at in the fitting with their counterparts from a simulation of gas gun data on 6061T6 Al at a shock strength of about 4.3 GPa and involving much larger plate dimensions (13). In the miniflyer fit, the plastic strain rate multiplier had to be increased ten fold and the dislocation multiplication right after the precursor had to be decreased by about 7 fold from the gas gun fits. In the backstress model, the miniflyer fit required about a seven fold smaller dislocation viscosity and a twenty fold increase in pinned dislocation density. The miniflyer fitting seems consistent with the sample foil being in a strongly work-hardened state from its rolling preparation, and, therefore, having a large initial dislocation density.

The calculated volumetric strain rate for the miniflyer spall was about $7.6 \times 10^7 s^{-1}$, many orders of magnitude above that of gas gun experiments. The high spallation strain rate obtainable in the miniflyer experiment is another example of the advantages this technique has to offer.

ACKNOWLEDGMENTS

We wish to thank Stephen Sheffield for constructive suggestions in the design of the experiments and Dennis Price and David Stahl for their help in assembling and conducting them. This work is supported by the United States Department of Energy under Contract W-7405-ENG-36.

REFERENCES

1.Barker, L. M. and Hollenbach, R. E., *J. Appl. Phys.* **43**, 4669–4675, (1972).

2.Hemsing, W. F., *Rev. Sci. Instrum.* **50(1)**, 73–78, (1979).

3.Paisley, D. L., Warnes, R. H., and Kopp, R. A., "Laser-driven flat plate impacts to 100 GPa with sub-nanosecond pulse duration and resolution for material property studies," *Shock Compression of Condensed Matter—1991*," 825–828, Williamsburg, VA.

4.Paisley, D. L., Warnes, R. H., and Stahl, D. B., *SPIE* **2273**, 167–172, (1994).

5.Barker, L. M. and Hollenbach, R. E., *J. Appl. Phys.* **41**, 4208–4226, (1970).

6.Wise, J. L. and Chhabildas, L. C., "Laser interferometer measurements of refractive index in shock-compressed materials," *Shock Waves in Condensed Matter*, 441–454, Spokane, WA, (1985).

7.McQueen, R. G., Marsh, S. P., Taylor, J. W., Fritz, J. N., and Carter, W. J., *High-Velocity Impact Phenomena*, New York, Academic Press, 1970, ch. 7.

8.Munson, D. E. and Barker, L. M., *J. Appl. Phys.* **37**, 1652–1660, (1966).

9.CTH is a code system under development at Sandia National Laboratory to model multi-dimensional, multi-material, large deformation, strong shock physics. Further information can be obtained from CTH Development Project, Department 1431, Sandia National Laboratories, Albuquerque, New Mexico, 87185-0819.

10.Johnson, J. N., and Tonks, D. L., "CHARADE: A Characteristic Code for Calculating Rate-Dependent Shock-Wave Response," Los Alamos Report LA-11993-MS, 1991.

11.Johnson, J. N., and Barker, L. M., *J. Appl. Phys.* **40**, 4321–4334 (1969).

12.Johnson, J. N., Hixson, R. S., Tonks, D. L., and Gray, G. T. III, "Shock Compression and Quasielastic Release in Tantalum," *High-Pressure Science and Technology—1993*, pp. 1095–1098, Colorado Springs, CO.

13.Johnson, J. N., Hixson, R. S., and Gray, G. T. III, *J. Appl. Phys.* **76**, 5706–5718 (1994).

LA-UR-95-2470 (Preprint for Proceedings of 1995 APS Topical Conference on Shock Compression of Condensed Matter, August 13 -18, 1995, Seattle, Washington)

EFFECTS OF INTERFACIAL BONDING ON SPALLATION IN METAL-MATRIX COMPOSITES

R.S. Hixson, J.N. Johnson, G.T. Gray III, and J.D. Price

Los Alamos National Laboratory, Los Alamos, NM, 87545, USA

Two metal-matrix composite systems are studied to determine the influence of inclusions on the spallation strength in plate-impact experiments. The first is an aluminum/ceramic system with several volume fractions of ceramic inclusion, and the second is a copper/niobium composite consisting of 15 vol. % niobium particles embedded in the copper matrix. Plate-impact experiments produce peak compressive stresses of ~5 GPa in the aluminum/ceramic system and ~10 GPa in the copper/niobium system. The characteristic code CHARADE is used to calculate detailed compression-release profiles in the composite systems, thus accurately quantifying the wave-evolution occurring between the spall plane and the particle velocity (VISAR) measurement at the rear free surface. The aluminum/ceramic system exhibits a strong dependence of the spall strength on inclusion concentration and morphology. In the case of the copper/niobium system, the spall strength remains essentially unchanged by the presence of 15 vol. % niobium particles embedded in the copper matrix.

INTRODUCTION

Composite materials are currently being proposed for use in a wide variety of applications. Some of these applications involve subjecting such materials to impact and dynamic tension. In this paper we present data obtained using shock compression techniques to spall several metal-matrix composites. These include three volume fractions of Al/ceramic materials and one metal-matrix/metal composite, Cu/Nb. Measurements are complemented by calculations performed with the characteristic code CHARADE (1), which gives the dynamic tensile (spall) strength at a point within the impacted sample.

EXPERIMENT

Experiments were performed on several materials. The metal-matrix/ceramic composites were of two kinds. The first material was 6061-T6 aluminum with embedded spherical particles of mullite ($3Al_2O_3$, $2SiO_2$). This material has a density of 2.840 gm/cm^3 and a volume fraction of mullite of approximately 20%. The other metal-matrix/ceramic composites (2) were 6061-T6 aluminum with angular alumina (Al_2O_3) inclusions at two volume fractions (8 and 17%). The material chosen for the metal-matrix/metal composite was Cu/Nb. This material consists of a Cu matrix with inclusions of Nb at a volume fraction of 15%; a metallograph of this material is shown in Figure 1.

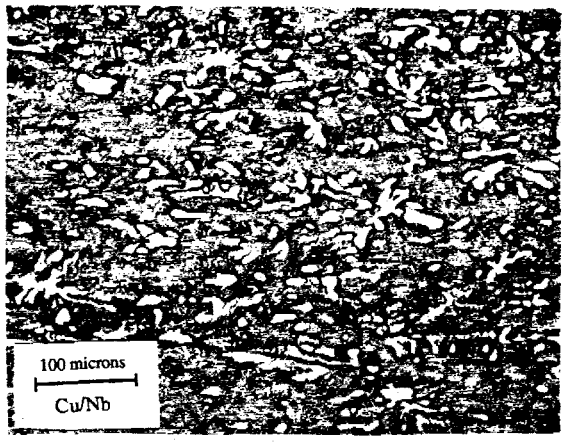

FIGURE 1. Metallography of Cu/Nb composite.

TABLE 1. Summary of Spallation Experiments.

Experiment	Projectile Velocity (m/s) [impactor]	Targ.(mm)/ Imp.(mm)	Vol. % Inclusion	Spall Str. (GPa)	Inclusion diam/morphology [composition]
Al959 (6061-T6)	550 [Qtz]	3.886/2.699	0	2.8	N/A
Com3	506 [Qtz]	3.744/2.840	20	1.9	25-50 μm/spherical [mullite/alumina]
Dur1	508 [Qtz]	3.978/2.803	8	2.0	8-10 μm/angular [alumina]
Als3_3	502 [Qtz]	3.820/2.918	17	1.1	20-25 μm/angular [alumina]
Cus2_10 (OFE Cu)	499 [Sapphire]	4.016/2.817	0	3.5	N/A
CuNb3	505 [Sapphire]	4.005/2.993	15	3.5	20-25 μm/oblong [niobium]

Measured ultrasonic velocities for the Cu/Nb material were C_l = 4.814 mm/μs and C_s = 2.199 mm/μs. Density of the Cu/Nb material was measured by an immersion technique to be 8.88 gm/cm^3 and the density for pure Cu was taken to be 8.93 gm/cm^3. Spall measurements were also performed on 6061-T6 aluminum and OFE copper to determine the spall strength of the matrix material alone; for these nominal impact conditions, the spall strength of the aluminum alloy is 2.8 GPa and that of copper is 3.5 GPa.

Shock-compression experiments were performed at two gas-gun facilities, one with a 50-mm bore and one with a 72-mm bore. Impactors used for the Al-based composites were Z-cut quartz glued to PMMA backing pieces and inlet into the nose of the projectile. Z-cut quartz was chosen because it responds elastically in the pressure range of these experiments. For the Cu-based composites Z-cut sapphire impactors were used. Various thicknesses of impactors were chosen depending upon experimental requirements. Experimental configurations were calculated using the MACRAME computer code (3). Edge-effect calculations were also carried out for each experiment to ensure one-dimensional flow for the entire time of interest. A summary of spallation (only) experiments is given in Table I.

Impact response was measured using time-resolved velocity interferometry, with a push/pull VISAR (4). This diagnostic system is capable of nanosecond level resolution, and yields particle velocity histories with less than 1% uncertainty. Particle-velocity data were taken at a free surface for spall experiments, and at a target/window interface for wave-profile experiments (not presented here).

LiF (100) windows were used for the Al-based composites and sapphire (Z-cut) for the Cu-based materials because of the close shock impedence match. For window experiments a thin (13 μm) aluminum shim was placed between the window and the target. We were able to perform free-surface (spall) experiments with no foil by slightly defocusing the VISAR laser spot.

CALCULATION

Analysis is carried out with the rate-dependent characteristic code CHARADE (1). The rate dependence in these calculations is contained in the micromechanical model of plastic flow and not in the fracture process. A simple tensile fracture model is used for spallation. The benefit of using a sophisticated rate-dependent elastic-viscoplastic model for compression and release comes from the

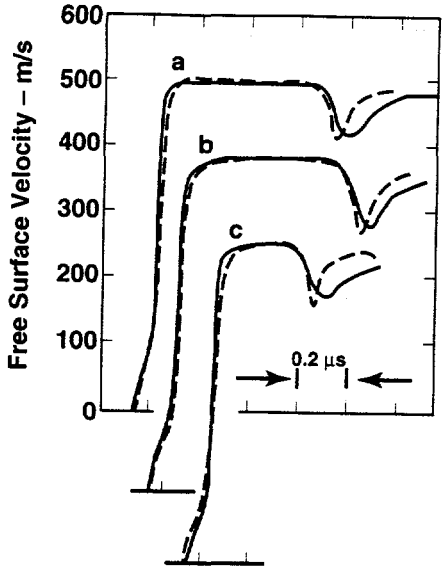

FIGURE 2. Spall signals for Al/ceramic composites; (a) Com3, (b) Dur1, and (c) Als3_3.

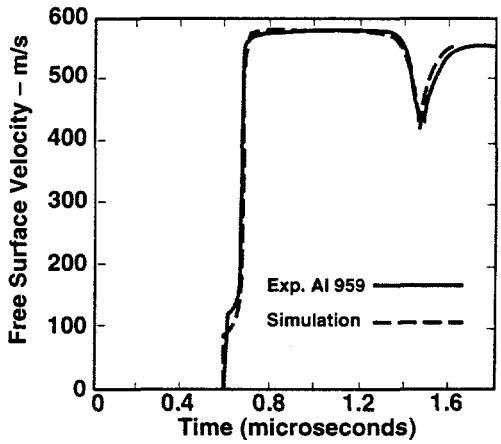

FIGURE 3. Spall signal for 6061-T6 Al.

ability to calculate accurately the evolution of complex waves that travel from the spall plane (where the fracture occurs) to the free surface (where the measurement is made).

CHARADE contains advanced models of rate-dependent elastic-plastic flow as well as micromechanical models of quasielastic release from the shocked state (5). This sophistication gives some assurance that the evolution of the spall signal will be faithfully simulated in the numerical calculation. Elastic moduli and equations of state of the composite materials are obtained from mixture theories described in reference (2).

RESULTS

In Figure 2 we show the spall results for the Al/ceramic composites (2). The spall strength of the composites may readily be seen to vary with volume fraction of ceramic reinforcement, and with shape. The presence of the alumina particles also changes the nature of the spall 'pullback' signal indicating sluggish behavior as compared to the 6061-T6 Al result: Figure 3. It is clear by comparing the results, with and without ceramic reinforcement, that the spall strength in the composites are all lower than that in 6061-T6 aluminum (Table 1). Spall results for the Cu/Nb composite and OFE Cu are shown in Figures 4 and 5. To within experimental uncertainties there is no difference in the spall behavior of these two materials, a somewhat surprising result.

One unusual feature observed in the spallation properties of the Cu/Nb composite is the small secondary spall resistance observed immediately following the minimum in the particle-velocity/time record of Figure 4. There is considerable structure in this region; it has the same qualitative features as found in the spallation of tantalum (6).

DISCUSSION

Wave-profile and spall experiments have been performed on two very different metal-matrix composites. The systems studied here were a metal-matrix/metal (Cu/Nb), and several metal-matrix/ceramic materials (Al/Al_2O_3 and Al/mullite). Results indicate that the Cu/Nb material is essentially indistinguishable from pure OFE Cu in wave-profile and spall-signal measurements. The spall strength of this material is 3.5 GPa.

Results for the Al/Al_2O_3 composites show that there is a considerable difference in spall behavior of these composites in comparison to 6061-T6 Al. The spall strength for 6061-T6 aluminum is 2.8

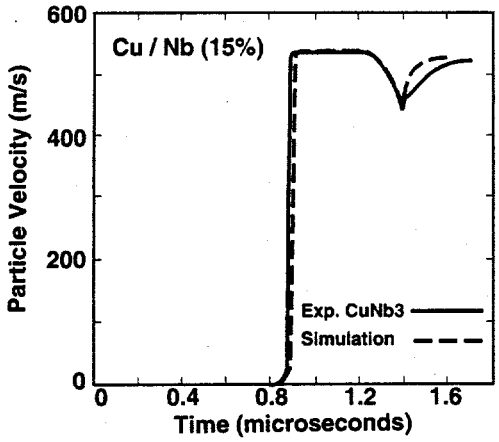

FIGURE 4. Spall signal for Cu/Nb composite.

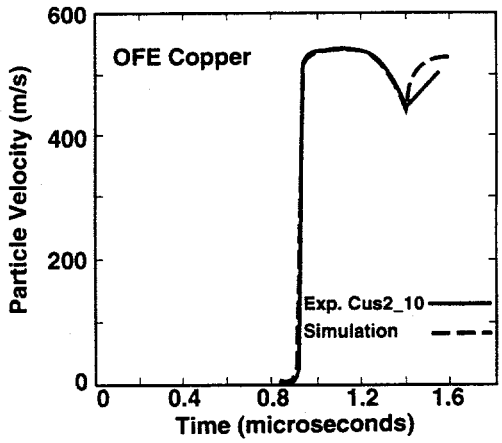

FIGURE 5. Spall signal for OFE copper.

GPa, while that for the aluminum/ceramic composites varies from 1.1 to 2.0 GPa depending on volume fraction of ceramic reinforcement and particle morphology. This complements the low-strain-rate results of Song, *et al* (7). The presence of ceramic inclusions strongly influences the dynamic material strength in tension. Our experiments show that not only does volume fraction of the ceramic reinforcement affect spall strength, but also particle shape plays a major role.

In the case of aluminum/alumina it might be suspected that the interfacial bond itself is weak; simply because of the difference between the electronic structure of metals and ceramics. However, it is believed that this bond is fairly strong and that the weakness comes from ductile failure in the metal (aluminum) adjacent to the interface between these two materials. The presence of significant elastic moduli differences contributes to substantial hydrostatic tension and causes voids to grow in the vicinity of the interface.

Additional work that would be of interest is the impact and spallation of materials which contain continuous reinforcement in the form of fine wires, for example. Experiments on this type of composite are described elsewhere in this conference (8).

REFERENCES

1. Johnson, J.N. and Tonks, D.L., "CHARADE: A Characteristic Code for Calculating Rate-Dependent Response," Los Alamos National Laboratory Report LA-11993-MS, Jan. (1991).

2. Johnson, J.N., Hixson, R.S., and Gray III, G.T., "Shock-Wave Compression and Release of Aluminum/Ceramic Composites," J. Appl. Phys. **76**, 5706-5718 (1994).

3. Fritz, J., Personal Communication (1994).

4. Hemsing, W.F., "Velocity Sensing Interferometer (VISAR) Modification," *Rev. Sci. Instrum.* **50**, 73-78 (1979).

5. Johnson, J.N., Hixson, R.S., Gray III, G.T., and Morris, C.E., "Quasielastic Release in Shock-Compressed Solids," J. Appl. Phys. **72**, 429-441 (1992).

6. Johnson, J.N., Hixson, R.S., Tonks, D.L. and Zurek, A.K., "Rate-Dependent Spallation Properties of Tantalum," this conference.

7. Song, S.G., Shi, N., Gray III, G.T., and Goldstone, J.A., "Particle Shape Effects on the Fracture Morphology and Ductility of Discontinuously-Reinforced 6061-Al Matrix Composites," submitted to Acta Metallurgica et Materialia (1995).

8. Gray III, G.T., Hixson, R.S., and Johnson, J.N., "Dynamic Deformation and Fracture Response of a 6061Al - 50 vol.% Al_2O_3 Continuous Reinforced Fiber Composite," this conference.

RATE-DEPENDENT SPALLATION PROPERTIES OF TANTALUM

J.N. Johnson, R.S. Hixson, D.L. Tonks, and A.K. Zurek

Los Alamos National Laboratory, Los Alamos, NM, 87545, USA

Spallation experiments are conducted on high-purity tantalum using VISAR instrumentation for impact stresses of 9.5 GPa and 6.0 GPa. The high-amplitude experiment exhibits very rapid initial spall separation, while the low-amplitude shot is only slightly above the threshold for void growth and thus exhibits distinct rate-dependent spallation behavior. These experiments are analyzed in terms of simple tensile fracture criteria, a standard rate-dependent void-growth model, and a rate-dependent void-growth model in which the expected plastic volume strain makes no contribution to the relaxation of the mean stress. Recovery tests and VISAR measurements suggest an additional resistance to spallation that follows the rapid coalescence of voids; this effect is termed the secondary spall resistance and is due to the convoluted nature of the spall plane and the resulting interlocking fracture pattern that is developed and for which the stress remains unrelieved until the spall planes have separated several hundred microns.

INTRODUCTION

Spallation in metals remains an important research subject in the field of shock compression science in spite of the wealth of existing spallation models and corresponding data. Spallation, like dynamic plasticity, is controlled by defects rather than the perfect lattice and hence substantial spall strength variation with impact amplitude and strain rate is sometimes seen where none is expected. In the case of tantalum (bcc) the plastic flow properties are controlled by the Peierls stress (inherent to the perfect lattice) and are not exceedingly sensitive to imperfections. The spall strength, however, is controlled by large-scale impurities that either provide initial porosity or act as nucleation sites for voids. Simple tensile fracture models are often unable to adequately represent material spall behavior because of the strong dependence on rate-dependent properties associated with void initiation, growth, and coalescence.

In this work we present a study of the spallation properties of tantalum (i) just above the spallation threshold and (ii) at an impact stress one and one-half times the spallation threshold. The experimental measurements are compared with those of Isbell, *et al* (1). The new results show the dependence of spall strength on impact amplitude and some of the complexities of the spallation process near threshold conditions when analyzed in detail in terms of void-growth models. A new phenomenon termed "secondary spall resistance" is observed and described theoretically.

EXPERIMENT

Shock-wave experiments are performed with a 50-mm-diameter gas gun. Projectile velocity and tilt are measured immediately before impact by means of a stepped circular array of shorting pins surrounding the target disk. For these experiments, tilts are typically 1.0-1.5 mrad, and impact velocities range from approximately 200 to 300 m/s: these velocities produce longitudinal stresses in the range of 6.0 to 9.5 GPa for symmetric impact.

A shock-release profile is measured using a push/pull VISAR (2) with a sapphire window. Spallation experiments are conducted with stress-free back surfaces, also with VISAR instrumentation.

The chemical composition of this material is as follows (in ppm): C(6), O(56), N(24), H(<1), Fe(19), Ni(25), Cr(9), W(41), Nb(26), Ta(balance).

CALCULATION

Following the establishment of the shock/release behavior (3,4) in the absence of spallation, a set of

calculations was performed on the theoretical spall response of tantalum at impact stresses of 6- and 9.5-GPa using a simple tensile-fracture criterion. These results are shown in Figure 1.

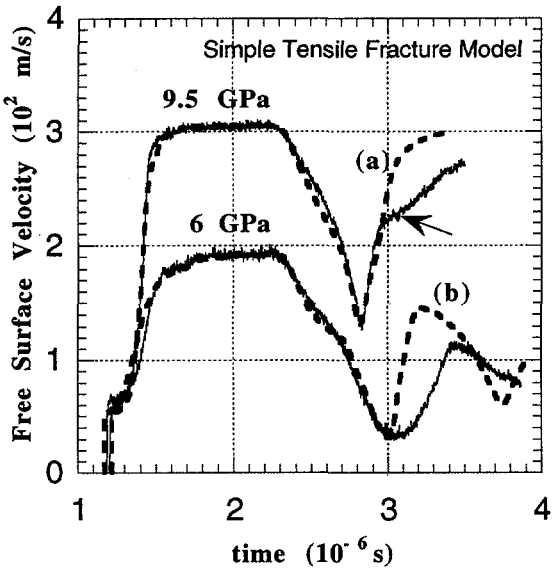

FIGURE 1. Simple tensile fracture criterion for spall.

The "spall strength" for the 6-GPa shot is 5.2 GPa and that for the 9.5-GPa shot is 7.3 GPa. It is also seen that the simple tensile-fracture criterion does not represent the obvious rate dependence observed in the lower amplitude experiment. In addition there is the peculiar deceleration that occurs shortly after the minimum particle velocity for the 9.5-GPa shot in Figure. 1 (arrow). This result is peculiar in the sense that once separation occurs at the spall plane, there should be nothing to cause further negative acceleration; in the 6-GPa experiment this resistance to rapid separation is to be expected because void growth controls the separation process - complete separation has not yet occurred.

Spall calculations were also performed with a void-growth model (5). The essential features of this model are contained in the following expressions for the time rate of change of porosity in the tensile region:

$$\dot{\varphi} = -\frac{\varphi^{1/3}}{\eta}\left[\frac{\varphi_o(1-\varphi)}{(1-\varphi_o)}\right]^{2/3}\Delta p \qquad (1)$$

$$\Delta p = \bar{p} + a_s(1-\varphi)\log\varphi \qquad (2)$$

where φ is the porosity (initial value designated by subscript 0), η is plasticity coefficient (units of viscosity), $\bar{p}$ is the mean stress, and a_s defines the flow stress for void growth.

The material constitutive relation which includes the effect of void growth is given by

$$\dot{\sigma} - (K + 4G/3)(\dot{\rho}/\rho) = F \qquad (3)$$

where F is the relaxation function given by

$$F = -2(G - \gamma\tau)\dot{\psi} + (K - \gamma\bar{p})f\dot{\varphi}/(1-\varphi) \qquad (4)$$

where G is the shear modulus, K is the bulk modulus, γ is the Grüneisen coefficient, τ is the generalized shear stress, and ψ is the plastic shear strain. The elastic moduli are degraded by a factor $(1-g\varphi)$ in comparison to the solid elastic moduli. The quantities f and g are used to control various contributions to the model; in the normal void-growth model f and g are both unity.

Calculations of spallation are performed for tantalum with Eqs. (3) and (4) with $f = 1$ and $g=1$. It is found that even qualitative agreement between theory and experiment is highly elusive, the start of the pullback signal is very abrupt [see, for example, the calculation for plate-impact-induced spall in copper, ref. 5]. These calculations and comparisons suggest that ideal, ductile void growth does not take place in this particular type of tantalum. Work done by Isbell, *et al* (1) definitely showed ductile void growth in the classical sense. The material used in their study was 99.5% pure. The tantalum studied here is considerably purer than 99.5%.

It is suspected that void growth *does* occur in these samples, but not homogeneously over the dimension of a computational cell (in these cases, the one-dimensional computational cells are 12 μm).

Calculations of the spall signals with the void-growth model omitting the void-growth term ($f=0$) in Eq. (4), but maintining the full degraded moduli ($g=1$), are shown in Figure 2. The initial porosity is taken to be 0.0005, a_s = 0.22 GPa, and η = 20 Poise as determined by numerous calculations of the spall profiles. Complete spall separation is controlled by a parameter φ_f, the maximum allowable porosity prior to rapid void coalescence.

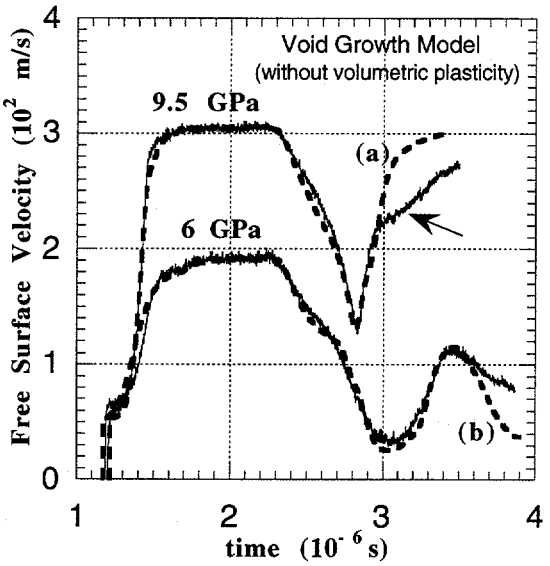

FIGURE 2. Void-growth model for spall: (a) φ_f=0.30; (b) φ_f=0.43.

The rate-dependent nature of the spall process for the 6-GPa experiment is obvious. The fracture porosity in this case is φ_f = 0.43. For the 9.5-GPa experiment φ_f = 0.30, and there is no essential difference between the calculated spall response for the simple tensile fracture criterion and for the void-growth model. The fact that the fracture porosities are different is unusual, and is something that requires further investigation.

If the link-up, or void coalescence, step in spallation were simply a rate-dependent plastic flow process, then it would be expected that higher rates of tensile loading would allow greater porosities to be achieved prior to fracture; the opposite is observed here.

The agreement shown in Figure 2 is suggestive of a material for which the void growth is limited to a small region within a computational cell (brittle fracture) and whose moduli are reduced by the presence of this damage, but whose volumetric plastic strain is not strongly affected.

SECONDARY SPALL RESISTANCE

One of the most interesting and peculiar observations associated with the 9.5 GPa spall signal is the sudden deceleration that occurs in the pull-back signal (arrow, Figure 1). It appears that the material has undergone complete spallation, i.e., material separation, and then finds that there remains a substantial restoring force tending to decelerate the spalled piece. This remained a puzzle until recovery experiments were performed to examine the nature of the actual spall plane. The spall region is shown in Figure 3 for a 9.5 GPa impact stress.

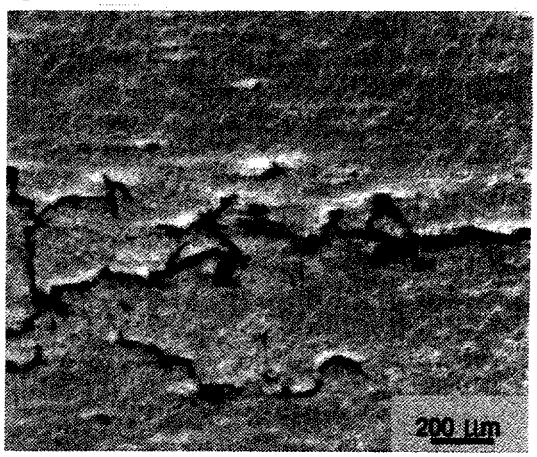

FIGURE 3. Spalled region for peak impact stress of 9.5 GPa.

It is seen from Figure 3 that the spall plane is not a distinct fracture surface, but rather is extended over several tens of microns in the direction of wave propagation (vertical). This observation suggests that the initial loss of strength takes place by the coalescence of voids to form a system of small cracks (long dimension perpendicular to impact direction) extended over a finite region of several tens of microns normal to the spall plane. The initial loss of material strength obtains from the formation and elastic opening of these cracks and the corresponding drop (to near zero) of the longitudinal tensile stress. Following this initial loss of tensile strength, the extended spall plane pulls apart and undergoes additional linking of these cracks to eventually form the separated spall plane, but not before developing considerable secondary resistance to separation: this is what we refer to as secondary spall resistance (SSR)

The SSR is modeled in terms of an additional tensile stress that develops following simple tensile fracture. As the separation distance x between the left and right sides of the spall surface increases, the SSR is given by:

$$\sigma_{SSR} = 0 \quad for \quad x < a \quad and \quad x > b \qquad (5a)$$

$$\sigma_{SSR} = f\sigma_s[(x-b)/(b-a)] \quad for\ a < x < b \qquad (5b)$$

where σ_s is the absolute magnitude of the spall strength and f is a nondimensional number less than unity. Generally a will be on the order of a few microns (the onset of SSR) and b will be on the order of a hundred microns (the end of SSR). Equations (3) represent the stress necessary to pull apart the convoluted spall plane shown in Figure 3.

Calculations of the spallation behavior with this model of SSR is shown in Figure 4 for a = 5 microns, b = 200 microns, and f = 0.20.

DISCUSSION

The fracture properties of metals are extremely complex. The combination of plastic flow properties and impurity content that control the fracture process provides very subtle differences that result in brittle behavior in some cases and fully ductile behavior in others. Temperature is another parameter that we have not yet even begun to investigate, but one that obviously has a strong influence on these properties.

Tantalum studied previously (1) (99.5% pure) exhibited classical ductile spallation properties in the range of impact stresses from approximately 7 GPa to 9 GPa. The material studied here quite obviously fails to behave in the ideal manner and consequently the ductile void-growth model must be modified in order to represent the time-resolved spallation data. It is found empirically that a fit to the data can be obtained by omitting the void-growth term from the relaxation function F, Eq. (4). This is clearly not very satisfying and other methods were sought in order to obtain a similar fit. A second method was found in which the factors f and g (multiplying the void-growth term in the relaxation function and in the damage term controlling the moduli) were equal and less than unity: $f = g \sim 0.05$. Additional calculations must be performed to determine the complete range of parameter space for which reasonable fits to the data can be obtained.

A new effect was observed in the 9.5 GPa experiment described here. This is termed

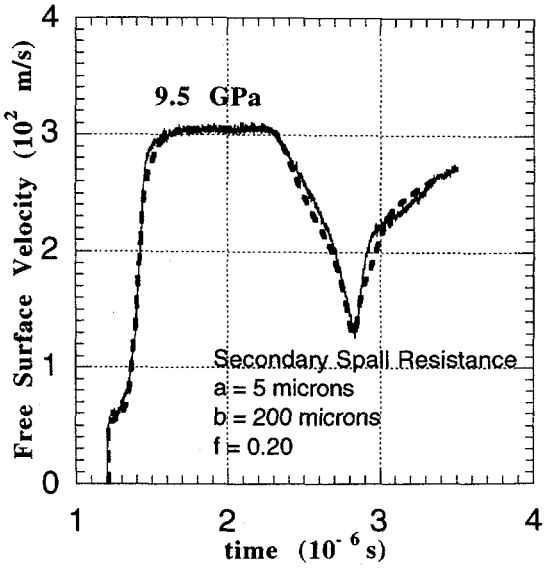

FIGURE 4. Calculation of spall signal with secondary spall resistance included.

Secondary Spall Resistance (SSR) and has to do with the resistance provided by the extended spall plane as it tries to pull apart in the fashion of a jigsaw puzzle. This effect is very pronounced, and is represented in terms of a secondary force that applies once the (left and right) spall surfaces have moved apart a few microns and continue until separation reaches a few hundred microns.

REFERENCES

1. Isbell, W.M., Christman, D.R., and Babcock, S.G., "Measurement of Dynamic Properties of Materials, Vol. VI, Tantalum," Defense Nuclear Agency Report DASA 2501-6, February (1972).

2. Hemsing, W.F., "Velocity Sensing Interferometer (VISAR) Modification," *Rev. Sci. Instrum.* **50,** 73-78 (1979).

3. Johnson, J.N., Hixson, R.S., Gray III, G.T., and Morris, C.E., "Quasielastic Release in Shock-Compressed Solids," J. Appl. Phys. **72,** 429-441 (1992).

4. Johnson, J.N., Hixson, R. S., Tonks, D. L., and Gray III, G.T., "Shock-Compression and Quasielastic Release in Tantalum," High Pressure Science and Technology - 1993, edited by S. C. Schmidt, J. W. Shaner, G. A. Samara, and M. Ross, American Institute of Physics Conference Proceedings 309, Part 2, 1095-1098 (1993).

5. Johnson, J.N., "Dynamic Fracture and Spallation in Ductile Solids," J. Appl. Phys. **52,** 2812-2825 (1981).

ORIENTATION-DEPENDENT SHOCK RESPONSE OF EXPLOSIVE CRYSTALS *

J. J. DICK

Group DX-1, MS P952, Los Alamos National Laboratory, Los Alamos, New Mexico 87545 USA

Some orientations of PETN crystals have anomalously high shock initiation sensitivity around 4 to 5 GPa. Results of a series of laser interferometry experiments at 4.2 GPa show that this is associated with an elastic-plastic, two-wave structure with large elastic precursors. Implications for the initiation mechanism in single crystals is discussed. Initial work on beta phase, monoclinic HMX is also described.

INTRODUCTION

Anomalous luminescent emission and initiation of detonation have been observed for two orientations of single crystals of pentaerythritol tetranitrate (PETN) in shock experiments near 4 GPa.(1) The crystals were more sensitive at 4.2 GPa than at 8.5 Gpa. From the data available it was not clear what was responsible for this anomaly. In addition to the sensitivity anomaly observed in wedge experiments, there was an unusual intermediate velocity transition between the initial shock velocity and the final detonation velocity in a wedge experiment on a [110] crystal. After consideration of these results it seemed that measuring time-resolved histories at several thicknesses through the initiation regime would be very helpful in clarifying the nature of the anomaly. Therefore a series of measurements of particle velocity vs time at several thicknesses through the initiation regime was undertaken using velocity interferometry. The results indicate that the anomaly is associated with separated elastic and plastic waves with large elastic precursors. In addition to the [110] experiments, experiments were performed at 4.2 GPa on [100] and [001] orientations as well. The records show orientation dependence in accord with previous luminescent emission experiments and a model of orientation dependence of shock sensitivity based on steric hindrance to shear.(2,1) Interferometry experiments were performed on [110] crystals at stresses ranging from 4.0 to 7.2 GPa in order to look at the variation in material response from the anomalous regime to the higher stress regime. The records show a continuous variation from one type of history to another. At higher stresses with a single shock, the initiating flow peaks further behind the shock wave. This results in slower shock growth at 6 and 7.2 GPa than at 4 to 5 GPa.

*Work performed under the auspices of the U. S. Department of Energy

EXPERIMENTAL TECHNIQUE

PETN crystals were subjected to shocks using a light-gas gun. Particle velocity vs time histories were recorded at the PETN/PMMA window interface using a velocity interferometer. Projectiles made of 2024 aluminum were impacted on Kel-F (polytrifluorochloroethylene) discs 50 mm in diameter and 5 mm thick. The PETN crystals were mounted on the Kel-F discs with a silicone elastomer. The crystals had typical lateral dimensions of 15 mm.

The measurement system used was a dual, push-pull, VISAR system.(3) The dual VISAR with different fringe constants removes ambiguity in determining the particle-velocity jump at the shock when extra fringes must be added. The light was transported from the argon-ion laser to the target and thence to the interferometer table with fiber optics.

EXPERIMENTAL RESULTS

In previous work(1) anomalous detonation was observed in a [110] PETN crystal in a wedge experiment at about 4.26 GPa. The run distance to detonation in wedge experiments was shorter at

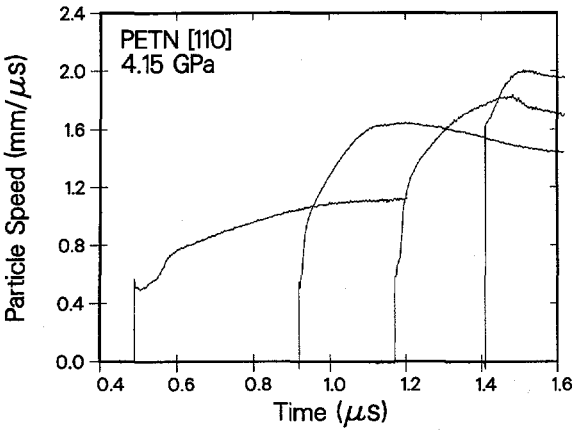

FIGURE 1. Particle vs time histories at the PETN/PMMA interface for a 4.15 GPa input shock at 1.825, 3.47, 4.44, and 5.55 mm PETN thicknesses of [110] orientation

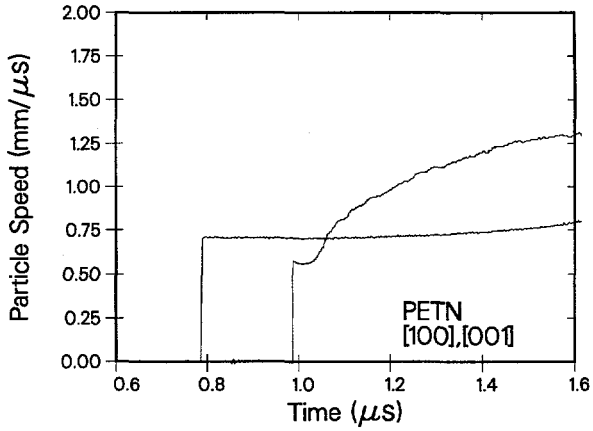

FIGURE 2. Particle vs time histories at the PETN/PMMA interface for a computed 4.15 GPa input shock strength for [001] and [100] orientations. The [001] crystal thickness was 3.79 mm and the [100] crystal thickness was 2.90 mm.

4.26 GPa than at 8.5 GPa. The run distance normally would increase and the sensitivity decrease with decreasing input shock stress. Furthermore, the run distance was the same at 4.2 Gpa and at 9.2 Gpa, a double-valued behavior. More experimental information was needed to clarify the behavior. In order to observe the behavior behind the leading shock wave, a series of four VISAR experiments was performed at 4.15±0.01 GPa on [110] crystals of different thicknesses in order to obtain particle vs time histories through the initiation regime. The first two with crystal thicknesses of 1.825, and 3.47 mm were in the region of constant initial shock velocity in the wedge experiment. The third at 4.44 mm thickness was at the onset of the intemediate velocity transition. The fourth experiment with a crystal thickness of 5.55 mm was in the region of the intermediate velocity transition. The particle velocity vs time histories obtained at the interface are shown in Fig. 1. It was unexpected to see a two-wave structure. In Ref.(1) the leading wave was thought to be the bulk or plastic wave to the final shock state.

The two-wave structure recorded at 1.825 mm is a large elastic shock followed by a more-dispersed plastic wave. The elastic wave amplitude is 2.74 GPa in PETN. This precursor strength is much larger than those seen for input shock strengths of 1.14 GPa. There the elastic precursor shock strength for [110] crystals was 1.0 GPa. Dependence of elastic precursor strength on input shock strength in [110] and [001] PETN crystals was noted in earlier work for shock strengths up to 2.7 GPa.(4) Elastic precursor strengths were as strong as 2.0 GPa after 5 mm of wave propagation in that work.

The profile behind the plastic wave is not flat and steady as would be expected in an inert material. Instead, there is evidence of exothermic initiation chemistry causing increasing particle velocity immediately behind the plastic wave. The initiating flow accelerates the second wave so that it completely overtakes the elastic shock by about 4.6 mm causing the intermediate velocity transition. The detonation transition was at 6.6±0.2 mm in the wedge experiment.

In Fig. 2 particle velocity vs time histories for [001] and [100] orientations for the same input stress are displayed. For the [001] orientation an elastic-plastic, two-wave structure is displayed similar to that observed in [110] orientation. The elastic precursor strength is 3.15 GPa, larger than observed in [110] orientation. However, the initiating wave is weaker than in [110] at that thickness. In contrast, the [100] crystal displays a single wave to the final state followed by a nearly constant particle velocity indicative of essentially inert behavior. These behaviors correlate with the relative steric hindrance to shear.

DISCUSSION OF THE RESULTS

Elastic-Plastic Wave Structure

In the [110] and [001] orientations there is an elastic-plastic wave structure in the region of the low-shock-stress sensitivity anomaly observed for [110] crystals. Initiation begins in or immediately behind the plastic wave. This is consistent with our model of steric hindrance to shear.(1,2) In the model the endothermic first step in explosive decomposition is chemical bond breaking in the sterically hindered shear flow in the plastic wave or shock. This leads to the exothermic decomposition steps on the way to initiation of detonation, especially at low stresses. Our previous geometric analysis of steric hindrance for rigid molecules found [110] and [001] orientations to be hindered and [100] and [101] orientations to be relatively unhindered. These results were corroborated by molecular mechanics analysis of deformable molecules for the cases considered, [100], [101], and [110]. For the [100] orientation there is a single wave with a flat following flow indicative of no initiation response. This is consistent with the minimal steric hindrance for this case. The small elastic precursor(2) has been overdriven by the plastic wave at this level of shock strength; i.e., the wave speed on the plastic Hugoniot is faster than the wave speed on the elastic Hugoniot for the input particle velocity of 0.616 mm/μs.

The two-wave structure explains another feature noted in earlier work.(1) From photodiode records of the luminescent emission it was inferred that there was an absorbing or dark zone behind the leading shock. This is consistent with the emission coming from the region of the plastic wave, not the leading elastic wave. The interpretation is that the peak in the photodiode signal and the subsequent fall in signal level is due to quenching of the emission in the crystal by the rarefaction from the free surface after arrival of the plastic wave. In Fig. 3 particle velocity records are shown of the elastic-plastic wave structure for [110] and [001] orientations. There are arrows on each record marking the time at which the photodiode peak would be based on data presented in our 1991 article.

In order to determine the position of the photodiode peak for the sample thicknesses corresponding to the VISAR experiments, the following analysis was performed. The photodiode records were obtained for crystal thicknesses different from those used in the VISAR experiments. For [110] orientation the photodiode record was for a crystal 2.79 mm thick vs 1.825 mm for the VISAR record. For [001] orientation the photodiode record was for a crystal 3.94 mm thick vs 3.79 mm for the VISAR record. The input shock stresses were were equal within 0.22 GPa for [110] orientation and within 0.11 for the [001] orientation. An analysis was performed in the position-time plane to determine the arrival time for the event associated with the photodiode peak at the sample thicknesses of the particle velocity records assuming a constant velocity for the disturbance. Account was taken of the particle velocity of the PETN/PMMA interface in the VISAR experiment and PETN free surface velocity in the emission experiment, but wave interactions were ignored. The disturbance arrival time t is given by:

$$t = \frac{t_0 - \frac{x_0}{u_i}}{1 - \frac{U_{pk}}{u_i}} \qquad (1)$$

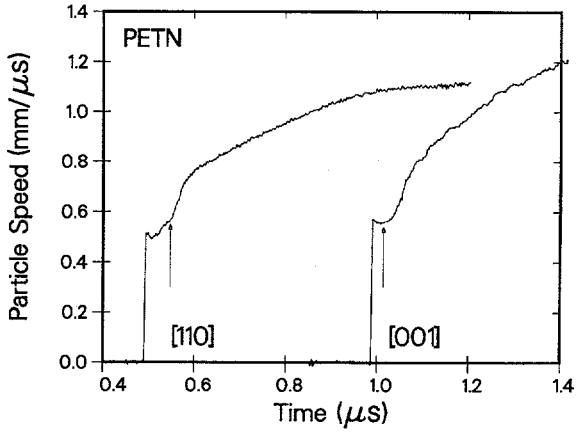

FIGURE 3. Particle vs time history at the PETN/PMMA interface for [110] and [001] crystals shocked to about 4.16 GPa. An elastic-plastic,two-wave structure is displayed by both records. The plastic wave is followed by increasing particle velocity due to exothermic initiation processes. In each case the arrow indicates the inferred position of the peak in emission as determined from a photdiode record in earlier work. The beginning of the fall in emission intensity coincides roughly with the beginning of the plastic wave. This indicates that the luminescent emission begins at the base of the plastic wave.

where t_0 is the elastic wave transit time in the VISAR experiment, u_i is the velocity of the PETN/PMMA interface in the VISAR experiment, and U_{pk} is the apparent velocity of the photodiode peak from the photodiode experiment.

The striking result as seen in Fig. 3 is that quenching of the emission begins as soon as the initial portion of the plastic wave arrives at the free surface, at least within the 10-20 ns accuracy of the analysis. This implies that the emission originates from the entire plastic wave not just behind it. It suggests that onset of emission coincides with the onset of sterically hindered shear. From time-resolved spectral measurements this emission was interpreted as due to excited electronic states of NO_2.(1) This raises the possibility that the emission is due to direct nonequilibrium excitation by the sterically hindered shear. As suggested in an earlier article(2) the endothermic first step in initiation may involve nonequilibrium excitation of molecules on a femtosecond time scale caused by a mechanical process, sterically hindered shear occuring in the plastic flow associated with the uniaxial strain in a plane shock. In the molecular mechanics calculations in that article the dihedral angle changed by up to 60°, a much larger change than that caused by thermal motion. Also, the calculations indicated that significant bond angle strain occurred in PETN for the most hindered cases. Ref. (5) suggests ways in which bond angle distortion can drastically change the electronic state of a molecule.

It is worth mentioning that the calculated homogeneous temperature rise at 4.2 GPa is about 100 °C. The peak in the spectral data corresponds to 5000 to 6000 K by Wien's law, an unreasonable heterogeneous temperature, much higher than detonation temperature. Furthermore the spectral curves do not fit those of a gray body with constant emissivity. Rather, the spectra have the character of a chemiluminescent edge on the blue side. This result substantiates the previous conclusion that the observed emission is due to luminescence from excited electronic states.(1) While we consider the nature and timing of the emission to be evidence for a mechanoluminescent mechanism, the possibility that the sterically hindered shear causes vibronic uppumping followed by bond breaking, and that the electronic excited states are due to subsequent chemical reactions on a nanosecond time scale cannot be ruled out.

HMX STUDIES

Work has begun on studying the unit cell of this monoclinic crystal. The space group is $P2_1/c$. Possible slip systems are being studied for relative steric hindrance for different possible shock orientations. Because of the reduced symmetry of the unit cell, there are many more cases to consider than for PETN. The known slip systems of anthracene and other molecular crystals of the same space group have been studied for possible guidance. The importance of twinning in deformation of HMX is another complication.(6,7) Crystals of 110 and 011 orientations in $P2_1/n$ have been cut into slabs in preparation for VISAR experiments.

REFERENCES

1. J. J. Dick, R. N. Mulford, W. J. Spencer, D. R. Pettit, E. Garcia, and D. C. Shaw, J. Appl. Phys. **70**, 3572 (1991).
2. J. J. Dick and J. P. Ritchie, J. Appl. Phys. **76**, 2726 (1994).
3. Willard F. Hemsing, Rev. Sci. Instrum. **50**, 73 (1979).
4. P. M. Halleck and Jerry Wackerle, J. Appl. Phys. **47**, 976 (1976).
5. J. J. Gilman, Phil. Mag. B **71**, 1057 (1995); in *High-Pressure Science and Technology-1993-Part 2, Amer. Inst. Phys. Conf. Proc. 309*, edited by S. C. Schmidt, J. W. Shaner, G. A. Samara, and M. Ross, p. 1349, New York, 1994, AIP Press.
6. S. J. P. Palmer and J. E. Field., Proc. R. Soc. Lond. A. **383**, 399 (1982).
7. R. W. Armstrong, H. L. Ammon, Z. Y. Du, W. L. Elban, and X. J. Zhang, in *Structure and Properties of Energetic Materials, MRS Symposium Proceedings, Vol. 296*, edited by D. H. Liebenberg, R. W. Armstrong, and J. J. Gilman, p. 227, Pittsburgh, 1993, Mat. Res. Soc. Press.

SHOCK INITIATION OF PBX-9502 AT ELEVATED TEMPERATURES

R. N. Mulford and R. R. Alcon

Los Alamos National Laboratory, Los Alamos, New Mexico 87544

The shock sensitivity of PBX-9502 is known to change with temperature. Both volume expansion and increased internal energy may contribute to this phenomenon. PBX-9502 was heated and its initiation and detonation behavior was examined, using MIV and shock tracker gauging on a light gas gun. Sensitivity and reactive wave profiles were measured. Complementary experiments were done on PBX-9502 made to undergo "ratchet growth", or non- reversible anisotropic thermal expansion, under carefully controlled thermal cycling. This process causes noticeable size changes and significant changes in sensitivity. Sensitivity and reactive wave profiles are discussed in terms of density and microscopic material morphology.

INTRODUCTION

TATB-based explosive PBX-9502 exhibits interesting thermal behaviors that may be expected to influence the sensitivity of the material at elevated temperatures. Both morphological and chemical changes may be important in understanding the response of PBX-9502 at temperatures above ambient.

Morphological changes include alteration in size and distribution of hotspots and a decrease in initial density with increasing temperature. On heating, TATB-based explosives undergo "ratchet growth," or non-reversible thermal expansion, as a result of grossly anisotropic thermal expansion of TATB crystallites in the material. The phenomenon is complicated, with the material exhibiting several different growth regimes at different temperatures,[1] due to interactions of crystallites and binder behavior. As the crystallites and binder are expanded and redistributed, intercrystalline porosities are believed to decrease, while intracrystalline porosities are believed[2] to increase, both of which may be expected to influence initiation properties.

Dependence of reaction rate on temperature almost certainly increases the reaction of the TATB at elevated temperatures, although extensive experiments by Buntain[3] have shown the increase in reactivity with increasing temperature to be small.

EXPERIMENTAL

Experiments are done on a single stage light gas gun, using in-material magnetic (MIV) gauging[4,5,6] in a target specially modified to allow controlled heating and temperature monitoring.

The target is heated front and back using silicone rubber flexible heaters[7] rated to 45W and 220°C. The entire target was insulated with household fiberglass insulation. Temperature was monitored at 4 locations including the gauge plane, using both wire and fine foil[8] copper constantan thermocouples. Thermocouple mortality was high during heating, possibly due to expansion of the PBX material onto which the TC was fastened. One minute before firing, the front heater and insulation was jettisoned using a spring assembly, to provide an unimpeded planar surface for projectile impact. Heating rates and temperature uniformity within the target were thoroughly studied, as was cooling after ejection of the front heater. Heating was performed at between 0.5 and 1°C/minute, to prevent thermal stresses, distortion, or cracking in the PBX material.

The gas gun generates reliably well-supported shock waves with a well-characterized wave shape. The square pressure pulse simplifies consideration of the time-dependent behavior of the growth of the reactive wave. The gas gun can reach

projectile velocities of up to 1.4 mm/usec, corresponding to pressures of up to about 10.5 GPa in full-density PBX materials when single crystal sapphire impactors are used. This maximum pressure is insufficient to detonate cold PBX-9502 within the observable time, but if the material is hot or has undergone non-reversible thermal expansion to a lower density, then the run to detonation will be short enough to provide good data. Particle velocity u_p was measured directly using ten nested magnetic gauges, and shock velocity U_s was obtained from time of arrival at the different gauges and from a shock tracker gauge.[6]

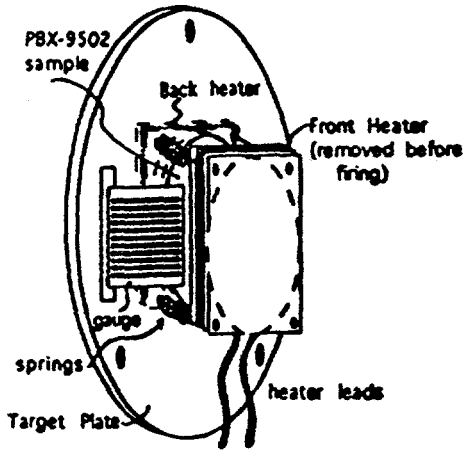

Figure 1. The hot MIV target

DISCUSSION

Heated material exhibits quite different reactive behavior from other detonable (HMX-based) PBX materials studied at these pressures. Waveforms observed in PBX-9502 at 80°C are shown in Figure 2. The mechanism for increased reactivity at high temperatures consists of two factors, temperature dependence of the reaction, and material morphology. These data confirm that significant changes in material morphologies occur between ambient and 100°C, as has been proposed to explain anomalous thermal expansion and contraction data[1].

Between 25°C and the pressing temperature of the material, which varies between 80°C and 100°C, TATB crystallites undergo thermal expansion to reoccupy the voids created when they cooled and contracted after pressing. This process produces some net volume expansion, but is generally recognized[2] to result in a decrease in porosity of the PBX material. Above the pressing temperature, further expansion of TATB crystallites pushes them apart. This "graphitic" growth along with increased flow of the binder increase the void fraction as the net volume increases rapidly. Porosity discussed here refers only to intercrystalline voids. It is anticipated that intracrystalline voids increase uniformly with temperature, but data is inconclusive.

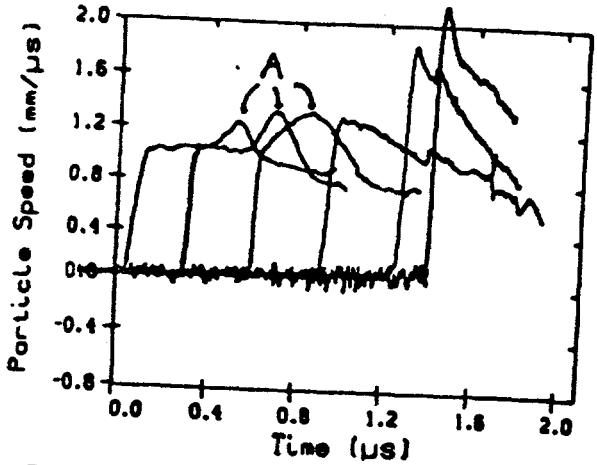

Figure 2. MIV gauge records for PBX-9502 reacting at 80°C. Baseline drift due to an electronic artifact has been corrected.

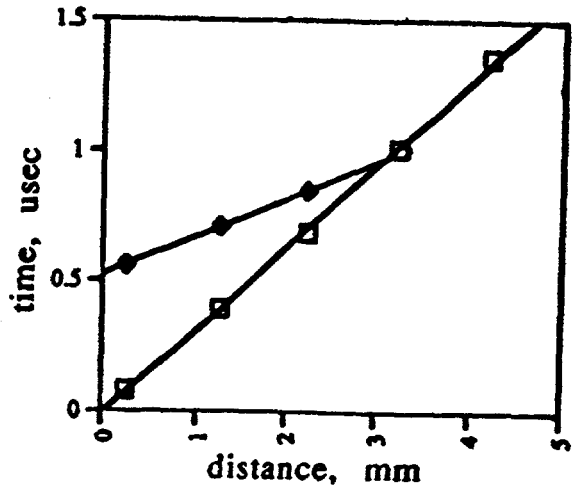

Figure 3. The x-t diagram drawn from experimental data shows the overtake of the shock (□) by the superdetonation. (◇)

Material near the pressing temperature can thus be expected to have quite low intercrystalline porosity, resembling a very dense solid or a liquid. The development of detonation in the absence of hot spots relies on homogeneous initiation,[9] in which the reactive wave or "superdetonation" arises in the hot shocked material after the shock front has passed, and then accelerates to join the shock front as a full detonation wave. The process is chemical, rather than mechanical. This "superdetonation" is clearly visible, marked "A" in the u_p records shown in Figure 2. The location of the reactive wave maximum is measured in each record, and the position of this wave is shown in the x-t diagram shown in Fig. 3. Further examples of this behavior in liquids may be found in the literature.[10]

At higher temperatures, the (intercrystalline) void fraction increases, restoring the material to a typical porous PBX, and the initiation to a homogeneous mechanism. The data shown in Figure 4 was taken at 100°C, and shows u_p profiles typical of heterogeneous initiation, comparable with that of room temperature HMX-based PBX materials.

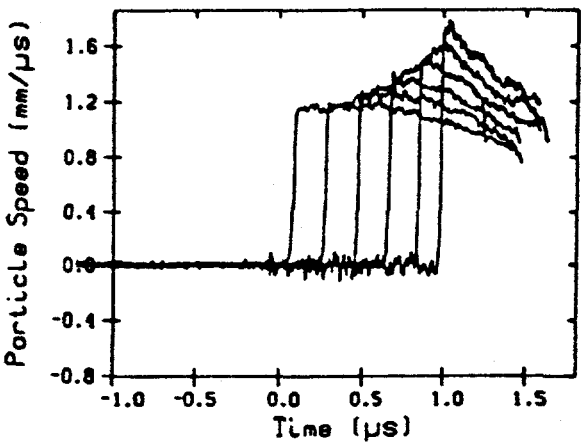

Figure 4. Detonation behavior of PBX-9502 at 100°C.

These records are consistent with the expectation that the material morphology is altered in different ways as the material passes through different temperature regimes, and that detonation behavior depends strongly on the material morphology, specifically on intercrystalline voids.

A second explanation should be considered for these data. The detonation behavior of TATB-based materials has been suggested to be homogeneous, because the void size is small relative to the reaction zone of the TATB. In this case, the 80°C data may be viewed as an extension of the room temperature behavior. The records obtained at 100°C may be anomalous, resulting from microcracking during heating. This kind of microcracking has been seen[11] in a few of many identical PBX-9502 samples subjected to the same very controlled heating. Microcracking has a marked effect on the growth of the reactive wave. A larger number of experiments will assist in distinguishing between these possibilities.

The apparent irrelevance of intracrystalline porosity to the initiation mechanism lends some support to the assertion that small voids do not assist in the hot spot initiation of the PBX-9502. However, the true behavior of intracrystalline voids with temperature is not well characterized.

The chemical contribution to the increase in reactivity at these elevated temperatures may be evaluated by comparison of the run distance for PBX-9502 at reduced density with the run distance vs. run time points for these heated samples. Plots are shown in Figure 5.

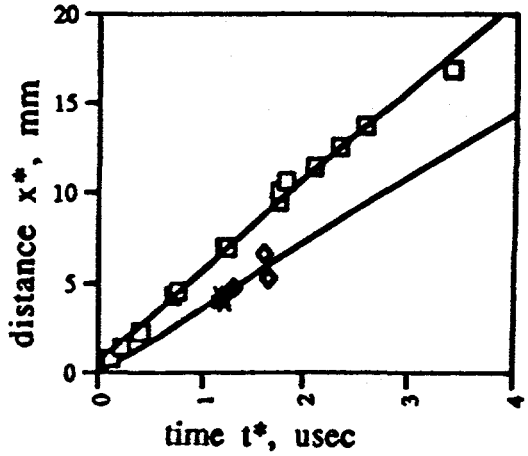

Figure 5. The run distance for the heated PBX-9502 sample (✱) is comparable to the run distance for PBX-9502 at initial density of 1.825 (◇), but differs from the run for cold PBX-9502. (□)

The points for reduced density material were obtained from shots done on cold PBX-9502 that had been subjected to ratchet growth by repeated heating in an oven to 211oC, cooling very slowly to room temperature in between cycles. The resulting samples were then machined into MIV wedges and fired cold on the gas gun. Wackerle and Dallman[2] show that the sensitivity of material expanded in this way does not differ from material pressed to the same reduced density, ruling out chemical decomposition during the heating cycles.

The density of the 80°C sample can be estimated[1,2] to be 1.848, compared with 1.825 for the expanded material, allowing for the possibility that its reaction may be slightly accelerated by temperature in order for its run distance to fall with that of lower density material. Points for both hot and expanded PBX-9502 fall on the Hugoniot given by Dallman and Wackerle[2] for PBX-9502 at 75°C.

CONCLUSION

The rate of chemical reaction of TATB is increased with temperature, since the 80°C sample exhibits a shortened run distance despite the decreased porosity of the sample and the homogeneous initiation mechanism, which is independent of hot spots.

In the temperature regime above the pressing temperature, porosity increases and hot spot density and activity dominate the reaction, masking bulk thermal effects on chemical rate. The initiation mechanism in this case is heterogeneous.

The observation of increased chemical reactivity supports Wackerle and Dallman's[2] proposal that those hot spots that are too small to cause significant reaction behind a given shock will, above a certain temperature, become effective and contribute to the initiation of the explosive.

The limits on the temperatures and porosities at which PBX-9502 will exhibit homogeneous initiation behavior will contribute interesting data to the understanding of hotspot reaction, yielding data on the interaction of chemical reaction rate and hotspot effectiveness.

1. Howard Cady, Los Alamos National Laboratory, M-1, informal report written to J. Dallman concerning high temperature materials property measurements on PBX-9502 and LX-17, May 1993.

2. J. Dallman and J. Wackerle, Tenth Symposium (International) on Detonation, #110, July 12-16, 1993.

3. G. A. Buntain, Los Alamos National Laboratory, M-1, informal report written to J. Dallman, M-1, concerning the impact sensitivity of TATB powders at ambient, 250°C, and 300°C, June 1990.

4. R. Mulford, S. Sheffield, and R. Alcon, in "High Pressure Science and Technology," Colorado Springs, 1993, p. 1405.

5. S. Sheffield and R. Alcon, in "High Pressure Science and Technology," Colorado Springs, 1993, p. 1405.

6. R. Mulford and R. Alcon, "Shock Tracker Configuration of In-material Gauge," this volume.

7. Watlow Corporation, 003030C1.

8. RDF Corporation, Hudson, New Hampshire.

9. A. W. Campbell, W. C. Davis, and J. R. Travis, Phys. Fluids 4, 498 (1961).

10. S. A. Sheffield, Ray Engelke, and R. R. Alcon, Ninth Symposium (International) on Detonation, p. 39 (1989).

11. R. Mulford, unpublished MIV records obtained from PBX-9502 subjected to thermal expansion and contraction.

WEDGE TEST DATA FOR THREE NEW EXPLOSIVES: LAX112, 2,4-DNI, AND TNAZ *

L.G. Hill, W.L. Seitz, J.F. Kramer, D.M. Murk, and R.S. Medina

Los Alamos National Laboratory, Los Alamos, New Mexico 87545 USA

High pressure Pop-plots and inert Hugoniot curves have been measured for three new explosives: LAX112 (3,6-diamino-1,2,4,5-tetrazine-1,4-dioxide), 2,4-DNI (2,4-dinitroimidazole), and TNAZ (1,3,3-trinitroazetidine). LAX112 and 2,4-DNI are of interest because of their insensitivity, while TNAZ is useful for its performance and castability. The shock sensitivity of LAX112 and 2,4-DNI fall between that of pressed TNT and PBX9502, LAX112 being the less sensitive. The shock sensitivity of TNAZ falls between that of pressed PETN and PBX9501. The inert Hugoniots for all three materials are comparable to those of other explosives.

INTRODUCTION

LAX112 (3,6-diamino-1,2,4,5-tetrazine-1,4-dioxide), Fig. 1a, was developed at Los Alamos in an effort to find an insensitive high explosive with better performance than TATB. LAX112 is distinguished by its high nitrogen content and the absence of nitro groups. It has a high detonation velocity ($\approx$ 8.3 mm/μsec), but cylinder tests show that its metal pushing performance, while marginally better than TATB, is significantly below that of HMX, RDX, and PETN based explosives (1).

2,4-DNI (2,4-dinitroimidazole), Fig. 1b, is another candidate for an insensitive high explosive. Its detonation velocity ($\approx$ 7.8 mm/μsec) is slightly less than that of LAX112, while its metal pushing performance appears to be slightly better (2). Drop-weight impact tests have shown significant batch-to-batch variations in sensitivity (as much as a factor of three), and 4-nitroimidazole impurities are the suspected cause (1).

TNAZ (1,3,3-trinitroazetidine), Fig. 1c, first appeared in the open literature in 1990 (3), but was initially of little practical interest due to excessive synthesis cost. Efforts at Los Alamos and the Aerojet corporation to find alternate synthesis routes (4) have been successful, and TNAZ is, at the time of this paper, starting to be produced in quantity by Aerojet. TNAZ is very promising in that it has a performance similar to HMX but is melt castable. Thus it is a potential replacement for octols, cyclotols, and even HMX-based PBXs in many applications.

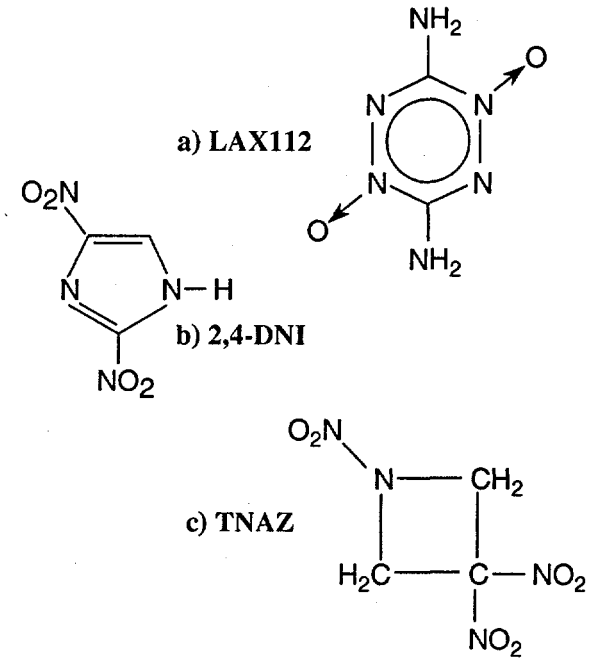

FIGURE 1. Molecular structures of LAX112, 2,4-DNI, and TNAZ.

*This work jointly supported by the US DoD and DOE.

EXPERIMENT

Sample Preparation

The LAX112 and 2,4-DNI materials were both plastic-bonded formulations. The samples were ram-pressed to cylindrical shape, sawn on a diagonal to form two wedges per cylinder, and finish-machined along the sawn faces.

The LAX112 samples were formulation X-0535, composed of 95 wt.% LAX112 and 5 wt.% OXY 461 (1). The molding powder was pressed at 42,000 psi and 110 C to achieve about 97.8% of the 1.829 g/cc formulation theoretical maximum density (TMD). X-0535 was found to have excellent mechanical properties— it was dimensionally stable, and pressed and machined well.

The 2,4-DNI samples were formulation X-0552, composed of 95 wt.% 2,4-DNI and 5 wt.% Estane. The molding powder was pressed at 42,000 psi and 90 C to achieve about 98.4% of the 1.720 g/cc formulation TMD (2). X-0552 pressed and machined rather poorly, and the quality of the data is correspondingly lower than for the other two materials.

TNAZ has a critical temperature far above its melting point so that it can be melt cast or hot-pressed. The TNAZ wedges were neat-pressed at 42,000 psi and 97 C directly to the final wedge shape. The densities achieved were between 99.1% and 99.4% of the 1.840 g/cc TMD, which alleviates concern about density variations near the corner opposite the pressing die (2). The sample quality using this technique was excellent.

Description of the Wedge Test

There have been many variations on the wedge test over the years; we used the so-called "mini-wedge" test of Seitz (5), as shown in Fig. 2. The sample is small (about 7 g) and so restricts the run distance to about 1 cm. But for new explosives existing only in small quantities, material minimization is critical. The driver system was a 7.8-inch diameter plane wave lens, a 2-inch thick pad of booster explosive, and up to three 0.5-inch thick attenuator plates to tailor the pressure delivered to the sample.

The diameter of the circular wedge face was 1 inch and the wedge angle was 30 degrees. This angle must be less than the "critical" value at which release waves travel into the material, so that the propagation of the shock/detonation wave will be unaffected by that boundary. The critical angle is rarely known precisely, but 30 degrees is considered sufficiently conservative for all materials. The elliptical face of the wedge is glued to the last attenuator plate, the circular face thus serving as the observation surface. This configuration gives a slightly longer run distance (before the release wave from the opposite free boundary affects the measurement) than the reverse orientation.

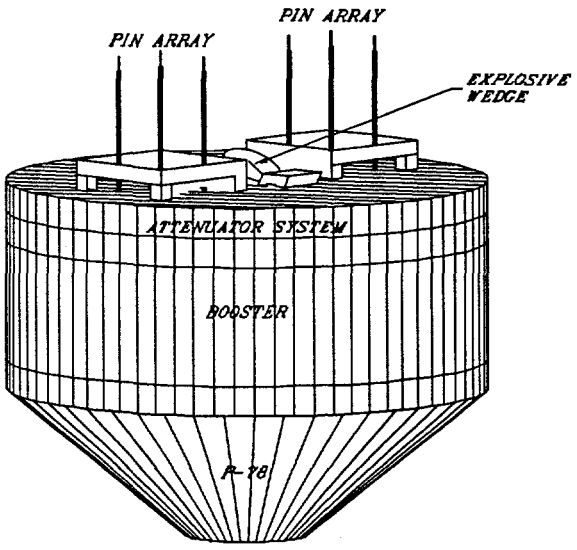

FIGURE 2. Schematic drawing of the wedge test (drawing by Herbert Harry).

The assembly in Fig. 2 is suspended upside down with the observation surface of the wedge parallel to the ground. Viewed from the side the wedge then appears as in Fig. 3a (with the attenuator plate now at 30 degrees to the ground), and viewed from below as in Fig. 3b. The image of the internal slit aperture is centered upon the wedge and, since the line of focus lies on the observation surface, there is no magnification variation or depth of field problem. The wedge is illuminated with an argon bomb, so that specularly reflected light from the observation surface is directed into the camera as in Fig. 3a. As the shock/detonation wave breaks out of the observation surface its reflectivity decreases and the light is attenuated as in Fig. 3b. Thus the wavefont appears as a curve of discontinuous exposure on the film.

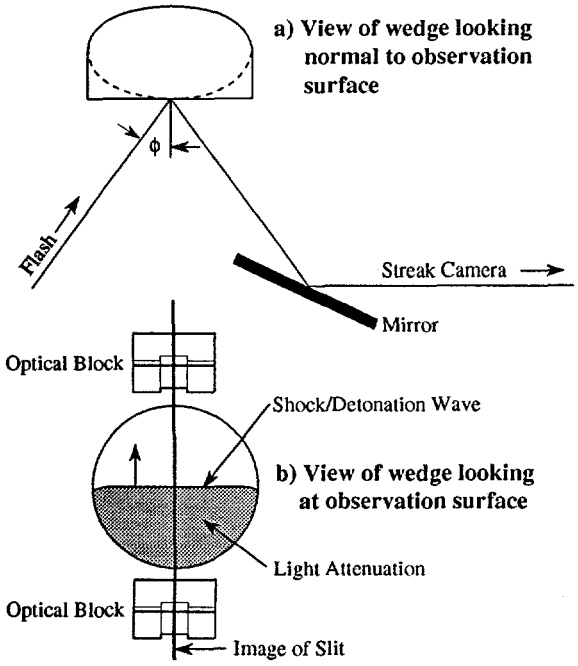

FIGURE 3. Optical configuration.

The other needed information is the free surface velocity of the final attenuator plate. Two methods were used for redundancy. In the first, two plexiglas blocks with 0.5 mm deep machined notches on one side were glued, notch side down, to the last attenuator plate, one on either side of the wedge and in the field of view of the camera slit (Fig. 3b). A thin layer of white paint was applied to the notch side of the blocks prior to gluing, so that the surface was initially reflecting to the flash light. Upon shock wave break out the attenuator reflectivity decreases. Later, the gap reflectivity decreases when impacted by the free surface. The difference between these two times is time-of-flight across the known gap width, from which the free surface velocity follows immediately. The second method involved two clusters of four piezoelectric pins spaced in increments of 0.5 mm from the plate (Fig. 2). As the free surface strikes the pins a voltage spike is produced. An x-t diagram is constructed from the known spacings and measured arrival times, and the velocity is found from the slope of a fit to the points as $x \to 0$. With good data the two methods typically agree to within a few percent.

ANALYSIS

Data was read directly from the film record by optical comparitor. By consideration of the geometry one finds that the run to detonation x^* and the time to detonation t^* are related to the respective film coordinates X^* and Y^* by

$$x^* = x_{toe}\cos\theta + \left(\frac{\sin\theta}{mag}\right)X^*,\ t^* = \frac{Y^*}{WrtSpd}, \quad (1)$$

where x_{toe} is the thickness of the wedge "toe" (it is never possible to achieve a knife edge), θ is the wedge angle, mag is the magnification, and $WrtSpd$ is the camera writing speed. The shock/detonation velocity $U_{s/d}$ is related to the angle of the film trace ψ by

$$U_{s/d} = \left(\frac{WrtSpd}{mag}\right)\sin\theta\cot\psi. \quad (2)$$

The input shock to the explosive is ideally a step rise to constant pressure, the value of which is inferred by impedance matching. The necessary ingredients are 1) the Hugoniot of the final attenuator plate, 2) the measured free-surface velocity of the final attenuator plate, 3) the measured initial shock velocity in the explosive, and 4) the initial density of the explosive. From this one can deduce the initial particle velocity in the explosive (hence the inert Hugoniot) and the initial pressure in the explosive (hence the Pop-plot). We assume that the isentrope for release wave reflected from the free surface of the final attenuator plate is the reflection of the incident shock Hugoniot (in p-u space) about its particle velocity. This is a good approximation for metal attenuators and, by comparison to more sophisticated methods, appears to be well within experimental error.

RESULTS

For a heterogeneous explosive one sees a constant initial shock velocity followed by a smooth acceleration to the detonation velocity. For a homogeneous explosive one sees a much sharper transition, followed by an overshoot in shock velocity, followed by a relaxation to the detonation velocity. LAX112 behaved like a classical heterogeneous explosive, whereas TNAZ behaved more like a homogeneous explosive. The 2,4-DNI

records were, due to the aforementioned formulation properties, somewhat erratic. But otherwise, heterogeneous behavior would be expected.

Run to detonation vs. input pressure for the three explosives is shown in Fig. 4 along with four common reference explosives. The sensitivity of LAX112 and 2,4-DNI both fall between that of pressed TNT and PBX9502, LAX112 being the less sensitive. The sensitivity of TNAZ falls between that of pressed PETN and PBX9501.

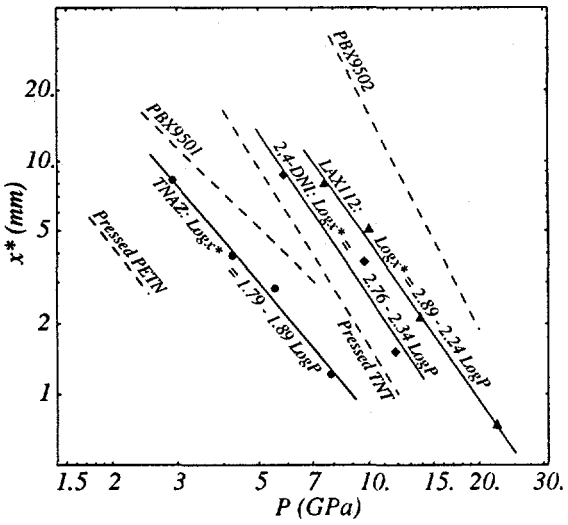

FIGURE 4. Run distance to detonation vs. input pressure (Pop-plot) points and linear fits for LAX112, 2,4-DNI, TNAZ, and selected other explosives.

The u_p-U_s inert Hugoniots for the three explosives and PBX9502 are shown in Fig. 5. The curves are similar to those of other explosives. For TNAZ the lowest velocity point agrees well with the gas gun of data of Sheffield et al. (6), indicated by square symbols. The two higher-velocity points deviate from the trend (perhaps suggesting some reaction or a phase transition) and are omitted from the fit. For the highest input pressure TNAZ case the run distance was too short to measure an accurate initial shock speed, yet the transition point could still be deciphered from the film. The Pop-plot point was therefore generated from the Hugoniot based on the other points.

The numerical values of the data points are given in Table 1. The times to detonation transition are also indicated.

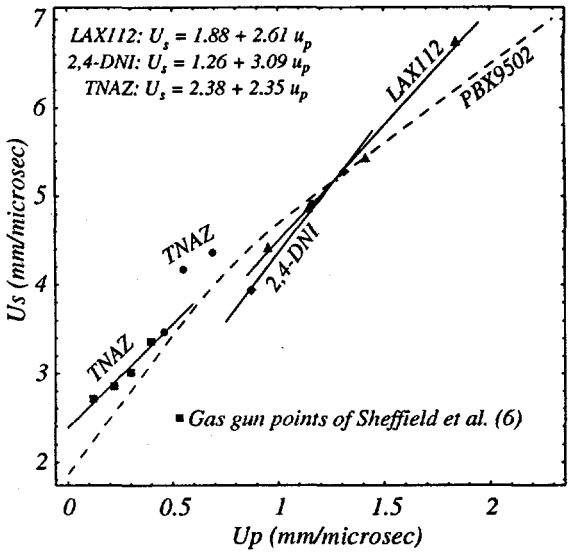

FIGURE 5. Inert Hugoniot points and linear fits for LAX112, 2,4-DNI, TNAZ, and PBX9502.

Table 1. Numerical values of the data points.

HE	ρ_0 g/cm^3	P_0 GPa	u_p km/s	U_s km/s	x^* mm	t^* μs
LAX112	1.793	7.5	0.95	4.41	8.00	1.67
	1.794	9.9	1.14	4.86	5.06	0.99
	1.794	13.7	1.41	5.43	2.12	0.36
	1.793	22.2	1.84	6.74	0.74	0.12
2,4-DNI	1.692	5.8	0.87	3.93	8.64	2.09
	1.692	9.6	1.16	4.90	3.63	0.74
	1.692	11.7	1.31	5.27	1.50	0.30
TNAZ	1.825	2.9	0.46	3.47	8.23	2.34
	1.826	4.2	0.55	4.17	3.88	1.09
	1.826	5.5	0.69	4.36	2.80	0.66
	1.828	7.8	0.85	—	1.21	0.41

REFERENCES

1. Kramer, J. F., et al. "Joint DoD/DOE Munitions Tech. Dev. Prog.", LANL Rpt. LA-12568-PR (1993).
2. Repa, J. V., et al. "Joint DoD/DOE Munitions Tech. Dev. Prog.", LANL Rpt. LA-12806-PR, V.1, (1994).
3. Archibald, T.G., et al., *J. Org. Chem.*, **55**, 2920 (1990).
4. Coburn, M. D., and Hiskey, M. A., "An Alternate Synthesis of 1,3,3-Trinitroazetidine.", LANL Rpt. LA-CP-95-145 (1995).
5. Seitz, W. L., "Short-Duration Shock Initiation of Triaminotrinitrobenzene (TATB)", in *Shock Waves in Condensed Matter*, J. R. Asay et al., eds. (1983).
6. Sheffield, S. A., et al., "Hugoniot and Initiation Measurements on TNAZ Explosive", These proceedings.

OBSERVATIONS OF SHOCK - INDUCED REACTION IN LIQUID BROMOFORM UP TO 11 GPa[†]

S. A. Sheffield, R. L. Gustavsen, and R. R. Alcon

Los Alamos National Laboratory, Los Alamos, NM 87545

Shock measurements on bromoform ($CHBr_3$) over the past 33 years at Los Alamos have led to speculation that this material undergoes a shock-induced reaction. Ramsay observed that it became opaque after a 1 to 2 μs induction time when shocked to pressures above 6 GPa (1). McQueen and Isaak observed that it is a strong light emitter above 25 GPa (2). Hugoniot data start to deviate from the anticipated liquid Hugoniot at pressures above 10 GPa. We have used electromagnetic particle velocity gauging to measure wave profiles in shocked liquid bromoform. At pressures below 9 GPa, there is no mechanical evidence of reaction. At a pressure slightly above 10 GPa, the observed wave profiles are similar to those observed in initiating liquid explosives such as nitromethane. Their characteristics are completely different from the two-wave structures observed in shocked liquids where the products are more dense than the reactants. As with explosives, a reaction producing products which are less dense than the reactants is indicated. BKW calculations also indicate that a detonation type reaction may be possible.

INTRODUCTION

Shock experiments on bromoform ($CHBr_3$) were done by Ramsay (1) at Los Alamos in the early 1960's. The objective of this work was to understand why some liquid explosives become opaque during shock-initiation. Nonexplosive liquids were also studied and bromoform was found to go opaque with an induction time of 1 to 2 μs when shocked above 6 GPa (1). Ramsay made Hugoniot measurements from 3 to 24 GPa, but from these no definitive reason for the material becoming opaque could be determined. He noted, however, that when compared with water, the Hugoniot had an odd shape in the shock-velocity vs. particle-velocity plane.

Experiments by McQueen and Isaak in the early 1980's showed that when bromoform is shocked to pressures above 25 GPa, the shock front emits radiation whose intensity varies with the shock pressure (2). In fact, light emission from shocked bromoform is used at Los Alamos as both a shock time-of-arrival detector and as an indicator of wave profile changes occurring in materials which are in contact with the bromoform. McQueen and Isaak's study did not lead to new information regarding a shock-induced reaction.

For some time we have been using the "universal" liquid Hugoniot developed by Woolfolk, Cowperthwaite, and Shaw (3) to estimate the Hugoniot for many liquids. Deviation from this Hugoniot often indicates the condition at which a shock-induced reaction might occur (4). When the Hugoniot data from Ramsay (1) and McQueen and Isaak (2) were plotted with the "universal" liquid Hugoniot for bromoform, deviations indicated that a reaction might be occurring at pressures as low as 10 GPa. Based on this, we have done further experiments to try to determine the shock pressure threshold and nature of the reaction.

EXPERIMENTAL DETAILS

Because bromoform has a relatively high density, 2.89 g/cm^3, pressures over 10 GPa could be obtained in single-shock experiments using our single-stage gas gun. Eight electromagnetic particle velocity gauging experiments of two different types have been completed in the pressure range of 3 to

[†] Work performed under the auspices of the U.S. Dept. of Energy.

10 Gpa. Parameters for these gas gun experiments are summarized in Table 1.

In the first type of experiments, called "Stirrup" experiments, magnetic "stirrup shaped" gauges at the front and back of the bromoform were used to measure the input and transmitted shock wave profiles. Stirrup experiments used a liquid cell 3 mm thick, 28.6 mm in inside diameter and 68.6 mm in outside diameter made from Kel-F plastic. A 3-mm-thick Kel-F front, and a 12-mm-thick Kel-F back plate completed the cell. The front, center ring, and back of the cell were epoxied and screwed together with nylon screws. Copper stirrup gauge elements, 5-μm thick on a 50-μm-thick Kapton substrate, were epoxied to the front and back cell pieces. The active gauge length was 9 mm, and the Kapton backing was in contact with the liquid. Five stirrup experiments were done.

The second type of experiment, called "MMG", for Multiple Magnetic Gauge experiment, consisted of a thin gauge package (with up to 10 particle velocity gauges in it) suspended at an angle in the liquid bromoform. This enabled the wave profile to be monitored at various depths in the liquid.

The MMG experiment is shown in an exploded view of Fig. 1. It consists of a two-piece PMMA body with an MMG package epoxied between the two pieces. The gauge package is on a plane at a 30 degree angle with the top of the cell. A Kel-F front completes a cell which is 40.6 mm inside diam. by 9 mm thick. The inside of the cell was lined with either Teflon or epoxy to keep the bromoform from dissolving or reacting with the PMMA. On some experiments a stirrup gauge was epoxied to the cell top as shown in Fig. 1. MMG cells were also epoxied and screwed together with nylon screws. Three of these experiments were completed.

Cells were filled just before the impact

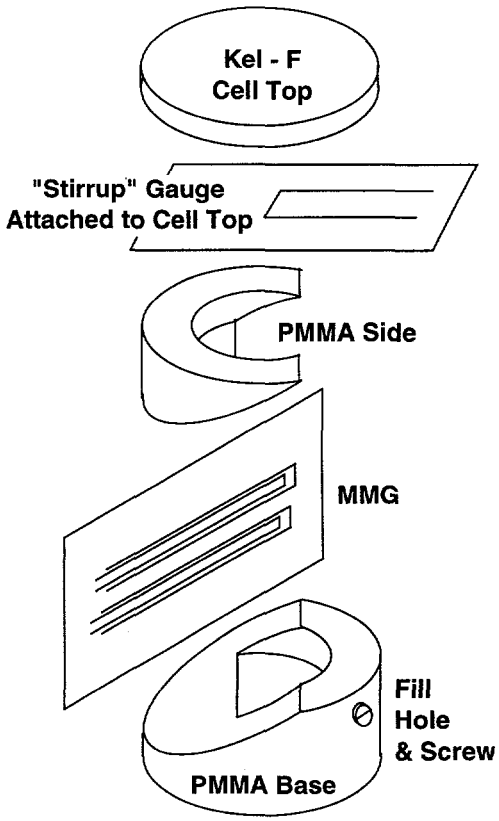

FIGURE 1. Exploded view of the MMG experiment showing the magnetic gauge and construction details.

experiment using Aldrich Chemical Co. bromoform (Aldrich #24,103-2). This bromoform is 99+ % pure, the major impurity being a small amount of ethanol stabilizer added by Aldrich.

Projectiles were made of Lexan and faced with impactors of either Vistal (pressed polycrystalline sapphire) or single crystal z-cut sapphire.

TABLE 1. Gas Gun Shot and Unreacted Hugoniot Data for Liquid Bromoform.

Shot No.	Type of Experiment	Impactor Material	Impact Velocity (mm/μs)	Particle Velocity (mm/μs)	Shock Velocity (mm/μs)	Shock Pressure (GPa)	Relative Volume (V/V_0)
741	Stirrup	Vistal	0.603	0.534	2.05	3.17	0.740
742	Stirrup	Vistal	0.798	0.680	2.45†	4.83	0.723
743	Stirrup	Vistal	1.000	0.840	2.58	6.26	0.674
744	Stirrup	Sapphire	(1.25)*	1.07	2.95	9.10	0.638
745	Stirrup	Sapphire	1.410	1.14‡	3.07‡	10.1‡	0.629‡
1033	MMG	Sapphire	0.964	0.83	2.542	6.09	0.674
1034	MMG	Sapphire	1.267	1.06	3.035	9.30	0.651
1035	MMG	Sapphire	1.391	1.16	3.147	10.6	0.631

† Back gauge data not good. * Projectile velocity estimated. ‡ Evidence of reaction so data suspect.

RESULTS AND DISCUSSION

With these techniques, it was possible to measure the shock velocity in the bromoform quite accurately. In the stirrup experiments, the cell was rigid and the distance between gauges accurately known. Shock velocity was the distance between gauges divided by the wave transit time. In the MMG experiments, there were several gauges at fixed depths. The slope of a line fitted to the gauge depth vs. the wave arrival time gave a good shock velocity measurement. These quantities were determined for each of the experiments, even those suspected of having reaction, and are presented in Table 1. They are also plotted in Fig. 2 along with the data of Refs. 1 and 2 and the universal liquid Hugoniot for bromoform. With both the shock and particle velocity known, the mechanical state of the bromoform could be completely determined. Relevant quantities are also presented in Table 1.

Figure 2 clearly shows that Ramsay's lower pressure data are different from ours. Since his data were obtained from explosively driven experiments, at relatively low pressures, the inputs may not be accurately known. Our gun data should be more accurate because the pressure input is constant and easily controlled with the projectile velocity. That our data fall on or near the expected liquid Hugoniot is another indication of their accuracy.

Starting at pressures between 10-15 GPa the data of Refs. 1 and 2 lie below the expected liquid

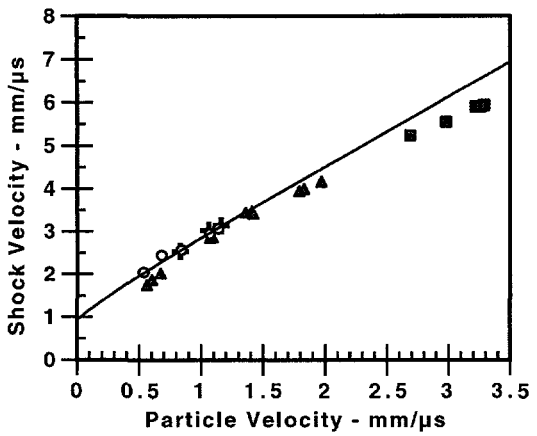

FIGURE 2. Hugoniot data for liquid bromoform. The line is the universal liquid Hugoniot using an initial condition sound speed of 0.931 mm/μs (5). Triangles are data from Ref. 1, and squares are data from Ref. 2. Data from our "stirrup" experiments are shown as circles and "MMG" data are shown as crosses.

bromoform Hugoniot. This is evidence that a reaction is occurring. Since the data are below the line, the products of the reaction are expected to be more dense than the reactants. This is similar to what has been observed in carbon disulfide (CS_2) (6), acrylonitrile (7), and other organic liquids. It is unknown whether or not this reaction causes the shocked bromoform to emit as indicated by McQueen and Isaak (2).

Ramsay states that bromoform becomes opaque at pressures above 6 GPa with an induction time of 1 to 2 μs (1). Neither the Hugoniot measurements nor the particle velocity waveforms measured in our study show any mechanical evidence of a reaction in the 6 to 9 GPa range. Particle velocity waveforms from a 9.3 GPa input MMG experiment are shown in Fig. 3a. There is no evidence in the waveforms of a chemical reaction. However, the bromoform has been held at pressure for scarcely one microsecond before the pressure is reduced by a rarefaction from the back of the impactor. It is possible that the reaction is too slow to be seen in this experiment. If a reaction does occur within one microsecond it does not result in a large enough volume change to be measurable with our particle velocity gauges. We do observe subtle waveform differences in this pressure regime but they are so small it would be unwise to interpret them as an indication of a reaction.

In contrast to the 9.3 GPa experiment of Fig. 3a very interesting waveforms were obtained at 10.6 GPa as can be seen in Fig. 3b. The four waveforms obtained from the MMG gauges in Fig. 3b are much like those obtained in homogeneous NM shock initiation experiments (8). In those experiments a reaction starts behind the shock front producing a spread out wave that then begins to move toward the shock front. As the reactive wave moves it steepens into a shock which grows in amplitude and eventually overtakes the initial shock. After overtake it has the character of a detonation wave. Analysis of the four waveforms shown in Fig. 3b indicates that bromoform is initiating in the same manner as the NM. In addition to this experiment, Shot 745 at 10.1 GPa had comparable behavior. Because there were only two gauges, one at the front and the other at the back of the bromoform, we did not understand what the waveforms meant until we saw the records obtained in Shot 1035.

Because bromoform has not been mentioned as an explosive material, these results were quite

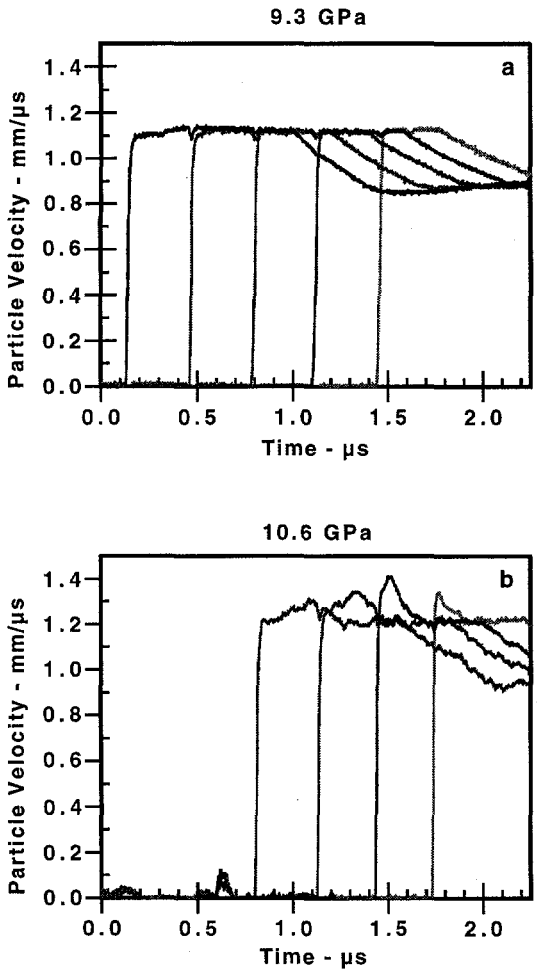

FIGURE 3. Magnetic particle velocity gauge waveforms from MMG experiments 1034 (a) and 1035 (b). Shot 1034 was at 9.3 GPa and showed no unusual behavior. Shot 1035 was at 10.6 GPa and has totally different waveforms. The two sets of waveforms are not time correlated because the gauges were at different depths.

surprising. A further evidence of bromoform's explosive behavior was that the aluminum shroud surrounding the target was expanded and cracked. This shroud protects the gun's target chamber from shrapnel originating from reacting explosive targets. It is never damaged during experiments on inert materials.

After this experiment was completed, we obtained BKW calculations on bromoform (9). These indicate that the expected reaction products are the gases HBr, Br_2, and CBr_4, and carbon as a solid. Further, a detonation could occur with a C-J pressure of 3.2 GPa. This C-J pressure does not agree with our measurements, but it does indicate that a regime in which the products are less dense than the reactants exists and explosive initiation like waveforms are expected. It is unknown at this time whether or not bromoform would detonate in a cylinder of finite diameter. Ours are 1-D measurements and do not really indicate what may happen in 2-D geometry.

Above 15 GPa, the Hugoniot data in Refs. 1 and 2 fall below the expected liquid Hugoniot, indicating the products are more dense than the reactant. Thus, either the reaction mechanism changes at this pressure or else some of the product gases are compressed to the point they become condensed. This remains to be determined, perhaps in MMG experiments at higher pressures on our two-stage gas gun.

In summary, some very interesting reactions occur in shocked bromoform. It apparently becomes opaque beginning at about 6 GPa but either in a slow reaction or with a small volume change. At 10 GPa a detonation like reaction (products less dense than the reactant) is observed. This changes in nature somewhere above an input of 15 GPa to be a reaction in which the products are more dense than the reactants. Clearly, there is room for more research to determine the exact nature of these reactions.

REFERENCES

1. Ramsay, J. B., unpublished Los Alamos data from 1962. For Hugoniot data see p. 552, *LASL Shock Hugoniot Data*, Ed., Marsh, S. P., (University of California Press, Berkeley, CA, 1980).
2. McQueen, R. G., and Isaak, D. G., *Shock Comp. of Cond. Matter-1989*, Eds. Schmidt, S. C., Johnson, J. N., and Davison, L. W., p. 125.
3. Woolfolk, R. W., Cowperthwaite, M., and Shaw, R., *Thermochimica Acta* **5**, 409 (1973).
4. Sheffield, S. A., *Bull. Am. Phy. S.* **33**(3), 710 (1988).
5. Moses, A. J., *The Practicing Scientist's Handbook: A Guide For Physical and Terrestrial Scientists and Engineers*, (Van Nostrand Reinhold Co., New York, 1978), p. 526.
6. Sheffield, S. A., *J. Chem. Phys.* **81**, 3048 (1984).
7. Yakushev, V. V., Nabatov, S. S., and Yakusheva, O. B., *Comb. Expl. and Shock Waves* **10**(4), 509 (1975).
8. Sheffield, S. A., Engelke, R. P., and Alcon, R. R., *in Ninth Symposium (Intl.) on Detonation*, 1989, pp. 39-49.
9. Baer, M. R., and Hobbs, M. L., Sandia National Laboratories, private communication.

LOW PRESSURE SHOCK INITIATION OF POROUS HMX FOR TWO GRAIN SIZE DISTRIBUTIONS AND TWO DENSITIES[†]

R. L. Gustavsen, S. A. Sheffield, and R. R. Alcon

Los Alamos National Laboratory, Los Alamos, NM 87545

Shock initiation measurements have been made on granular HMX (octotetramethylene tetranitramine) for two particle size distributions and two densities. Samples were pressed to either 65% or 73% of crystal density from fine (≈ 10 μm grain size) and coarse (broad distribution of grain sizes peaking at ≈ 150 μm) powders. Planar shocks of 0.2 - 1 GPa were generated by impacting gas gun driven projectiles on plastic targets containing the HMX. Wave profiles were measured at the input and output of the ≈ 3.9 mm thick HMX layer using electromagnetic particle velocity gauges. The initiation behavior for the two particle size distributions was very different. The coarse HMX began initiating at input pressures as low as 0.5 GPa. Transmitted wave profiles showed relatively slow reaction with most of the buildup occurring at the shock front. In contrast, the fine particle HMX did not begin to initiate at pressures below 0.9 GPa. When the fine powder did react, however, it did so much faster than the coarse HMX. These observations are consistent with commonly held ideas about burn rates being correlated to surface area, and initiation thresholds being correlated with the size and temperature of the hot spots created by shock passage. For each grain size, the higher density pressings were less sensitive than the lower density pressings.

INTRODUCTION

The present work is a continuation of our efforts to develop an understanding of the low pressure shock compaction and initiation of highly porous HMX (1-3). References contained in our previous work (1,2) and others (4-7) indicate that the initiation sensitivity for porous explosives is a complex function of density (porosity), particle size, pulse duration, and input pressure. In an effort to determine how these parameters affect the initiation of HMX, we prepared samples with densities of 65% and 73% of TMD, grain sizes varying by more than an order of magnitude (from ≈ 10 μm to ≈ 150 μm) and used input pressures varying from 0.2 - 1 GPa. Sustained pulses were used and the response of the explosive was recorded using particle velocity gauges.

EXPERIMENTAL DETAILS

Description of HMX Powders

Two different lots of HMX powder with two different particle size distributions were used in this series of experiments. One powder was composed of "coarse" particles which had the appearance both to the naked eye and under a microscope of granulated sugar. This HMX was made by Holston (Lot HOL-920-32) and had a bulk or pour density of ≈ 1.16 g/cm^3 (8). The material was screened to eliminate agglomerates and a few of the largest particles. Sieve analysis of the powder done by Dick (8) is given in Table 1 and shows a broad particle size distribution with a peak near 150 μm. All the crystals have sharp corners and edges.

TABLE 1. Particle Size Distribution for "Coarse" HMX, Holston Lot 920-832.

Sieve Opening μm	500	350	250	177	125	88	62	44	Subsieve
Weight % Retained on Sieve	1.3	4.0	15.6	18.2	27.8	11.8	12.1	4.9	4.3

[†] Work performed under the auspices of the U.S. Dept. of Energy.

The second powder, whose size distribution is shown in Table 2, was composed of "fine" particles and had the appearance of powdered sugar. This HMX was also manufactured by Holston (Lot HOL-83F-300-023) and also had a bulk or pour density of ≈ 1.16 g/cm^3. The particle size at the peak of the distribution is about 10 μm. Particle sizes were determined by Microtrac analysis. The mean particle size of the coarse and fine HMX is different by a factor of more than 10. Photographs show that this powder also contains an occasional large particle with a diameter of ≈ 50 μm. The rounded appearance of the particles indicates that this material was probably prepared by milling.

Gas Gun Experimental Setup

The experimental setup for the initiation experiments is shown in Figure 1. Experiments used gas gun driven projectiles to obtain sustained-shock input conditions. HMX powder was confined in sample cells which had a polychlorotrifluoro-ethylene (Kel-F) front face and a poly 4-methyl-1-pentene (TPX) or polymethylmethacrylate (PMMA) cylindrical plug back. The front face was attached with screws to a Kel-F confining cylinder with an outside diameter of 68.6 mm and an inside diameter of 40.6 mm. The pressed HMX (between the Kel-F and TPX) was ≈ 3.9 mm thick. The back plug was pressed into the Kel-F confining cylinder and held in place with an interference fit. Projectiles faced with Kel-F impacted on the Kel-F target face.

Magnetic particle velocity gauges were located on the front and back surfaces of the HMX. These were constructed of a 5 μm thick aluminum "stirrup" shaped gauge on a 12 μm thick FEP Teflon sheet. The active region of the gauge was 10 mm long. Particle-velocity histories were measured at both the front and back of the HMX sample. The gauge at the interface of the Kel-F front disk and HMX gives the input or loading profile. The gauge at the interface of the back plug and HMX gives the transmitted wave profile. The transmitted wave profile is not equivalent to what would be observed if the gauge was suspended in the HMX powder because of the impedance mismatch between the HMX and the plastic back plug. However, it is representative of the transmitted wave profile and gives a reasonable

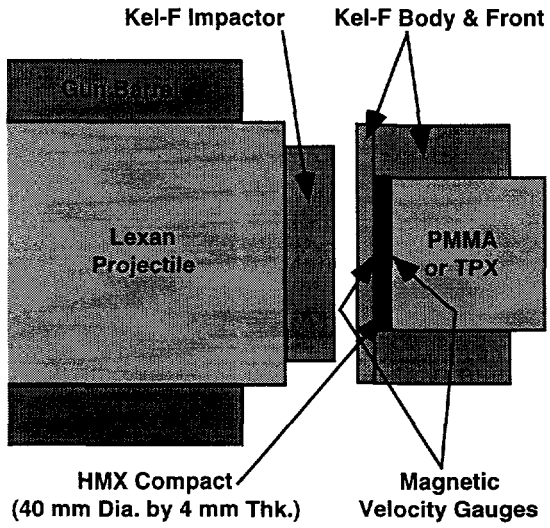

FIGURE 1. Cross section view of the projectile and target.

estimate of the rise time. Wave profiles were recorded on fast digitizing oscilloscopes.

RESULTS

A total of sixteen experiments were performed; four each for each of the two particle size distributions and for each of the two nominal densities. The nominal densities used were 1.24 g/cm^3 or 65% TMD (35 % porous) and 1.40 g/cm^3 or 73% TMD (27 % porous).

Figure 2 shows wave profiles for four experiments. The projectile velocities on these experiments were very close to the same at ≈ 0.6 mm/μs, resulting in an input to the HMX of ≈ 0.72 GPa. Complete results for the entire series of experiments will be presented elsewhere. With this input, the coarse HMX (Fig. 2a and 2c) begins to react as soon as the wave passes the front gauge and enters the powder. The front particle velocity decreases because the reacting HMX is decelerating the cell front where the gauge is located. Stress measurements show the stress at this interface increasing (1,2). The transmitted wave is growing and steepening up considerably. By the time the wave reaches the back of the HMX, the particle velocity has doubled. There appears to be a little

TABLE 2. Particle Size Distribution for "Fine" HMX, Holston Lot 83F-200-023

Particle Diameter μm	> 45	25.1	17.7	12.5	8.9	6.3	4.4	3.1	2.2	1.3	0.8	0.6
Weight % of Particles	6	8.3	10.3	11	15.8	12.5	11.3	9.5	5.8	5.0	3.0	1.5

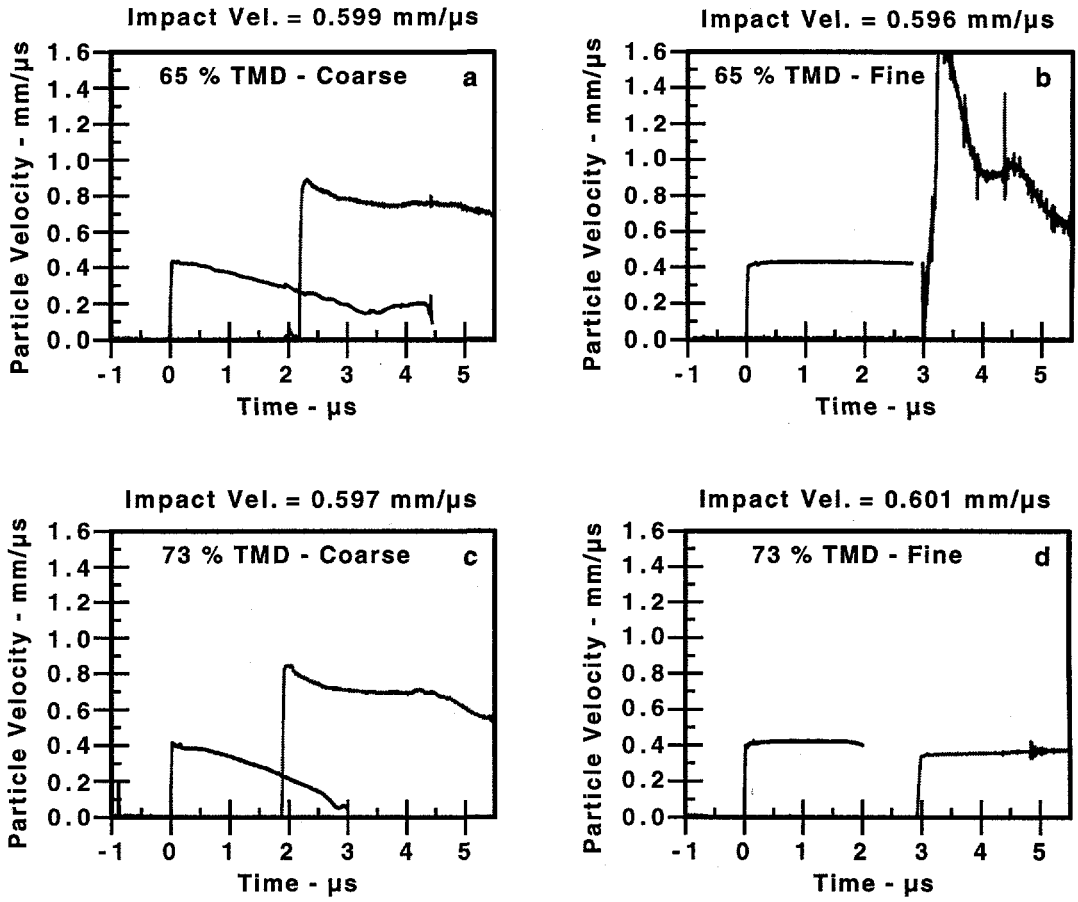

FIGURE 2. Input and transmitted particle velocities in porous HMX compacts. All the samples were about 3.9 mm thick. (a) 1.24 g/cm^3 (65% TMD), "coarse" particle powder. This experiment had a TPX back disk. (b) 1.24 g/cm^3 (65% TMD), "fine" particle powder. This and items c and d shown in this panel had a PMMA back disk. (c) 1.40 g/cm^3 (74% TMD), "coarse" particle powder. (d) 1.40 g/cm^3 (74% TMD), "fine" particle powder.

more reaction in the 1.24 g/cm^3 (Fig. 2a) than the 1.40 g/cm^3 (Fig. 2c) coarse material.

In this regime of 0.5-1 GPa, the reactivity of the fine particle HMX differs greatly from that of the coarse particle HMX. In these ≈ 0.72 GPa input experiments in particular, there is no reaction evident in the front gauge profile at either density for the fine HMX. (See Figs. 2b and 2d.) The transmitted wave profile in the 1.40 g/cm^3 fine powder (Fig. 2d) also shows no reaction.

The transmitted wave profile in the 1.24 g/cm^3 fine particle powder (Fig. 2b), however, shows a great deal of reaction. After the wave reflects off the back PMMA disk, the initial ≈ 0.72 GPa pressure in the HMX is approximately doubled. There is no reaction for several tens of nanoseconds. Then reaction begins and proceeds very rapidly. We have estimated this reaction to be more than 10 times more rapid than that shown by the input gauge in the coarse HMX.

DISCUSSION

From the four experiments shown in Figure 2 and others like it but at different inputs, we have drawn the following conclusions. Reaction (reactivity) depends slightly on density for both the fine and coarse particle HMX. In general the higher density HMX seems to be less sensitive. This is what might be expected from looking at the energy deposited during compaction. Less energy is

deposited in the higher density material for a given input pressure.

Reactivity depends a great deal on the initial particle size. For the coarse particle material, reaction occurs immediately when inputs are above 0.7 GPa. We have observed reaction begin at the front gauge with inputs as low as 0.5 GPa (after an induction time of several hundred ns). The fine particle HMX, by contrast, does not show any reaction at inputs less than ≈ 0.72 GPa at either the front gauges or in the higher pressure transmitted and reflected waves. With ≈ 0.72 GPa inputs and above, there is evidence of reaction, but only after the wave has reflected off the back PMMA disk and the pressure is approximately doubled. This reaction, which occurred only in the lower density powder, had a short induction time and was extremely rapid.

In addition to these features, the wave profile characteristics of initiating coarse and fine particle explosives are different. Jerry Dick's Manganin gauge measurements on coarse HMX (65 % TMD) for inputs of 0.81 GPa and thicknesses of 2, 3, and 4 mm, clearly show the wave growing in the front as the wave traverses the HMX compact (9). This is seen also in our more than doubled particle velocity at the back gauge (Figs. 2a and 2c). By contrast, run distance to detonation measurements in very fine particle HNS powders (nominal particle size 1-2 μm) showed strong velocity overshoots at the onset of detonation (4). These results suggested that a reactive wave developed well behind the shock front and caught up during the transition to detonation. This is similar to the mechanism by which a homogeneous explosive builds up to detonation (10). Thus, coarse particle explosives have a growing reactive wave at the shock front while fine particle explosives likely have a growing reactive wave behind and eventually overtaking the shock front.

These observations are generally explained in the following way. Most hot spot reaction theories indicate that the size of a hot spot is very nearly the size of a particle or of a void. Large particles thus lead to large hot spots. The initial temperature of the hot spot is scaled by the shock pressure. Large hot spots would cool slowly enough that they could begin reacting, even if the hot spot temperature was fairly low. The following reaction is relatively slow because the large particles don't have much surface area. By contrast, the small particles lead to small hot spots. These small hot spots cool more rapidly. Thus it takes higher pressures and higher hot spot temperatures to get the fine grained explosive to ignite before the hot spot cools. Once ignited, however, the reaction is relatively fast because the small particles have a large amount of surface area.

ACKNOWLEDGMENTS

Mr. J.G. Archuleta obtained the particle size distribution for the fine HMX shown in Table 2.

REFERENCES

1. Sheffield, S. A., Gustavsen, R. L., Alcon, R. R., Graham, R. A., and Anderson, M. U., "Shock Initiation Studies of Low Density HMX Using Electromagnetic Particle Velocity and PVDF Stress Gauges," presented at the Tenth Symposium (International) on Detonation, July 12-16, 1993, Boston, Mass.
2. Sheffield, S. A., Gustavsen, R. L., Alcon, R. R., Graham, R. A., and Anderson, M. U., "Particle Velocity and Stress Measurements in Low Density HMX," in *Proceeding of joint AIRAPT/APS Conference on High Pressure Science and Technology*, Edited by S.C. Schmidt, J.W. Shaner, G.A. Samara, and M. Ross, 1993, pp. 1377-1380.
3. Gustavsen, R. L., and Sheffield, S. A., "Unreacted Hugoniots for Porous and Liquid Explosives," in *Proceeding of joint AIRAPT/APS Conference on High Pressure Science and Technology*, Edited by S.C. Schmidt, J.W. Shaner, G.A. Samara, and M. Ross, 1993, pp. 1393-1396,
4. Setchell, R.E., "Microstructural Effects in Shock Initiation of Granular Explosives," *in Proceedings of the International Symposium on Pyrotechnics and Explosives*, Ding Jing, Ed. China Academic Publishers, Beijing, 1987, pp. 635-643.
5. Hayes, D.B., "Shock Induced Hot-Spot Formation and Subsequent Decomposition in Granular, Porous HNS Explosive," in *Shock Waves, Explosions, and Detonations*, edited by J.R. Bowen, N. Manson, A.K. Oppenheim, and R.I, Soloukhin, Vol. 87 of Progress in Astronautics and Aeronautics, 1983 pp. 445-467.
6. Moulard, H., "Particular Aspect of the Explosive Particle Size Effect on Shock Sensitivity of Cast PBX Explosives," *Ninth Symposium (Intl.) on Detonation*, Office of the Chief of Naval Research Report OCNR-113291-7, Arlington, VA, 1989, pp. 18-24.
7. Simpson, R. L., Helms, F. H., Crawford, P. C., and Kury, J. W., "Particle Size Effects in the Initiation of Explosives Containing Reactive and Non-Reactive Continuous Phases," *Ninth Symposium (Intl.) on Detonation*, 1989, pp. 25-38.
8. Dick, J. J., *Combustion and Flame* **54**, 121-129 (1983).
9. Dick, J. J., *Combustion and Flame* **69**, 257-262 (1987).
10. Sheffield, S. A., Engelke, R. P., and Alcon, R. R., "In-Situ Study of the Chemically Driven Flow Fields in Initiating Homogeneous and Heterogeneous Nitromethane Explosives," *Ninth Symposium (Intl.) on Detonation*, 1989, pp. 39-49.

HUGONIOT AND INITIATION MEASUREMENTS ON TNAZ EXPLOSIVE[†]

S. A. Sheffield, R. L. Gustavsen, and R. R. Alcon

Los Alamos National Laboratory, Los Alamos, NM 87545

Particle velocity measurements have been made on samples of TNAZ (1,3,3-trinitroazetidine) explosive pressed to 98 - 99% of theoretical maximum density. Measurements were made with magnetic particle velocity gauges and a VISAR interferometer. Stirrup shaped magnetic particle velocity gauges were mounted on the front and back of the TNAZ pressing. The back gauge was located at the interface of the TNAZ and a PMMA window and was also used as the diffuse reflector for the VISAR measurement. This allowed the simultaneous measurement of particle velocity by both a magnetic gauge and a VISAR. Well defined inputs to the TNAZ, ranging from 0.6 to 2.4 GPa, were produced by gas gun projectile impact. Unreacted Hugoniot data were obtained from the front gauge measurement and shock transit times through the TNAZ. A linear shock velocity vs. particle velocity fit of $U_s = 2.38 + 2.33u_p$ mm/μs was obtained for the unreacted Hugoniot and should be accurate to at least 3.0 GPa. An elastic-plastic transmitted wave, similar to that which has been seen in other explosive materials, was observed in the 0.6 GPa input experiment. Considerable amounts of reaction were observed in experiments with inputs of 1.6 and 2.4 GPa.

INTRODUCTION

TNAZ (1,3,3-trinitroazetidine, see Fig. 1) is a relatively new explosive that has an output similar to that of HMX (octahydro-1,3,5,7-tetranitro-1,3,5,7-tetrazocine) based plastic bonded explosives, such as PBX9404, but has a relatively low melting point near 100 °C. Experiments have been done on TNAZ at both Los Alamos and LLNL to characterize the initiation behavior and the unreacted Hugoniot. Wedge experiments were completed by Hill et al. (1) of Los Alamos and Manganin pressure gauge measurements were made at LLNL (2). These studies indicate that TNAZ is slightly more sensitive to sustained shock initiation than PBX 9404.

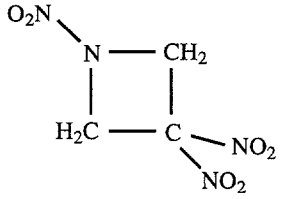

FIGURE 1. Chemical structure of TNAZ, $C_3H_4N_4O_6$.

Because there was considerable variation in the unreacted Hugoniot data measured in Refs. (1) and (2), we made measurements to characterize the shock and initiation properties of this material up to 2.4 GPa. Particle velocity waveforms were recorded as a function of time at both the input and output faces of the TNAZ. This allowed us to obtain initiation profiles on the higher pressure shots at the same time we were measuring Hugoniot points.

EXPERIMENTAL DETAILS

TNAZ samples used in these experiments had densities of 1.81 - 1.82 g/cm^3, or 98 - 99% of the 1.84 g/cm^3 theoretical maximum density (TMD). Density measurements were made on each sample.

Impact experiments were performed using a gas gun to provide well controlled inputs to the TNAZ. A cross-section view of the experimental setup is shown in Fig. 2. A Lexan projectile, faced with a single-crystal z-cut sapphire impactor, strikes a target comprised of the TNAZ sample (25.4 mm diam. by 7.8 mm thick), a Kel-F confinement ring, and a PMMA back window. Stirrup shaped

[†] Work performed under the auspices of the U.S. Dept. of Energy.

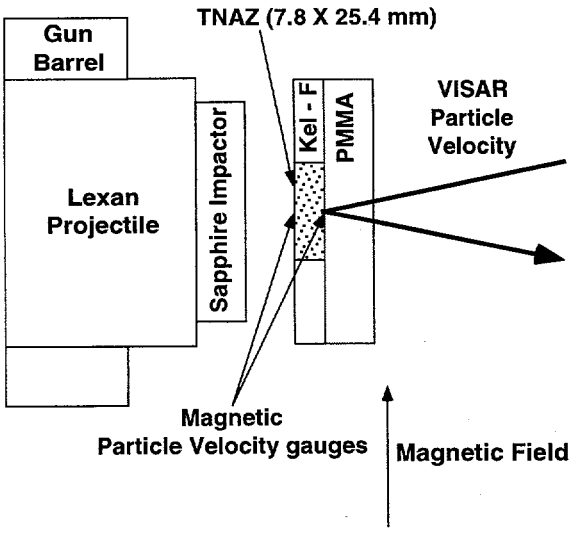

Figure 2. Experimental setup for magnetic gauge and VISAR particle velocity measurements in TNAZ.

magnetic particle velocity gauges, fabricated from 5 μm thick aluminum foil, were located on the impact surface and at the interface of the TNAZ and PMMA window. The front gauge was insulated on both sides with 12 μm of Kapton film. The back gauge was insulated on the side next to the TNAZ with 12 μm of FEP Teflon. The active element of these gauges is 10 mm long. The center of the back gauge was used as a diffuse mirror for VISAR measurements (3).

Because of the aspect ratio of the TNAZ samples, we were concerned about the length of time the 10 mm long back stirrup gauge would remain in one dimensional strain. (The Kel-F confinement ring was one method we used to help maintain 1-D strain.) The small VISAR measurement area (≈ 100 μm diam.) on the axis of the target should be in 1-D strain for ≈ 1 μs longer than the edges of the stirrup gauge. Differences in the stirrup gauge and VISAR measurements indicate that the back stirrup gauge is no longer in a state of 1-D strain.

Because the PMMA window has a lower shock impedance than TNAZ, a small rarefaction is sent back into the TNAZ when the shock wave reaches this interface. The transmitted wave profile is thus perturbed by a small amount, but is still representative of the transmitted wave.

RESULTS AND DISCUSSION

Four experiments, covering an input stress range of 0.6 to 2.4 GPa, were completed. Shot data, including unreacted Hugoniot points, are summarized in Table 1. All the waveforms from the magnetic gauges and the VISAR were successfully obtained in each experiment.

Particle velocities for the Hugoniot measurements were obtained from the front gauge record. Shock velocities were obtained by dividing the TNAZ thickness by the shock transit time. Unreacted Hugoniot data for each experiment are presented in Table 1 and are plotted in Fig 3.

In Shot 1030, with an input of 2.4 GPa, there was considerable reaction in the wave as it traveled through the TNAZ. Analysis of the back gauge record indicates that most of the reactive growth is behind the shock front. The reactive wave had not quite caught up to the shock front at the time it reached the gauge plane. This means the shock velocity should be reasonably accurate despite the reactivity. However, since the shock front has grown a little bit, a slight error in shock velocity (on the high side) would be expected.

The unreacted Hugoniot data from this study are plotted in the shock-velocity vs. particle-velocity plane in Fig. 3. The data fit a linear relationship with $U_s = 2.387 + 2.319u_p$ where U_s is the shock velocity and u_p is the particle velocity. Also shown

TABLE 1. Gas Gun Shot and Unreacted Hugoniot Data for TNAZ.

Shot No.	Impactor Material	Impact Velocity (mm/μs)	Initial TNAZ Density (g/cm^3)	Particle Velocity (mm/μs)	Shock Velocity (mm/μs)	Shock Pressure (GPa)	Relative Volume (V/V_0)
1028	Sapphire	0.134	1.82	0.121	2.716†	0.60	0.9555
		(Elastic wave data)‡		0.058	2.774	0.29	0.9791
1027	Sapphire	0.247	1.81	0.221	2.86	1.14	0.9227
1029	Sapphire	0.336	1.81	0.300	3.016	1.63	0.9007
1030	Sapphire	0.454	1.81	0.397	3.363	2.41	0.8820

† Shock velocity obtained by using the time to 1/2 maximum particle velocity on back gauge waveform.
‡ Elastic wave data obtained by using the first part of the back gauge waveform to determine both U_s and u_p.

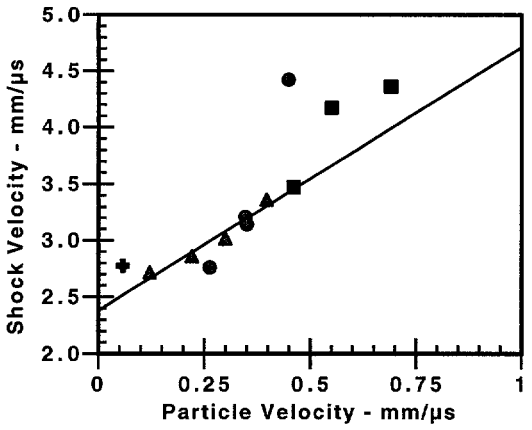

FIGURE 3. Unreacted TNAZ Hugoniot plot. Data from this study are the triangles, Hill et al's. wedge test data (1) are the squares, and data from the LLNL Manganin gauge experiments (2) are the circles. The cross is the point for the elastic wave.

are the earlier data from Los Alamos (1) and LLNL (2). Our data are in good agreement with the lowest pressure Los Alamos wedge test data point and with two of the points from LLNL. If we discard the low pressure LLNL point (because of its poor resolution and large error bars) as well as the high pressure LLNL point and the two highest pressure Los Alamos points, the fit is $U_s = 2.38 + 2.33u_p$. This should be considered a good unreacted Hugoniot for TNAZ of density 1.81 - 1.82 g/cm^3 for inputs below 3.0 GPa. We cannot at present explain the differences between our fit and the higher pressure data, although it appears to be systematic. It may be due to a transition to a lower density phase, such as a liquid.

Particle velocity waveforms for two of the experiments are shown in Fig. 4a and 4b, and cover the regime from very little reaction to a great deal of reaction. Front and back particle velocity waveforms for Shot 1027, which had an input of 1.14 GPa, are shown in Fig. 4a. The front gauge shows no evidence of reaction in this shot. (The rarefaction which appears at ≈ 2 μs comes from the back of the 10-mm-thick sapphire impactor.)

The back gauge waveforms obtained from the VISAR (light line) and the magnetic gauge are essentially identical up to ≈ 4 μs, at which time the magnetic gauge record gets increasingly lower than the VISAR record. This indicates that the stirrup gauge is experiencing 2-D strain. The drop in particle velocity which occurs at a time of ≈ 3.5 μs is due to the rarefaction from the back of the sapphire

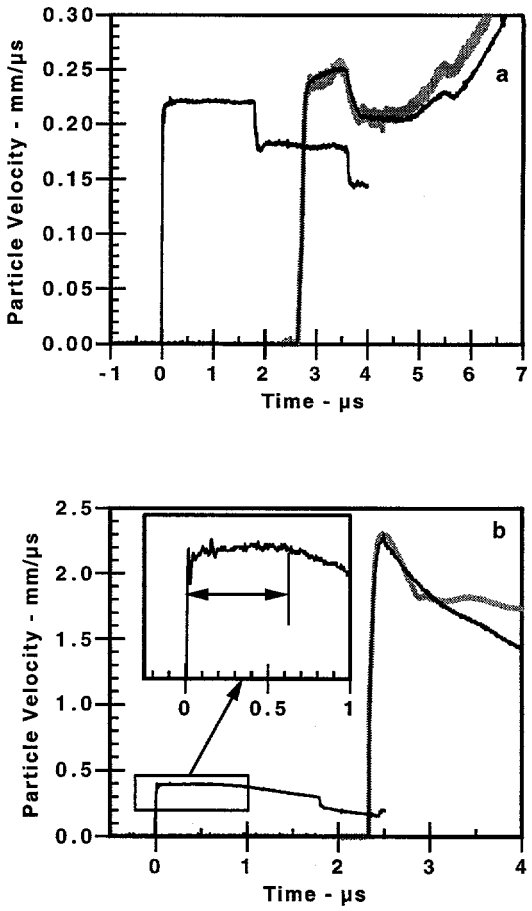

FIGURE 4. Particle velocity waveforms obtained from Shot 1027 with a 1.14 GPa input are shown in (a). Those from Shot 1030, with a 2.41 GPa input, are shown in (b). The dark line is the magnetic gauge measurement and the light line is the VISAR measurement.

impactor. The particle velocity measured by the VISAR and the back magnetic gauge were very close at early times in all four experiments. This agreement gives us confidence in the accuracy of both measurements.

No reaction was observed in the front gauge records for the shots with inputs of 0.6, 1.14, and 1.63 GPa. Shot 1030, with an input of 2.41 GPa (shown in Fig. 4b) showed evidence of reaction at the front gauge after an induction time of about 0.6 μs. This is shown by the particle velocity decrease starting at ≈ 0.6 μs and is clearly seen in the inset in Fig. 4b. The particle velocity decreases because the TNAZ is reacting, causing the pressure to increase and the impact interface (gauge plane) to

decelerate. If other shots were done at input pressures above and slightly below 2.4 GPa, an induction time vs. input pressure relationship could be determined.

After reaction starts near the front gauge plane, it is not extinguished by the rarefaction from the back of the sapphire impactor. Evidence for this comes from the particle velocity/time slope being about the same before and after arrival of the rarefaction. An estimate of the pressure decrease due to the rarefaction is ≈ 0.6 GPa or 25% of the initial pressure. With a reaction rate that is sensitive to pressure one might expect the rate to change dramatically due to this decrease in pressure.

As mentioned earlier, for this experiment there is a shock front followed by a large reactive wave (with a particle velocity of about 2.3 mm/μs) that is just about to overtake the shock front at the time it interacts with the back gauge/PMMA interface. The shock front has grown from 0.4 to 0.9 mm/μs. That this much of an increase has occurred may indicate that the reactive wave has already started to overtake the front. The large reactive wave is not a shock but has a steep front with a risetime of 60 - 70 ns. We estimate that the wave would evolve into a detonation in 2 or 3 mm more of travel, i.e., the run distance would be about 10 to 11 mm. This estimate compares favorably with the wedge data Pop-plot (1) which gives a run distance of 12.4 mm for a 2.41 GPa input.

From this single experiment it is not possible to determine if the initiation is more homogeneous than heterogeneous in character. Because the reactive wave is very large behind the shock front, and the shock front amplitude has increased very little, we think the initiation is behaving more homogeneously than heterogeneously. Multiple embedded gauge experiments would be needed to verify this.

Shot 1029 with an input of 1.63 GPa showed no reaction at the front gauge or in the shock front as it moved through the sample. Reaction did begin after the shock interacted with the PMMA window. This is puzzling because the PMMA has a lower impedance than the TNAZ and interaction of the wave with this interface reduces the pressure. An estimate of the reaction rate at the back gauge is ≈ 0.4 μs^{-1}.

An interesting material response was observed in Shot 1028, the lowest input experiment at 0.6 GPa. Figure 5 shows the transmitted wave profile. The wave is composed of a shock with a sharp jump up

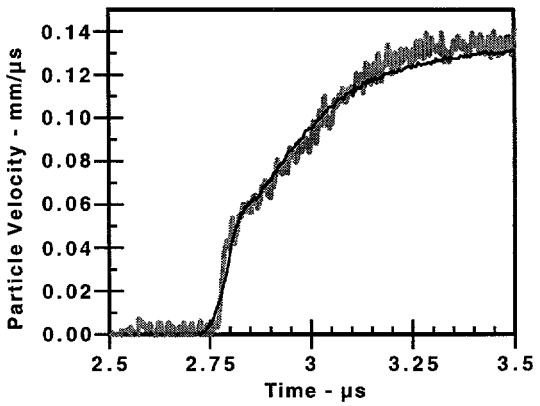

FIGURE 5. Transmitted wave profile for Shot 1028 showing elastic-plastic behavior. The dark line is the magnetic gauge measurement and the light line is the VISAR measurement.

to 0.04 mm/μs followed by a disperse wave spread out over ≈ 0.5 μs. We think this is elastic-plastic behavior, similar to that which has been seen in other explosives by Lemar et al. (4), Dick et al. (5), and Wasley and Walker (6). Using the initial jump, the elastic wave in TNAZ has an amplitude of about 0.29 GPa. This can be compared to the estimate of 0.14 GPa for Comp B-3 (4). The elastic wave would be overdriven by a wave with a particle velocity greater than 0.2 mm/μs.

ACKNOWLEDGMENT

We thank John Kramer of DX-16 at LANL for providing the TNAZ samples.

REFERENCES

1. Hill, L. G., Seitz, W. L., Kramer, J. F., and Murk, D. M., "Wedge Test Data for Three New Explosives: LAX-112, 2-4-DNI and TNAZ," These proceedings.
2. Lawrence Livermore National Laboratory, unpublished experimental data on TNAZ, 1995.
3. Barker, L. M. and Hollenbach, R. E., *J. Appl. Phys.* **41**, 4208–4226, (1970).
4. Lemar, E. R., Forbes, J. W., Watt, J. W., Elban, W. L., *J. Appl. Phys.* **59**, 3404-3408, (1985).
5. Dick, J. J., Forest, C. A., Ramsay, J. B., Seitz, W. L., *J. Appl. Phys.* **63**, 4881-4888, (1988)
6. Wasley, R. J., and Walker, F. E., *J. Appl. Phys.* **40**, 2639-2648, (1969).

DYNAMIC DEFORMATION AND FRACTURE RESPONSE OF A 6061-T6 Al - 50 vol. % Al_2O_3 CONTINUOUS REINFORCED COMPOSITE

G.T. Gray III, R.S. Hixson, and J.N. Johnson

Los Alamos National Laboratory, Los Alamos, NM, 87545, USA

In this paper results are reported on the influence of strain rate and shock loading on the deformation and fracture response of a 6061-T6 Al - 50 vol.% Al_2O_3 continuous fiber-reinforced composite as a function of composite orientation. The stress-strain response was found to vary substantially as a function of loading orientation; the quasi-static yield changing from nominally 300 MPa transverse to the fibers to ~1000 MPa parallel to the fibers. Increasing the strain rate to 2000 s^{-1} was observed to only slightly increase the yield strength of either orientation. Transverse VISAR wave profile and spall measurements revealed a small, well defined elastic precursor followed by a reasonably sharp shock rise. The failure response of the composite transverse to the fibers, under both uniaxial stress (quasi-static and dynamic) and uniaxial strain loading, display a protracted but substantial load drop after yield followed by continued degradation in load carrying capacity. Lack of ideal parallel fiber construction leads to systematic bending failure of the alumina fibers through the sample under uniaxial stress and slow spallation kinetics as various fibers fail and pull out of the matrix across the spall plane.

INTRODUCTION

Over the last decade there has been increased industrial interest, from both the civilian and defense sectors, in metal-matrix composites (MMC's), in particular Al-matrix based composites. Although their mechanical response has been extensively studied over a wide range of strain rates(1-3) the majority of previous studies have focused on particle-reinforced composites(4-6). The focus of this study is on an aluminum-alloy composite reinforced with ceramic **fibers** of alumina. This fiber metal-matrix composite represent a material which: 1) contains two distinctly different constituents in terms of structural, physical, and mechanical properties, 2) exhibits strongly directional elastic and plastic anisotropy, and 3) achieves some of its properties due to interfacial effects that influence plastic flow and fracture behavior. These three attributes strongly affect the structure/property relationships of composites subjected to shock loading(3-6). Differences in shock velocity are known to influence the dispersive effects of the composite and thereby significantly change the loading and release wave profiles in particulate composites (4). In this paper initial findings on the dynamic and shock response of a fiber-reinforced metal-matrix composite are presented.

EXPERIMENTAL

The material used for this investigation was a 6061Al-50 vol. % Al_2O_3 fiber matrix composite produced by 3M Corporation as shown in Figure 1. A unidirectional fiber preform containing Nextel^{TM} 610 Al_2O_3 fibers is pressure infiltrated to produce a porosity-free metal-matrix composite(MMC). The measured ultrasonic wave speeds normal to the fiber direction are 7.865 mm/μs for the longitudinal-wave velocity and 4.406 mm/μs for the shear-wave velocity with polarization along the fiber direction. Using the method of cells to represent this composite material, Aboudi(7) obtains analytical expressions for the elastic constants of uniaxial-fiber composites; the calculated longitudinal- and

shear-wave speeds obtained from Aboudi's results are 7.79 mm/μs and 4.02 mm/μs, respectively. The calculated longitudinal wave speed is in very good agreement with measurement, but the calculated shear-wave speed is considerably lower. The elastic constants used in these calculations are 77.37 GPa (0.345) and 252.1 GPa (0.236) for the bulk moduli (Poisson's ratio) of aluminum and alumina, respectively.

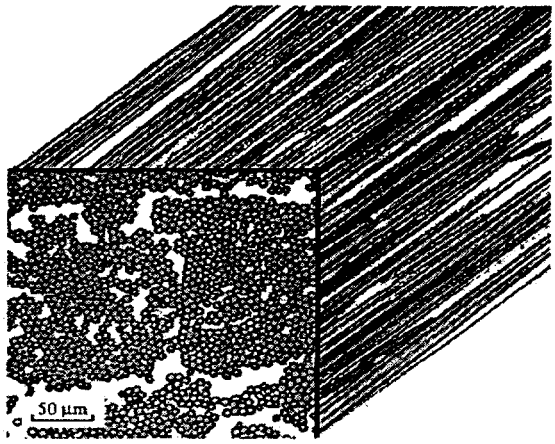

FIGURE 1. Optical metallography of 3M 6061Al-50 vol.% Al_2O_3 Fiber-Reinforced Composite

The conventional mechanical response of the MMC was measured in compression using solid-cylindrical samples 8.0 mm in dia. by 12.0 mm long. Quasi-static compression tests were conducted on a screw-driven load frame at strain rates of 0.001 and $0.1s^{-1}$. Dynamic tests, strain rates of 1000-8000 s^{-1}, were conducted as a function of strain rate and temperature utilizing a Split-Hopkinson Pressure Bar.

Shock-wave experiments were performed with a 72-mm-diameter gas gun. Projectile velocity is measured immediately before impact by means of shorting pins. Impactors used for the Al-MMC were Z-cut quartz glued to backing pieces. Foam backing was used for the profile (window) experiment. Z-cut quartz was chosen because it responds elastically in the pressure range of these experiments. The wave and spall profiles for the 3M-fiber-reinforced composite are compared to a 20 vol.% alumina-6061Al particulate reinforced composite(4). Impactor thicknesses were chosen depending upon experimental requirements (as given in Table I for both the 3M fiber and particle composite), and experimental configurations were calculated using the MACRAME computer code. Edge effects calculations were also done for each experiment to ensure that one dimensional flow was realized for the entire time of interest.

TABLE I: Summary of impact parameters for 3M-fiber and particle reinforced MMC's

Exp. *type*	Density g/cm^3	Target mm	Driver mm	Velocity m/s
Fiber *spall*	3.3418	5.160	1.511	497
Fiber *profile*	3.3418	5.196	1.527	500
Particle *spall*	2.840	3.744	2.554	506
Particle *profile*	2.840	3.897	1.520	509

Shock wave profiles were measured using time-resolved velocity interferometry, with a push/pull VISAR (7). This diagnostic system is capable of nanosecond level resolution, and yields particle velocity histories with less than 1% uncertainty. The wave profile was taken at a free surface for spall experiments, and at a target/window interface for other experiments. LiF windows were used for the Al based composites because of the close shock impedance match. On all the 3M fiber MMC experiments a thin (13 μm) aluminum shim was used on the target because of the poor reflectivity of the MMC. Shims were not used for the particle MMC tests. For these experiments, tilts are typically 1.0-1.5 mrad, and impact velocities were very close to 0.5 mm/μs which corresponds to a target pressure of ~5.0 GPa.

RESULTS AND DISCUSSION

The stress-strain response of the 3M-fiber composite is seen to vary with fiber orientation, strain rate, and temperature as seen in Figure 2. The composite yield strength parallel to the fibers is ~4x that exhibited orthogonal to the fibers quasi-statically at 298K. This finding is consistent with the high strength of alumina carrying the bulk of the stress when loading is parallel to the fibers. The lack of rate sensitivity at 298K parallel to the fibers follows the documented weak

rate dependency of alumina(3). The samples tested in this orientation failed via buckling or "brooming" of the alumina fibers.

The strain rate and temperature dependency of the composite when loaded orthogonal to the fibers reflects the rate and temperature behavior of the high-density dislocation substructure in the Al-matrix formed during fabrication(1-3).

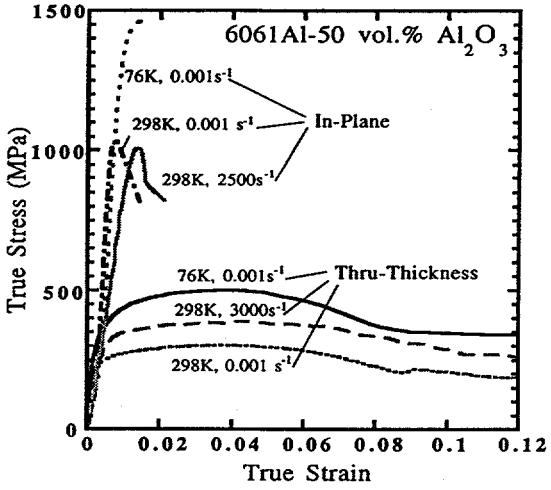

FIGURE 2. Stress-Strain Response of 6061Al-Al_2O_3 MMC in the in-plane and thru-thickness directions as a function of rate and temperature.

Preliminary wave profile data obtained for the continuous fiber reinforced Al/Al_2O_3 composite, measured across the fibers, is shown in Figure 3 along with data obtained under similar loading conditions for particle reinforced Al/Al_2O_3 (4). In both cases Z-cut quartz impactors were used, and a projectile velocity very close to 0.5 mm/μs was realized. In spite of the very similar impact conditions the final particle velocities are quite different for the two materials. It is also clear that the elastic precursors are different in nature; the fiber material shows a well defined although low amplitude elastic wave, but the particle material shows dispersive behavior. Shock rise times are similar for the two data sets, but the fiber material exhibits what looks like a multiple wave structure. This is possibly an experimental artifact caused by the impedance mismatch at the sample/LiF window interface. as discussed by Gray and Morris(9). More data is needed with a higher impedance window to determine the origin of this feature. The bulk part of the release paths agree well, with the final particle velocity for the fiber material lower than that for the particle material. This is due to the use of a glass reinforced foam backing on the quartz impactor for the fiber experiment, with PMMA used for the particle-MMC experiment.

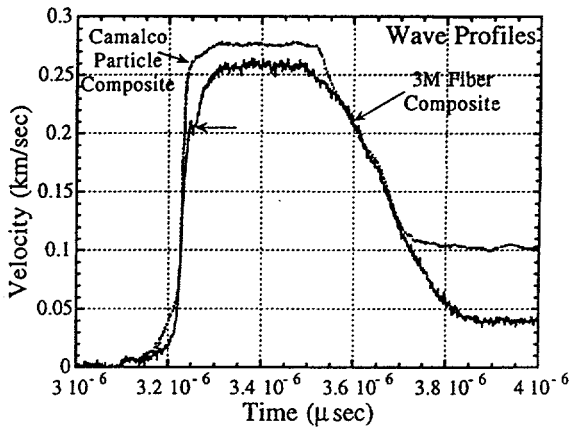

FIGURE 3. Wave-profiles for Camalco Particle and 3M Fiber MMC's.

Experiments done on the above materials to measure spall strength (no windows) are compared in Figure 4. Results are very different, and these results are preliminary. More experiments are needed to determine reproducibility. Elastic behavior is essentially identical to that described above, but the fiber material shows unusual spall behavior. This experiment was done with an aluminum foil on the sample free surface because of the poor reflectivity of the MMC, and this needs to be looked at in more detail. Spall experiments without foils were done successfully on the particle-reinforced MMC. If these results are verified, it is clear that the fiber material has a very low spall strength. The origin of the overshoot on the plastic wave is unknown but if found to be reproducible may indicate complex flow in the 3M fiber MMC.

Another interesting observation is the very distinct separation between the elastic precursor and the plastic wave in the fiber-MMC This was not observed in the material containing discontinuous reinforcement(4). The behavior of the uniaxial-fiber-reinforced MMC may have something to do with its unique plasticity properties and material anisotropy, which result in

enhanced separation between elastic and plastic waves, and a very distinct particle-velocity overshoot in the precursor; the latter is reminiscent of an upper/lower yield point and rapid dislocation multiplication at the elastic wave front. This response is not characteristic of 6061-T6 Al. The difference in behavior between continuous (fiber) reinforcement and that of the matrix material alone (as well as that of Al-alumina MMC's at low volume fractions of discontinuous reinforcement) is dramatic in this regard.

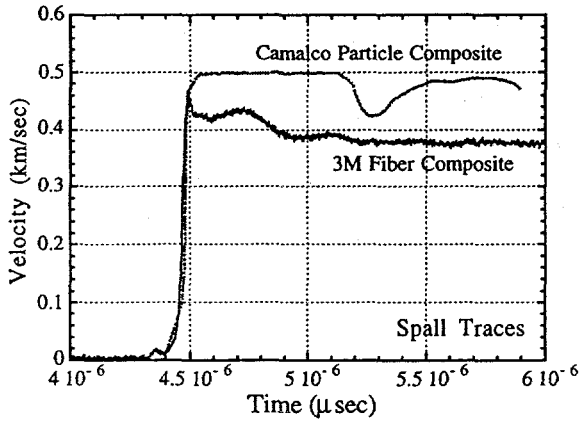

FIGURE 4. Spall traces for Camalco Particle and 3M-Fiber MMC's.

CONCLUSIONS

Based upon a study of the dynamic deformation and fracture of a 6061Al-50 vol. % Al_2O_3 fiber composite the following conclusions can be drawn: 1) the stress-strain response was found to vary substantially as a function of loading orientation; increasing the strain rate was observed to only slightly increase the yield strength of either orientation, 2) the failure response of the composite transverse to the fibers, under both uniaxial stress and uniaxial strain loading, display a protracted but substantial load drop after yield followed by continued degradation in load carrying capacity, and 3) lack of ideal parallel fiber construction leads to systematic bending failure of the alumina fibers through the sample under uniaxial stress and slow spallation kinetics as various fibers fail and pull out of the matrix.

ACKNOWLEDGMENTS

The authors acknowledge 3M Corporation for providing the 3M fiber MMC and M. Lopez and R. Carpenter II for their assistance with the experiments. This work was performed under the auspices of the U.S. Department of Energy.

REFERENCES

1. Hong, S.I., Gray III, G.T. and Lewandowski, J.J., "Microstructural Evolution in an Al-Zn-Mg-Cu Alloy-20 vol. % SiC Composite Shock Loaded to 5 GPa," *Scripta Metall. et Materialia* 27, 431-436 (1992).
2. Hong, S.I., Gray III, G.T. and Lewandowski, J.J., "Dynamic Deformation Behavior of Al-Zn-Mg-Cu Matrix Composites Reinforced with 20 vol.% SiC," *Acta Metall. Materialia,* 41, 2337-2351 (1993).
3. Huang, J.C., Lo, Y.-S., and Gray III, G.T., "The Response of Metal-Matrix Composites subjected to Quasi-Static and Shock-Wave Deformation," *Matls. Chem. and Physics,* 35, 71-85 (1993).
4. Johnson, J.N., Hixson, R.S., and Gray III, G.T., "Shock-wave Compression and Release of Aluminum / Ceramic Composites," *J. Appl. Phys.* 76, 5706-5718 (1994).
5. Gray III, G.T., "Shock-Loading Response of Advanced Materials," High-Pressure Science and Technology-1993, edited by S.C. Schmidt, J.W. Shaner, G.A.Samara, and M. Ross, American Institute of Physics Conference Proceedings 309, Part 2, 1161-1164(1993).
6. Vecchio, K.S. and Gray III, G.T., "Shock-Loading Response of 6061-T6 Aluminum-Alumina Metal-Matrix Composites," *Metallurgical and Materials Transactions A* (1995) in press.
7. Aboudi, J., "Closed Form Constitutive Equations for Metal Matrix Composites," Int. J. Engng. Sci., Vol. 25, No. 9, pp. 1229-1240 (1987).
8. Hemsing, W.F., "Velocity Sensing Interferometer (VISAR) Modification," *Rev. Sci. Instrum.* 50, 73-78 (1979).
9. Gray III, G.T. and Morris, C.E., "Influence of Peak Pressure on the Substructure Evolution and Shock-Wave Profiles of Ti-6Al-4V," Sixth World Conference on Ti, edited by P. Lacombe, R. Ticot, and G. Beranger, Les Editions de Physique, pp. 269-274 (1989).

SHOCK TRACKER CONFIGURATION OF IN-MATERIAL GAUGE

R. R. Alcon and R. N. Mulford

Los Alamos National Laboratory, Los Alamos, New Mexico 87544

A special configuration of electromagnetic in-material gauge enables measurement of shock time of arrival at up to forty-one points in 10 mm of run distance. This measurement clearly defines the shock line for Lagrangian analysis, and provides sufficient shock velocity data to determine time of turnover to detonation. The measurement mimics a wedge test, with the advantage that data is obtained inside the material, rather than at a surface. The technique has been applied to the reactive systems X-0407, PBX-9404, and thermally damaged PBX 9502. Response to multiple shock inputs is linear, and shock tracker data can be seen to reflect the velocities of the separate shocks. Several configurations will be discussed.

INTRODUCTION

Use of embedded magnetic gauges provides unique measurements in the Lagrangian frame of the time evolution of the shocks. Use of multiple gauges gives independent measurements of particle velocity u_p, shock velocity U_s, and, from impulse records, P. The precision of the gauges is better than 2%.

The shock tracker gauge supplements the MIV configuration, providing a set of shock arrival times at 0.25 mm intervals in the material. Data from MIV records is complemented by the detailed shock velocity (U_s) data provided by the shock tracker.

Lagrange analysis of MIV gauge data[1] depends for its success on definition of a shock line for the experiment. Deriving this shock line solely from ten available gauge records yields an inadequately defined x-t locus. In particular, the slope, and hence the velocities, at the end points are ill-defined. This shock locus is used to give projectile velocity u_p and pressure P in between gauges. It can also define the shock jump at the gauge itself, when the gauge record falls off the line defined by other gauges. This can result in a "kink" in the surface constructed around the line, a discontinuity which is amplified as the surface is expanded away from the shock line. A well defined shock line smooths the surface to more nearly resemble the physical case, and permits more accurate determinations of parameters derived from derivatives along the line or surface.

The shock tracker provides a measurement of acceleration and velocity analogous to the record obtained in a wedge shot, with the added benefits of a reliable, supported, reproducible input plane wave and data at each 1/4 mm. Unlike a wedge shot, the shock tracker gauge is inside the material, and is not susceptible to critical angle or other surface effects.

EXPERIMENTAL

MIV gauges (Magnetic Impulse and Velocity) gauges have been used for many years to directly measure particle velocity in materials accelerated by shock waves. The gauge consists of a set of fine wire loops, actually a 0.2 mil thick aluminum pattern etched onto a 1 mil plastic substrate.[3] The entire shock experiment is conducted in a uniform magnetic field generated by large fixed magnets, with the active region of the gauge perpendicular to the field. When the material under study is accelerated, the MIV loops yield a current as they are carried through this external magnetic field at the particle velocity of the material. The gauge is glued onto a precisely machined planar surface interior to the material to be studied, at a specified angle as shown in Figure 1.

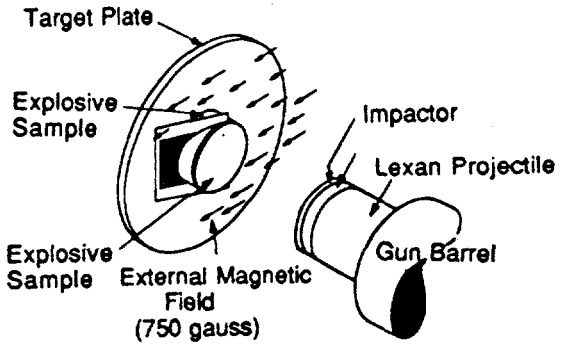

Figure 1. The MIV gauge measures particle velocity as it is propelled through an external magnetic field.

The shock tracker configuration supplements these configurations, as shown in Figure 2. The original design for the shock trackers was developed and tested by John Vorthman.[2]

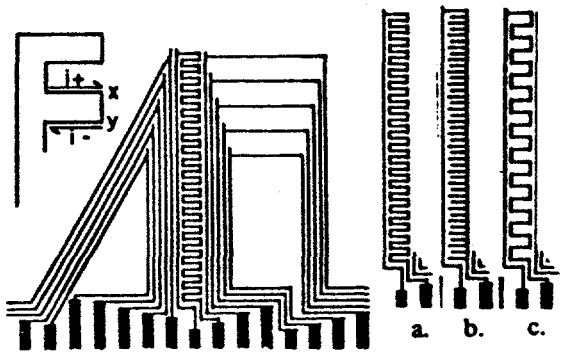

Figure 2. The shock tracker is located in the middle of the MIV gauge. Configurations a), b), and c) have been used.

The shock tracker consists of a large number of accurately spaced elements perpendicular to the magnetic field direction. Different configurations are shown in Figure 2. A closed loop is required, as configuration b was proven to give no response to the shock. Right- and left-going bars on each loop of the tracker generate positive and negative current in response to the velocity jump, as the active loop of the tracker is propelled across the flux lines of the magnetic field. The minimum interelement spacing used is 0.5 mm. The gauge is employed at an angle to prevent each incremental element from perturbing the flow at the next succeeding element. At the usual angle of 30°, the 0.5 mm spacing yields data every 0.25 mm.

Experiments described here are done on a single stage light gas gun. Waves generated are one-dimensional for about 4 μsec.

RESULTS

Examples of tracker traces are shown in Figures 3, 5, and 8. Figures 3 and 4 are data from detonating X-0407, Figures 5 and 7 are data from PBX 9502 at 80°C before detonation is reached, and Figure 8 shows the tracker response to multiple shocks.

The X-0407 sample shown in Figure 3 demonstrates how the frequency of the center crossings reflects the shock velocity. Both frequency and particle velocity increase smoothly as initiation and growth to detonation occur. Center crossings are measured and plotted against the location of each shock tracker loop in the material, to generate a graph of the shock line, analogous to a wedge record. Velocity data is summarized in the graph in figure 4, showing the turnover to detonation at 1.5 μsec.

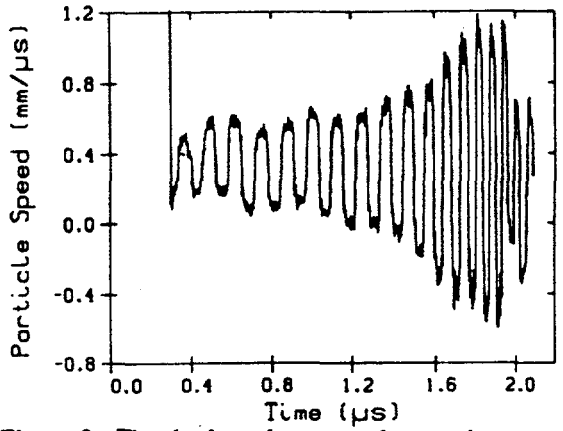

Figure 3. The shock tracker responds to each traverse of a horizontal element by the shock.

The increase evident in the positive and negative u_p amplitude is due to the acceleration of the shock as it traverses a single loop, as shown in Figure 2. The current in leg y will cancel that generated by leg x, unless acceleration of y relative to x enables it to traverse more flux lines than x, in which case the negative current contribution will more than cancel the positive current contribution, and the current excursions will increase in amplitude.

At around 1.9 μsec, the velocity becomes constant at the detonation velocity and the particle velocity returns to its steady state amplitude, reflecting zero acceleration.

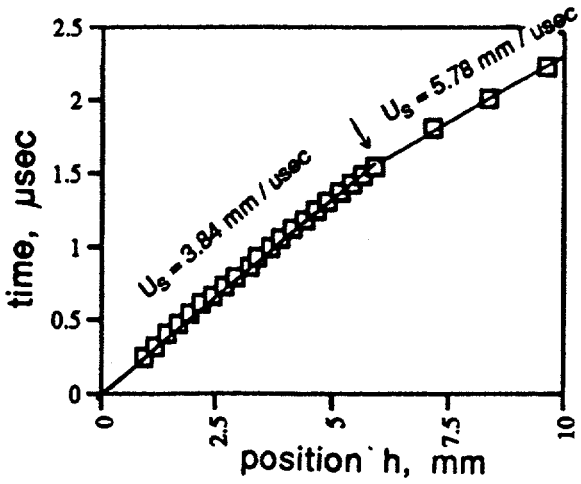

Figure 4. The shock line of the reacting X-0407 is defined by the zero crossings of the shock tracker record. It shows the turnover to detonation much as a wedge record does.

Shock velocities are easily obtained from the shock tracker data. The shock line gives a much higher degree of statistical precision than can be obtained from a few gauge positions, particularly when the shock velocity is not constant.

PBX 9502 subjected to ratchet growth before installation of the gauge yielded the record shown in Figure 5. Abrupt velocity changes due to density discontinuities or cracks are clearly evident in the tracker record and in the shock line, Figure 6, generated from the tracker data. This behavior is also evident in the u_p gauge records.

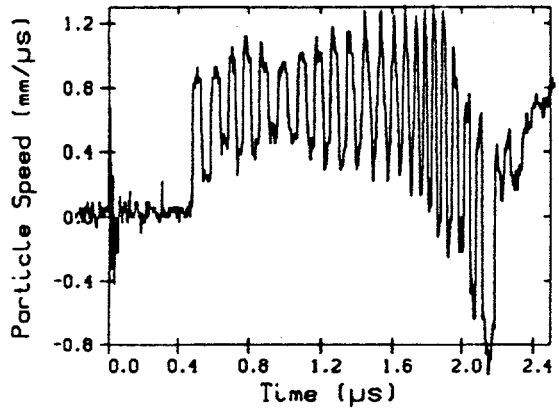

Figure 5. The shock tracker record of PBX 9502 that has undergone irreversible thermal expansion, or "ratchet growth".

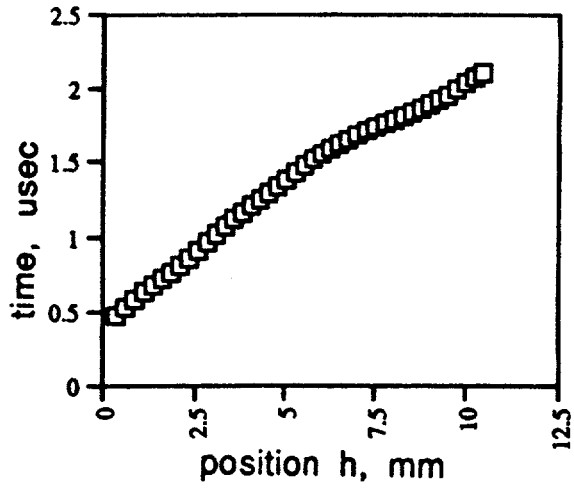

Figure 6. The shock line of PBX 9502 that has undergone irreversable thermal expansion, or "ratchet growth".

Hot PBX 9502 running to detonation generates the example shown in Figure 7. In this material, the shock tracker indicates inert or constant velocity behavior, and even a slight deceleration of the input shock. Comparison with u_p gauge records shown in Figure 8 shows that homogeneous reaction is occurring, with a reactive wave running behind the initial shock. Thus the two regions of the shock tracker are being propelled at different rates, creating a more complex output than arises from simple heterogeneous detonation, one that reflects acceleration of the material behind the shock front.

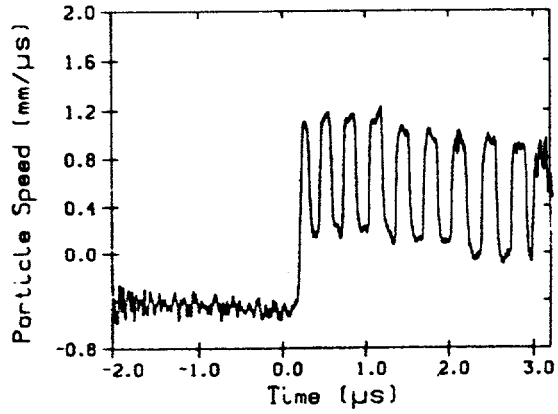

Figure 7. The shock tracker record of PBX 9502

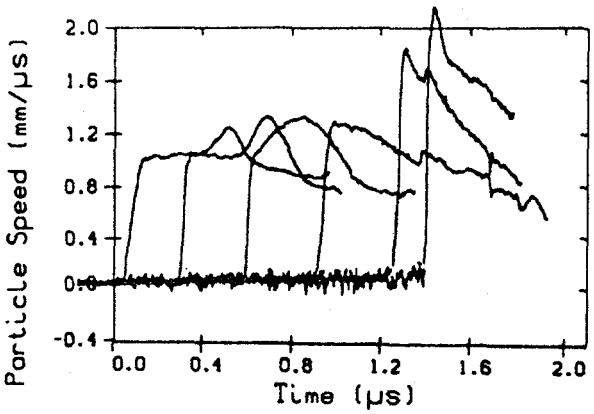

Figure 8. Particle velocity records showing reaction in PBX 9502.

Comparison of shock tracker and particle velocity gauge data in Figs. 8 and 9 indicates that the tracker yields an incomplete description of the reaction in the material, since tracker data does not reflect acceleration behind the shock front. By analogy, it may be that standard wedge experiments yield the same incomplete picture. Use of the shock tracker coupled with the particle velocity gauges is clearly important in accurately describing the turnover to detonation in materials such as hot PBX 9502.

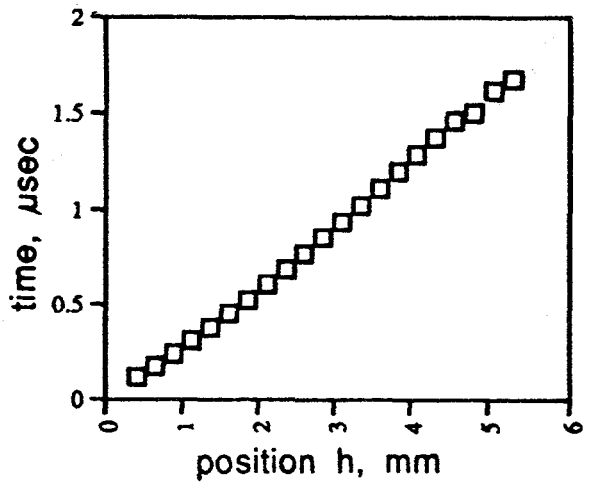

Figure 9. The shock line of reacting PBX 9502

Shock tracker response to two successive square shocks is shown in Figure 10. The data from this shot is well modeled by summing the response of the tracker to the two individual shocks, indicating that the gauge retains its shape in the flow, and is not damaged by the passage of the first shock. Thus, distortion of the portion of the gauge in the flow behind the front is not contributing current to the net output of the gauge.

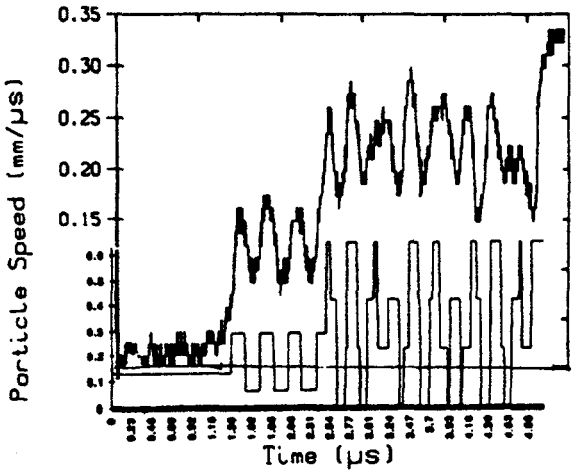

Figure 10. The shock tracker record of PBX 9502 responding to two square waves is a sum of responses to each wave.

Limitations on the accuracy of the gauge are precision of the construction and measurement of the location of the elements, and the risetime of the signal as the shock traverses a given element.

Risetimes of the individual cross bar response signals are slightly longer than the traversal time of the gauge thickness by the shock wave. The ratios of observed risetime to calculated traversal time in two X-0407 experiments are 1.76 and 1.78.

SUMMARY

These shock tracker gauges have been used in gun shots to observe the growth of the reactive wave in several explosives. The shock tracker data resembles wedge shot data, with an adequate density of points to define the shock line and characterize the turnover to detonation.

1. C.A. Forest, "Lagrangian Analysis, Data Covariance, and the Impulse Time Integral", in Shock Compression of Condensed Matter, 191, Elsevier 1992.

2. John Vorthman, private communication

3. RDF Corporation proprietary method. RDF Corporation, Hudson, New Hampshire.

OVERTAKING WAVE INTERACTION, REFLECTED SHOCK OR REFLECTED RELEASE? *

J. N. Fritz

Los Alamos National Laboratory, Los Alamos, New Mexico 87545 USA

Modern experiments involving shocks are frequently more complicated than just sending a shock wave through a material. Multiple waves of interest occur in some experiments. When a wave overtakes another wave in a material a reflected wave is produced. It is valuable to know the nature of the reflected wave. A general expression giving the answer to this question is presented. For the fluid approximation and a material described by $u_s = c_0 + su_p$ and $\rho\gamma$ a constant (γ is the Grüneisen function) the answer is particularly simple. If $s(1+s\eta) - \gamma_0 > 0$ ($\eta \equiv 1 - \rho_0 V = u_p/u_s$) a small shock overtaking the shock defined by η will reflect as a release; < 0, it will reflect as a shock.

INTRODUCTION

Courant and Friedrichs(1) discuss overtaking waves for gases. They quote a result from a report by von Neumann; if $\gamma \leq 5/3$ (the specific heat ratio) then a shock overtaking a shock results in a reflected rarefaction, *i.e.*, $S_{\rightarrow}S_{\rightarrow} \rightarrow R_{\leftarrow}TS_{\rightarrow}$. (In this notation T represents a contact discontinuity.) This behavior is not universal; it depends on the gas equation-of-state. These reflected waves are usually much smaller than the major waves of interest, and they are commonly neglected. However, if we have probes that can measure these waves so that they serve as markers to locate important interactions, then it is important to know what kind of waves to expect. Mulford *et al.*(2) examine a case where such a reflected wave could have either enhanced or suppressed a reaction in explosives. In this case the reflected wave may have had an influence disproportionate to its size. Our goal is a relation giving the type of the reflected wave from general EOS considerations.(3)

INTERACTIONS

Fig. 1 shows an elementary interaction. Given a sufficient number of these connected in the appropriate manner, one can solve most any 1D wave problem. Such a scheme forms the basis of Lynn Barker's SWAP9 code and the author's MACRAME code. The language of these interactions serves well for our current problem. Fig. 2 shows the dynamics of an interaction, complementing the kinematics shown in Fig. 1. Besides wave-wave interactions, the interactions of waves with interfaces (various contact discontinuities) are important. In the particular interaction shown in this figure the $T \rightarrow V$ state production is a release, and in an "honest" calculation it would only be used if this wave step were a small one.

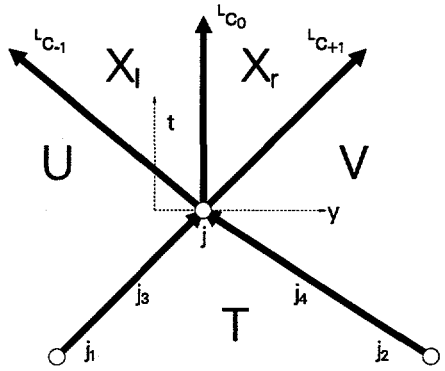

FIGURE 1. An interaction diagram. Two rays, waves or contact discontinuities, come together to form an interaction. A forward and backward wave (and possibly a contact discontinuity) emerge from the interaction. This interaction is shown in the Lagrangian (material) plane (t–y), the outgoing interface is vertical. The states U and V interact to form the X_l and X_r states, which have a common P and u. The state T disappears.

*This work supported by the US Department of Energy.

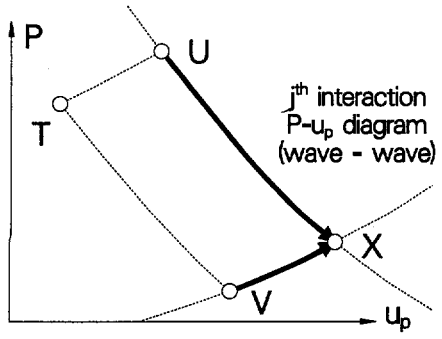

FIGURE 2. A wave-wave interaction in $P(u)$. Both U and V have been created from T by waves that are about to collide. At collision, T vanishes, and the resultant state X is determined by the cross-curves attached to U and V. These cross-curves (shock up and isentrope down) have opposite slopes so a simple solution is usually feasible. The U cross-curve represents a backward-facing wave with a negative slope (opposite for V).

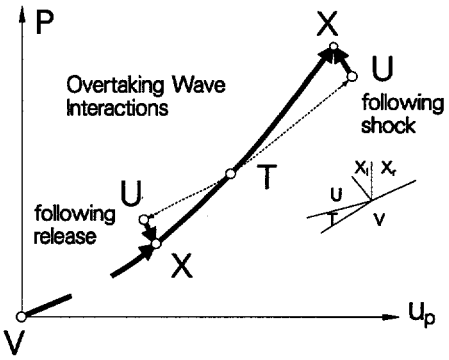

FIGURE 3. Overtake (t–y in inset). Both a small release and a small shock for the $T \rightarrow U$ wave are shown. In this figure the slope of the T cross-curve is less than the slope of the principal Hugoniot ($g < 0$).

THE OVERTAKE INTERACTION

In Fig. 3 we show a wave overtaking an initial shock into a material. The state T is the first shocked state. A following wave, produced by some interaction off to the left, transforms T to U. At overtake T has disappeared, and U interacts with the original state V to produce X. Both T and X lie on the Hugoniot centered at V. For a small following wave, the nature of the reflected wave (the $U \rightarrow X$ behavior) depends on the relative values of the slopes of the forward cross-curve through T and slope of the Hugoniot at T. The figure depicts a common case (for condensed fluids) where the latter exceeds the former. We define:

$$g = \left(\frac{dP_S}{du}\right)^2 - \left(\frac{dP_h}{du}\right)^2 \qquad (1)$$

The slope of the cross-curve is the slope of the isentrope (the slope of the second shock curve matches it to second order at the junction). From the jump conditions $P_h - P_0 = \rho_0 u_s u$ and $u/u_s = 1 - \rho_0 V_h \equiv \eta$ we obtain

$$\frac{dP_h}{du} = \rho_0(u_s + uu_s'), \quad \frac{dV_h}{du} = -\frac{u_s - uu_s'}{\rho_0 u_s^2} \qquad (2)$$

where $u_s' = du_s(u)/du$. Now $dP_S/du = \rho c$ for a forward facing wave, and $\rho c^2 = B_S$, the isentropic bulk-modulus. The Hugoniot modulus is $B_h = -V dP_h/dV = -V(dP_h/du)(du/dV_h)$, then from eq. (2) and the jump conditions we get

$$B_h = \rho_0 u_s(u_s - u)(u_s + uu_s')/(u_s - uu_s') \qquad (3)$$

The Grüneisen function γ links B_S and B_h by $(\gamma/2V_h)(V_0 - V_h) = (B_h - B_S)/(B_h - B_{\rm ch})$, where $B_{\rm ch} = V_h(P_h - P_0)/(V_0 - V_h)$. We use it as

$$B_S = \left[1 - \frac{\gamma}{2V_h}(V_0 - V_h)\right] B_h + \frac{\gamma}{2}(P_h - P_0) \qquad (4)$$

We combine all this, and after some algebra and convenient cancelation we obtain

$$g = \frac{\rho_0 u u_s' \rho_0 u_s u}{u_s - uu_s'}\left[u_s'(1 + \frac{uu_s'}{u_s}) - \frac{\gamma\rho}{\rho_0}\right] \qquad (5)$$

The sign of this general expression for g is (usually) controlled by the factor in the square brackets. For $g < 0$ we have the case shown in Fig. 3, a following shock reflects as a shock and a following rarefaction reflects as a rarefaction. For $g > 0$ the nature of the following wave changes upon reflection.

Linear $u_s(u)$, constant $\rho\gamma$

For this case the factor in square brackets becomes $s(1+s\eta)-\gamma_0$. For most dense fluids (and for solid media where we neglect stresses other than the pressure) we typically have $s < \gamma_0$. Then for small shocks we have the $g < 0$ case. For stronger shocks ($\eta > \eta^* = (\gamma_0 - s)/s^2$, if this is attainable) we change to $g > 0$. For stainless steel 316

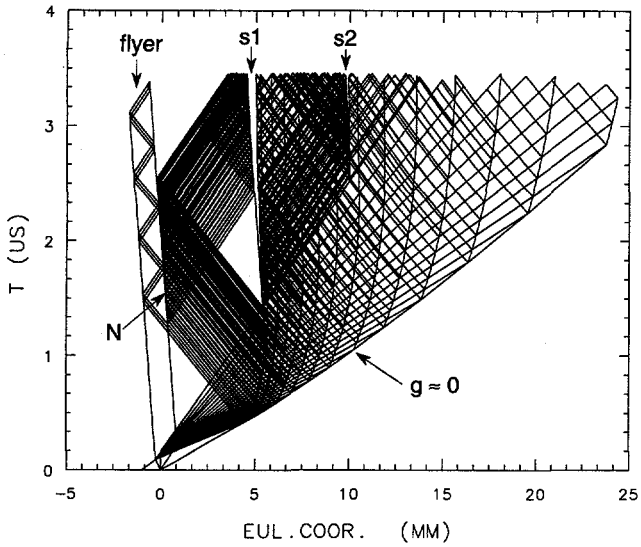

FIGURE 4. An impact problem. A 1 mm thick flyer of 316 stainless steel with $u_d = 8\,\mathrm{mm}/\mu\mathrm{s}$ impacts a thick layer of the same material. Shocks advance in both directions from the point of impact. The backward-facing shock reflects from the rear of the flyer as a rarefaction fan. This fan overtakes the shock in the other direction. The overtake interactions of current interest are strung out along the decaying shock. The initial pressure in the metal is 3.4 Mbar. In this particular approximation each of the "wavelets" in the rarefaction fan carries about 250 kbar (this varies somewhat from wave to wave). The reflected shock from the first overtake interaction is 2 kbar. As the shock decays these reflected waves decrease in size and we change from $g > 0$ to $g < 0$ between the 8th and 9th interaction on the shock front in accordance with Eq. (5). Subsequent reflected waves are releases. At the 8th interaction, the one indicated by the arrow, the code decided the reflected wave was too weak to bother with and discarded it. The switch in behavior occurs at 150 GPa on the decaying shock rather than the 118 GPa quoted in the text because we do not quite have $\rho\gamma$ a constant in the code. These reflected waves work their way back through the large rarefaction fan and arrive at the flyer/anvil interface (N). Ordinarily a wave-gathering mechanism in the code would have combined and averaged a lot of these little waves. Here we have turned off this mechanism so that we can see all the waves produced by the interactions.

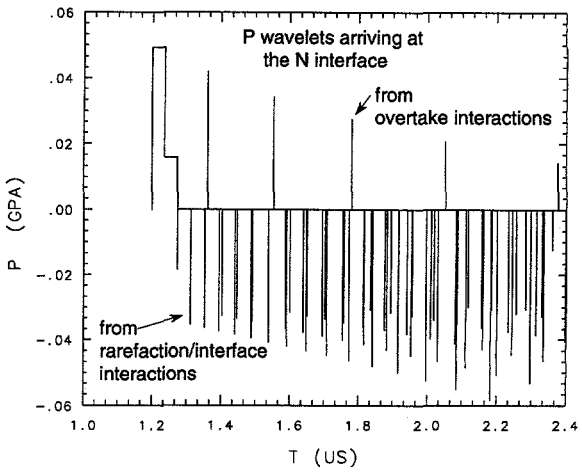

FIGURE 5. P impulses at the anvil surface. The first wave is from the first overtake interaction. This is a shock and the flyer and anvil maintain contact. However, we immediately start getting negative pressure pulses from interactions between the large rarefaction fan and contact discontinuities left by earlier overtaking interactions. This rapidly drops the pressure at the flyer/anvil interface and they separate for $P < 0$. A small reverberating pressure wave is trapped in the flyer. The subsequent pulses are pressure "delta functions" arriving at the anvil free surface. They reflect here into their opposites, and the pressure stays zero on the free surface. If we were to look at these waves along the tail of the large rarefaction fan, they would be cumulative, and indeed, there is an increasing pressure trough in this region that eventually turns into a spall ($s1$ in the previous figure). This spall cuts off communication to the anvil free surface so we only get to look at the first six waves from the overtake interactions. They are decreasing and if we could see them in this plot we would see them switch sign between interactions 8 and 9. We note that the 2 kbar wave from the first interaction has decayed to 0.5 kbar by going through the large release fan. The delta functions displayed in this plot are approximations to continuous waves and combining the pulses appropriately would wash out the pressure pulses from the pure overtake type of interactions (except for the leading edge). The shock nature of the wave coming out of the *extended* interaction does not last as long as the g-condition would lead one to expect.

($\rho_0 = 7.96\,\mathrm{g/cm^3}$, $c_0 = 4.464\,\mathrm{km/s}$, $s = 1.544$) we have $\eta^* = 0.262$ or a pressure on an initial shock of 118 GPa.

For $S_{\rightarrow}S_{\rightarrow}$ or $R_{\rightarrow}S_{\rightarrow}$, where $R_{\rightarrow}$ is a relatively small rarefaction, a single elementary overtake interaction and the g-condition from Eq. (5) tells us what to expect. However, if $R_{\rightarrow}$ is an extended release the interactions between the release fan and contact discontinuities produced by early overtake interactions profoundly affect the overall reflected wave coming out of the extended interaction. We study such an interaction and show the results in Figs. (4,5).

Ideal Gas

The Hugoniot for an ideal gas can be represented as $y = \sqrt{1+x^2} + x$, where $y = u_s/c_0$ and $x = (\gamma+2)u/(4c_0)$. (In this section γ is the Grüneisen constant and $\gamma = \gamma_{\text{s.h.}} - 1$.) We have $y' = dy/dx = y/(y-x)$, $u_s' = y'(\gamma+2)/4$, and $\rho_0/\rho = 1 - 4x/(y(\gamma+2))$. If we insert all this in Eq. (5) we find for a residual factor controlling the sign of g

$$\frac{2-3\gamma}{4} + \frac{\gamma}{2}x(\sqrt{1+x^2} - x) \qquad (6)$$

Thus for a weak shock (small x) we recover von Neumann's result: for $\gamma < 2/3$ we have $g > 0$. The $f(x)$ in Eq. (6) monotonically increases from 0 to 0.5. Thus for strong shocks γ can approach 1 from below and still have $g > 0$. If γ exceeds 2/3–1 for the appropriate x then $g < 0$ and a following shock will reflect as a shock. Typical γ's used in a constant-γ law EOS to represent explosives exceed these values, so if one uses this EOS one can expect reflected shocks from following overtaking shocks.

DISCUSSION

We have obtained a general expression that answers the question about the nature of the reflected wave from the interactions $S_{\rightarrow}S_{\rightarrow}$ and $R_{\rightarrow}S_{\rightarrow}$. (Our interaction diagram does not directly apply to the interesting interaction $S_{\rightarrow}R_{\rightarrow}$.) It is valid for *small* overtaking waves and for a *fluid* EOS. The result is seen to be a competition between the non-linearity of the shock curve ($s > 0$) and the pressure produced by an increment of energy at constant volume (γ). If an EOS is used that imposes a non-physical relation between these two different EOS paths then a non-physical result for the predicted types of waves may result.

For solids the slope of the T cross-curve is likely to be steeper. It depends on how close the T state is to the yield surface at this pressure. If this state is not near the yield surface, then the material will respond elastically to a small following wave. We should then increase the ρc of the T cross-curve to correspond to an elastic velocity. This can be achieved by multiplying the first term in Eq. (1) by the factor $3(1-\nu)/(1+\nu)$, where ν is the appropriate Poisson's ratio at pressure. Unfortunately multiplying this term by this factor eliminates a lot of the convenient cancelation that occurred on the way to Eq. (5) and the result is considerably complicated. We can say that the effect of a non-hydrostatic stress is to favor the case $g > 0$.

For strong following shocks the extension of $T \rightarrow U$ will eventually rise above the extension of the first shock curve $T \rightarrow X$ in $P(u)$. Eventually we will have $S_{\rightarrow}S_{\rightarrow} \rightarrow R_{\leftarrow}TS_{\rightarrow}$. These two curves can be represented as $P_1(u) - P_0 = \rho_0(u_s/u)u^2$ and $P_2(u) - P_1 = \rho_1(u_s(\Delta u)/\Delta u)(\Delta u)^2$, where $\Delta u = u - u_1$ and the subscript 1 without a functional variation refers to the T state. For strong shocks $u/u_s = \eta$ tends toward a limit determined by having the factor $1 - (\gamma/2V)(V_0 - V)$ vanish. We then have $\lim_{u\rightarrow\infty}\eta = 2/(2+\gamma)$. Then $\lim_{u\rightarrow\infty} P_2(u)/P_1(u) = \rho_1(2+\gamma_2)/[\rho_0(2+\gamma_1)]$, where γ_1 and γ_2 are the limiting values of the Grüneisen parameter reached along the first and second shock Hugoniots respectively. They are likely the same, of the order of 2/3; and the respective positions of the two curves are controlled by the initial density and the density at the T state, *i.e.* $P_2/P_1 \rightarrow \rho_1/\rho_0$.

REFERENCES

1. R. Courant and K. O. Friedrichs, *Supersonic Flow and Shock Waves*, Pure and Applied Mathematics, Interscience Publishers, Inc., New York, New York, 1948, p. 178.
2. R. N. Mulford, S. A. Sheffield, and R. R. Alcon, Preshock desensitization of PBX explosives, in *High-Pressure Science and Technology—1993*, edited by S. C. Schmidt, J. W. Shaner, G. A. Samara, and M. Ross, number 309 in AIP Conference Proceedings, pages 1405–1408, New York, 1994, American Institute of Physics, AIP Press.
3. Something more definitive than "it depends on γ"!

II.

TWENTY-SECOND

INTERNATIONAL PYROTECHNICS SEMINAR,

JULY 15-19, 1996,

FORT COLLINS, COLORADO

LA-UR-96-1837

Momentum Transfer in Indirect Explosive Drive

J. E. Kennedy, Los Alamos National Laboratory, Los Alamos, NM 87545
C. R. Cherry, Sandia National Laboratories, Albuquerque, NM 87185
C. R. Cherry, Jr.
R. H. Warnes, Los Alamos National Laboratory, Los Alamos, NM 87545
S. H. Fischer, Sandia National Laboratories, Albuquerque, NM 87185

Abstract

Material which is not in direct contact with detonating explosives may still be driven by the explosion through impact by driven material or by attachment to driven material. In such circumstances the assumption of inelastic collision permits estimation of the final velocity of an assemblage. Examples of the utility of this assumption are demonstrated through use of Gurney equations. The inelastic collision calculation may also be used for metal parts which are driven by explosives partially covering the metal. We offer a new discounting angle to account for side energy losses from laterally unconfined explosive charges in cases where the detonation wave travels parallel to the surface which is driven.

1. Introduction

The Gurney model and equations for predicting the velocity to which metal is driven by detonating explosives implicitly assume that the explosive is in contact with (all) the metal that is being driven. This paper addresses two geometries for which that assumption does not hold, and offers a method for predicting the behavior under these circumstances. The basic idea is that of inelastic collision; this amounts to momentum sharing between "primary" metal, which is directly driven by being in contact with the explosive, and "secondary" metal (not in contact with the explosive), which interacts with and travels with the primary metal.

We present experimental data which support this idea, and which also contain a surprise. The results of computational modeling and Gurney calculations provide insight into the surprising result.

2. Inelastic collision of free-flying plates and secondary objects

A range safety problem arose some years ago that was not described well by Gurney equations or by wave-code simulations because the system was rather complex. The problem was that of determining the maximum distance traveled by fragments from the detonation testing of a weapon assembly. In the weapon some relatively thin metal layers were driven through direct contact with the detonating explosive, and aerodynamic analysis indicated that fragments from these layers were not massive

enough to travel very far before being stopped by air drag. However, parts of these thin fragment layers impacted rather massive weapon components and drove those heavy components. The aerodynamic drag of the heavy components was proportionally so much less than that of the light ones that it became important to estimate the velocity to which the heavy components would be driven.

The idea which we applied for this analysis was that the light fragments would collide inelastically with the heavy component. It was postulated that the light and heavy pieces would then "stick together" and move off together with the momentum contributed by the initial velocity of the light fragments. Denoting mass and velocity respectively as M and v, the light fragment(s) as 1, the heavy component as 2, and the velocity of the combined mass as v_{1+2}, we then simply have

$$Momentum = M_1 v_1 = (M_1 + M_2) v_{1+2}. \qquad (1)$$

We conserve momentum rather than energy because momentum can be conserved without having to create energy, while the converse is not true.

Light fragment velocities were calculated with Gurney equations and the air drag of the heavy components was estimated for tumbling flight (Ref. 1). Aerodynamic analysis predicted that the heavy components, driven by impact of light fragments, would travel farther than the faster free-flying light fragments, and this was indeed found to be true. The maximum distance predicted for a heavy component was 1786 ft. and the range measured for that component was 1746 ft. This exceeded the range of light fragments that were recovered. This good agreement suggests that this model for momentum transfer has merit.

3. Cherry Experiments

Another set of experimental data which involved indirect drive of some metal was generated by the Cherry family as part of a science fair project (Ref. 2). The efficiency of explosive slab charges of a fixed mass but different shapes was studied by Christopher Cherry, Jr. and his father, Christopher. The mass to be driven, a 4-in.-square , 3/4-in.-thick steel plate, was placed on top of a wooden post at a constant height of four feet, and leveled carefully. A charge of North American Explosives Primasheet 1000 explosive weighing approximately 8.5 g and a rubber buffer sheet were attached to the rear face of the steel plate, as shown in Fig. 1. The charge was detonated by an electric blasting cap, and the distance which the plate flew before landing on a dirt road was measured, as shown on Fig. 2. The rubber buffer was intended to prevent damage to the steel plate in the form of spallation or indenting of the plate; its use accomplished these

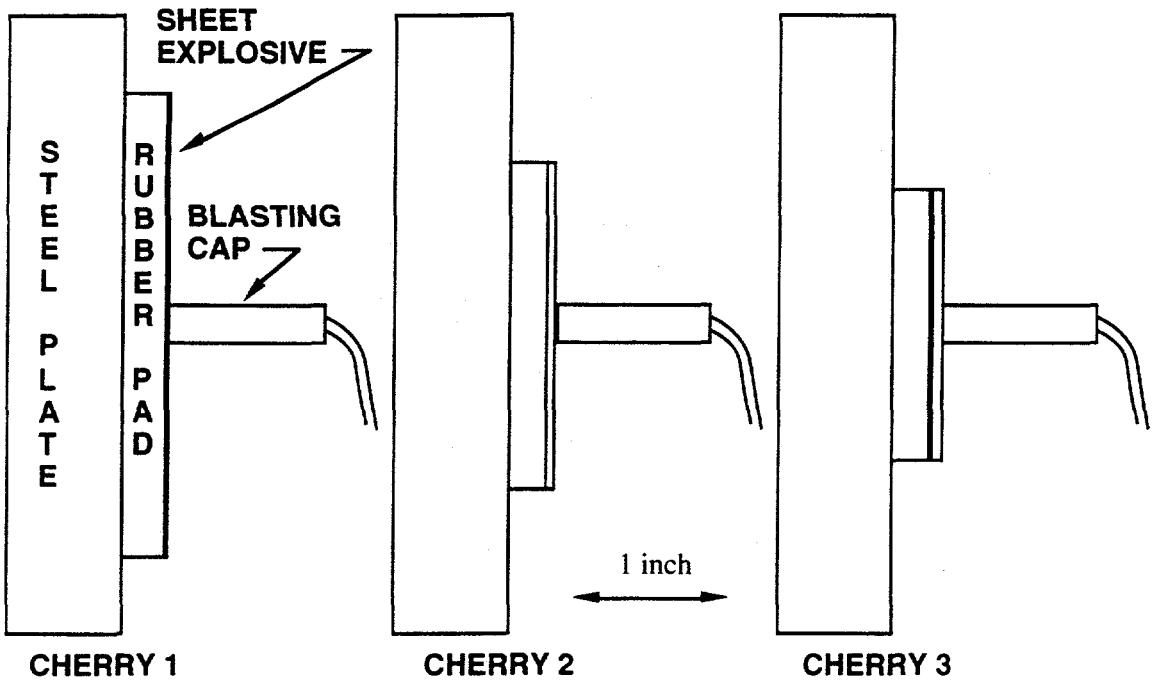

Fig. 1. Configuration of Explosive and Inert Parts of Cherry Experiments, to Scale

objectives, and the Cherrys were able to use the same steel plate for the entire test series.

Experimental results were consistent for each charge shape, as indicated by the range of velocities over four trials in each experiment. The data in Table I show clearly that the thinnest charge (Cherry 1), covering the greatest area on the plate surface, drove the plate to the highest velocity by a significant margin. This would not be expected on the basis of Gurney calculations of the plate velocity. If the entire plate mass (1633 g) and entire charge mass were used in asymmetric-sandwich Gurney calculations (Ref. 3), the predicted velocity would be approximately constant at 11.1 m/s for all three test configurations.

Table I

Results of Cherry Experiments Compared with Gurney Calculations

Experiment	Primasheet Explosive		Observed	Velocity by Gurney,
	Size	Weight	Velocity	Based on $\alpha^* = 30^\circ$
Cherry 1	3 in. sq. x 0.042 in.	8.39 g	10.90 ± 0.20 m/s	10.92 m/s
Cherry 2	2.125 in. sq. x 0.084 in.	8.65 g	9.66 ± 0.18 m/s	10.93 m/s
Cherry 3	1.75 in. sq. x 0.126 in.	8.77 g	8.99 ± 0.12 m/s	10.76 m/s

*Discounting angle, measured from a normal to the surface to be driven .

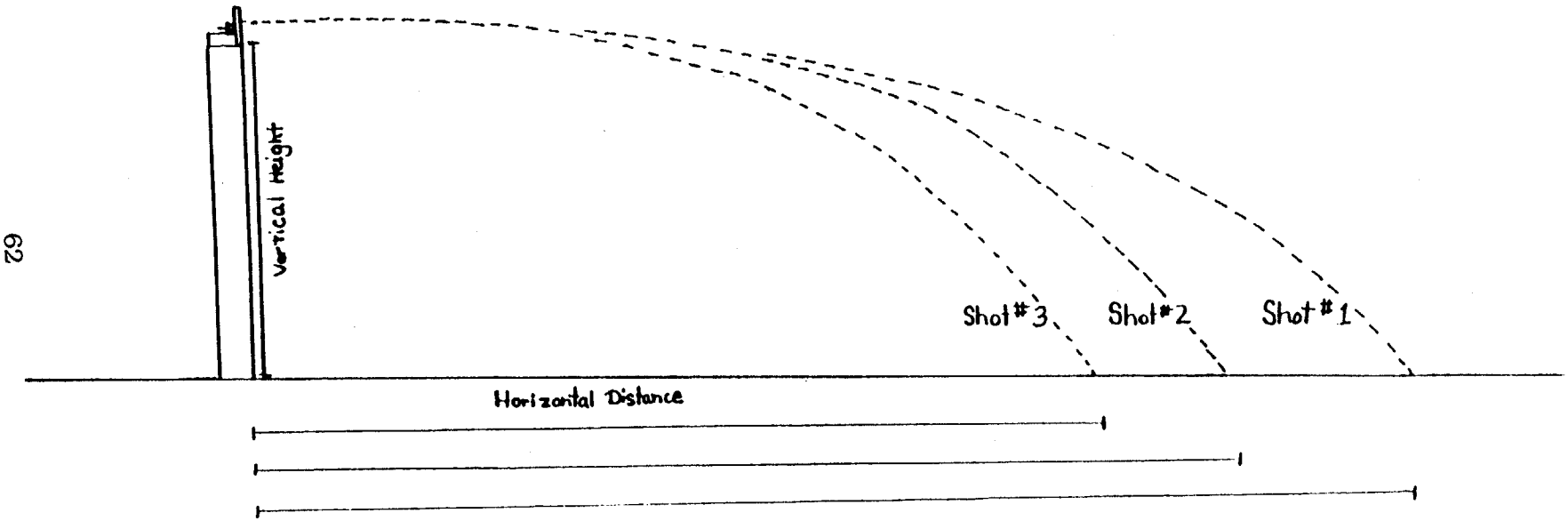

Fig. 2. Cherry's Experimental Arrangement for Comparing Efficiencies of Various Charge Shapes in Driving a Steel Plate

The asymmetric-sandwich Gurney formula is

$$v = \sqrt{2E}\left[\frac{\left(1+2\frac{M}{C}\right)^3+1}{6\left(1+\frac{M}{C}\right)}+\frac{M}{C}\right]^{-\frac{1}{2}}, \qquad (2)$$

where M and C are the driven mateerial (metal plus rubber in this case) and explosive masses, respectively; $\sqrt{2E}$ is 2.50 km/s, the Gurney velocity characteristic of Detasheet C (Ref. 4), which is similar to Primasheet 1000; and v is the metal plate velocity. But the data show that the velocities varied with charge configuration, from 10.9 m/s to 9.0 m/s.

In regard to the velocity imparted to a driven plate, there are energy losses from the sides of an unconfined charge. One can account for these losses in a Gurney calculation by disregarding the explosive mass within a 30° angle from a normal to the plate around the perimeter of the explosive (Ref. 5). When such a correction is applied to the calculations for the Cherry experiments, the predicted velocity for all three configurations decreases, and the velocity for the thinnest charge decreases least of all. This trend is consistent with the experimental data, but the magnitude of the experimentally observed differences among configurations is much greater than the differences predicted by this correction. Velocities calculated with the 30°-angle correction are also shown in Table I.

3.1 Partial-area coverage with explosive

Our first attempt to model the variation in velocities among the Cherry experiments focused upon the variation in area of the explosive. It was assumed that the metal directly adjacent to the explosive charge was primary metal, driven directly by the explosive, and that the perimeter of the plate was secondary metal, carried along progressively through momentum sharing analogous to inelastic collision. Thus while the mass of explosive was constant in all three Cherry experiments, the mass of the primary metal was different for each experiment.

The asymmetric-sandwich formula (Eq. 2) was applied in this case. Note that the asymmetric sandwich formula collapses to a momentum form when $M/C >> 1$, and this applies to all of the Cherry experiments, even considering the reduced metal mass associated with the primary metal approach. This is shown from Eq. 2 as follows (Ref. 2):

$$\lim_{\frac{M}{C}\to\infty} v = \lim_{\frac{M}{C}\to\infty} \sqrt{2E}\left[\frac{\left(1+2\frac{M}{C}\right)^3+1}{6\left(1+\frac{M}{C}\right)}+\frac{M}{C}\right]^{-\frac{1}{2}} = \sqrt{2E}\cdot\sqrt{\frac{3}{4}}\cdot\frac{C}{M}. \quad (3)$$

Specific impulse, I_{sp}, is defined as:

$$I_{sp} = \frac{Momentum}{C} = \frac{Mv}{C}, \quad (4)$$

so from Eqs. 3 and 4,

$$I_{sp} = \sqrt{1.5E}. \quad (5)$$

This indicates that for M/C >> 1 in an asymmetric sandwich configuration, the explosive delivers an impulse (momentum) that is linear with the explosive mass loading of the surface.

The momentum imparted to the primary metal in the Cherry experiments thus varies with the thickness of the explosive. But when the momentum of the primary metal is shared with the secondary metal, the final momentum of the plate is predicted to be the same in all three Cherry experiments. This result is not consistent with the observed velocities, so another approach is needed to explain the results.

3.2 Gasdynamics Behavior According to Wave-code Simulations

We performed wave-code computations to simulate the Cherry experiments for the purpose of understanding the gasdynamics which we postulated was causing the differences in performance. The question we addressed was whether the direction of detonation propagation was strongly affecting the effective side losses from the perimeter of the explosive charge. All three configurations of the Cherry experiments had configurations that were quite flat, so that the detonation resembled grazing detonation traveling nearly parallel to the surface of the plate and perpendicular to the sides of the charge. The detonation wave then projects gaseous detonation products parallel to the surface of the steel plate at a velocity approximately equal to detonation velocity. It was suspected that this velocity significantly exceeded the velocity of lateral expansion in the "normal" Gurney configuration, which we could represent as plane-wave initiation of the flat charges.

The CTH code, under development at Sandia (Ref.6), was used to perform two-dimensional axisymmetric representations of the experiments. For computational simplicity we converted the problem into a 2-D

axisymmetric problem by modifying the shape of the steel plate, rubber buffer and explosive material to be right circular cylinders of the same respective masses. We used an equation of state for the detonation products of duPont Detasheet EL506C sheet explosive (similar in detonation properties and composition to Primasheet 1000) from Ref. 7.

When we included the rubber buffer layer in the problem, the code would essentially shut off before momentum transfer from the explosive to the steel plate was complete. This may have been due to rebound of the rubber from the steel, opening a gap into which the detonation product gases would flow. Such flow would cause tremendous distortion in the mesh for the product gases, and the distortion may have caused tangling of the computational mesh. It should be noted that the rubber buffer pad was found about 10-15 ft. behind the firing position in the experiments, indicating that the rubber did bounce backward off the steel.

Our next step was to eliminate the rubber from the problem description, so that the explosive rested directly on the steel. The steel description was modified to suppress spall behavior, so as to make the simulations consistent with the experimentally observed behavior in this regard.

Fig. 3 and Table II show the setup and results for computations done in this way. The computed velocity values shown in Table II are low by about 25% in comparison with the experimental values. This is quite surprising, and we can only attribute it to probable error in the JWL parameters for Detasheet C. We shall use the computed velocity results only for comparison with other computed results, and not in any absolute sense.

Fig. 3 also compares the flow of product gases at the same time interval after completion of detonation of the charge for the cases of small area initiation (similar to the experiment) and planar initiation. The results show that lateral expansion of the gas is indeed faster with small area initiation, which produces grazing detonation, but only by a factor of about 1.2.

Table II shows the computed metal velocity differences that are caused by the differences in lateral expansion, which should be viewed as a loss mechanism in regard to momentum transfer to the plate. The result is that planar initiation drives the plate to higher velocity, but only by 3-5% more than small area initiation (and grazing detonation). The difference in computed velocity between Cherry 1 and Cherry 3 configurations is 8%; this is substantially less than the differences in velocity observed among the experiments, which are shown again in Table II.

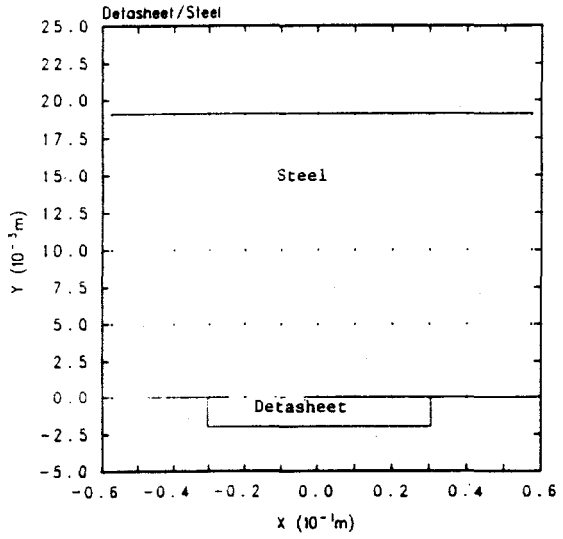

(a)

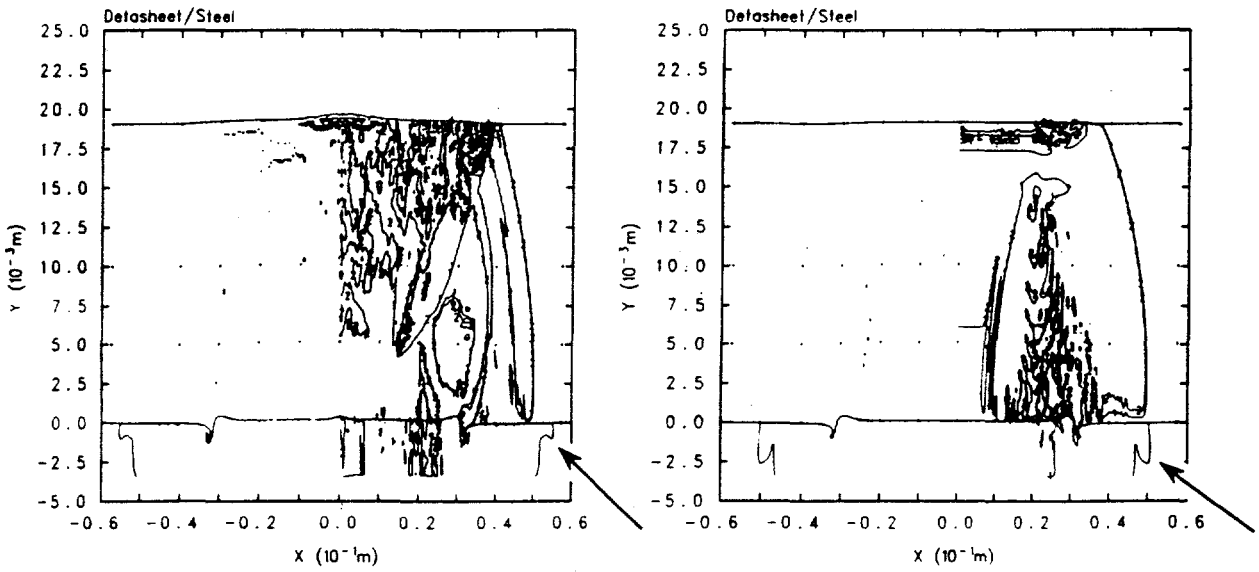

(b) (c)

Fig. 3. (a)—The initial configuration of one of the CTH calculations. (b)—A two-dimensional plot of the small-area initiation of the Detasheet at a time when the gas expansion wave is approaching the outer edge of the steel (denoted by the arrow). (c)—A two-dimensional plot of the full-back-surface initiation of the Detasheet, showing the position of the gas expansion wave at an equivalent time from explosive breakout to that in (b), see arrow.

Table II
Results of CTH Wavecode Analysis of Cherry Experiments

Configuration	Initiation	Computed Velocity	Observed Velocity
Cherry 1	Small area	8.01 m/s	10.90 m/s
	Planar	7.99 m/s	
Cherry 2	Small area	7.68 m/s	9.66 m/s
	Planar	7.89 m/s	
Cherry 3	Small area	7.35 m/s	8.99 m/s
	Planar	7.72 m/s	

The difference in computed plate velocity in cases where detonation was parallel to the driven surface (grazing detonation) and where detonation was normal to the driven surface suggests that the loss factor be increased when the detonation is parallel to the driven surface. Based upon the results in Table II, we conclude that use of a discounting angle of 36° would improve the ability of the Gurney model to reproduce computed results when detonation of a laterally unconfined charge proceeds parallel to the surface which is being driven.

3.3 Inelastic Collision Modeling of Cherry Experiments

The rubber buffer pads caused some decoupling of the detonation wave from the steel because the rubber impedance was much lower than that of both the detonating explosive and the steel. The thickness of the rubber pad was constant at 1/4 in. in these experiments, and the rubber was the same area as the explosive, which varied from one Cherry experiment to another. Thus the mass of the rubber varied from one Cherry experiment to the next. This suggested the possibility that the variation in mass of the rubber played a role in the variation in coupling from the explosive to the steel plate in the Cherry experiments.

Although the rubber buffer pads were in contact with both the explosive and the steel plate, we carried out a bounding calculation using the asymmetric-sandwich Gurney formula (Eq. 2) in which the explosive was assumed to drive the rubber alone, and then the rubber was assumed to collide inelastically with the steel (Eq. 1). The results of this calculation, which uses a Gurney discounting angle of 36° (see Fig. 4), are shown in Table III.

Table III
Results of Inelastic Collision with Driven Rubber Buffer

Configuration	Rubber Buffer Weight	Rubber Buffer Velocity*	Plate Velocity by Inelastic Collision	Observed Velocity
Cherry 1	36.8 g	428 m/s	9.42 m/s	10.90 m/s
Cherry 2	18.5 g	762 m/s	8.53 m/s	9.66 m/s
Cherry 3	12.5 g	1012 m/s	7.68 m/s	8.99 m/s

*Calculated by asymmetric sandwich formula, Eq. 2, with M = rubber buffer mass.

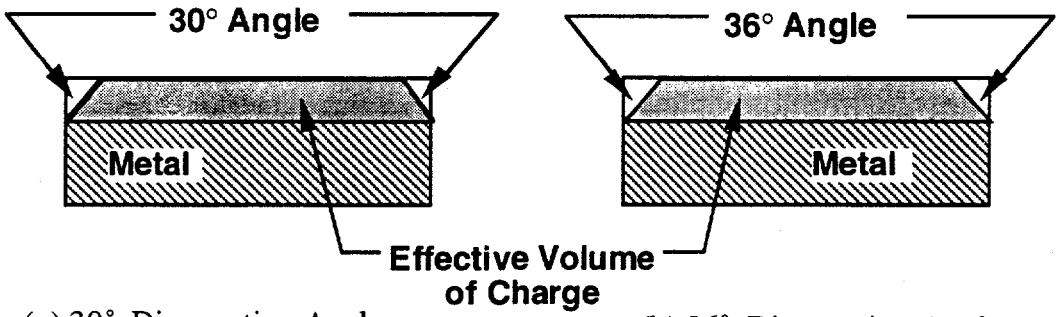

(a) 30° Discounting Angle (b) 36° Discounting Angle

Fig. 4. Discounting angle for laterally unconfined charge is increased from 30° to 36° when detonation wave travels parallel to the metal surface being driven.

The values of the steel plate velocity are lower than the observed values by 12-15%, but the calculated differences in velocities are quite similar to the observed differences. The inelastic collision assumption is the only analysis that reflects the differences in velocity among the three Cherry experiments. Therefore we conclude that the rubber decoupling is the dominant factor in the behavior of the Cherry experiments, and this analysis represents another example of the usefulness of the inelastic collision model. As an explanation for the fact that observed velocities are higher than those predicted by the inelastic collision model, we suggest that some additional impulse is imparted by the detonation product gas pressure acting over the entire area of the steel plate at relatively late times in the process.

It should be noted that one of us (C.R.C.) offers another explanation for the differences among Cherry 1, 2, and 3. He suggests that the layers of explosive further from the surface of the steel plate are less effective than that which is in contact with the plate, resulting in the observation that the Cherry 3 configuration is less efficient than Cherry 1.

4. Summary

The findings of this research are as follows.

• To calculate the velocity of metal configurations that are driven indirectly by explosive detonation, the use of an **inelastic collision model** provides good results and insight into the interaction process. This model applies for metal that is directly driven by the explosive, and then impacts and travels along with other objects. We recommend that it be applied for plates or other shapes which are partially in contact with explosive, where the entire body remains intact (i.e., does not shear). It even worked better than other models to explain decoupling of detonation drive from a heavy steel plate by the use of a rubber buffer plate inserted between the explosive and the steel plate.

• Based upon the results of computer simulation, we recommend the use of a 36° discounting angle (rather than the conventional 30° discounting angle) for laterally unconfined charges in which the detonation wave travels parallel to the surface to be driven. More experiments should be done to determine the best method of discounting explosive material some distance from the metal interface (i.e., discounting angle or another approach).

5. Acknowledgments

Part of this work was supported by the United States Department of Energy under Contract W-7405-ENG-36.

References

1. H. Spahr, S. H. Fischer and J. E. Kennedy, Sandia National Laboratories unpublished results, 1984.

2. C. R. Cherry, Jr., "Determining the Propulsive Efficiency of a Geometrically Shaped High Explosive Charge," Report to Hope Christian School, Grade 8, Albuquerque, NM, 1995.

3. J. E. Kennedy, "Gurney Energy of Explosives: Estimation of the Velocity and Impulse Imparted to Driven Metal," Sandia National Laboratories Report SC-RR-70-790, Albuquerque, NM, Dec., 1970.

4. J. Roth, Portola Valley, CA, private communication, 1971.

5. F. A. Baum, K. Stanyukovich and B. I. Shekhter, Physics of an Explosion, p. 505-507, Moscow, 1959 (English translation from Federal Clearinghouse AD 400151).

6. R. L. Bell, M. G. Elrick, E. S. Hertel, G. I. Kerley, J. M. McGlaun, S. A. Silling, P. A. Taylor, and S. L. Thompson, "CTH User's Manual and Input Instructions, Version 2.00," Albuquerque, NM, Aug. 19, 1994.

7. B. M. Dobratz and P. C. Crawford, LLNL Explosives Handbook: Properties of Chemical Explosives and Explosive Simulants, Lawrence Livermore National Laboratory Report UCRL-52997 Change 2, Jan. 31, 1985.

III.

TWENTIETH

INTERNATIONAL SYMPOSIUM ON SHOCK WAVES,

JULY 24-28, 1995,

PASADENA, CALIFORNIA

Dynamic compaction of granular materials in a tube with wall friction, applied to deflagration-to-detonation transition

Larry G. Hill
Los Alamos National Laboratory
Los Alamos, NM, 87545, USA

Ashwani K. Kapila
Rensselaer Polytechnic Institute
Troy, NY, 12180, USA

Abstract: A theoretical problem is considered in which a granular material is pushed through a tube of arbitrary cross-section by a constant velocity-piston against the resistance of compaction work and wall friction. The crushing of the material is dictated by a simple yet physically reasonable compaction law. By considering two special cases— the limit of vanishing friction and the quasi-static limit— we identify the two basic compaction wave structures. We then consider the general case in which the two waves interact. Estimates suggest that for typical deflagration-to-detonation tests, explosive at the wall melts on time scales that are short compared to the experiment.

Key words: Compaction, DDT, Friction, Granular explosive, Ignition, Melting

1. Introduction

Many investigators have examined deflagration-to-detonation transition (DDT) of granular explosives using shock-tube like experiments (e.g., McAfee et al. 1989). Often a piston is driven explosively into the bed, and the resulting compaction work is thought to initiate combustion which ultimately leads to detonation. We examine an aspect of the DDT tube problem that has received little attention, namely the resistance and resulting energy dissipation due to wall friction. Wall friction has a large effect in ram-pressed charges (Elban & Chiarito 1986)— essentially the quasi-static limit of the DDT tube test— so that one expects even greater effects for the longer-aspect-ratio DDT tubes. The resistance mechanism is that axial stress applied by the piston is transmitted to the walls, giving rise to a proportional frictional drag. Since particles are interlocked, resistance at the wall is transmitted throughout the interior. The entire bed resists motion in proportion to how hard it is pushed upon— much like the ubiquitous "chinese finger" but acting in compression.

2. Rheology

Because a confined granular material exhibits solid-like properties it is appropriate to adopt the generalized definition of pressure used in elasticity, i.e., $p = -(\sigma_x + \sigma_y + \sigma_z)/3 = -(\sigma_r + \sigma_\theta + \sigma_z)/3$, where all stresses are force per unit *total* area, normal stress components are positive in tension, and pressure is positive in compression. We define an ideal granular material whose loading state is dictated by a *compaction law* (Herrmann 1969) of the form $\phi = \rho/\rho_s = f(p)$, where ϕ is the solid volume fraction, ρ is the mixture density, and the subscript s means "solid". To determine analytic solutions we choose a simple but physically realistic form for $f(p)$, where S_0 and ϕ_0 are the zero-pressure slope and volume fraction, respectively:

$$\phi = 1 - \frac{(1-\phi_0)^2}{S_0\, p + (1-\phi_0)}\,. \tag{1}$$

We consider Class-A granular HMX explosive as an example, and infer its compaction law from pressing data (Elban & Chiarito 1986) using the fact that the experimental geometry enforced nearly uniaxial strain. Both this task and the formulation of the equations of motion in Section 3 are greatly simplified by the inference that Poisson's ratio, ν, remains constant and equal to its solid value during crushing. This follows from pressing data (e.g., Campbell et al. 1988) for which the ratio of normal to axial stress, which depends only on ν (specifically, $\sigma_n/\sigma_z = \nu/(1-\nu)$), remains constant. The inferred compaction law is shown in Fig. 1 together with a least-squares fit to Eqn. 1.

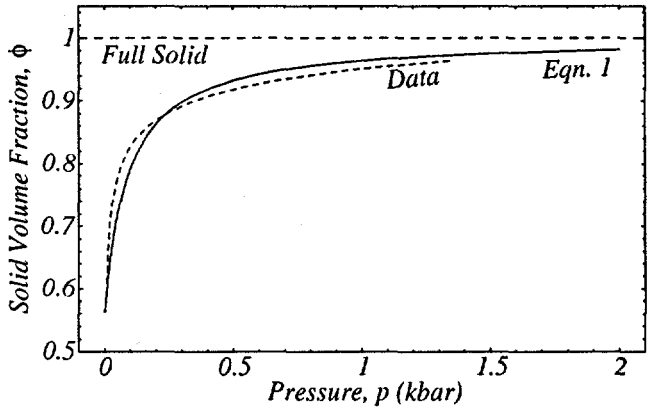

Figure 1. Compaction law for Class A HMX, $\phi_0 = 0.563$: data vs. fit to Eqn. 1.

The wall drag is assumed to obey a standard friction law except that, because the solid area fraction in contact with the wall increases as the material is

crushed, the friction coefficient is not constant. Intuitively one expects that the coefficient should be weighted by the solid area ratio, $\mu/\mu_s = A_s/A = \phi$. Equating the solid area and volume fractions is a common practice following from the statistical argument that for many randomly arranged particles, each plane within a volume element intersects the same solid area. This behavior for μ can be more rigorously justified, but here we merely note that the limits $\phi \to 0$ (no material) and $\phi \to 1$ (solid material) are both sensible.

3. Formulation

Consider a cylindrical semi-infinite tube of arbitrary cross-section, filled with powder and sealed at the origin by a piston, as shown in Fig. 2. The initial

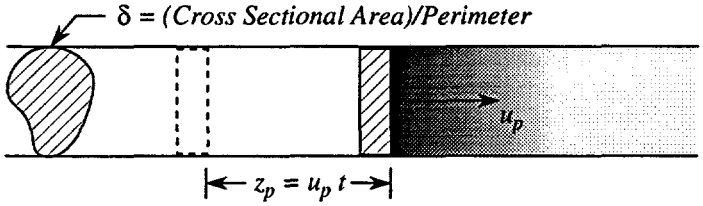

Figure 2. Schematic diagram of the problem.

conditions are uniform mixture density and zero pressure. At $t = 0^+$ the piston is moved impulsively to the right at a constant velocity u_p. The resulting material motion is assumed to be always and everywhere one dimensional. To simplify the equations we transform to a Lagrangian coordinate system, whereby the spatial coordinate z is replaced by the mass-weighted spatial coordinate h. Then, incorporating the above results and assumptions, the dimensionless equations for mass and momentum conservation become:

$$\frac{\partial \phi}{\partial \tilde{t}} + \phi^2 \frac{\partial M}{\partial \tilde{h}} = 0\,, \tag{2}$$

$$\frac{\partial M}{\partial \tilde{t}} = -\frac{\partial \tilde{p}}{\partial \tilde{h}} - \tilde{p}\,. \tag{3}$$

Here, $M = u/a_0$ is the Mach number, and the "tilded" quantities have been scaled as follows: $\tilde{p} = S_0\, p$, $\tilde{h} = h/l_f$, and $\tilde{t} = a_0 t/l_f$. The reference quantities l_f (the "friction" length) and a_0 (the longitudinal sound speed) are given by:

$$l_f = \frac{1-\nu}{\nu}\frac{\delta}{\mu_s}, \quad a_0 = \sqrt{\frac{3(1-\nu)}{1+\nu}\frac{1}{\rho_s S_0}}\,, \tag{4}$$

with δ the area-to-perimeter ratio of the cross section.

4. Results

4.1. Zero friction limit

In the absence of friction the second term on the right-hand side of Eqn. 3 does not appear. The piston drives a steady compaction shock (sw) into the powder, whose speed M_{sw} and amplitude $\tilde{p}_{sw}$ are given by:

$$M_{sw} = \frac{M_p}{2(1-\phi_0)}\left(1+\sqrt{1+\frac{4(1-\phi_0)^2}{M_p^2}}\right), \qquad \tilde{p}_{sw} = \phi_0\, M_p\, M_{sw}\,, \tag{5}$$

where $M_p = u_p/a_0$ is the piston Mach number. In reality the shock has a finite thickness which depends on its amplitude (e.g., McAfee et al. 1989).

4.2. Quasi-static limit

This case corresponds to a vanishingly small piston speed. Over correspondingly long time intervals Eqn. 2 survives intact but the left-hand side of Eqn. 3 is negligible. Subject to the requirements that the initial piston pressure is zero and that the powder far upstream is undisturbed, an analytic solution emerges:

$$\tilde{p}(\tilde{t},\tilde{h}) = \tilde{p}(\tilde{t},0)e^{-\tilde{h}}, \quad \phi(\tilde{t},\tilde{h}) = 1-\frac{(1-\phi_0)^2}{\tilde{p}(\tilde{t},\tilde{h})+(1-\phi_0)}, \tag{6}$$

$$\tilde{p}(\tilde{t},0) = \phi_0(1-\phi_0)\left[\exp\left(\frac{\phi_0}{1-\phi_0}M_p\tilde{t}\right)-1\right]. \tag{7}$$

The pressure and compaction fields, mapped back to the Eulerian frame, are shown in Fig. 3. The wave is not truly steady as the pressure is always rising. But, due to the compaction law shape, the compaction field assumes a steady profile $\approx 5\,l_f$ wide following a start-up transient. The downstream state of the developed frictional wave (fw) is fully compacted, so its (Eulerian) speed is:

$$M_{fw} = \left(\frac{1}{1-\phi_0}\right)M_p\,. \tag{8}$$

4.3. General case

One expects the general solution, corresponding to nonzero friction and order unity piston speeds, to involve a friction-attenuated shock. One may further surmise that to a good approximation the problem can be divided into two distinct regions: the leading shock for which inertial forces dominate, and the downstream flow in which frictional forces dominate. A perturbation solution valid for short times, or equivalently, small friction coefficient (not presented

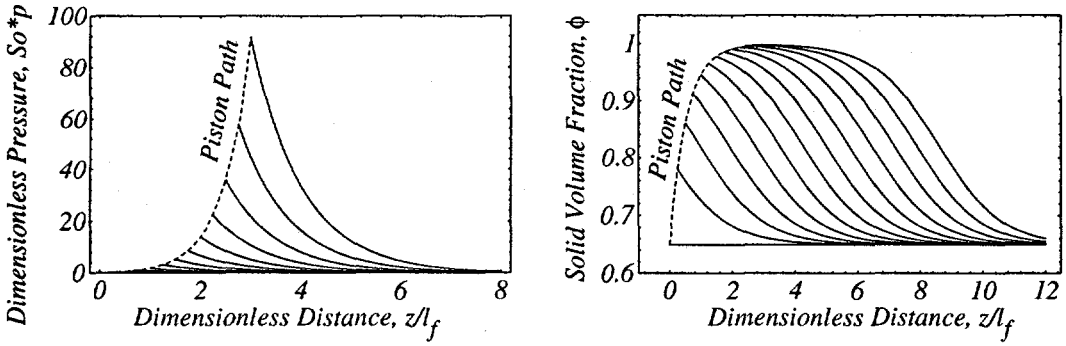

Figure 3. Pressure, compaction fields in quasi-static limit; $\phi_0 = 0.65$, $\Delta\tilde{t} = 0.25$.

here), finds the correction to the particle speed between the piston and the shock to be time independent, which supports this notion. In this inertialess approximation Eqn. 3 formally reduces to that for the quasi-static limit, but the initial piston pressure is the zero-friction shock pressure corresponding to the prescribed piston speed, and the solution extends only to the shock location $\tilde{h}_{sw}(\tilde{t})$, at which point it is matched to shock jump conditions. There are now two coupled first-order ODEs that must be solved numerically. A phase-plane analysis of the two equations, also not presented here, shows that below a critical value of M_p, $M_{pcrit} = 1 - \phi_0$, the strength of the leading shock decays to zero asymptotically. Above M_{pcrit} its amplitude decays to a finite value.

Fig. 4 compares the results of this inertialess approximation (again mapped to the Eulerian frame) to the results of a full numerical solution. Their agreement is remarkable, with respect to both pressures and shock location.

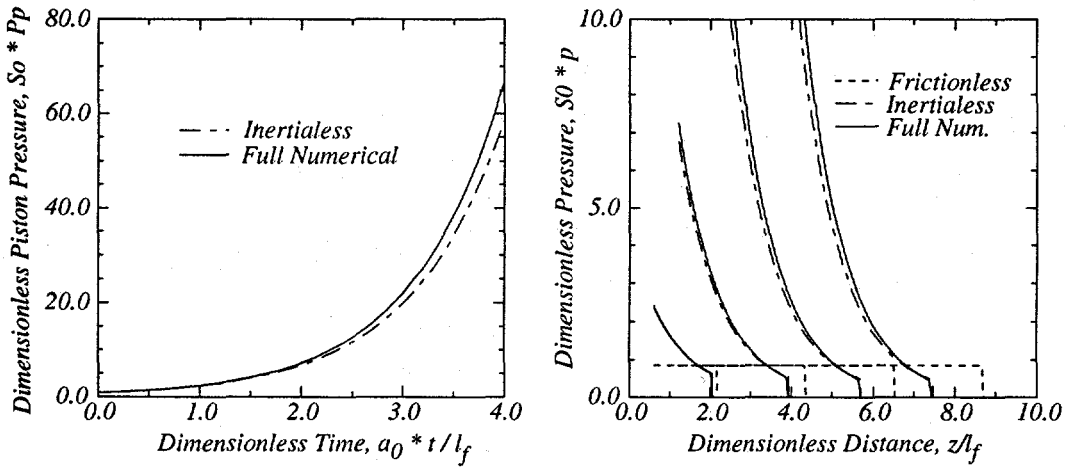

Figure 4. Pressure for full problem; $\phi_0 = 0.65$, $\Delta\tilde{t} = 1$, $M_p = 0.6$, $M_{pcrit} = 0.35$.

5. Wall temperature

Heat generation at the wall can be equated to the frictional work there: $\dot{q_w} = \dot{w_f} = \mu_s \phi(-\sigma_n) u$. The problem is simplified by noting that most of the heat flux flows into the (metal) wall, and that the temperature distribution is, for short times, confined to a thin boundary layer. The wall temperature is then:

$$T_w(z,t) = T_{w0} + \left(\frac{3\nu}{1+\nu}\right)\left(\frac{\mu_s}{\sqrt{\pi} b_w}\right) \int_0^t \frac{\phi(z,\tau)\, p(z,\tau)\, u(z,\tau)\, \mathrm{d}\tau}{\sqrt{t-\tau}}, \qquad (9)$$

where b_w is the wall heat-penetration coefficient. After the leading shock passes one may briefly assume a constant state. Then for a steel wall and $u_p \approx 100$ m/s, $\mathrm{d}T_w/\mathrm{d}t$ is of order 100 C/μs. The melting temperature (247 C) is reached in order 1 μs— the same time scale as the leading shock rise. One expects a melt layer to lubricate, decreasing further frictional resistance and energy dissipation. The question of wall ignition may therefore depend strongly on the difference between the melting and critical temperatures of the explosive.

6. Conclusions

Without wall friction, an impulsively started piston drives a narrow compaction shock through the tube. In the quasi-static limit with wall friction a different kind of compaction wave occurs whose width is proportional to the tube diameter and inversely proportional to the friction coefficient. In general, both wave types are present, and their interaction is such that the amplitude of the leading shock is attenuated. Neglecting inertia behind the shock yields an excellent approximation to the wave structure. In a typical DDT test the rate of work at the wall is sufficient to cause rapid melting and, possibly, ignition.

Acknowledgement. This work was supported by the U.S. D.O.E. and by the N.S.F. We thank the "DDT team" for their interaction. AKK also thanks Don Schwendeman for sharing his numerical expertise and Arwen Warlock Dixon for helpful discussions.

References

Campbell RL, Elban WL, Coyne PJ (1988) Side-wall pressure measurements in quasi-static compaction of porous beds of HMX powders and ABL 2523 casting powder. JANNAF Propulsion Sys Hazards Mtg Los Angeles, CA

Elban WL & Chiarito MA (1986) Quasi-static compaction study of coarse HMX explosive. Powder Technology 46: 181

Herrmann W (1969) Constitutive equation for the dynamic compaction of ductile porous materials. J Appl Phys 40: 2490

McAfee JM, Asay BW, & Campbell AW (1989) Deflagration to detonation transition in granular HMX. 9th Symp (Int) on Det Portland, OR: 265

IV.

JOURNAL OF MOLECULAR SPECTROSCOPY 176, (1996)

ARTICLE NO. 0098

JOURNAL OF MOLECULAR SPECTROSCOPY **176,** 369–374 (1996)
ARTICLE NO. 0098

Measurement and Analysis of the Fourier Transform Spectra of the ν_3 Fundamental and $\nu_1 + \nu_3$ Combination of NpF_6

Roberta N. Mulford and Kyu C. Kim

Los Alamos National Laboratory, Los Alamos, New Mexico 87545

Received April 20, 1995; in revised form January 8, 1996

The high resolution spectrum of NpF_6 complements existing work on UF_6 and PuF_6. Unlike these molecules, NpF_6 has an unpaired spin, requiring a different mathematical formalism for analysis of the data than was used for the closed shell molecule UF_6. Like UF_6, NpF_6 exhibits rotational manifold structure. Scalar constants for the molecule and some examples of manifolds are presented here, and available constants are compared with those of UF_6 and PuF_6.

INTRODUCTION

Measurement of the spectrum of the ν_3 and $\nu_1 + \nu_3$ vibrations of NpF_6 at high resolution yields values for the band origins, rotational constants, and Coriolis constant for ν_3. This work complements high resolution (resolution greater than 0.005 cm^{-1}) studies done on PuF_6 and UF_6. The ν_3 and $\nu_1 + \nu_3$ bands of NpF_6 show characteristics typical of the vibrational bands of the other octahedral heavy atom fluorides. For these molecules, typically $B\zeta$ is small. Many closely spaced rotational states are populated, resulting in a spectrum with P and R branches extending to high values of J. Low-lying vibrational states of nearly coincident frequencies (*1*) result in clustering of hot bands in the Q branch. Clustering of fine structure components within each rotational state forms a distinct rotational band with a profile dependent on J.

In UF_6, these characteristics enabled exact analysis of the spectrum in terms of the theory of Moret-Bailly (*2, 3*). In the UF_6 ν_3 band (*4*), all transitions from the vibrational ground state with J values up to $P(77)$, $Q(91)$, and $R(67)$ were assigned and seven spectroscopic parameters were determined; scalar quantities m, n, p, q, and v and tensor terms g and h. These values allowed calculation of the molecular constants B, ζ_3, and r_0 and of vibrational and force field parameters. Similarly, the UF_6 $\nu_1 + \nu_3$ band (*5*) yielded five spectroscopic constants. The ν_3 band of PuF_6 has been measured in detail (*6*), and appears to have discernible J manifolds up to $R(32)$, with distortion evident in higher manifolds and in the Q branch. Scalar parameters of NpF_6 can be compared with the other hexafluorides in the actinide series, as summarized in Table III. The theory of Moret-Bailly has been applied to a number of other spherical top molecules (*7*).

The NpF_6 ν_3 and $\nu_1 + \nu_3$ spectra presented here exhibit J manifolds, and are consistent with the scalar part of the theory. NpF_6 has half-integral spin, unlike UF_6 and PuF_6, so the exact shape of the J manifolds, dictated by fine structure components, is not anticipated to be the same as for the integral spin case (*8, 9*). For this reason, we have restricted our analysis to determination of scalar quantities, and did not attempt to determine tensor quantities from poorly resolved fine structure, pending extension of the theory to properly treat octahedral molecules with half integral spin (*10*).

The reduced resolution of the NpF_6 spectra relative to the UF_6 and PuF_6 spectra may also increase the difficulty of distinguishing ground state fine structure from hot bands. By analysis of the gross features of the spectrum, spectroscopic parameters can nonetheless be determined, without reliance on the fine detail of the J manifolds.

Actinide hexafluorides have many low frequency bending vibrations which contribute to predominant population of hot bands at experimental temperatures (*1*). Cooling technology used to combat this hot band population in work done on UF_6 and PuF_6 used either nozzle expansion (*4*) or a static low temperature sample (*5, 6, 11, 12*) with a long path length compensating for low vapor pressure, as was used in these experiments on NpF_6. Measurements described here are the first reported at resolution sufficient to resolve rotational bands in NpF_6. The Fourier transform infrared spectroscopy used in these experiments does not provide the high resolution attainable with diode laser spectroscopy (*4, 5, 12*), but allows acquisition of continuous spectra of large spectral regions in a relatively short time, at a resolution adequate to allow unique identification of rotational manifolds, as was done for the ν_3 band of UF_6 (*13*).

In the high resolution spectra of both ν_3 and $\nu_1 + \nu_3$, overall band contours are used to estimate the Coriolis coupling constants. The ground state Q branch is presented and discussed and a band origin is determined. Rotational manifolds in the R branch are presented. Approximate manifold centers are found and used to obtain the band origin by

0022-2852/96 $18.00

regression on the best estimate of J assignment. Rotational constants n and p are also determined from the least squares fit to these manifold centers.

Spectroscopic constants m, n, p, and ζ_3 determined for ν_3 are consistent with the frequency of 624 cm^{-1} determined for the first reported infrared spectrum (*14*) of NpF_6 and with the Q branch maximum of 624 cm^{-1} and ζ_3 found in subsequent low resolution survey spectra (*15*).

Spectroscopic constants m, n, and p determined for $\nu_1 + \nu_3$ are consistent with the reported Q branch maximum of 1274 cm^{-1} reported for this band (*15*).

EXPERIMENTAL

NpF_6 gas was prepared in glovebox isolation from NpO_2, obtained from oxidation of metal of 99.999% purity. Direct fluorination at 400°C with F_2 containing no more than 5% HF resulted in a yield of NpF_6 between 85% and 95%. The sample was subsequently distilled at −62°C. NpF_6 gas was distilled at −85°C (the available cold finger temperature) every 20 hr to remove impurities. This corresponds to redistillation approximately every 100 scans. Predominant impurities are F_2, HF, CO, and CO_2. Other impurities appear over several days, resulting from reaction of NpF_6 with other materials to form SiF_4, CF_4, and other fluorinated hydrocarbons. A small amount of COF_2 is also seen, a product of the reaction of NpF_6 with CO_2 and CO. These impurities did not interfere with the spectrum between 620 and 630 cm^{-1}.

The apparatus consists of a Bomem Fourier transform spectrometer (Model DA 3.002) and a 4-m cell with White cell optics for variable path length (*16, 17*) designed to contain radioactive materials. The net path length for these experiments was 64 m. Data were obtained at a resolution of 0.005 cm^{-1} after Hamming apodization. Coaddition of 600 single scans was required to provide a signal to noise ratio of 5 at 628 cm^{-1}. The cell is thermostated and is stable to within 2°C. Because a thermal gradient of as much as 5°C can exist within the cell, temperature readings are an average over four positions along the length of the cell. Data on ν_3 were taken at 203 K, at 110 ± 8 μTorr (14.6 ± 1.1 mPa) of pressure. Data on $\nu_1 + \nu_3$ were taken at 240 K, at 220 ± 4 μTorr (29.2 ± 0.5 mPa) of pressure. Under these conditions the NpF_6 was stable for several days.

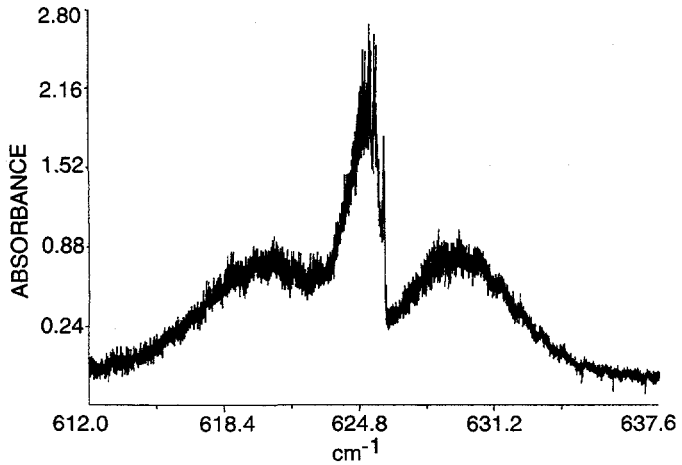

FIG. 1. The complete *PQR* profile of NpF_6 ν_3. The ground state Q branch is visible as a sharp spike at 626.0 cm^{-1}.

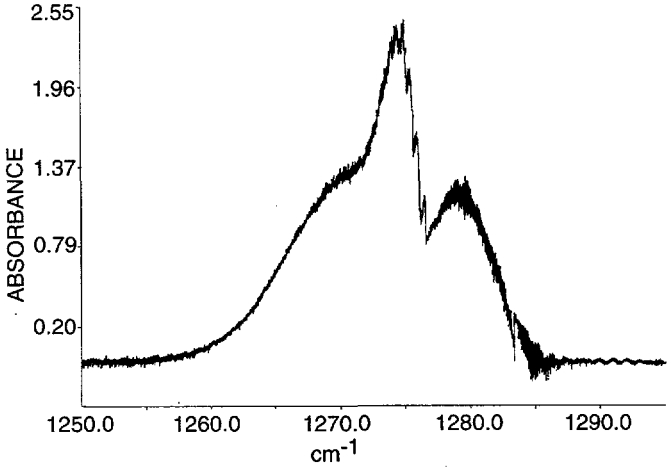

FIG. 2. The complete PQR profile of NpF_6 $\nu_1 + \nu_3$. The ground state Q branch is visible as a sharp spike at 1276.6 cm^{-1}.

RESULTS AND ANALYSIS

Overall Band Contours

The rotational profile of the NpF_6 ν_3 band extends from 612 cm^{-1} to 638 cm^{-1}, and shows PQR structure, as shown in Fig. 1. The *PQR* structure of the $\nu_1 + \nu_3$ band, between 1255 cm^{-1} and 1285 cm^{-1}, is shown in Fig. 2.

At the ν_3 experimental temperature of 203 K, only 5.6% of a contour results from ground state absorptions, and 13.3% from a single quantum in any one of the three bending vibrations, the rest arising from other hot bands.

The ground state Q branch of ν_3 is visible in Fig. 3 as a narrow peak at the most blue edge of the Q branch cluster, with its origin at 626.0 cm^{-1}. The ground state Q branch of $\nu_1 + \nu_3$ is also shown, a structure starting at 1276.5 cm^{-1}, isolated from the bulk of the Q branch cluster. The population in the bending vibrations, and the 17.9% in the first overtones of the bending vibrations and the combinations of two bending vibrations, are clearly visible as maxima in the Q branch cluster structures of both bands, as shown in Fig. 3. Hot band structure is particularly pronounced in $\nu_1 + \nu_3$. The bulk of the Q branch cluster is due to the remainder of the population, in higher hot bands. Resolution of low-lying J manifolds in the P branch is obscured by these Q branch cluster hot bands.

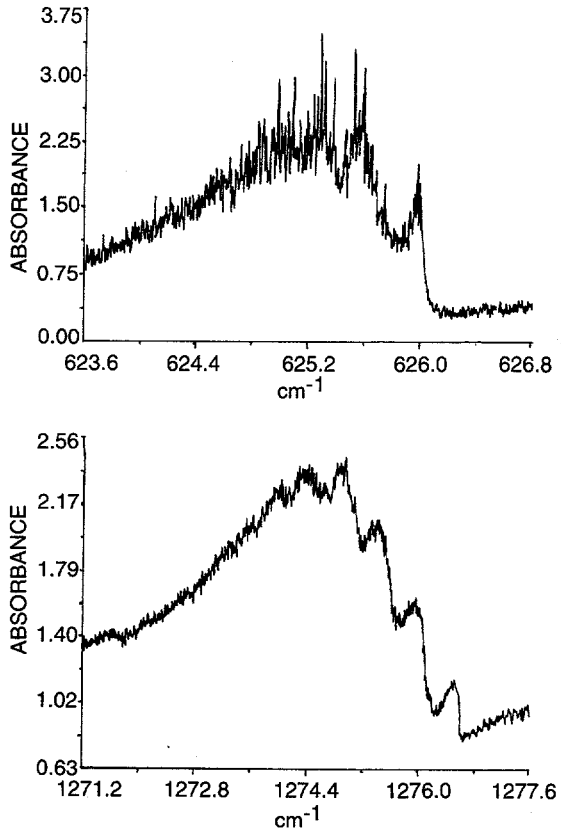

FIG. 3. The Q branch profiles of NpF_6 ν_3 (above) and $\nu_1 + \nu_3$ (below). Hot bands due to higher vibrations are clearly visible at energies below the ground state Q branches.

The P and R branch contours are broad continua, as seen in Figures 1 and 2. The fine peaks superimposed on this continuous absorption are not noise, but are largely due to resolved ground state rotational transitions. Some resolved hot bands contribute to this structure. P branch manifolds are somewhat obscured by these hot bands.

The Coriolis coupling constant, ζ_3, can be estimated from maxima in the P and R band contours, according to

$$P(J_{max}) - R(J_{max}) = -4B(1 - \zeta_3)(kT/B_0hc)^{1/2} \quad [1]$$

A good estimate of B is obtained by using the bond length determined by electron diffraction (*18*), 1.981(8) Å for NpF_6. The P–R separation at 203K is about 9.13 ± 0.09 cm^{-1}, giving a value of 0.19 for ζ_3. The major source of error is in determination of the P and R band maxima. This ζ_3 value is comparable to the values of 0.199 for UF_6 (*4*) and 0.191 for PuF_6 (*6*), and to the value of 0.18 reported for NpF_6 (*15*).

Analysis of Q Branches

The Q branches of the ν_3 and $\nu_1 + \nu_3$ bands of NpF_6 are shown in Figs. 4 and 5. The Q branch for ν_3 begins at 626.00 cm^{-1} and the Q branch for $\nu_1 + \nu_3$ at 1276.567 cm^{-1}.

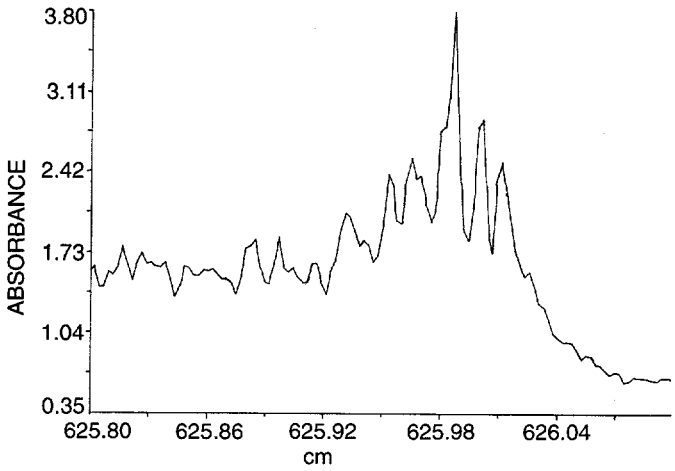

FIG. 4. The ground state Q branch of NpF_6 ν_3 shows definite band head structure similar to that seen in Q branches of spherical top molecules (Brock's class ii).

Most of the Q branch cluster lies to the red of the band origin in both the ν_3 and the $\nu_1 + \nu_3$ spectra. The narrow profiles of these Q branches indicate that ΔB_Q is quite small for NpF_6, as it is for other actinide hexafluorides.

Estimation of Q branch origins is done by analogy with spherical top Q branch structures given for molecules with no unpaired spins (*7*).

The ν_3 Q branch exhibits band heads reminiscent of those seen in spherical tops (*7*) (Brock's class ii). The band heads do not follow the anticipated spacing given by the equation (*7*) $\nu_N = \alpha N(N + 1)$. A special structureless example of the somewhat symmetrical case (Brock's case iii) is consistent with the observed violation of the $\nu_N = \alpha N(N + 1)$ rule for spherical top molecules. By analogy with the spherical top

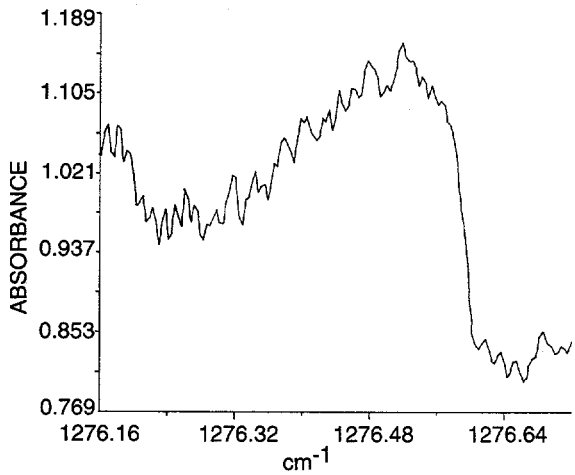

FIG. 5. The ground state Q branch of NpF_6 $\nu_1 + \nu_3$ shows structure similar to that seen in highly asymmetric Q branches of spherical top molecules (Brock's class i).

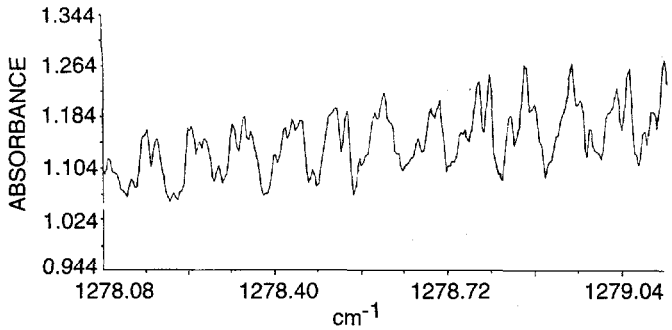

FIG. 6. The R branches of the NpF_6 ν_3 and $\nu_1 + \nu_3$ bands comprise separated manifolds. Manifolds for $J = 17.5$ (partial) through $J = 29.5$ (partial) of NpF_6 $\nu_1 + \nu_3$ are shown.

case (either Brock's case ii or iii), we take the Q branch origin at the first peak, at 626.009 cm^{-1}.

Similarly, the $\nu_1 + \nu_3$ spectrum has a Q branch, shown in Fig. 5, which resembles a highly asymmetric case (Brock's case i) in spherical tops, showing a structureless sharp rise near the band origin. Structure is evident on the top and trailing edge of the envelope. The origin is taken at the blue extreme of the Q branch structure, at 1276.567 cm^{-1}.

Hot bands in both Q branch clusters are clearly separated from the ground state Q branch, as shown in Figure 3. The hot bands are red-shifted in both cases ν_3 and $\nu_1 + \nu_3$ and cluster into single and multiple quanta of bending modes ν_4, ν_5, and ν_6. This clustering is most pronounced in the $\nu_1 + \nu_3$ Q branch. This behavior is consistent with observations in UF_6 and PuF_6 that red shifts are approximately proportional to the absolute frequency of the mode (*1*).

In the ν_3 band, the first hot band is red shifted by about 0.4 cm^{-1} relative to the ground state Q branch and subsequent hot bands appear in a progression of about this spacing due to clustering of vibrational frequencies in actinide hexafluoride molecules (*1*). In $\nu_1 + \nu_3$, the shift is 0.55 cm^{-1}.

Analysis of P and R Branches

Well-resolved rotational structure is evident in the P and R bands, as shown in Fig. 6. Such structure is clearly evident in the P and R branches of ν_3 between $M = 27/2$ ($J'' = 25/2$) and $M = 81/2$ ($J'' = 79/2$), and in the R branch of $\nu_1 + \nu_3$ between $M = 3/2$ and $M = 125/2$. In the R branches, rotational structure is resolved into manifolds of octahedral fine structure components. Unlike the cases of closed shell octahedral molecules in which the locations of the fine structure components have been derived using a standard expression (*2, 3*), these clusters in NpF_6 do not adhere to the known patterns observed in those of the closed shell molecules (*8, 9*). Hence, we use a simplified expression, omitting explicit description of fine structure:

$$\nu_{P,R} = m + nM + pM^2 + \cdots$$

+ hyperfine structure (tensor) terms within cluster. [2]

The scalar terms m, nM, and pM^2 in Eq. [2] specify positions of the centers of gravity of the fine structure manifolds in terms of any particular J state M. For the R branch, $M = J'' + 1$, and for the P branch, $M = -J''$. The tensor terms describe the manifold structure itself.

For the octahedral closed-shell case of UF_6, the last term describes the structure of each particular J manifold in terms involving the fourth order tensor quantities, the symmetry-adapted fourth-order tensor coefficients ($\mathcal{F}^4$) of Moret-Bailly (*2*). Resolved octahedral structure within a J manifold is unique to J. In UF_6, this allowed a definitive assignment of J manifolds, and permitted the wavenumber of the center of gravity of each observed manifold to be determined by comparing the fine structure with the $\mathcal{F}^4$ tensor coefficients. In NpF_6 this method is not available, since the location of fine structure components for molecules with an unpaired spin are unknown.

In this analysis we derived the scalar constants m, n, and p from rotational manifold centroids. The location of the centroids was estimated. A value of J was assigned to each manifold by estimating the displacement from the Q branch origin.

The center of gravity of each rotational manifold is estimated from the edges of the rotational manifold. Noting that since C_3 and C_4 symmetry clusters are preserved (*8*) in the spin 1/2 case, we take the location of the manifold center to be approximately 2/5 of the manifold width. In spherical tops, this estimate is increasingly accurate as J increases. This practice will yield a fairly accurate rotational constant, since the error in placement of the manifold center will be nearly identical between manifolds, and will affect only the intercept of the extrapolated line. In ν_3, we take g, consistent with the Q branch shape, to be negative (*6*), giving a center closer to the low frequency edge of the manifold. A negative g is assumed for $\nu_1 + \nu_3$. If g is positive (*6*), manifold centers will be raised in frequency by 1/5 of the manifold width, producing a systematic error of 0.009 cm^{-1} at low J, and less than 0.018 cm^{-1} throughout. The most likely source of error in the manifold centers comes from taking the wrong edge of the manifold to be the positive side. A good estimate of the error in the band origin is 1/5 of the spacing of the rotational manifolds, or 0.018 cm^{-1}. This error is small compared to the error that might be introduced by misidentification of the J value, about 0.09 cm^{-1}.

The accuracy in the location of the manifold centers is comparable to the deviations indicated in Tables 1 and 2. The values determined for the manifold centers are fitted to the scalar portion of Eq. [2] to determine the scalar values. These assignments are supported by the expected agreement between the calculated band origin and the head of the Q branch (used to establish the J assignment) to within the possible error of 0.03 cm^{-1}, and the good quality of the fit to the scalar constants.

For ν_3, a least-squares fit of R branch manifold centers

TABLE 1
Frequencies of Manifolds in NpF_6 ν_3 *R* Branch

J"	M	frequency ν, cm^{-1}	residual $\nu_{obs.} - \nu_{calc.}$
12.5	13.5	627.234	0.005
13.5	14.5	627.325	0.007
14.5	15.5	627.413	0.005
15.5	16.5	627.498	0.001
16.5	17.5	627.581	-0.005
17.5	18.5	627.661	-0.015
18.5	19.5	627.757	-0.008
19.5	20.5	627.856	0.002
20.5	21.5	627.952	0.009
21.5	22.5	628.032	0.000
22.5	23.5	628.117	-0.004
23.5	24.5	628.200	-0.010
24.5	25.5	628.288	-0.010
25.5	26.5	628.394	0.007
26.5	27.5	628.484	0.008
27.5	28.5	628.562	-0.002
28.5	29.5	628.650	-0.003
29.5	30.5	628.741	-0.000
30.5	31.5	628.828	-0.002
31.5	32.5	628.929	0.011
32.5	33.5	629.026	0.020
33.5	34.5	629.098	0.003
34.5	35.5	629.180	-0.003
35.5	36.5	629.266	-0.005
36.5	37.5	629.361	0.002
37.5	38.5	629.438	-0.009
38.5	39.5	629.529	-0.006
39.5	40.5	629.624	0.001

was made for rotational manifolds between $M = 27/2$ ($J'' = 25/2$) and $M = 81/2$ ($J'' = 79/2$). The analysis yields a mean rotational constant, n of 0.0903 ± 0.0014 cm^{-1} and a linear centrifugal distortion term, p, of $(-3.1 \pm 2.5) \times 10^{-5}$ cm^{-1}. Extrapolation to $J = 0$ gives a band origin of 626.015 ± 0.017 cm^{-1}, which compares adequately with the observed Q branch maximum at 626.009 cm^{-1}.

The ν_3 P branch manifolds were difficult to identify, and were distorted and obscured by hot bands. Location of manifold centers was approximate. Nonetheless, a large enough number of P branch manifolds were identified to adequately define molecular constants. Analysis of 42 P branch manifolds between $J = 9/2$ and $J = 113/2$ yields a band origin of 626.015 ± 0.009 cm^{-1} and a rotational constant of 0.1011 ± 0.0003 cm^{-1}. P branch data are sufficiently less accurate than R branch data to be discounted in determining molecular constants.

The $\nu_1 + \nu_3$ band R branch is analyzed between $M = 3/2$ ($J'' = 1/2$) and $M = 103/2$ ($J'' = 101/2$). The mean rotational constant n obtained is 0.0868 ± 0.0004 cm^{-1}, with a first linear centrifugal distortion constant p of $(-2.9 \pm 0.7) \times 10^{-5}$. The least-squares analysis gives a band origin at 1276.564 ± 0.004 cm^{-1}, which differs from the observed origin of 1276.567 cm^{-1} by 0.003 cm^{-1}. This difference is less than one spacing, 0.086, indicating a correct choice of J assignment, and less than 1/5 of the spacing, 0.017 cm^{-1}, indicating a correct choice of the sign of g. Measurement of band centers assuming a negative value of g would yield a band origin at 1276.576 ± 0.004, differing from the head of the Q branch by 0.009 cm^{-1}. No attempt was made to analyze the P branch of the $\nu_1 + \nu_3$ band.

SUMMARY

Spectroscopic values determined for the NpF_6 ν_3 and $\nu_1 + \nu_3$ bands are summarized in Table 3. The spectra of these bands do not adhere to the tensor theory for closed shell spherical tops, but do form clusters very similar to bands for closed shell spherical tops, consistent with the spin-orbit term making a small contribution to the rotational Hamiltonian for such a massive molecule. As well as the unpaired spin, the fine structure may be disrupted by an internal perturbation or by interference from other near-resonant vibrations.

TABLE 2
Frequencies of Manifolds in NpF_6 $\nu_1 + \nu_3$ *R* Branch

M	frequency ν, cm^{-1}	residual $\nu_{obs.} - \nu_{calc.}$	M	frequency ν, cm^{-1}	residual $\nu_{obs.} - \nu_{calc.}$
1.5	1276.704	0.010	32.5	1279.362	0.006
2.5	1276.800	0.019	33.5	1279.450	0.009
3.5	1276.877	0.009	34.5	1279.533	0.007
4.5	1276.960	0.006	35.5	1279.617	0.006
5.5	1277.047	0.006	36.5	1279.700	0.004
6.5	1277.127	-0.000	37.5	1279.793	0.013
7.5	1277.203	-0.011	38.5	1279.869	0.004
8.5	1277.286	-0.014	39.5	1279.948	-0.002
9.5	1277.375	-0.012	40.5	1280.035	0.001
10.5	1277.460	-0.013	41.5	1280.127	0.008
11.5	1277.550	-0.009	42.5	1280.204	0.001
12.5	1277.635	-0.010	43.5	1280.267	-0.021
13.5	1277.722	-0.009	44.5	1280.364	-0.008
14.5	1277.812	-0.005	45.5	1280.449	-0.007
15.5	1277.902	-0.001	46.5	1280.525	-0.015
16.5	1277.987	-0.002	47.5	1280.605	-0.020
17.5	1278.070	-0.005	48.5	1280.697	-0.012
18.5	1278.156	-0.005	49.5	1280.790	-0.003
19.5	1278.252	0.005	50.5	1280.889	0.012
20.5	1278.341	0.009	51.5	1280.984	0.023
21.5	1278.420	0.002	52.5	1281.097	
22.5	1278.506	0.002	53.5	1281.210	
23.5	1278.587	-0.002	54.5	1281.302	
24.5	1278.679	0.004	55.5	1281.399	
25.5	1278.763	0.003	56.5	1281.501	
26.5	1278.851	0.006	57.5	1281.598	
27.5	1278.936	0.005	58.5	1281.695	
28.5	1279.012	-0.004	59.5	1281.784	
29.5	1279.104	0.003	60.5	1281.877	
30.5	1279.192	0.006	61.5	1281.971	
31.5	1279.273	0.002	62.5	1282.064	

TABLE 3
Scalar and Coriolis Coupling Constants for Actinide Hexafluoride Molecules

molecule	UF_6[a]	UF_6[b]	NpF_6[c]	NpF_6[c]	PuF_6[d]
mode	ν_3 (cm^{-1})	$\nu_1+\nu_3$ (cm^{-1})	ν_3 (cm^{-1})	$\nu_1+\nu_3$ (cm^{-1})	ν_3 (cm^{-1})
constant					
m	625.70178(7)	1294.3278(3)	626.015(17)	1276.564(4)	619.7610(14)
n	0.0892061(16)	0.089165(4)	0.0903(14)	0.0868(4)	0.09238(11)
p	$-3.978(5)\times10^{-5}$	$-8.40(4)\times10^{-5}$	$-3.1(2.5)\times10^{-5}$	$-2.9(7)\times10^{-5}$	$-6.0(5)\times10^{-5}$
ζ_3	0.199(2)		0.189		0.191

a Aldridge, et. al., reference [4].
b RS McDowell, MJ Riesfeld, et. al., reference [5].
c this work.
d KC Kim, et. al., reference [6].

The experimental data allow us to discern some of the spectral characteristics of NpF_6 and compare them to other actinide hexafluorides. However, the moderately high resolution, the spectral complexity brought about by the overlapping hot bands, and the altered fine structure positions all restrict analysis to determination of scalar quantities.

REFERENCES

1. K. C. Kim and R. N. Mulford, *J. Mol. Struct. (THEOCHEM)* **207,** 293–299 (1990).
2. J. Moret-Bailly, *J. Mol. Spectrosc.* **15,** 344–354 (1965).
3. B. Bobin and K. Fox, *J. Phys. (Paris)* **34,** 571–582 (1973).
4. J. P. Aldridge, E. G. Brock, H. Filip, H. Flicker, K. Fox, H. W. Galbraith, R. F. Holland, K. C. Kim, B. J. Krohn, D. W. Magnuson, W. B. Maier II, R. S. McDowell, C. W. Patterson, W. B. Person, D. F. Smith, and G. K. Werner, *J. Chem. Phys.* **83,** 34–48 (1985).
5. R. S. McDowell, M. J. Reisfeld, N. G. Nereson, B. J. Krohn, and C. W. Patterson, *J. Mol. Spectrosc.* **113,** 243–249 (1985).
6. K. C. Kim, B. J. Krohn, R. A. Briesmeister, and S. J. David, *J. Mol. Spectrosc.* **132,** 207–215 (1988).
7. E. G. Brock, B. J. Krohn, R. S. McDowell, C. W. Patterson, and D. F. Smith, *J. Mol. Spectrosc.* **76,** 301–321 (1979).
8. W. G. Harter and C. W. Patterson, *J. Chem. Phys.* **66,** 4872–4885, 4886–4892 (1977).
9. W. G. Harter, *Comput. Phys. Rep.* **8,** 293–396 (1988).
10. V. Boudon and F. Michelot, *J. Mol. Spectrosc.* **165,** 554–579 (1994).
11. K. C. Kim and B. J. Krohn, *J. Chem. Phys.* **77**(4), 1645 (1982).
12. K. C. Kim and W. B. Person, *J. Chem. Phys.* **74,** 171–178 (1981).
13. R. N. Mulford, *J. Mol. Spectrosc.* **147,** 260–266 (1991).
14. J. G. Malm, B. Weinstock, and H. Claassen, *J. Chem. Phys.* **23,** 2191–2192 (1955).
15. W. B. Person, K. C. Kim, G. M. Campbell, and H. J. Dewey, *J. Chem. Phys.* **85,** 5524–5528 (1986).
16. R. A. Briesmeister, G. W. Read, K. C. Kim, and J. R. Fitzpatrick, *Appl. Spectrosc.* **38,** 35–38 (1984).
17. K. C. Kim, E. Griggs, and W. B. Person, *Appl. Opt.* **17,** 2511–2515 (1978).
18. M. Kimura, V. Schomaker, D. W. Smith, and B. Weinstein, *J. Chem. Phys.* **48,** 4001–4012 (1968).

V.

JOURNAL OF APPLIED PHYSICS

(TO BE PUBLISHED)

Overdriven-Detonation and Sound-Speed Measurements in PBX-9501 and the "Thermodynamic" CJ Pressure

J. N. Fritz, R. S. Hixson, M. S. Shaw, C. E. Morris, and R. G. McQueen*
Los Alamos National Laboratory, Los Alamos, New Mexico, 87545
(January 15, 1996)

Abstract

Sound speeds, at pressure, and the overdriven Hugoniot have been measured for the plastic-bonded explosive PBX-9501. These two curves intersect at the CJ state because of the sonic condition $D = c + u$. This permitted a novel determination of the "thermodynamic" CJ pressure. A value of 34.8±0.3 GPa was obtained. The data permit a direct experimental determination of the isentropic gamma, $\gamma_S = -(\partial \ln P/\partial \ln V)_S$, and the Grüneisen parameter, $\gamma = V(\partial P/\partial E)_V$, in the overdriven pressure range. Some thermodynamic relations about an equilibrium CJ state are obtained.

47.40.-x

*This work supported by the U. S. Department of Energy.

I. INTRODUCTION

Plane-wave Chapman-Jouguet (CJ) detonation experiments have been used extensively to study detonation physics and the equation-of-state (EOS) of detonation products (DP). These experiments can be readily diagnosed and are amenable to numerical modeling. The difficulty these experiments present is that the reaction-zone hydrodynamics and the EOS hydrodynamics are intimately coupled. In analyzing these experiments one is required to choose compatible reaction-rate and EOS models to simulate experiments. Choosing a different reaction model, *e. g.*, a fast and slow two-rate model versus a single-rate model, would require a different EOS to duplicate the experimental results. As a consequence these experiments can't uniquely determine reaction-rate and EOS models.

In this paper we will describe experiments that decouple reaction-rate effects from EOS effects to the maximum extent possible. To accomplish this we utilize overdriven-detonation (OD) states. These constant states can be accurately measured with techniques that have been used successfully to characterize inert materials. In addition, sound waves can be propagated through these constant states and their velocity of propagation measured, again using techniques that have been applied successfully to inert materials. Since sound velocities can be measured with the same precision as the detonation velocities, derivatives on the EOS surface can be determined to the same accuracy as the EOS surface. The results obtained are independent of EOS models and their accuracy depends only on the inherent precision of the experimental measurements. The sound-speed measurements allow direct determination of the adiabatic gamma. Knowledge of the OD Hugoniot and sound-speed curves allow calculation of the Grüneisen gamma, also a thermodynamic variable of significant interest. The combination of sound-speed and OD Hugoniot data allow a novel determination of the CJ pressure. We use the sonic condition, $D = c = u$ (the detonation velocity is the sound speed plus the particle velocity), that exists at the CJ state. To determine this "thermodynamic" CJ state one simply locates the intersection of the $c + u$ curve with the OD Hugoniot in the shock velocity-particle velocity plane. Because the velocities are measured with 1-2% precision the "thermodynamic" CJ pressure can be determined with excellent precision using thermodynamic states that are essentially decoupled from reaction-zone effects.

II. DETONATION HUGONIOT USING A CONSTANT-γ_S MODEL

Before we describe details of our experiments it is informative to discuss general features of overdriven detonations and sound-velocity variations along these curves. For shock waves with a steady profile propagating into a material at rest conservation of mass, momentum and energy gives the Rankine-Hugoniot equations [1].

$$\rho_0 u_s = \rho(u_s - u_p), \tag{2.1}$$

$$P - P_0 = \rho_0 u_s u_p, \tag{2.2}$$

$$E - E_0 = \tfrac{1}{2}(P + P_0)(V_0 - V). \tag{2.3}$$

These equations relate the pressure, P, specific internal-energy, E, and specific volume, V, behind the shock to those same quantities in front of the shock in terms of shock velocity u_s and particle velocity u_p (or just u). The initial-state parameters represented by ρ_0, P_0, and E_0 are often referred to as the centering point of the Hugoniot. For our calculations we will make the usual assumption for condensed explosives that P_0 is negligible relative to OD Hugoniot pressures. Measurement of any two of the variables P, V, E, u_s, u_p with the above equations is sufficient to determine the remaining variables. Equations (2.1) and (2.2) can be combined to give

$$\rho_o^2 u_s^2 = (P - P_0)/(V_0 - V), \tag{2.4}$$

$$u_p^2 = (P - P_0)(V_0 - V). \tag{2.5}$$

To illustrate features of detonation Hugoniots we will use a constant-γ_S EOS [2] given by

$$E - E_0 = \frac{PV}{\gamma_S - 1} - Q, \tag{2.6}$$

where Q is the constant heat of detonation stored in the explosives per unit mass and γ_S is the adiabatic gamma defined by the relation,

$$\gamma_S \equiv -\left(\frac{\partial \ln P}{\partial \ln V}\right)_S. \tag{2.7}$$

For the constant-γ_S EOS, the adiabatic gamma is a constant and is equal to the γ_S in Eq. (2.6). In general, this is not necessarily the case. Eq. (2.6) has far-reaching consequences. In fact, given the initial density ρ_0 and a CJ state (u_{cj}, P_{cj}), the detonation Hugoniot curve and the sound speeds along it are completely specified. The parameters in Eq. (2.6) are completely defined by these conditions. There is no flexibility to fit real data away from the CJ point and the resulting forms do not fit the data. The chief advantages of this EOS are the resulting simple analytic equations and the *qualitatively* correct features of the detonation Hugoniot and sound-speed curves.

With constant-γ_S EOS (Eq. (2.6) and Hugoniots Eqs. (2.1–3)) the OD Hugoniot for this EOS can be determined

$$u_s = \frac{u_{cj}^2 + u_p^2}{(1 - \mu^2)u_p}, \tag{2.8}$$

where $\mu^2 = (\gamma_S - 1)/(\gamma_S + 1)$ and $u_{cj}^2 = 2\mu^2 Q$. For the Hugoniot shown in Fig. 1 we chose EOS parameters that approximate the behavior of PBX-9501 at the CJ state. The values used were $\gamma_S = 3$, $Q = 4.84\,\mathrm{kJ/g}$, and $\rho_0 = 1.835\,\mathrm{g/cm^3}$. The OD Hugoniot has positive curvature over the entire particle-velocity range and a minimum detonation-velocity at the Chapman-Jouguet (CJ) state where sonic flow $D = c + u$ exists. The zero slope at the CJ state is a common feature of all detonation Hugoniots and is a consequence of the sonic condition at this state. (See Appendix A.) The derivative of $u_s(u_p)$ is given below.

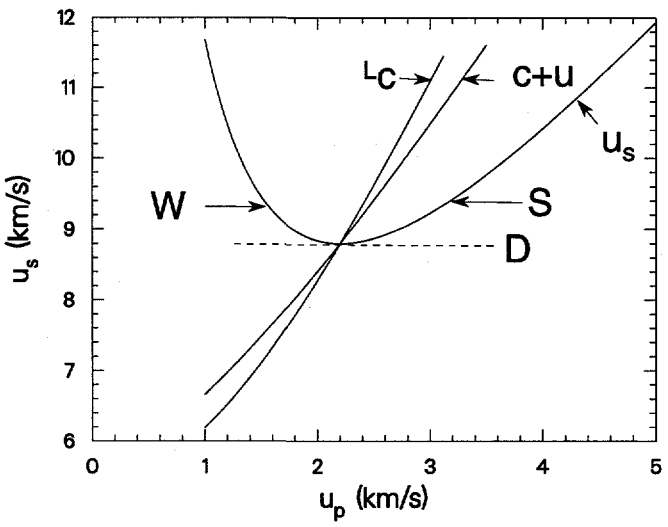

FIG. 1. Detonation Hugoniot and sound-speed curves for the constant-γ_S model.

$$\frac{du_s}{du_p} = \frac{1-(u_{cj}/u_p)^2}{1-\mu^2}. \tag{2.9}$$

The location of the minimum, the CJ state, is given by $u_p^2 = u_{cj}^2 = 2\mu^2 Q = D^2/(\gamma_S+1)^2 = (2.20\text{km/s})^2$, and $u_s = D = 8.80\,\text{km/s}$. From Eq. (2.2) the pressure along the detonation Hugoniot is

$$P = \rho_0(u_{cj}^2 + u_p^2)/(1-\mu^2). \tag{2.10}$$

At CJ $P_{cj} = 2\rho_0 u_{cj}^2/(1-\mu^2) = \rho_0 D^2/(\gamma_S+1) = 35.5\,\text{GPa}$. The sample strain can be calculated using Eq. (2.1).

$$\eta \equiv (1-V/V_0) = (1-\mu^2)u_p^2/(u_{cj}^2+u_p^2). \tag{2.11}$$

At the CJ state $\eta_{cj} = 1/(\gamma_S+1) = 0.25$ and the large-strain limit is $\eta = 2/(\gamma_S+1) = 0.50$. The physical strain-domain for the OD Hugoniot is from 0.25 to 0.50.

By plotting the detonation Hugoniot in the u_s-u_p plane one can identify three distinct cases for various values of detonation velocity. For detonation velocities less than the CJ detonation-velocity, *e. g.*, $u_s = 8.0\,\text{km/s}$, no solution exists, because the horizontal line $u_s = 8.0\,\text{km/s}$ doesn't intersect the detonation Hugoniot. For $u_s = D$, the CJ detonation-velocity, only one solution exists at the CJ state. For detonation velocities greater than D, *e. g.*, $u_s = 9.2\,\text{km/s}$, two solutions exist; a solution labeled W, that lies on the weak-detonation branch of the Hugoniot and a solution labeled S, that lies on the strong-detonation branch of the Hugoniot.

In this paper sound speeds along the detonation Hugoniot are of particular interest. For the constant-γ_S EOS sound speeds can be calculated from the following equation.

$$B_S = -V\left(\frac{\partial P}{\partial V}\right)_S = \rho c^2 = \gamma_S P, \tag{2.12}$$

which was derived by noting the energy variation along an isentrope is given by $dE = -PdV$. From Eqs. (2.8) and (2.12) one can obtain an expression for the sound speed along the detonation Hugoniot.

$$c^2 = \gamma_S(u_{cj}^2 + \mu^2 u_p^2)/(1-\mu^2). \tag{2.13}$$

A plot of the Eulerian sound-velocity $c+u$ is given in Fig. 1. At the CJ state $c = \gamma_S u_{cj}$, hence $c+u = D = u_{cj}(\gamma_S+1)$. Because the sonic condition exists at the CJ state, the intersection of the $c+u$ curve with the detonation Hugoniot provides a novel method to determine CJ states. The CJ state determined using this approach is labeled the "thermodynamic" CJ state, because the intersection of two thermodynamic curves is used to determine the state. The slope of the $c+u$ curve in the wave velocity-particle velocity plane is given by

$$\frac{d(c+u_p)}{du_p} = 1 + \left(\frac{\gamma_S \mu^4}{(1-\mu^2)} \frac{u_p^2}{(u_{cj}^2 + \mu^2 u_p^2)}\right)^{1/2} \tag{2.14}$$

At the CJ state $d(c+u_p)/du_p = 1 + (\gamma_S - 1)/2 = 2$, where $\tan^{-1} 2 = 63\,\text{deg}$. This large angle of intersection allows the CJ state to be accurately determined. The large intersection angle between these two curves is typical of any reasonable EOS model used to describe detonation-product behavior.

It is apparent from the relative position of the u_s and $c+u$ curves in Fig. 1 that the flow is supersonic in the weak-detonation branch, because $u_s > c+u$. Similarly, the flow is subsonic in the strong-detonation branch, because $u_s < c+u$. Only at the CJ state is the flow sonic, where $u_s = c+u$. These relationships are true for all detonation-product Hugoniots.

The Lagrangian velocity is another thermodynamic variable of interest. In the sound-speed experiments that will be described later, it is the ratio of the Lagrange sound-velocity to the shock velocity that is directly measured. The Lagrange sound-velocity is given by $\rho_0 {}^L c = \rho c$, *i. e.*, it is the velocity the wave must have in the uncompressed material to traverse mass points equivalent to those the real wave encounters. For the constant-γ_S EOS ${}^L c$ is given by

$$({}^L c)^2 = \frac{\gamma_S}{(1-\mu^2)} \frac{(u_{cj}^2 + u_p^2)^2}{(u_{cj}^2 + \mu^2 u_p^2)}. \tag{2.15}$$

At the CJ state $u_{cj}(\gamma_S+1) = {}^L c = c+u = D$. These three curves only coincide at the CJ state. The slope of the Lagrange sound-velocity curve is

$$\frac{d^L c}{du_p} = \frac{\gamma_S}{(1-\mu^2)} \frac{u_p}{{}^L c} \frac{(u_{cj}^2 + u_p^2)}{(u_{cj}^2 + \mu^2 u_p^2)} \left(2 - \frac{\mu^2 (u_{cj}^2 + u_p^2)}{(u_{cj}^2 + \mu^2 u_p^2)}\right) \tag{2.16}$$

At the CJ state the Lagrange sound-speed slope is $d^L c/du_p = (\gamma_S+1)^2/2\gamma_S = 8/3$, where $\tan^{-1}(8/3) = 69\,\text{deg}$. The derived slope for $d^L c/du_p$ was specific to the constant-γ_S EOS. A general derivation for this slope at the CJ state for a generalized EOS is given in Appendix A (Eq. A21). The derived general relationship is

$$\left(\frac{d^L c}{du_p}\right)_{cj} = \frac{1}{2}\left(\frac{V_0}{V_{cj}}\right)\left(1 + \frac{dB_S}{dP}\right)_{cj} \tag{2.17}$$

Fig. 1 graphically illustrates the interrelation of the thermodynamic variables important to our experiments. Even though the specific behavior of the variables was for the constant-γ_S EOS, the general relationships discussed are true for any EOS. At the CJ state some

very special relationships/conditions exist. In particular it divides the weak-detonation branch from the strong-detonation branch. However, there is nothing anomalous from an EOS perspective. The thermodynamic variables are well behaved on both branches of the detonation Hugoniot. In general this is true for any well- behaved EOS.

III. EXPERIMENTAL—OVERDRIVEN DETONATIONS

The PBX-9501 used in these experiments was fabricated by group M-1 of the Los Alamos National Laboratory. The samples were standard pressings [3] with the standard composition 95 wt% HMX/ 2.5 wt% Estane/ 2.5 wt% BDNPA:BDNPF eutectic. The Hugoniot-sample densities were 98.7 % of the theoretical density 1.860 g/cm^3.

Samples used for the Hugoniot experiments were $16 \times 22 \times 5$mm. The lateral dimensions are chosen large enough to ensure 1D waves. The 5 mm dimension is large enough to get the desired precision but not so large as to allow overtake from the rear of the flyer plate used to generate the pressure. Most of the Hugoniot data were generated by conventional methods [1]. Typically six explosive samples were mounted on a 5 mm thick 6061 aluminum base plate along with two standard samples. The pressure was generated by an explosively-driven stainless-steel flyer that impacted the base plate. Two experiments used the direct-impact Hugoniot (DIH) technique [4]; here, the plate directly impacts the unknown samples. Two experiments were performed with the base plate in direct contact with the driving explosive (composition-B and PBX-9501). These did not overdrive the detonation and were not used in the fitting procedures. The Hugoniot samples were ideal for density measurements. The density for these samples was 1.836 ± 0.002 g/cm^3, with the maximum and minimum values less than twice the standard deviation. Densities were not measured on the sound-speed step wedges, we relied on the similarity of the initial material and the fabrication techniques.

The results for each of the individual samples are shown in Fig. 2. Arrival times are indicated by light from gas gaps on the surface of samples (sometimes the sample is covered by a thin aluminum layer–a shim) and adjacent reference surfaces. Corrections for the time to compress and flash the gas in the gap were significant. A typical flash gap is 0.08 mm thick, about 2% of the sample thickness. Ordinarily the symmetry between the reference and sample flash-gaps causes this correction to cancel out, but for the unshimmed explosive-samples this symmetry is lacking. The DIH experiments were done as an add-on to the sound-speed experiments. They were not as well centered as the samples with the underlying base-plate. The samples were thinner. The DIH experiments do not begin with a clean shock. The gas trapped between the flyer and sample introduces an early wave into the sample. This perturbation is minimized by filling the intervening space with helium or hydrogen. The DIH experiments have the advantage of requiring only the Hugoniot of the flyer for analysis. In the base-plate (BP) experiments we require the cross-curve (second-shock Hugoniot up and isentrope down from the initial state of the BP) of the 6061 aluminum used for the base plate. This has always had the question of high-pressure elastic-plastic flow associated with its use. However, aluminum is a reasonable impedance-match to PBX-9501 and excursions from the initial state of the aluminum are small. The agreement between the two different techniques is satisfactory.

For an explosive, in contrast to an inert, the final shocked-state is not chemically the same as the initial state. We believe the Hugoniot states we have measured are representative of

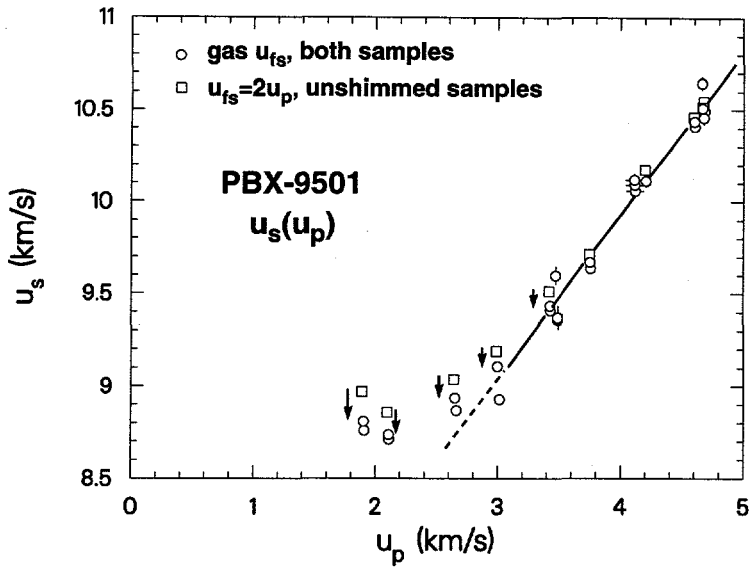

FIG. 2. Raw Hugoniot data. Two or more PBX-9501 samples were placed on each experiment. Samples were in pairs. One had a shim and the other released directly into the flash-gap gas. When a gas-like EOS was used for the release into the flash-gap the correction for the finite thickness of the gap brought the two samples into agreement as shown in the figure. The results from the shimmed samples are indifferent to this choice. The result for the shimmed sample at $u_p \approx 3$ was flawed by a bad reference trace. It was discarded from the averages.

detonation products and not of unreacted explosive. The POP plot [5,6] indicates a run to detonation distance of 0.4 mm at 25 GPa with an extrapolated run to detonation of 0.2 mm at the CJ state of PBX-9404/PBX-9501. Another indication that the shocked states resulted in the creation of detonation products was the nature of gap corrections required to get the same detonation velocities between explosive samples that were shimmed and unshimmed. To get the same detonation velocities a free-surface velocity characteristic of a gas needed to be used rather than a solid free-surface velocity that was approximately equal to twice the Hugoniot particle-velocity.

Another concern is whether the measured detonation velocities represent steady-state velocities. Davis [7] measured detonation-velocity transients in PBX-9404 and Composition B-3. Over the distance range 18–200 mm the measured detonation-velocity in PBX-9404 was constant and equal to the steady-state detonation-velocity. The experiments were initiated with a Baratol plane-wave lens. For Composition B-3 the departure of the measured detonation-velocity from its steady-state value was still appreciable after 80 mm of run. In the overdriven Hugoniot measurements of Kineke and West [8], no detonation-velocity variation was observed within experimental error for samples ranging in thickness from 0.5 to 2.0 mm. This was true for all the explosives (Baratol, TNT, Composition B and PBX-9404) studied. Similarly, Green *et al.* [9] measured overdriven detonations for LX-07, LX-17, PBX-9404 and RX-26-AF. Their results for PBX-9404 are similar to ours, and lie slightly above our data in the u_s-u_p plane. The average shock-velocity for the first 2.8 mm of run was within 1% of the detonation velocity measured from 2.0 mm to 4.8 mm run distance. In light of these results we feel safe in using samples 5 mm thick. Thicker samples would be desirable but these run into overtaking-wave problems from the rear of the flyer.

TABLE I. PBX-9501 Hugoniot Data.

Exp. I.D.	n[a]	u_d (km/s)	u_p (km/s)	u_s (km/s)	ρ (g/cm^3)	P (GPa)
8C4382	2	2.51[b]	1.905±0.010	8.783±0.044	2.35	30.7
8C4326	2	2.75[b]	2.109±0.011	8.724±0.044	2.42	33.8
8C4308	2	3.41	2.655±0.013	8.879±0.054	2.62	43.3
8C4332	1	3.84	2.996±0.015	9.108±0.045	2.73	50.1
8C4306	2	4.38	3.429±0.017	9.420±0.047	2.89	59.3
8C4819	3[c]	4.69	3.485±0.017	9.458±0.081	2.91	60.5
8C4383	2	4.79	3.754±0.019	9.654±0.048	3.00	66.5
8C4808	3[c]	5.55	4.114±0.071	10.087±0.050	3.11	76.4
8C4304	2	5.38	4.206±0.021	10.112±0.050	3.14	78.0
8C4331	2	5.88	4.601±0.023	10.424±0.052	3.28	88.0
8C4325	2	5.97	4.671±0.023	10.495±0.052	3.30	89.9
8C4305	2	5.98	4.673±0.023	10.543±0.072	3.29	90.3

[a]The number of samples averaged for this result.

[b]This is an equivalent u_d. These were in-contact experiments with BP pressures of 35.6 and 40.1 GPa respectively.

[c]DIH experiments. It takes more u_d to get to the same pressure.

Averaged points are given in Table I and will be plotted later along with the measured sound-speeds. The quoted errors arise from estimated errors in film writing-speed, sample dimensions, and reading the film traces; with the latter being the primary source. This usually results in a rather optimistic error bar. The primary indication of some unknown underlying error is erratic film traces. Scatter between similar samples also indicates this. When these two sources indicated a larger error we kept it. The optimistic error bars were increased to 1/2% when they fell below this threshold. The intervals should be regarded as the one sigma level. Errors in measurements on the standard samples translate into errors in u_p in this table. (The u_d have relative errors similar to u_p; we omitted them from the table.) The original optimistic error bars are shown in Fig. 2 if they are large enough to extend beyond the data symbols.

The standard state (*i. e.*, the pressure in the base plate or the flyer velocity) was determined by measuring u_s in BP material on BP experiments. In DIH and sound-speed experiments a "u_b" was measured. In this method [1] a bar of material (usually the same as the flyer or BP) is impacted by the flyer. On the impact side channels are cut in the bar. The differential time between the flyer velocity u_d in the channel and the u_s in the shoulder of the channel with the known EOS of the bar yields the standard state for the experiment. On a few experiments the standard state was determined by multiple flash-gaps in a stack of PMMA layers.

Table II gives parameters defining the EOS of standard materials used in these experiments. A linear $u_s(u_p)$ and constant $\rho\gamma$ were used. (Above 24 GPa a segmented fit for PMMA was used.) The standards used are probably accurate to 0.5–1.0% in u_s and 1.0–2.0% in P.

TABLE II. EOS parameters of standard materials.

Material	ρ_0 (g/cm^3)	c_0 (km/s)	s	γ_0
Al6061	2.703	5.288	1.3756[a]	2.14
SS316	7.960	4.464	1.544	2.17
PMMA	1.186	2.65	1.494	

[a]We don't know s this well, but this number was used.

IV. EXPERIMENTAL—SOUND VELOCITIES.

Sound velocities in overdriven PBX-9501 were measured using a rarefaction overtake technique as described by McQueen *et al.* [10]. This technique will be summarized here.

This technique measures rarefaction-wave velocities in a shocked material, and relies upon the fact that the leading release-wave travels at the longitudinal sound-velocity in a solid, followed by a wave traveling at the bulk velocity. In a fluid, the leading wave travels at the bulk velocity. The experimental geometry for such measurements is shown in Fig. 3 for the case of an opaque target-material. A relatively thin flyer impacts the target material with a velocity u_d, sending shocks forward into the target, and backwards into the flyer. In front of the target is a transparent analyzer-material, chosen for its high density and ability to radiate like a black body when shocked. When the shock wave that is moving forward into the target reaches the target/analyzer interface, the analyzer emits light due to the high temperature that occurs just behind the shock front. This light is detected with photo-multipliers through optical fibers and collimators. The collimators were designed to collect light from a small area (approximately 1 mm^2) to insure a sharp rise in the light output. When the shock that is moving backwards in the flyer reaches the rear surface of the flyer it is reflected as a rarefaction wave, which is now moving forward. This wave is a simple centered-release wave, and is shown in Fig. 3 as a fan. The release wave traveling at the local sound-speed in both the flyer and high explosive will eventually overtake the shock that is moving forward into the target/analyzer, because the states being studied are on the strong-detonation branch of the Hugoniot. It is evident from Fig. 3 that there is a time interval, equal to the round trip time in the flyer, that gives the high explosive a chance to equilibrate any transients that are present before it is probed by the release wave. When overtake occurs in the analyzer there is a discontinuity in the slope of the light intensity versus time curve. This allows the time at which overtake occurred to be accurately determined. For explosives there is the complication that as one approaches the CJ state from overdriven conditions the sound speed approaches the detonation velocity, and the overtake ratio becomes very large.

In the spectral and temperature range where the PM tubes are operating, the radiation intensity is proportional to something greater than the fourth power of the pressure. Consequently, one has a very sensitive way to detect wave arrival. In contrast, if one were to use a VISAR (measuring $u(t)$ at an interface via interferometry) the signal varies linearly with the stress amplitude associated with the release wave.

A stepped-target design was used for these experiments, allowing for several target thicknesses on a single experiment. This design is necessary for opaque target-materials. The

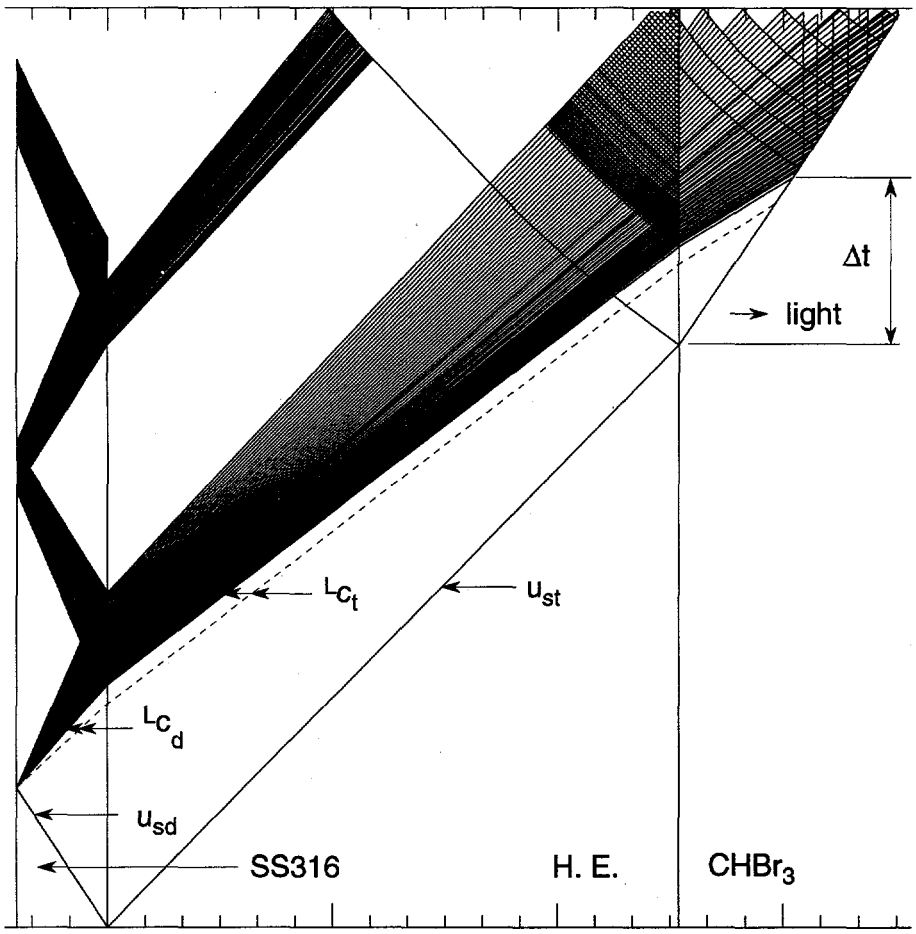

FIG. 3. Impact of a 316 stainless-steel flyer plate on the layers PBX-9501/$CHBr_3$. The lines (we are in a time-Lagrange coordinate plane) show the waves and interfaces resulting from a flyer plate with a $u_d = 5.5\,\mathrm{km/s}$ impacting the PBX-9501. The solid lines assume bulk waves. In our experiments the flyer does not melt and we needed to use the elastic release in the flyer. The path dictated by this release is shown as a dotted line in the figure.

experiment is designed so that overtake will occur very close to the thickest step; for thinner steps overtake will occur in the analyzer material. The light signal as seen by the photo-multipliers at each step consists of a sharp increase in light when the initial shock enters the analyzer, constant light output for some time, and then a reduction in light output when overtake occurs. A constant light level is detected as the shock moves through the analyzer material because light output is only from the vicinity of the shock front, and light coming from any appreciable distance behind the shock front is not seen (*i. e.*, the shock front is relatively opaque). Examples of these photo-multiplier records are shown in Fig. 4 for two target thicknesses. These records are measured to determine Δt, the time between light turn-on and light reduction due to the arrival of the release wave. These Δt values are plotted against the various target-step thicknesses x_{ti} as shown in Fig. 5 to obtain x_o. This is the distance at which overtake occurs.

Concern has been expressed about the linearity of $\Delta t(x_{ti})$. From Fig. 3 one sees that Δt is the result of solving for the intersections of a finite [11] number of waves and interfaces. If reaction rates are *very slow* or *very fast* compared to the time scale of the experiment the

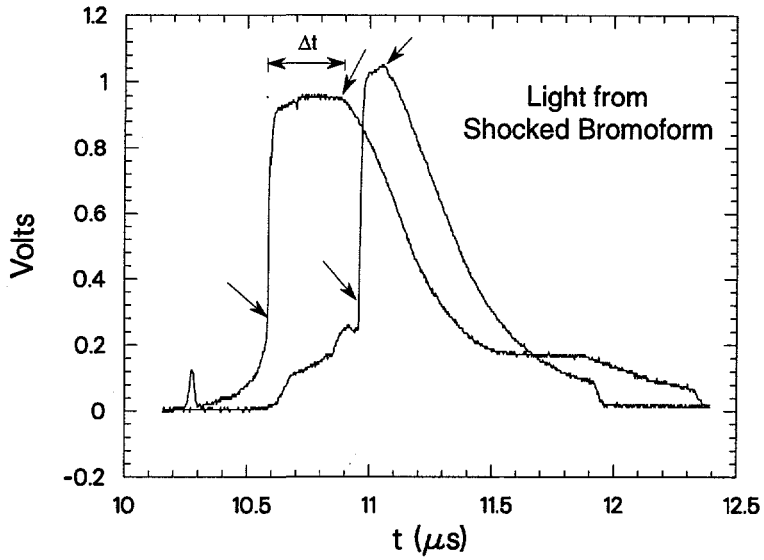

FIG. 4. Two bromoform light traces from 8C4819. The traces were chosen to show some of the character one sometimes has to contend with in obtaining a Δt. Some crosstalk from other levels is apparent. The early rapid rise from the shock at the local level and the break when the release arrives are readily distinguishable.

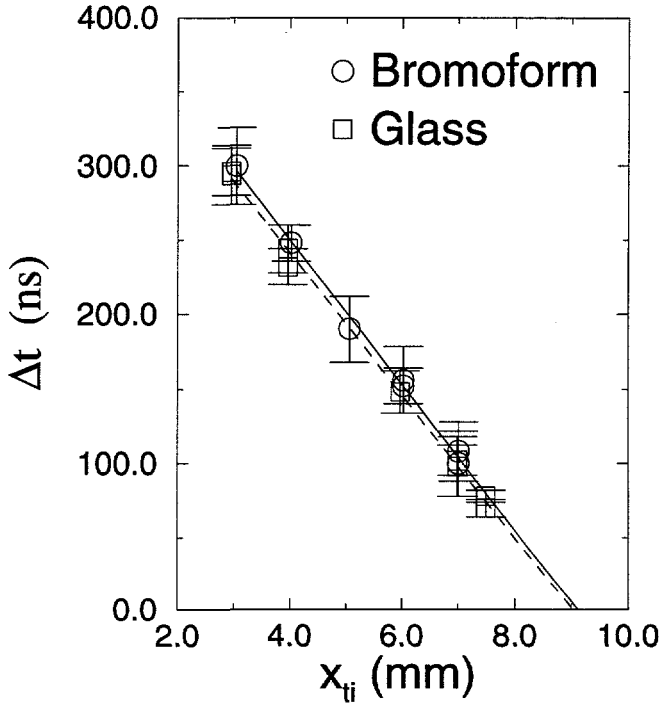

FIG. 5. $\Delta t(x_{ti})$ plots. On 8C4819 one step wedge was covered with a high-density glass and the other was covered with bromoform. The agreement in x_o (9.03 ± 0.08 and 9.11 ± 0.12 mm respectively) between the two different analyzers is excellent. The glass signals have a character different than the bromoform (prelight, sometimes a pip from the H.E./glass interface, more crosstalk), but shock entry into the glass and release arrival at the shock in the glass are usually readily discernible. The slopes of the lines for these two different analyzers is the same; this is a coincidence and was previously observed.

slopes of these waves do not depend on the thicknesses of the layered materials. Solving all the wave intersections then results [12] in a Δt linear with x_{ti}. In the case of explosives the detonation wave has a steady reaction-zone connected to the detonation front. This, in principle, can introduce a perturbation to the flow that produces a non-linear component to the extrapolation process. None of our experiments exhibited a non-linear extrapolation. This is probably due to the small size of the reaction zone [13,14] for PBX-9501.

The intrinsic accuracy of the experiment is enhanced because wave arrivals are measured at several locations and then statistically analyzed. This is in contrast to the use of one level for VISAR experiments. Also by extrapolating Δt to zero the effects of wave interaction at the explosive/bromoform interface are eliminated. For single-level velocity measurements using a VISAR, these interactions have to be addressed to calculate accurate wave-velocities [15,16].

The above experimental technique allows the overtake distance x_o to be measured. From this we calculate the overtake ratio:

$$R = x_o/x_d \tag{4.1}$$

where x_d is the flyer (driver) thickness. At exact overtake we have

$$\frac{x_d}{u_{sd}} + \frac{x_d}{{}^L c_d} + \frac{x_o}{{}^L c_t} = \frac{x_o}{u_{st}} \tag{4.2}$$

We define $R_d^* \equiv {}^L c_d/u_{sd}$ and $R_t^* = {}^L c_t/u_{st}$. The R^*'s are state variables; they only depend on the states achieved by shocks in the flyer and target. Then Eq. (4.2) becomes

$$\frac{1}{R_t^*} = 1 - \frac{u_{st}}{R u_{sd}}\left(1 + \frac{1}{R_d^*}\right) \tag{4.3}$$

For symmetric impacts $u_{st} = u_{sd}$, $R_t^* = R_d^*$ and Eq. (4.3) reduces to

$$R^* = (R+1)/(R-1). \tag{4.4}$$

The inverse of this for R has the self-similar form $R = (R^*+1)/(R^*-1)$. Here the R-value is sufficient to obtain $R_t^* = {}^L c_t/u_{st}$. For obvious reasons we do not have a symmetric impact and we must use Eq. (4.3). We use a flyer material, type 316 stainless-steel, that has been previously characterized so that we know $R_d^*(u_{sd})$, and u_{st} and u_{sd} are calculated from the known Hugoniots of the flyer and target and the measured flyer velocity u_d.

For these experiments the pressure range utilized is below the pressure range where sound speeds were measured in 316 stainless steel, so we have used extrapolated R_d^* values. For the longitudinal sound-speed we used $c(\mathrm{km/s}) = -1.374 + 0.933\rho(\mathrm{g/cm^3})$ [17]. This is a reliable procedure because of the observed linear variation of sound velocity with density for stainless, and because the fit to the solid-stainless data is observed to extrapolate to ambient sound-speed very well.

Experiments were performed using explosively-driven flyer plates. Large (12 in. diameter) type 316 stainless-steel plates were accelerated with a combination of plane-wave lenses and booster explosives. The thickness of the plates and the explosive systems were varied to obtain desired final velocities, and expected pressures in the PBX-9501 targets. Before

TABLE III. PBX-9501 Sound-Speed Data

Exp. I.D.	x_d (mm)	u_d (km/s)	u_{pt} (km/s)	u_{st} (km/s)	P (GPa)	ρ (g/cm^3)	R	R_t^*	^Lc_t (km/s)	c (km/s)
3R0014	1.215	3.69±0.12	2.736	8.977	45.1	2.64	17.20±0.90	1.1717	10.52±0.11	7.31
3R0016	0.873	4.29±0.06	3.187	9.250	54.1	2.80	13.08±0.29	1.2351	11.43±0.07	7.49
8C4819	0.875	4.69±0.03	3.486	9.470	60.6	2.91	10.49±0.17	1.3097	12.40±0.06	7.84
8C4798	1.506	4.85±0.12	3.605	9.564	63.3	2.95	9.64±0.40	1.3461	12.87±0.21	8.02
3R0021	1.190	5.49±0.05	4.079	9.967	74.6	3.11	8.61±0.17	1.4034	13.99±0.13	8.26
8C4808	0.873	5.55±0.10	4.122	10.007	75.7	3.12	8.76±0.17	1.3937	13.95±0.14	8.20
8C4799	0.864	6.34±0.15	4.703	10.547	91.1	3.31	7.47±0.17	1.4967	15.79±0.24	8.75

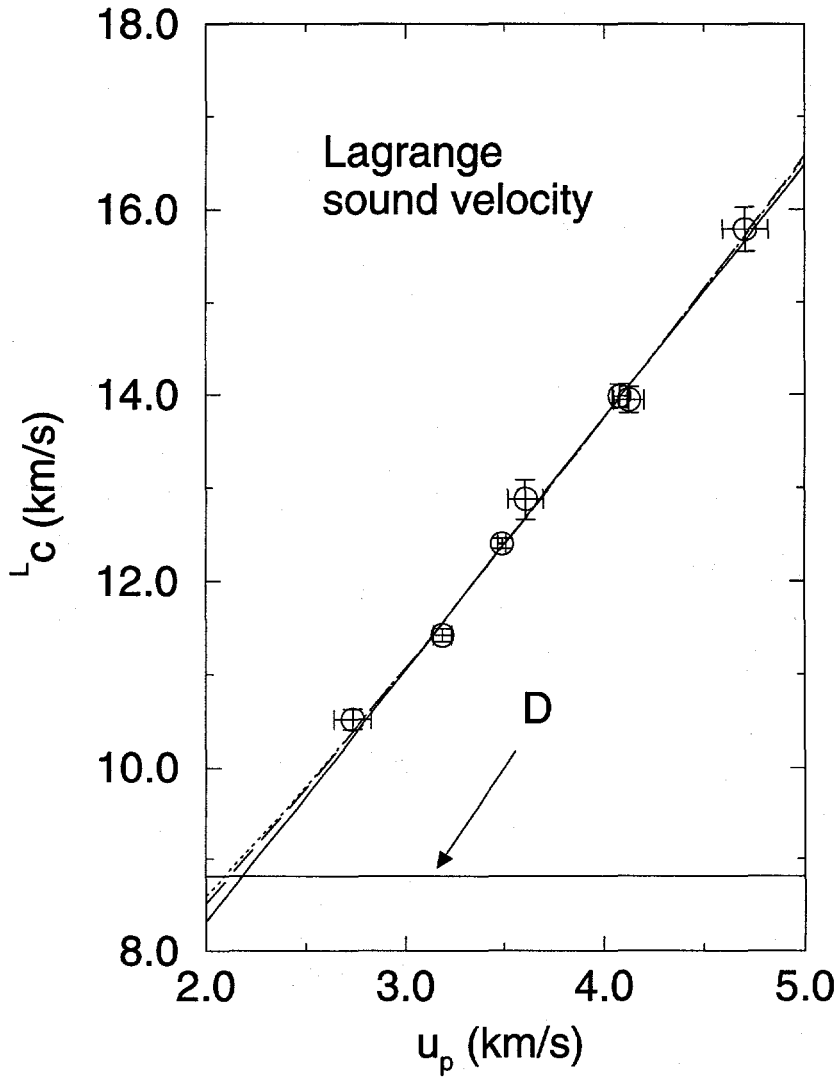

FIG. 6. Lagrange sound-speed data versus particle velocity. Weighted least-squares fit to data: linear (solid line), quadratic (dashed line), and cubic (dotted line). The CJ particle velocity is given by the intersection with the constant detonation-velocity determined from rate-stick data (also solid line).

doing experiments with PBX-9501 we found that our analyzer material (bromoform) dissolved the plastic-binder matrix for the HMX in the target material within a short time. For this reason we placed a thin (.025 mm) layer of FEP Teflon on the surface of the target that is exposed to the analyzer. This Teflon layer was also aluminized to make it opaque and thus decouple light from the analyzer from the self light of the detonating PBX-9501. This technique was found to work very well. We obtained photo-multiplier records that were indistinguishable from those obtained for metals.

Experimental results are given in Table III. Values for u_s are those from the fitting procedures given in section V. Pressures for these experiments range from 44 GPa to 91 GPa, and over this range the data show linear variation with particle velocity. The data also show linear behavior with density to within experimental error. Perfect linearity with particle velocity implies a slight deviation from linearity in density and *vice versa.* For this set of data one cannot choose one variable over the other. Also shown in Table III are the error bars assigned to the individual experiments. These error estimates take into account all known sources of error. The data shows an average deviation from the fit to density of about 1.7%, which is consistent with our experimental error-estimates. The data is plotted against particle velocity in Fig. 6. Also shown is the measured value for detonation velocity [18], which is taken as $D = 8.814\,\mathrm{km/s}$.

V. DATA FITTING

There are two basic approaches discussed here to determine the CJ state from this data. First is a polynomial curve fit to the ${}^{L}c$ data. The CJ conditions are then determined by the intersection of this extrapolated curve with the measured value of D, the infinite-diameter detonation velocity. The other method is to assume a general functional form for the equation of state and fit sound-speed, Hugoniot, and detonation-velocity data simultaneously. One advantage of this approach is that all relevant data contribute to the least-squares fitting process, and in addition a functional form for the Grüneisen parameter is obtained.

Linear least-squares fitting to data is discussed in many texts. The functional form being fit is given by

$$ {}^{L}c(u_p) = \sum_{i=0}^{n} c_i u_p^i. \tag{5.1} $$

The CJ particle velocity is then found by solving $D = {}^{L}c(u_p)$. Extrapolation of rate-stick data yields a very precise value for D. For PBX-9501 at a density of $1.832\,\mathrm{g/cm^3}$, D=8.802±0.006 km/s [18]. Measured detonation velocities are very nearly linear functions of the initial density. Using a slope of 3.4 km/s per $\mathrm{g/cm^3}$ from HMX and RDX data, we obtain a value of D=8.814 km/s for $\rho_0 = 1.8356\,\mathrm{g/cm^3}$, the average of the EOS samples.

Table IV shows the least-squares-fit coefficients for the n-values 1–3. The corresponding values at CJ of u_p and γ_S are given along with the an estimate of error in these values using the error matrix [19].

A convenient measure of the goodness of fit to the data is given by χ^2 where

$$ \chi^2 = \sum_{i=1}^{N} \frac{(y_i - \xi_i)^2}{\sigma_i^2}, \tag{5.2} $$

TABLE IV. Polynomial fits to the Lagrange sound-speed using Eq. (5.1), the corresponding CJ values of u_p and γ_S, and $\chi^2/(N-r)$.

n	c_0	c_1	c_2	c_3	γ_S	u_p	$\chi^2/(N-r)$
1	2.884	2.719			3.042±.110	2.181±.059	0.877
2	3.868	2.182	0.072		3.161±.428	2.118±.181	1.059
3	4.804	1.403	0.285	-0.019	3.212±.613	2.092±.262	1.410

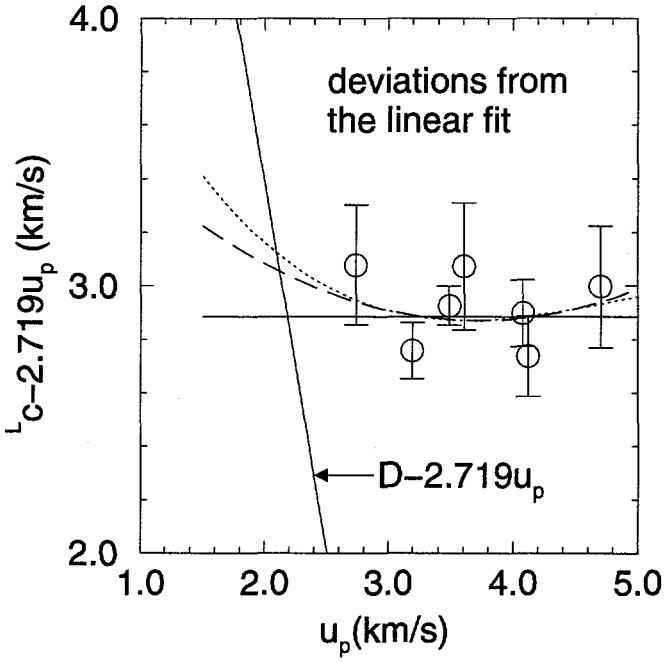

FIG. 7. Same as Fig. 6 except that the linear fit (except for a constant) has been subtracted from all quantities to emphasize differences.

and y_i is the i-th data point measured at the independent variable x_i, ξ_i is the value of the fitting function at that point, and σ_i is the standard deviation of that measurement. In this case, y is ${}^Lc$, x is u_p, and ξ is the right hand side of Eq. (5.1).

Estimation of an effective value of σ is rather complicated and is described in detail in Appendix B. Briefly, the two measured quantities, R and u_d, have the estimated uncorrelated errors described previously. These quantities are transformed into the relevant quantities ${}^Lc$ and u_p. The transformation introduces correlation in the variables and there is significant uncertainty in the independent variable as well as the dependent variable.

The best fit to the data was determined by minimizing χ^2 with respect to the parameters c_i. The total number of fitting constants is given by $r = n + 1$. Statistically, the expected value of χ^2 for N data points and r constants is $N-r$. In Table IV, we note that $\chi^2/(N-r)$ is near the expected value of 1.0 for all three fits. While the linear fit matches the data and extrapolates to CJ conditions well, the higher-order fits merely increase the uncertainty of extrapolation without giving a significantly better fit to the data. In this case, the linear fit and error estimate give the only reliable values to use for this method of evaluating the CJ conditions. Fig. 6 shows the data along with the fits and their intersection with D. Fig. 7 shows the same information with the linear fit (except for the constant term) subtracted

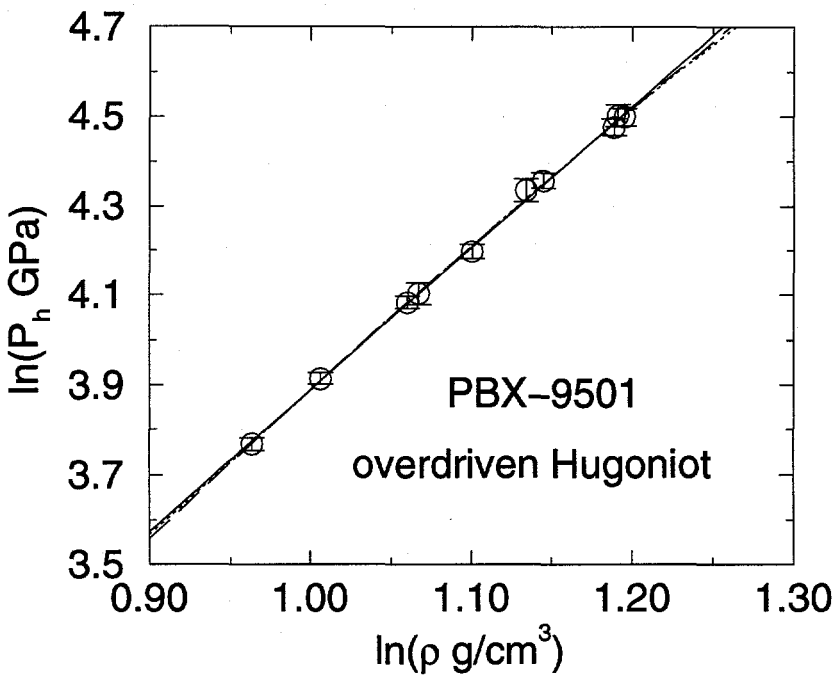

FIG. 8. Overdriven Hugoniot data transformed to $\ln P$ versus $\ln \rho$. Weighted least-squares fit to data: linear (solid line), quadratic (dashed line), and cubic (dotted line).

from each curve.

The second approach requires a general functional form for the equation of state. Eqs. (2.4–5) show that u_p, u_s, and D (which is just the minimum value of u_s) are all determined by $P_h(V)$. If we add γ_{gh}, the Grüneisen parameter along the Hugoniot, we also have ${}^L c$ (see Eq. (A13)). If we had a complete form for the Grüneisen function, $\gamma(P,V)$, then Eq. (A4) with the Hugoniot curve would yield a global $E(P,V)$.

Care must be taken in choosing functional forms to represent $P_h(V)$ and γ_{gh}. We need a good representation of the data with low-order fits. Otherwise the extrapolation to the CJ conditions will introduce unnecessary errors. We assume γ_{gh} is slowly varying and that we can fit it with the form:

$$\gamma_{gh}(V) = \sum_{j=0}^{m} b_j V^j. \tag{5.3}$$

The values $b_0 = 0$ and $b_1 \neq 0$ yield the common approximation $\rho\gamma =$ a constant.

For P_h, a relevant slowly-varying function is the adiabatic gamma, $\gamma_S = B_S/P$. A frequent approximation is that this variable is constant, or slowly varying. We could integrate γ_S to get a reference isentrope and use the Mie-Grüneisen form of EOS (*i. e.*, Eq. (A4) with the isentrope as the reference curve). This has the disadvantages of not having the reference curve on the Hugoniot and strongly mixing the overdriven Hugoniot data and the sound-speed data. We can consider a similar function on the Hugoniot, $\gamma_h = B_h/P = d\ln P_h/d\ln\rho$. If γ_h was constant, the overdriven Hugoniot data should fall on a straight line when plotted as $\ln P_h$ versus $\ln \rho$. Fig. 8 shows the data in this plane and a least-squares fit by a straight line. Fig. 9 shows the same graph with the linear fit subtracted from the data. Also shown are higher-order fits minus the linear fit. These linear and near-linear representations will

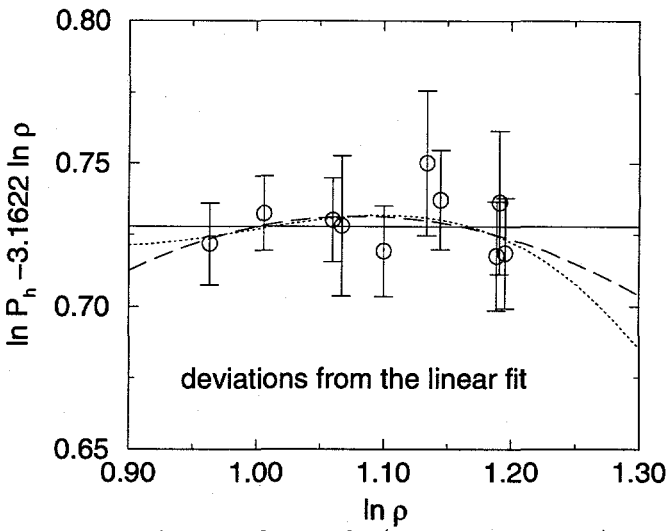

FIG. 9. Same as Fig. 8 except that the linear fit (less the constant) has been subtracted from all quantities to emphasize differences.

give a good form for extrapolation. So for the last equation needed for the EOS we adopt the form

$$\ln P_h = \sum_{i=0}^{n} a_i (\ln \rho)^i. \tag{5.4}$$

Using the equations above, we perform a nonlinear weighted least-squares fit of a_i's and b_j's to the data for P_h, ${}^L c$, and D (the minimum value of u_s). Powell's method [20] is used to find the minimum of χ^2 with respect to the parameters. Again, the estimated values of σ's are determined by the method described in Appendix B. Table V shows the results for γ_S, u_p, and D at the CJ conditions for several values of n and m. Note that the higher-order fits do not significantly decrease the weighted sum of squares of deviations from the data. Therefore, the recommended values for the CJ conditions are those for $n = 1$, $m = 0$. The resulting CJ pressure is 34.80 ± 0.27 GPa. Further entries in the table merely illustrate the increased uncertainty if parts of the data sets are eliminated.

Since the fitting form is nonlinear (for ${}^L c$ and D), an estimate of the probable error in derived quantities is not as straightforward as for the linear case. Although an iterative linearized formulation could be used, it is straightforward to numerically evaluate the error estimate using random sampling. Given the standard deviation of each experimental point and a good estimate of the true value for each point, we can construct the probability distribution, $P(y_1, y_2, \cdots, y_N)$, of obtaining a given set of data points in a repeat of the experiment. Using the values ξ_i from the fit as the estimate for the true values, then

$$P(y_1, y_2, \cdots, y_N) \propto exp[-\sum_{i=1}^{N} \frac{(y_i - \xi_i)^2}{\sigma_i^2}]. \tag{5.5}$$

Numerically choosing a random sample from this distribution, we obtain an artificially repeated experiment. This "experiment" is then fit as described above to obtain the CJ values of interest. Repeating the process 100 times, the distribution of CJ values is used to estimate the standard deviation of these derived quantities.

TABLE V. Fits and CJ values for various data sets.

data sets	n	m	a_0	a_1	a_2	a_3	b_0	b_1	D	γ_{SCJ}	u_{pCJ}	$\frac{\chi^2}{(N-r)}$
c^L, P_H, D	1	0	0.802	3.096			0.445		8.812	3.096±.026	2.151±.015	0.534
	1	1	0.804	3.094			0.675	-0.722	8.812	3.094±.028	2.152±.016	0.567
	2	0	0.843	3.012	0.042		0.460		8.812	3.087±.054	2.156±.029	0.570
	2	1	1.038	2.625	0.231		1.388	-2.706	8.813	3.038±.099	2.182±.054	0.583
	3	0	2.209	-0.835	3.620	-1.099	0.497		8.813	3.003±.141	2.201±.077	0.580
	3	1	1.966	-0.109	2.909	-0.863	0.729	-0.699	8.813	3.008±.240	2.199±.119	0.627
c^L, P_H	1	0	0.726	3.164			0.548		8.742±.064	3.164±.064	2.100±.047	0.478
	1	1	0.727	3.164			0.555	-0.020	8.742±.066	3.164±.069	2.100±.050	0.514
	2	0	0.667	3.278	-0.055		0.537		8.737±.067	3.181±.092	2.090±.059	0.511
	2	1	0.163	4.213	-0.486		-1.072	4.856	8.666±.179	3.370±.420	1.983±.207	0.528
	3	0	-0.262	5.832	-2.390	0.709	0.535		8.712±.113	3.281±.379	2.035±.185	0.547
	3	1	0.835	2.231	1.452	-0.627	-1.566	6.349	8.670±.162	3.332±.459	2.001±.211	0.572
P_H, D	1		0.804	3.094					8.812	3.094±.027	2.153±.015	0.404
	2		1.134	2.436	0.324				8.813	3.015±.096	2.195±.053	0.382
	3		8.965	-20.38	22.34	-7.044			8.814	2.804±.197	2.317±.115	0.306
P_H	1		0.728	3.163					8.743±.055	3.163±.060	2.100±.043	0.301
	2		0.052	4.4019	-0.581				8.650±.176	3.415±.440	1.959±.227	0.298
	3		3.153	-4.253	7.478	-2.489			8.719±.328	3.135±1.04	2.109±.449	0.344

In Fig. 10 we see our preferred fit to the data (line 1 in Table V). As expected from the small value of $\chi^2/(N-r)$, the fit to data is quite good. The resulting Lagrange sound-speed is very nearly a straight line. The two dotted lines demonstrate the effect of setting $\gamma_{gh} = 0$ (upper curve) and $\gamma_{gh} = 1$ (lower curve) with the same Hugoniot.

The sound-speed data are easily transformed to the adiabatic gamma γ_S using the fit to the Hugoniot, the definition of ${}^L c$, and Eq. (2.7). Note that the uncertainty in γ_S is dominated by the uncertainty in ${}^L c$. In Fig. 11 we show how several fits compare with the data. In addition, the resulting curves for γ_h are shown for the same fits. A slowly-varying γ_S is found over the range of interest. Likewise, the assumption of a slowly-varying γ_h is also validated through the EOS connection between γ_h and γ_S, provided the Grüneisen parameter γ_{gh} is slowly varying. These dimensionless representations of the bulk moduli on the Hugoniot and isentrope, γ_h and γ_S, intersect at the CJ state due to the tangency condition between the Hugoniot and the CJ isentrope. Another approach to finding the CJ state would be to fit γ_S and look for the intersection with this condition. In this plane, the sonic condition $D = {}^L c$, becomes $\gamma_S = \rho_0/(\rho - \rho_0)$. This function of ρ should intersect the $\gamma_h(\rho)$ and $\gamma_S(\rho)$ curves at their common intersection.The result from the intersection of the γ_h, γ_S curves (a weighted fit linear in ρ is used for the latter) is $\gamma_S = 3.16 \pm 0.06$. This is the same result as line 7 in table V. Note that an unweighted fit to the data will give a higher value for γ_S at CJ.

Similarly the Grüneisen gamma γ_{gh} can be determined from sound-speed data, using the

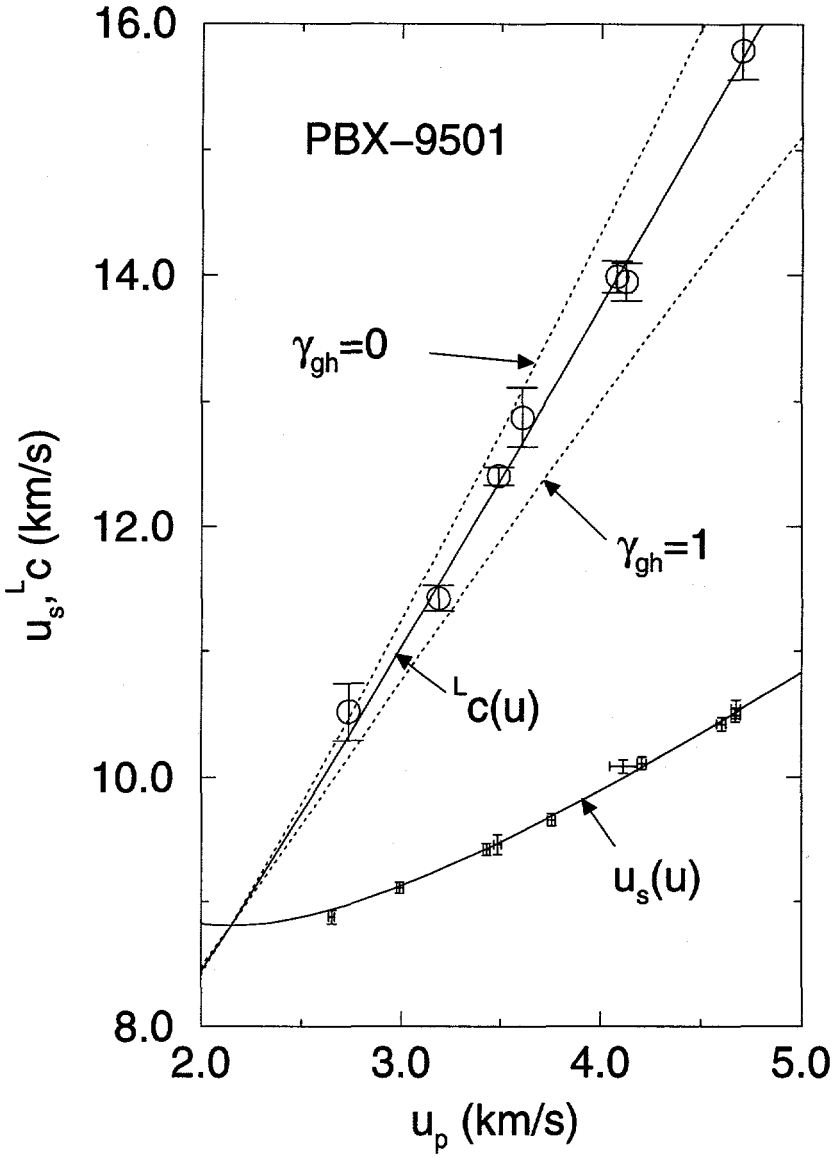

FIG. 10. Shock-velocity (two-dimensional error bars) and Lagrange sound-speed (circle) data versus particle-velocity. The solid lines are for the same quantities from our preferred fit. Dotted lines are illustrations of the effect of setting γ_{gh}=0 (upper curve) and γ_{gh}=1 (lower curve) with the same Hugoniot.

fit to the Hugoniot, the definition of ^{L}c, and Eq. (A12). Again the uncertainty in γ_{gh} is dominated by the uncertainty in ^{L}c. From Fig. 10 it is also obvious that the uncertainty in γ_{gh} increases when the density approaches ρ_{CJ}. In Fig. 12 we show how several fits compare with the data. Although the error bars are relatively large, the trend is still consistent with a slow variation in γ_{gh}.

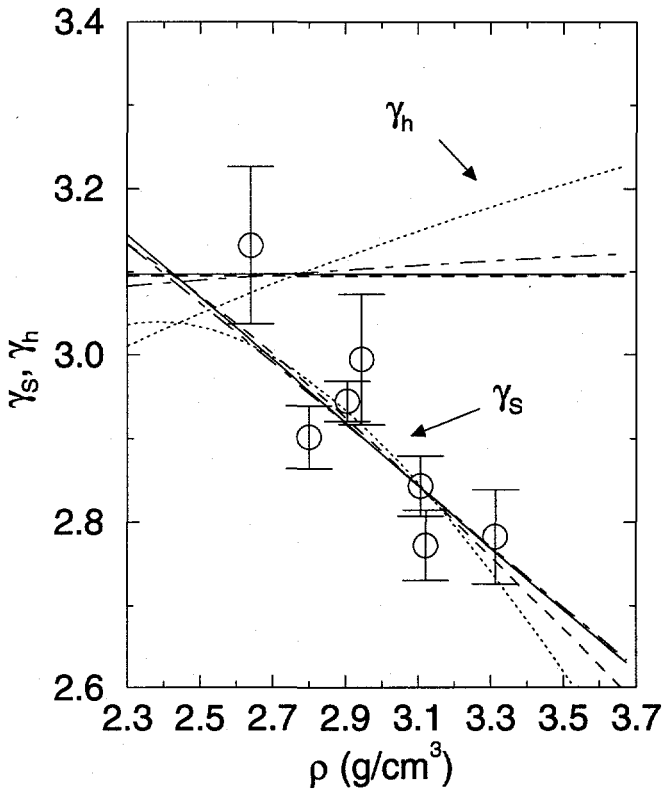

FIG. 11. Adiabatic gamma γ_S data (circle) versus density. The lower set of curves are values of γ_S from various EOS fits: $n = 1, m = 0$ (solid line), $n = 1, m = 1$ (dashed line), $n = 2, m = 0$ (chain dashed line), and $n = 2, m = 1$ (dotted line). The upper set of curves are γ_h with the same set of labels.

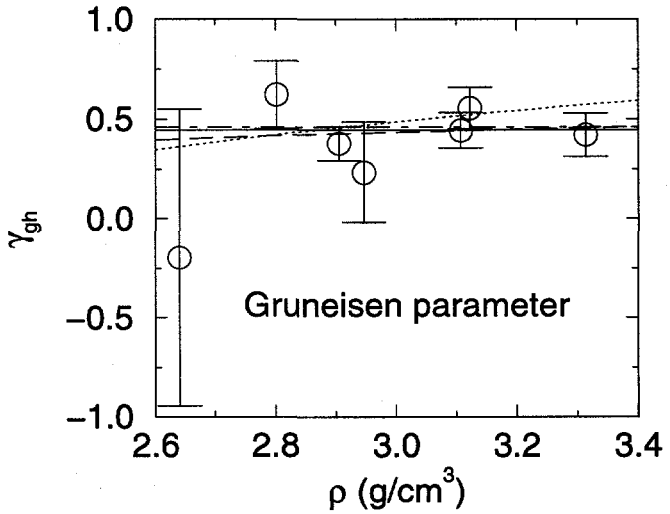

FIG. 12. Grüneisen gamma γ_{gh} versus density. Same labels as Fig. 11.

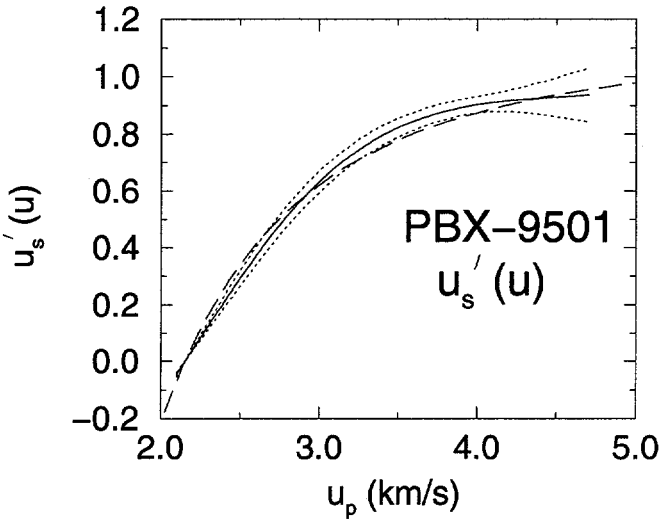

FIG. 13. The slope $u_s'(u)$ (solid line) from local running fits. The dotted lines indicate error limits. The dashed line is the slope from our previous analytical fit.

A. Detonation Hugoniot Fitting Without a Functional Form

Least-squares fitting of experimental data is commonly done by assuming an analytic function and optimizing the fit through a particular choice of adjustable parameters. Depending on the appropriateness of the analytical function the derivative of the function may or may not accurately represent the data. An alternative approach is to have a running local fit to the data with a level of smoothing compatible with the precision of the data. A tabular function developed by C. A. Forest at the Los Alamos National Laboratory and briefly described in Appendix C was used to fit the detonation-Hugoniot data in Table I with particle velocities greater than the particle velocity of the CJ state. The slope u_s' of the tabular function was set equal to zero at the u_{pCJ} from our preferred fit, but the detonation velocity was allowed to vary. The tabular function representing the slope of the detonation Hugoniot is presented in Fig. 13.

The characteristic shape of the PBX-9501 detonation Hugoniot is graphically displayed in this figure. The slope is zero at the CJ state and monotonically increases with increasing particle velocity. The slope linearly increases near the CJ state and then gradually flattens out at larger particle velocities to essentially a maximum slope. The general shape of u_s' is common to other detonation Hugoniots we have studied (Composition B, PBX-9502, and TNT). However, for some of these explosives the maximum asymptotic slope was not attained over the particle-velocity range investigated. For these explosives there was still a small non-zero slope to $u_s'(u)$ at large particle velocities.

The dashed lines above and below the fitted curve represent the two-sigma error limits at the 95% probability limit. The error limits are close together at the CJ state, because of the slope constraint, and gradually increase at intermediate particle velocities. The large error limits at the end of the data range occur because central centered differences can no longer be taken over the usual interval. The other curve in Fig. 13 is the analytic fit shown in Fig. 8.

From the figure we estimate an asymptotic slope for the OD Hugoniot of 0.95±0.10. The

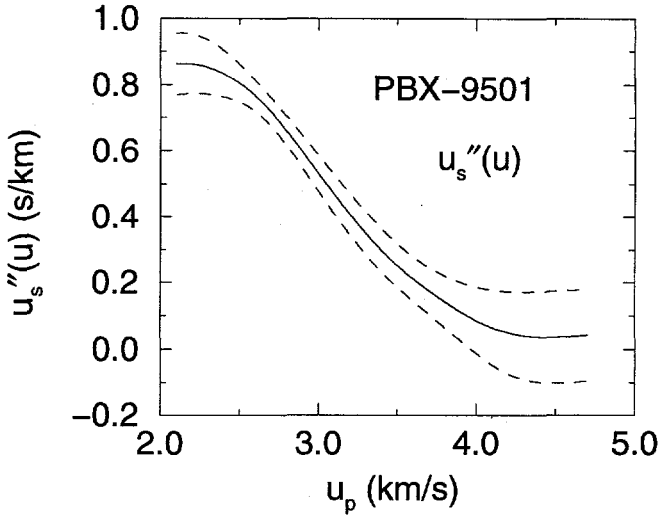

FIG. 14. The derivative $u_s''(u)$ from the running fits. Error limits are shown.

RHS of the approximate relation Eq. (A33) then (with our best estimate for the CJ state) predicts 2.50±0.3 for ${}^{L}c'(u)$. The measured value 2.712 falls within this range.

Menikoff and Plohr [21] define a fundamental derivative $\mathcal{G} = -VE_S'''/2E_S''$. This is equivalent to $\mathcal{G} = \frac{1}{2}(1 + dB_S/dP)$. Eq. (2.17) becomes

$$ {}^{L}c'_{cj} = (V_0/V_{cj})\mathcal{G}_{cj} \tag{5.6} $$

The slope of our sound-speed curve is closely related to their fundamental derivative, and our measured ${}^{L}c'(u)$ implies $\mathcal{G} = 2.05$.

In our data fitting we were able to choose analytical forms that adequately represented the data. This just means the data doesn't uniquely specify a particular functional form. However, we do recommend that any functional form chosen duplicates the u_s' shape given in Fig. 13. This insures that both u_s and u_s' are smooth continuous functions, which are necessary constraints to obtain thermodynamic variables that are well behaved.

In Fig. 14 the second derivative of the detonation Hugoniot is given. The tabular function code was also used to calculate this curve. The curvature is a maximum at the CJ state and monotonically decreases to zero at the end of the data range. The two-sigma error limits are also shown and have the usual behavior at the constrained and unconstrained end points. The exact relation (Eq. (A21)) gives 1.36 s/km at CJ. This is considerably larger than the 0.87±0.1 value indicated on the graph. This is not too surprising. There weren't a lot of points in the vicinity of the CJ state measuring the curvature.

VI. DISCUSSION

The CJ pressure (sometimes more appropriately called the detonation pressure) is an important parameter used to describe the ability of explosives to accelerate metal plates. Typical plane-wave CJ detonation experiments involve monitoring the motion of inert materials placed on explosives [22,23]. From these studies reflected-shock or release states centered at the CJ state can be measured and used to ultimately determine the CJ state.

To determine these reflected detonation/release states the experimental variables (usually $u_{\rm fs}$ or u_s) are extrapolated to zero plate-thickness from thicknesses large enough so that the effects of the reaction zone are usually eliminated. Because of the smooth transition from the reaction zone to the Taylor wave one can't make this extrapolation reliably. One can't unambiguously identify where the reaction zone ends and the Taylor wave begins. Another complication is that multiple rate processes are most likely involved that have yet to be characterized. A manifestation of this fact is experimenters claim 1% to 2% accuracy, whereas their results sometimes differ by more than 10%.

Cost *et al.* [24] used magnesium plates of various thicknesses, to infer a CJ pressure of 37.5 GPa for PBX-9404 (94 wt% HMX, 3 wt% NC, 3 wt% CEF). Jameson and Hawkins [25] obtain a CJ pressure of 34.5 ± 1.0 GPa by measuring the shock velocity through Plexiglas plates of differing thickness for PBX-9404. Davis [26], using an ASM probe [27] positioned at the PBX-9404/Teflon interface, predicted a CJ pressure of 35.6 ± 1.0 GPa. For a 95 wt% HMX/5 wt%inert explosive Burrows *et al.* [28] used manganin gages to measure pressure directly. Using the shape of the Taylor wave they inferred a CJ pressure of 35.5 GPa, which was 2.0 GPa greater than the measured peak pressure. Davis and Ramsay [29] summarized the research at the Los Alamos National Laboratory over the last several years. From free-surface velocity measurements they noted 12.5 mm and 25.4 mm PBX-9404 samples suggested CJ pressures respectively of 32.5 GPa and 34.5 GPa, whereas thicker samples suggested a CJ pressure of 35.6 GPa. Based on these results and the ASM probe measurements they concluded that reaction-rate processes may be involved that haven't previously been considered. A similar conclusion was reached by Lee *et al.* [30] for LX-14 (95 wt% HMX, 5 wt% polyurethane). They noted a different EOS was needed to model thin (0.1–0.2 mm) versus thick(> 0.5 mm) plate push experiments. Both aluminum and copper plates were used in these tests. For most of their experiments a CJ pressure of 36.0 GPa was used to model their results.

The inability of plane-wave CJ detonation experiments to accurately measure CJ pressures was a motivating factor to examine alternative experiments. Overdriven detonation experiments were chosen because they produced constant detonation states that could be accurately measured. They also effectively decouple reactive hydrodynamics from EOS hydrodynamics. In this manner problems that complicated CJ detonations were avoided. The "thermodynamic" CJ state determination makes use of the fundamental property of the CJ state, mainly the sonic condition.

A. Constant-γ_S Model

As was mentioned previously in section II, once the CJ state is determined, all the parameters in the constant-γ_S model can be calculated, *e. g.*, for $D = 8.814$ km/s and $u_{cj} = 2.151$ km/s we have $\gamma_S = D/u_{cj} - 1 = 3.097$. The detonation Hugoniot can be determined using Eq. (2.8). The resulting Hugoniot is considerably stiffer than the experimental Hugoniot. At the high-pressure end of our data the difference between the "constant-γ_S model" Hugoniot and the experimental Hugoniot is 1.0 km/s. A constant γ_S also disagrees with experiment. The experimental γ_S linearly decreases with increasing particle-velocity. From Eq. (2.6) the relation $\gamma = \gamma_S - 1 = 2.097$ can be obtained for the constant-γ_S model. This is considerably different from the $\gamma = 0.45$ experimental value. This is because this

model places the ridiculous burden on the Grüneisen parameter of accounting for the compression curve behavior as well as the thermal part of the EOS. Even though the constant-γ_S model can approximate some regimes of the release isentrope, it can not predict quantitatively the high-density states on the detonation Hugoniot.

VII. CONCLUSIONS

We have presented a comprehensive review of properties of equilibrium detonation Hugoniots. To illustrate the qualitative features a constant-γ_S model was used. More general thermodynamic relations are also presented. Particular attention was given to properties of the detonation Hugoniot at the CJ state and how sound-speed measurements can be utilized to further define the EOS. Overdriven detonation states were used in these experiments. This was a critical innovation, because these OD states can be accurately characterized and they effectively decouple reaction-rate hydrodynamics from EOS hydrodynamics, at least for PBX-9501.

A tabular function was used to fit the experimental detonation Hugoniot data. An interesting functional form for the derivative $u_s'(u)$ of the detonation Hugoniot was observed, mainly a derivative that's zero at the CJ state and monotonically increases with increasing particle velocity until a constant maximum value is attained. The measured Lagrange sound-velocities displayed a linear dependence with increasing particle velocity. The intersection of the Lagrange sound-velocity curve with the detonation Hugoniot allowed a novel determination of the "thermodynamic" CJ state with a resulting CJ pressure of 34.8±0.3 GPa. The lower value of our CJ pressure relative to previous measurements suggests ongoing chemical reactions may have influenced measurements made at "CJ conditions".

Several possible EOS models were examined to fit our experimental data. A particularly simple and effective analytical form was a linear $\ln P$–$\ln \rho$ relationship. The experimentally determined sound velocities directly determine the adiabatic gamma γ_S, which shows a linear decrease with increasing particle velocity. The combination of detonation-Hugoniot and sound-velocity data allows the determination of the Grüneisen parameter. Near the CJ state the Grüneisen parameter is not well constrained because the difference in slopes between the detonation Hugoniot, the isentrope and the Rayleigh line approach zero (see Eq. (A12)). For particle velocities greater than the CJ particle velocity, the differences between these respective slopes becomes larger, resulting in meaningful Grüneisen parameter determinations. The Grüneisen parameter displays a near constant behavior (see Fig. 12) with a mean value of 0.45 on the detonation Hugoniot.

The near-validity of Eq. (A33) suggests that EOS models with relatively constant curvature (Murnaghan EOS's, linear u_s-u_p) might also describe detonation products very well. The linear base curve would have to be lower in the u_s-u_p plane than the OD Hugoniot. The variations that u_s' goes through on the OD Hugoniot would have to be achieved through an initial energy offset (*i. e.*, the "reverse snowplow" model discussed in Appendix A).

PBX-9501, with its fast reaction rate, has been an ideal first candidate for this type of experimental study. Studies of less ideal explosives will probably show more evidence of reaction-rate effects in the lower-pressure range of the overdriven states.

ACKNOWLEDGMENTS

We would like to dedicate this paper to R. G. McQueen who passed away October 18, 1994 in Los Alamos. Bob was a friend and co-worker of ours for many years. Because of Bob's love and dedication to shock-wave physics for over forty years he had a unique insight into the subject. His consuming passion was to conduct "perfect experiments" that could not be improved upon. An example of this is the optical-analyzer experiment that can measure sound velocities at high pressure with unparalleled precision. This technique was used to measure sound velocities in detonation products. Iron was the first material studied using this technique. Two solid-solid phase transitions and one melting phase transition were observed. This dramatically illustrated the capability of this technique to observe shock-induced phase transitions that were previously undetectable.

We want to acknowledge Dennis Price and Connie Gomez for the assembly of the over-driven detonation Hugoniot experiments, and Dennis Price for developing the experimental assemblies that allowed precise sound-velocities to be measured. These assemblies were a work of art. We also want to acknowledge Dennis Shampine for his meticulous care in firing these shots. His data-acquisition skills were an important part of this experimental program. We are also grateful to Charles Forest for the fits he provided, which he describes in Appendix C. They gave us an insight to the analytical forms that best described our experimental data.

APPENDIX A: SHOCK THERMODYNAMICS

We give a brief review of fluid thermodynamics applicable to shock waves. Some new thermodynamic relations are obtained. We also use this section to set some of our notation.

To relate shocks to thermodynamics we require the specific internal energy as a function of pressure and specific volume, $E(P,V)$. The natural variables [31] for energy are entropy and specific volume, $E(S,V)$. The first-order differential coefficients for $E(S,V)$ are the temperature T and pressure P (this is just the reversible form of the first law). In contrast, the first-order coefficients for $E(P,V)$ involve the second-order coefficients for $E(S,V)$. If $E(S+\Delta S, V+\Delta V) = E(S,V) + \Delta E^{(1)} + \Delta E^{(2)} + \ldots$ we have:

$$\Delta E^{(1)} = \frac{\partial E}{\partial S}\Delta S + \frac{\partial E}{\partial V}\Delta V \equiv T\Delta S - P\Delta V, \tag{A1}$$

$$\begin{aligned} 2!\Delta E^{(2)} &= \frac{\partial^2 E}{\partial S^2}\Delta S^2 + 2\frac{\partial^2 E}{\partial S \partial V}\Delta S\Delta V + \frac{\partial^2 E}{\partial V^2}\Delta V^2 \\ &= \frac{\partial T}{\partial S}\Delta S^2 + 2\frac{\partial T}{\partial V}\Delta S\Delta V - \frac{\partial P}{\partial V}\Delta V^2 \\ &\equiv \frac{T}{C_V}\Delta S^2 - 2\frac{\gamma T}{V}\Delta S\Delta V + \frac{B_S}{V}\Delta V^2. \end{aligned} \tag{A2}$$

The terms in Eq. (A2) increase by an order of magnitude from left to right for a Hugoniot curve in our experimental range. The specific heat at constant volume C_V, the Grüneisen function γ, and the isentropic bulk-modulus B_S are the natural second-order coefficients to describe $E(S,V)$.

One meaning for γ can be obtained by picking off corresponding coefficients in Eq. (A2); along an isentrope, $dT/T = -\gamma dV/V$. Temperature ratios from one point of an isentrope to the next are determined solely by $\gamma(S,V)$ and the compression. Temperatures on different isentropes can be defined by C_V on a constant-volume curve, $dT = TdS/C_V = dE/C_V$. The Maxwell relation $\partial^2 E/\partial S\partial V = \partial T/\partial V = -\partial P/\partial S$ offers another interpretation of γ; $\gamma T dS = \gamma dE = V dP$, or

$$\gamma(P,V) = V\left(\frac{\partial P}{\partial E}\right)_V. \tag{A3}$$

The importance of the Grüneisen function is evident from this equation. If we have some cross-curve $P_x(V)$ (one where the volume is varying) and we know the energy along this curve (isentropes and Hugoniots are two types of curves where the energy is readily obtained), then we can express the energy in the desired $E(P,V)$ form:

$$E(P,V) = E_x(V) + \int_{P_x(V)}^{P} dpV/\gamma(p,V), \tag{A4}$$

where p is an integration variable with V held constant. In this paper a bare γ will always mean the Grüneisen variable, and, in general, it should be regarded as a function of the current pair of variables being used to describe the EOS.

If we have a curve $P_x(V)$ we define the modulus for that curve as $B_x = -VdP_x/dV$. The isentropic bulk-modulus B_S is related to the velocity c of a small-amplitude wave in a fluid media by $B_S = \rho c^2$ [32]. This velocity is with respect to the compressed media at rest. It is convenient to work with the Lagrangian velocity ${}^L c = \rho c/\rho_0$. We have:

$$c^2 = B_S/\rho, \quad {}^L c^2 = \rho B_S/\rho_0^2. \tag{A5}$$

Other moduli will be useful. Along a Hugoniot curve $P_h(V)$ we define $B_h = -VdP_h(V)/dV$. The chord connecting the initial state to the final shocked-state is the Rayleigh line. We define a modulus associated with this slope as $B_R = V_0(P-P_0)/(V_0-V)$. Eq. (2.4) then takes the form $B_R = \rho_0 u_s^2$. For the chord the choice for the multiplying volume is ambiguous. We also define $B_{\rm ch} = V(P-P_0)/(V_0-V) = \rho_0 u_s(u_s-u)$. This will permit a pleasing symmetry in an equation we shall derive for the Grüneisen function.

The dimensionless curvature of a $P_x(V)$ curve is also of interest. If $B_x = -VP_x'$ (a prime on P will usually denote a volume derivative), then $dB_x/dV = -P_x' - VP_x''$. Alternatively we have $dB_x/dV = (dP_x/dV)(dB_x/dP) = -(B_x/V)(dB_x/dP)$. Equating these yields:

$$\frac{V^2 P_x''}{B_x} = 1 + \frac{dB_x}{dP}. \tag{A6}$$

Dimensionless forms for the moduli are frequently used. We define $\gamma_x = B_x/P_x$. The isentropic gamma

$$\gamma_S = \frac{B_S}{P} = -\left(\frac{\partial \ln P}{\partial \ln V}\right)_S = \frac{\rho c^2}{P}. \tag{A7}$$

is a variable frequently used to describe detonation-product isentropes. Unfortunately this variable is frequently denoted as a bare γ, the same symbol we use for the Grüneisen function.

We shall always use the subscript form. Sometimes a subscripted γ is used to denote the Grüneisen function along a particular path. We will use a functional notation to denote this case, *e. g.*, $\gamma(P_h(V), V)$ for γ along a Hugoniot. As an alternative to this we'll occasionally use $\gamma_{gh} = \gamma(P_h, V)$, *etc.*

The natural equations of state for $E(S,V)$ are $T(S,V)$ and $P(S,V)$. The differential forms for these may be obtained from the appropriate coefficients in Eq. (A2), $dT/T = dS/C_V - \gamma dV/V$ and $VdP = \gamma TdS - B_S dV$. A rearrangement of the latter gives a $TdS(dP, dV)$, and with the first law gives our desired $dE(dP, dV)$.

$$TdS = \frac{V}{\gamma}dP + \frac{B_S}{\gamma}dV, \tag{A8}$$

$$dE = \frac{V}{\gamma}dP + \left(\frac{B_S}{\gamma} - P\right)dV. \tag{A9}$$

Following Courant and Friedrichs [32] we use the Hugoniot function $h(P,V) = E - E_0 - \frac{1}{2}(P + P_0)(V_0 - V)$. (We use a small h to distinguish this function from the enthalpy H.) Clearly $h = 0$ defines $P_h(V)$. Other curves with constant-h correspond to Hugoniots with a different energy in the initial state. From the first law and Eq. (A8) we get

$$\begin{aligned} dh &= TdS - \tfrac{1}{2}(V_0 - V)dP - \tfrac{1}{2}(P - P_0)dV \\ &= \left(\frac{V}{\gamma} - \frac{V_0 - V}{2}\right)dP + \left(\frac{B_S}{\gamma} - \frac{P - P_0}{2}\right)dV. \end{aligned} \tag{A10}$$

For $dh = 0$ we obtain

$$-V\left(\frac{\partial P}{\partial V}\right)_h \equiv B_h = \frac{B_S - (\gamma/2)(P - P_0)}{1 - (\gamma/2V)(V_0 - V)}. \tag{A11}$$

This equation can be solved for the Grüneisen function:

$$\frac{\gamma}{2V}(V_0 - V) = \frac{B_h - B_S}{B_h - B_{\text{ch}}}. \tag{A12}$$

These B's all have a common V-factor, so this ratio of differences can also be regarded as the ratio of differences of the slopes of the various curves. Eq. (A11) can also be solved for B_S:

$$B_S = \left\{1 - \left(\frac{\gamma}{2V}\right)(V_0 - V)\right\}B_h + \frac{\gamma}{2}(P - P_0). \tag{A13}$$

This, with (A5), gives the sound speed *on the* Hugoniot.

For an exothermic Hugoniot (more precisely, for $h(P_0, V_0) > 0$) the "first" solution for a shock is obtained when we raise the Rayleigh line to be tangent to the Hugoniot curve, *i. e.*, $B_h = B_{\text{ch}}$. *At the tangent point* we can make the following observations. If we insert this condition in Eq. (A13) we find $B_S = B_{\text{ch}}$. This result in Eq. (A5) implies ${}^L c = u_s$. This, combined with the relation between ${}^L c$ and c and Eq. (2.1) implies $c = u_s - u$, the

sonic condition. The u_s at this minimum shock-velocity is denoted by D, the CJ detonation-velocity. The argument is reversible, the sonic condition implies the triple-tangency between the Hugoniot, Rayleigh line, and isentrope. The usual caveats apply; these results are valid when reaction rates are fast enough to get a close approach to equilibrium.

In this paper we are particularly interested in the curves ${}^{L}c_h(u)$ (the Lagrange sound-speed along the Hugoniot) and $u_s(u)$ (the OD Hugoniot) as they extend above the CJ state. As we go higher in pressure we expect reaction rates to be faster, and we expect that our measured results will be closer to true equilibrium values. The equilibrium Lagrange sound-speed can be obtained as a functional of the OD Hugoniot and the Grüneisen function with the aid of Eqs. (A5) and (A13), *i. e.*, ${}^{L}c_h(u) = f : u_s(u), \gamma$. These would directly express ${}^{L}c(P, V)$. We would like it in the u_s-u plane. The jump conditions (Eqs. (2.1–2) and their inverses (2.3–4)) can be regarded as transformations between these two planes of variables. Differential forms of the transformation, or equivalently the following:

$$-dV/du = V_0(u_s - uu_s')/u_s^2, \tag{A14}$$

$$dP/du = \rho_0(u_s + uu_s'), \tag{A15}$$

where $u_s' = du_s/du$, can be used to effect the transformation to the velocities plane. An intermediate result, using the definition of B_h, is

$$B_h = \rho_0 u_s(u_s - u)\frac{u_s + uu_s'}{u_s - uu_s'}. \tag{A16}$$

One notes that $B_h = B_{\mathrm{ch}}$ implies $2uu_s' = 0$, *i. e.*, you can have this condition at the beginning of the Hugoniot ($u = 0$), or if the tangency occurs for finite u the slope of the $u_s(u)$ Hugoniot must be zero. We then have:

$$\begin{aligned}\left(\frac{{}^{L}c_h}{u_s}\right)^2 &= \left\{1 - \left(\frac{\gamma V_0}{2V}\right)\frac{u}{u_s}\right\}\frac{u_s + uu_s'}{u_s - uu_s'} + \left(\frac{\gamma V_0}{2V}\right)\frac{u}{u_s} \\ &= G/(u_s - uu_s'),\end{aligned} \tag{A17}$$

where

$$G = u_s + uu_s'\left\{1 - \left(\frac{\gamma V_0}{V}\right)\frac{u}{u_s}\right\}. \tag{A18}$$

We take the logarithm of Eq. (A17) and then the derivative to obtain:

$$2\left(\frac{{}^{L}c_h'}{{}^{L}c_h} - \frac{u_s'}{u_s}\right) = \frac{uu_s''}{u_s - uu_s'} + \frac{G'}{G}, \tag{A19}$$

where

$$G' = u_s' + (u_s' + uu_s'')\left\{1 - \left(\frac{\gamma V_0}{V}\right)\frac{u}{u_s}\right\} + uu_s'\left(\frac{u_s - uu_s'}{u_s^2}\right)\frac{\gamma V_0}{V}\left\{\frac{u}{u_s - u}\frac{d\ln(\gamma/V)}{d\ln V_h} - 1\right\}. \tag{A20}$$

We expect ${}^Lc_h' \equiv d{}^Lc_h/du$ to be approximately constant over our data range. The complexity of (A19) is due to the structure a Hugoniot has when it represents a detonation. We switch quickly from $u_s' = 0$ and a non-zero curvature at CJ to u_s' a constant and $u_s'' \approx 0$ in the linear range of the OD Hugoniot. The complicated form for ${}^Lc_h'$ is probably required to keep it roughly constant. At the CJ state we have $u_s' = 0$, ${}^Lc = u_s = G = D$, and thus:

$$\left(\frac{d{}^Lc_h}{du}\right)_{cj} = u_{cj}u_s''\left\{1 - \left(\frac{\gamma V_0}{2V}\right)_{cj}\frac{u_{cj}}{D}\right\}. \tag{A21}$$

This equation gives a close connection between the slope of our experimental sound-speed and the curvature of the OD Hugoniot at the CJ state. This equation is likely to be used to establish a good value for the curvature rather than the other way around. If a very accurate u_s'' could be obtained from the Hugoniot curve an estimate of γ *at* the CJ state could be made.

What we would really like is a relation between ${}^Lc_h'$ and some other readily measurable EOS parameter, *e. g.*, the asymptotic slope of $u_s(u)$. We have concentrated on ${}^Lc_h(u) = f : u_s(u), \gamma$. We may expect a simpler result if we consider ${}^Lc_h(u) = f : P_S(V), \gamma$, where $P_S(V)$ is the CJ isentrope. It does not have the complications that the Hugoniot does. We do have the additional complication that we follow the sound speed along the Hugoniot experimentally, and not along the isentrope. In Eq. (A4) we let the x-curve be the CJ isentrope. Then with Eq. (2.3), $E_{cj} - E_0 = \frac{1}{2}(P_{cj} + P_0)(V_{cj} - V_0)$, and $E_x = E_{cj} - \int P_S dV$; we obtain:

$$\tfrac{1}{2}(P_h + P_0)(V_0 - V) = \tfrac{1}{2}(P_{cj} + P_0)(V_0 - V_{cj}) - \int_{V_{cj}}^{V} dV P_S(V) + \int_{P_S}^{P_h} dp \frac{V}{\gamma(p,V)}, \tag{A22}$$

i. e., we have $P_h = f : P_S, \gamma$. We take the volume derivative of (A22) and rearrange the terms slightly:

$$\frac{-VP_h'}{\gamma_{gh}}\left\{1 - \frac{\gamma_{gh}}{2V}(V_0 - V)\right\} = \tfrac{1}{2}(P_h + P_0) - P_S - \frac{VP_S'}{\gamma_{gS}} + \int_{P_S}^{P_h} dp \frac{\partial}{\partial V_p}\left(\frac{V}{\gamma(p,V)}\right). \tag{A23}$$

This combines with (A13) to yield:

$$\frac{B_S(P_h,V)}{\gamma_{gh}} = \frac{B_S(P_S,V)}{\gamma_{gS}} + (P_h - P_S) + \int_{P_S}^{P_h} dp \frac{\partial}{\partial V_p}\left(\frac{V}{\gamma(p,V)}\right). \tag{A24}$$

We note that this equation is the integral form of the Maxwell relation from Eq. (A9), $(\partial(B_S/\gamma - P)/\partial P)_V = (\partial(V/\gamma)/\partial V)_P$. It does not depend on the P's being on particular curves; any two pressures would do. Combined with Eq. (A5) it does give us the sound speed along the Hugoniot in terms of the sound speed along the isentrope plus a term proportional to the offset $P_h - P_S$. We have a slowly-varying major term and a linearly-increasing minor term which combine (in view of the experimental result) to give a linear variation of sound speed with velocity. This is in contrast to Eq. (A19) where both u_s' and u_s'' are major players and switch roles as we move from the CJ state to an asymptotic linear $u_s(u)$. We then have:

$${}^Lc_h^2 = \frac{\rho\gamma_{gh}}{\rho_0^2}\left\{\frac{B_S(P_S,V)}{\gamma_{gS}} + (P_h - P_S) + \int_{P_S}^{P_h} dp \frac{\partial}{\partial V_p}\left(\frac{V}{\gamma(p,V)}\right)\right\}. \tag{A25}$$

A chain-law derivative for Eq. (A25) poses the inverse problem solved by Eq. (A14). From Eq. (2.5) we obtain:

$$\frac{dV}{du} = \frac{2\sqrt{(P_h - P_0)(V_0 - V)}}{P_h'(V_0 - V) - (P_h - P_0)} = -\frac{2V\rho_0 u_s}{B_h + B_{\rm ch}}. \tag{A26}$$

We could write down the complete equation for ${}^L c_h'$ by introducing a lot of γ-derivatives, but this is not particularly illuminating. We concentrate on the derivative at the CJ state. There, any term with $P_h - P_S$ as a factor will vanish because of the tangency of the isentrope and Hugoniot. The derivative of γ_{gh}/γ_{gS} has a factor $P_h' - P_S'$ and similarly vanishes. The only term contributing is $\rho B_S = -P_S'$. Then, from ${}^L c_h' = (dV/du)(d{}^L c_h/dV)$ we obtain at the CJ state (freely using ${}^L c = u_s = D$ and $B_h = B_{\rm ch} = B_S$):

$$2\,{}^L c_h' = (V_0/V)\frac{V^2 P_S''}{B_S} = \left(\frac{V_0}{V}\right)\left(1 + \frac{dB_S}{dP}\right). \tag{A27}$$

Eq. (A23) retains an explicit connection between the isentrope and Hugoniot that we lost in going to (A24). If we take the volume derivative of (A23) and use the simplifications at CJ we get a simple relation between the second derivatives of the isentrope and Hugoniot at the CJ state:

$$P_h'' = P_S'' / \left\{1 - \frac{\gamma}{2V}(V_0 - V)\right\}. \tag{A28}$$

If we apply the chain rule (A26) to Eq. (2.4) we obtain the general equation:

$$u_s'(u) = \frac{V_0\,(P_h' + (P_h - P_0)/(V_0 - V))}{P_h'(V_0 - V) - (P_h - P_0)} = \frac{V_0}{V_0 - V}\frac{B_h - B_{\rm ch}}{B_h + B_{\rm ch}}. \tag{A29}$$

A linear $u_s(u)$, where $u_s' = s$, a constant, describes many inert materials. This is clearly not the case for a OD Hugoniot, where $B_h = B_{\rm ch}$ at CJ and $u_s' = 0$ there; and then increases to an asymptotic value for the high-pressure range. If we apply the chain rule again we obtain:

$$uu_s'' = \frac{(\rho/\rho_0)B_{\rm ch}}{(B_h + B_{\rm ch})^3}\left\{4B_{\rm ch}V^2 P_h'' - \frac{2V}{V_0 - V}(B_h - B_{\rm ch})(3B_h + B_{\rm ch})\right\}. \tag{A30}$$

At CJ this reduces to:

$$uu_s'' = \frac{\rho}{2\rho_0}\frac{V^2 P_h''}{B_{\rm ch}}. \tag{A31}$$

This, in (A21), with the aid of (A28) and (A6) again leads to (A27).

For a linear $u_s(u)$, $P_h = \rho_0 c_0^2 \eta/(1 - s\eta)^2$, and we can evaluate $1 + dB_h/dP$, a measure of the curvature $P_h''(V)$ as:

$$1 + \frac{dB_h}{dP} = 4s\frac{(1 + s\eta/2)(1 - \eta)}{(1 + s\eta)(1 - s\eta)}. \tag{A32}$$

This "curvature" has the value $4s$ times a slowly-varying function of η. At the centering point $1 + dB_h/dP = 1 + dB_S/dP$ because of the second-order contact between the isentrope

and Hugoniot. We only have first-order contact at the CJ state. A linear $u_s(u)$, an initial porous-state, and an appropriate Grüneisen function works well (the snowplow model) for many materials, at least for higher pressures. In the high-pressure range the $u_s(u)$ for the porous media asymptotes to a line slightly below and parallel (*i. e.*, the same s) to the linear $u_s(u)$ for the solid material. A similar description is possible for an OD Hugoniot; one changes the E_0 for the centering point from its regular thermodynamic value just as one changed V_0 to represent a porous material. The OD Hugoniot would then asymptote to the base linear Hugoniot from above. Setting $1 + dB/dP$ constant is the basis for the Murnaghan family of equations of state. If this quantity is constant for detonation products and the reverse "snowplow" model is valid, the following relation is suggested between the slope of the measured sound-speed and the asymptotic s of the OD Hugoniot:

$$ {}^{L}c_h' \approx 2s(V_0/V)_{\rm cj}. \tag{A33}$$

We consider the relation between the slope of $c + u$ and ${}^{L}c$. From $c = (\rho_0/\rho){}^{L}c = (1 - u/u_s){}^{L}c$ we obtain:

$$ \frac{d(c+u)}{du} = 1 - \frac{u_s - uu_s'}{u_s^2}{}^{L}c + \frac{\rho_0}{\rho}\frac{d^{L}c}{du}. \tag{A34}$$

At CJ this reduces to

$$ \frac{d(c+u)}{du} = \frac{\rho_0}{\rho}\frac{d^{L}c}{du} = \frac{1}{2}\left(1 + \frac{dB_S}{dP}\right) \approx 2s. \tag{A35}$$

APPENDIX B: FITTING DATA WITH TWO DIMENSIONAL UNCERTAINTIES

The usual least-squares fit is made for measurements where the uncertainty in the independent variable x_i is negligible compared to that of the dependent variable y_i. In the case considered here the uncertainties are comparable for x_i and y_i. The case is further complicated by the important quantities being derived functions of x and y. Let $s(x, y)$ be the derived "independent" variable and $t(x, y)$ the derived "dependent" variable. Specifically, the two applications of these derivations will be for x, y, s, and t taking on the identities: (1) u_p, u_s, ρ, and P; (2) u_d, R, u_p, and ${}^{L}c$. We will use a superscript '0' to designate the "true value" of a measured quantity.

For a given measurement, we assume an uncorrelated normal distribution of the probability for achieving a given pair of measured values

$$ P(x, y) = \frac{1}{2\pi\sigma_x\sigma_y}\exp\Big[-\Big(\frac{(y-y^0)^2}{2\sigma_y^2} + \frac{(x-x^0)^2}{2\sigma_x^2}\Big)\Big], \tag{B1}$$

where the standard deviations obey the relations $\sigma_x^2 = \langle(x-x^0)^2\rangle$ and $\sigma_y^2 = \langle(y-y^0)^2\rangle$. The lack of correlation between x and y is given by $\langle(x-x^0)(y-y^0)\rangle = 0$. For the derived variables s and t, this is not necessarily the case and we assume a correlated normal distribution in two dimensions

$$P(s,t) = \frac{1}{2\pi\sigma_s\sigma_t\sqrt{1-r^2}} \exp\Big[\frac{-1}{1-r^2}\Big(\frac{(t-t^0)^2}{2\sigma_t^2} - r\frac{(t-t^0)(s-s^0)}{\sigma_s\sigma_t} + \frac{(s-s^0)^2}{2\sigma_s^2}\Big)\Big], \quad \text{(B2)}$$

where we have used r to designate the correlation coefficient instead of the more commonly used ρ in order to avoid confusion with the density. Again, the relevant terms can be extracted from averages over the distribution: $\sigma_s^2 = \langle (s-s^0)^2 \rangle$, $\sigma_y^2 = \langle (y-y^0)^2 \rangle$, and $\sigma_s\sigma_t r = \langle (s-s^0)(t-t^0) \rangle$.

We define $\delta x \equiv x - x^0$ and $\delta y \equiv y - y^0$. The lowest order terms in a Taylor-series expansion gives $\delta s = (\partial s/\partial x)\delta x + (\partial s/\partial y)\delta y$ and $\delta t = (\partial t/\partial x)\delta x + (\partial t/\partial y)\delta y$. It is straightforward to show that to lowest order

$$\sigma_s^2 = \langle \delta s^2 \rangle = \Big(\frac{\partial s}{\partial x}\Big)^2\sigma_x^2 + \Big(\frac{\partial s}{\partial y}\Big)^2\sigma_y^2, \quad \text{(B3)}$$

$$\sigma_t^2 = \langle \delta t^2 \rangle = \Big(\frac{\partial t}{\partial x}\Big)^2\sigma_x^2 + \Big(\frac{\partial t}{\partial y}\Big)^2\sigma_y^2, \quad \text{(B4)}$$

$$\sigma_s\sigma_t r = \langle \delta s \delta t \rangle = \Big(\frac{\partial s}{\partial x}\frac{\partial t}{\partial x}\Big)\sigma_x^2 + \Big(\frac{\partial s}{\partial y}\frac{\partial t}{\partial y}\Big)\sigma_y^2. \quad \text{(B5)}$$

Now we can turn around the meaning of Eq. (B1) and Eq. (B2) so that we define a new function where the experimental quantities are the independent variables. That is, given x and y (or s and t) then $P^0(x^0, y^0) = P(x, y)$ (or $P^0(s^0, t^0) = P(s, t)$) is the probability density that x^0 and y^0 (or s^0 and t^0) are the true values of the measured quantities.

Consider a function of the form $\xi(s; a_1, a_2, \cdots, a_n)$ where the a_i are parameters and for some choice of a_i's this function is a good approximation to the desired function $t^0(s^0)$. We can now construct the likelihood function L which is the probability density that a set of parameters a_i will give the true function for each data point.

$$L = \prod_{k=1}^{N} \frac{1}{2\pi\sigma_{s_k}\sigma_{t_k}\sqrt{1-r_k^2}} \exp\Big[\frac{-1}{1-r_k^2}\Big(\frac{(t-\xi(s_k^*))^2}{2\sigma_{t_k}^2} - r_k\frac{(t-\xi(s_k^*))(s-s_k^*)}{\sigma_{s_k}\sigma_{t_k}} + \frac{(s-s_k^*)^2}{2\sigma_{s_k}^2}\Big)\Big], \quad \text{(B6)}$$

where we have dropped the parameters from the notation for ξ for compactness. Contrary to a one-dimensional representation, the fitting function is not necessarily evaluated at the same value of s_k as measured in the experiment. The value of the independent variable s_k^* is treated as a parameter just like the a_i. The best choice of parameters is the one with maximum likelihood. This is equivalent to minimizing χ^2, twice the negative of the exponent in L,

$$\chi^2 = \sum_{k=1}^{N}\Big[\frac{1}{1-r_k^2}\Big(\frac{(t-\xi(s_k^*))^2}{\sigma_{t_k}^2} - 2r_k\frac{(t-\xi(s_k^*))(s-s_k^*)}{\sigma_{s_k}\sigma_{t_k}} + \frac{(s-s_k^*)^2}{\sigma_{s_k}^2}\Big)\Big]. \quad \text{(B7)}$$

Minimization of χ^2 with respect to the s_k^* (*i. e.* $\partial\chi^2/\partial s_k^* = 0$), gives a generalized distance of closest approach between the fitting function and the data point. For our nonlinear choice

of ξ, both sets of parameters could be determined by a numerical search for the minimum of χ^2 given in Eq. (B7).

Another approach involves the transformation of Eq. (B7) into the form of the more common least-squares method with uncertainties only in the dependent variable. The only approximation involved is that each s_k^* is close enough to the corresponding s_k to truncate a Taylor series expansion after the linear term. That is,

$$t_k^* \doteq \xi_k + \xi_k'(s_k^* - s_k), \tag{B8}$$

where $\xi_k = \xi(s_k)$, $\xi' = d\xi/ds$, and $\xi_k' = \xi'(s_k)$. Let us define reduced variables $\theta_k = (t_k - t_k^*)/\sigma_{t_k}$ and $\eta_k = (s_k - s_k^*)/\sigma_{s_k}$. The kth term in Eq. (B7) (and the only term depending on s_k^*) is then

$$\chi_k^2 = \frac{1}{1-r_k^2}(\theta_k^2 - 2r_k\theta_k\eta_k + \eta_k^2). \tag{B9}$$

Using Eq. (B8), we obtain the reduced variable form $\theta_k = A_k + B_k\eta_k$ where $A_k \equiv (t_k - \xi_k)/\sigma_{t_k}$ and $B_k \equiv \xi'\sigma_{s_k}/\sigma_{t_k}$. Setting $\partial\chi^2/\partial\eta = 0$ we have

$$\eta_k = A_k\Big(\frac{r_k - B_k}{B_k^2 - 2r_kB_k + 1}\Big) = A_kC_k, \tag{B10}$$

where C_k is defined as the term in parenthesis. Note that A_k is a factor of both η_k and consequently θ_k. We can now rewrite Eq. (B9) as

$$\chi_k^2 = A_k^2D_k^2 = \Big(\frac{t_k - \xi_k}{\sigma_{t_k}}\Big)^2 D_k^2, \tag{B11}$$

where $D_k^2 = (1 + B_kC_k)^2 - 2r_kC_k(1 + B_kC_k) + C_k^2$. If we now define σ_k^2 as

$$\sigma_k^2 = \sigma_{t_k}^2(1 - r_k^2)/D_k^2, \tag{B12}$$

then χ^2 becomes

$$\chi^2 = \sum_{k=1}^{N} \frac{(t_k - \xi_k)^2}{\sigma_k^2}, \tag{B13}$$

which is the standard form for the usual case of one-dimensional error bars. There is a weak dependence of σ_k on the fitting form that enters through the factor ξ_k' in B_k.

The first application of these derivations will be for x, y, s, and t taking on the identities u_p, u_s, ρ, and P respectively. From the Hugoniot jump conditions, $\rho = \rho_0/(1 - u_p/u_s)$ and $P = \rho_0u_su_p$. Evaluating Eq. (B3), Eq. (B4), and Eq. (B5), we have simple analytic expressions for this case.

$$(\sigma_P/P)^2 = (\sigma_{u_p}/u_p)^2 + (\sigma_{u_s}/u_s)^2, \tag{B14}$$

$$\frac{\sigma_\rho}{\rho} = \frac{\sigma_P}{P}\Big(\frac{u_p/u_s}{1 - u_p/u_s}\Big), \tag{B15}$$

TABLE VI. One and Two Dimensional Error Estimates for $P(\rho)$

ρ_0 (g/cm^3)	u_p (km/s)	σ_{u_p}/u_p	u_s (km/s)	σ_{u_s}/u_s	P (GPa)	σ_P/P	ρ (g/cm^3)	σ_ρ/ρ	r	σ_k/P
1.837	2.655	0.005	8.879	0.006	43.3	.0078	2.62	.0033	-.180	.0140
1.835	2.996	0.005	9.108	0.005	50.1	.0071	2.73	.0035	0	.0129
1.836	3.429	0.005	9.420	0.005	59.3	.0071	2.89	.0041	0	.0144
1.836	3.485	0.005	9.458	0.0085	60.5	.0099	2.91	.0058	-.486	.0242
1.836	3.754	0.005	9.654	0.005	66.5	.0071	3.00	.0045	0	.0156
1.840	4.114	0.017	10.087	0.005	76.4	.0177	3.11	.0122	+.841	.0248
1.835	4.206	0.005	10.112	0.005	78.0	.0071	3.14	.0051	0	.0171
1.834	4.601	0.005	10.424	0.005	88.0	.0071	3.28	.0056	0	.0187
1.834	4.671	0.005	10.495	0.005	89.9	.0071	3.30	.0057	0	.0189
1.832	4.673	0.005	10.543	0.0068	90.3	.0084	3.29	.0067	-.298	.0247

TABLE VII. One and Two Dimensional Error Estimates for ${}^Lc(u_p)$

u_d (km/s)	σ_{u_d}/u_d	R	σ_R/R	${}^Lc$ (km/s)	$\sigma_{{}^Lc}/{}^Lc$	u_p (km/s)	σ_{u_p}/u_p	r	$\sigma_k/{}^Lc$
3.69	0.033	17.20	0.052	10.52	0.010	2.74	0.034	0.451	0.021
4.29	0.014	13.08	0.022	11.42	0.006	3.19	0.014	0.524	0.009
4.69	0.006	10.49	0.016	12.40	0.005	3.49	0.006	0.318	0.006
4.85	0.025	9.64	0.041	12.87	0.016	3.60	0.025	0.461	0.018
5.49	0.009	8.61	0.020	13.99	0.009	4.08	0.009	0.374	0.009
5.55	0.018	8.76	0.019	13.95	0.010	4.12	0.018	0.662	0.011
6.34	0.024	7.47	0.023	15.79	0.015	4.70	0.024	0.673	0.014

$$r = \frac{(\sigma_{u_p}/u_p)^2 - (\sigma_{u_s}/u_s)^2}{(\sigma_{u_p}/u_p)^2 + (\sigma_{u_s}/u_s)^2}. \tag{B16}$$

Note that $r = 0$ if the relative standard deviations for u_p and u_s are the same. From the fit to the Hugoniot, we know that $d\ln P/d\ln\rho$ is about 3.1 which leads to $B_k \approx 3.1(u_p/u_s)/(1-u_p/u_s)$. The effective one-dimensional standard deviation is then readily evaluated. Results are given in Table VI.

The other relevant application will be for x, y, s, and t taking on the identities u_d, R, u_p, and ${}^Lc$, respectively. In this case, there is no simple analytic representation of the relevant quantities. Instead, numerical derivatives are evaluated at the experimental values of u_d and R. The resulting error estimates are given in Table VII.

APPENDIX C: DATA FITTING WITHOUT A FUNCTIONAL FORM

Least-squares fitting of data is often done by assuming a particular functional form and optimizing with respect to its parameters. In examining a property of the determined function (such as its derivative) it may be unclear whether the property is strongly related

to the data or is principally a result of the assumed functional form. To circumvent this uncertainty, least-squares can be done with functions that have no particular functional form, for instance cubic splines are commonly used. Another choice, which is used here, is to represent the fitting function as a uniformly-spaced table which is interpolated by a local cubic Lagrange polynomial. The functional values of the table are then the parameters of the fitting function. Smoothness of the fitting function is induced by adding to the merit function a weighted sum of squares of the n^{th} order forward-difference operator over the domain of the table. Let $\{x_i, y_i\}$ be the data set and $\{t_i, f_i\}$ be the table where t_i are uniformly spaced over the interval $\min\{x_i\}$ to $\max\{x_i\}$. Let $F(x)$ be the local central-interval cubic Lagrange interpolation polynomial for the table $\{t_i, f_i\}$. Then the merit function for optimization is:

$$\mathcal{E} = \sum_{i=1}^{n_{\text{data}}} \left(F(x_i) - y_i\right)^2 + wt \sum_{i=1}^{m_{\text{table}}} \left(\Delta^n f_i\right)^2 . \tag{C1}$$

The normal equations are then:

$$\frac{\partial \mathcal{E}}{\partial f_i} = 0, \quad \text{for} \quad i = 1, m_{\text{table}}. \tag{C2}$$

Because the optimizing parameters are the f_i's, which are local function-values and thereby are directly associated with the residuals of the least-squares, the so determined function is highly dominated by the data and gives residuals randomly distributed about zero.

The derivative table $\{t_i, f_i'\}$ is calculated from the $\{t_i, f_i\}$ table by using a running 4^{th}-degree polynomial about central points. A table $\{t_i, f_i''\}$ is constructed similarly from $\{t_i, f_i'\}$.

REFERENCES

[1] R. G. McQueen *et al.*, in *High-Velocity Impact Phenomena*, edited by R. Kinslow (Academic Press, New York, New York, 1970), Chap. 7.

[2] W. Fickett and W. C. Davis, *Detonation, Los Alamos Series in Basic and Applied Sciences, David H. Sharp and L. M. Simmons Jr., editors* (University of California Press, Berkeley, California, 1979).

[3] T. R. Gibbs *et al.*, in *LASL Explosive Property Data, Los Alamos Series in Dynamic Material Properties*, edited by T. R. Gibbs and A. Popolato (University of California Press, Berkeley, CA, 1980), p. 109.

[4] In the direct-impact technique one essentially just removes the base plate. Additional constructional material may be added to hold the samples in place and may affect the analysis of the resulting time measurements, but the important feature is to have the flyer directly impact the unknown sample.

[5] J. B. Ramsay and A. Popolato, in *Fourth Symposium (International) on DETONATION*, U. S. Naval Ordnance Laboratory (U. S. Government Printing Office, Washington, D. C., 1965), pp. 233–238.

[6] J. N. Johnson, P. K. Tang, and C. A. Forest, J. Appl. Phys. **57**, 4323 (1985).

[7] W. C. Davis, Phys. Fluids **22**, 1407 (1979).

[8] J. H. Kineke, Jr. and C. E. West, Jr., in *Fifth Symposium (International) on DETONATION*, U. S. Naval Ordnance Laboratory (U. S. Government Printing Office, Washington, D. C., 1970), pp. 533–546.

[9] L. Green, E. Lee, A. Mitchell, and C. Tarver, in *Eighth Symposium (International) on DETONATION*, Office of Naval Research NSWC MP 86-194, edited by J. M. Short (Naval Surface Weapons Center, White Oak, Maryland, 1985), pp. 587–595.

[10] R. G. McQueen, J. W. Hopson, and J. N. Fritz, Rev. Scient. Instr. **53**, 245 (1981).

[11] For the case of explosive on bromoform a reflected shock occurs when the overdrived detonation strikes the interface and we indeed have a finite number of waves. If a release should occur a fan will go back into the unknown material and the overtaking wave will have a curved section. However, we can approximate this fan by n wavelets. For fixed n we can apply the preceding argument and prove linearity. This is true for any n, and so we conclude that even in the limit, where the release has a curved section, we still have linearity.

[12] J. N. Fritz, C. E. Morris, R. S. Hixson, and R. G. McQueen, in *High-Pressure Science and Technology—1993*, No. 309 in *AIP Conference Proceedings*, American Institute of Physics, edited by S. C. Schmidt, J. W. Shaner, G. A. Samara, and M. Ross (AIP Press, New York, 1994), pp. 149–152.

[13] L. G. Green, C. M. Tarver, and D. J. Erskine, in *Ninth Symposium (International) on DETONATION*, Office of Naval Research OCNR 113291-7, edited by W. J. Morat (Office of Naval Research, Arlington, Virginia, 1989), pp. 670–682.

[14] J. B. Bdzil, J. Fluid Mech. **108**, 195 (1981).

[15] C. E. Morris, J. N. Fritz, and R. G. McQueen, J. Chem. Phys. **80**, 5203 (1984).

[16] J. N. Johnson, R. S. Hixson, G. T. Gray, III, and C. E. Morris, J. Appl. Phys. **72**, 429 (1992).

[17] R. S. Hixson, R. G. McQueen, and J. N. Fritz, in *High-Pressure Science and Technology—1993*, No. 309 in *AIP Conference Proceedings*, American Institute of

Physics, edited by S. C. Schmidt, J. W. Shaner, G. A. Samara, and M. Ross (AIP Press, New York, 1994), pp. 105–108.
[18] A. W. Campbell and R. Engelke, in *Sixth Symposium (International) on DETONATION*, Naval Surface Weapons Center, Office of Naval Research—Dept. of Navy, edited by D. J. Edwards (U. S. Government Printing Office, Washington, D. C., 1976), pp. 642–652.
[19] J. Mathews and R. L. Walker, *Mathematical Methods of Physics*, 2nd ed. (W. A. Benjamin, Inc., Menlo Park, California, 1970).
[20] W. H. Press, B. P. Flannery, S. A. Teukolsky, and W. T. Vetterling, *Numerical Recipies: The Art of Scientific Computing* (Cambridge Univ. Press, Cambridge, 1986).
[21] R. Menikoff and B. J. Plohr, Rev. Mod. Phys. **61**, 75 (1989).
[22] W. E. Deal, J. Chem. Phys. **27**, 796 (1957).
[23] W. E. Deal, Phys. Fluids **1**, 523 (1958).
[24] J. C. Cost, H. C. Hornig, and J. W. Kury, Technical Report No. UCRL 50645, Laurence Livermore National Laboratory, Livermore, CA (unpublished).
[25] R. L. Jameson and A. Hawkins, in *Fifth Symposium (International) on DETONATION*, Office of Naval Research ACR-184 (U. S. Government Printing Office, Washington, D. C., 1970), pp. 23–29.
[26] W. C. Davis, in *Sixth Symposium (International) on DETONATION*, Office of Naval Research ACR-221 (U. S. Government Printing Office, Washington, D. C., 1976), pp. 637–641.
[27] An electromagnetic u_p measuring technique using a thin embedded aluminum foil.
[28] K. Burrows *et al.*, in *Sixth Symposium (International) on DETONATION*, Office of Naval Research ACR-221 (U. S. Government Printing Office, Washington, D. C., 1976), pp. 625–636.
[29] W. C. Davis and J. B. Ramsay, in *Seventh Symposium (International) on DETONATION*, Office of Naval Research NSWC MP 82-334, edited by J. M. Short (Naval Surface Weapons Center, White Oak, Maryland, 1981), pp. 531–539.
[30] E. Lee *et al.*, in *Eighth Symposium (International) on DETONATION*, Office of Naval Research NSWC MP 86-194, edited by J. M. Short (Naval Surface Weapons Center, White Oak, Maryland, 1985), pp. 613–624.
[31] E. A. Guggenheim, *Thermodynamics, An Advanced Treatment for Chemists and Physicists*, 2nd ed. (North-Holland Publishing Company, Amsterdam, 1950).
[32] R. Courant and K. O. Friedrichs, *Supersonic Flow and Shock Waves, Pure and Applied Mathematics* (Interscience Publishers, Inc., New York, New York, 1948).

VI.

JOURNAL OF CHEMICAL PHYSICS 101 (12),

15 DECEMBER 1994

Chemical dimerization of crystalline anthracene produced by transient high pressure

Ray Engelke and Normand C. Blais
Los Alamos National Laboratory, Los Alamos, New Mexico 87545

(Received 1 August 1994; accepted 7 September 1994)

We report the production of a chemically bound dimer of anthracene produced by the shock compression of crystalline anthracene. The experimental probe used to detect the dimer structure was time-of-flight (TOF) mass spectrometry. The principal method used to produce the shock compression was the impact of electrically accelerated flyers ("slappers") with the surface of the anthracene crystals. Our work correlates well with earlier experimental and theoretical work concerning chemical processes that can occur in pressurized anthracene and other aromatic materials. We briefly review the earlier work. The anthracene crystals were shocked to various pressures in the interval 9 to 22 GPa. Also various crystal thicknesses were employed; this allowed us to control the time interval over which various anthracene "particles" in the crystal were held at high pressure and temperature. At a pressure of ~22.1 GPa we observe dimer formation in 20 ns or less. For a shock pressure of 9 GPa no dimer is produced, whereas for shock pressures of 18.4 GPa or higher dimer production is always observed. Under some conditions significant conversion of monomer to dimer is seen (up to a conversion of over 50%). A remarkably simple experimental observation is that the *only* new chemical species observed in the experiments at 18.4 GPa and higher is the dimer species. We present evidence that the dimerization is the result of a pressure-driven Diels–Alder reaction and that such reactions are characteristic of materials containing aromatic rings when they are shocked to high pressure.

I. INTRODUCTION

Pressure-induced chemical reactions, though they are of considerable interest, remain more difficult to study than chemical reactions produced thermally; this is particularly true of pressure-driven reactions produced by transient high pressure. The occurrence of chemical reactions produced by transient high pressure can sometimes be detected mechanically. However, in such cases, the nature of the underlying microscopic events are usually only inferred and not determined by direct measurement. In the experiments to be described here, we show that the appearance of a dimer of anthracene coincides with the shock-wave-induced changes in the pressure-volume response of anthracene observed in mechanical (shock-wave) experiments. Furthermore, we will argue from the experimental conditions present in our shock-wave experiments that the dimer being observed is chemically bound and is not a van der Waals dimer.

Dick[1] and Warnes[2] made thorough shock-wave studies of certain alkanes, cycloalkanes, cycloalkenes, and arene structures; their data show that the arene structures studied exhibit qualitatively different behavior from the other molecular forms under shock loading. A salient result of their work is that the Hugoniots (see below) of the aromatic (arene) structures examined show prominent evidence of the occurrence of a rate phenomenon (e.g., a chemical reaction), while the Hugoniots of the other substances studied do not.

After this experimental evidence was discovered, theoretical observations were put forward as to the microscopic nature of this rate phenomenon in the aromatic materials. For example, Pucci and March[3] presented a phenomenological model in support of the rate process being due to aromatic-ring *pi* bonds being converted to interring sigma bonds. This idea was pursued further in theoretical quantum-chemical studies in which the energetics of such cross-linked structures were examined quantitatively.[4,5] In particular, in Ref. 5(b), it was suggested that the likely pressure-driven reaction mirrored in the Hugoniot behavior of the aromatics is a [4+2] symmetry-allowed Diels–Alder cross linking between the aromatic rings.

There is a body of static high-pressure work that bears on the present study. The work of Drickamer and his coworkers is noteworthy—see Ref. 6 and references therein. These workers suggested early on, on the basis of the static high-pressure experiments, that aromatic structures can undergo interring cross linking under pressure.

Below, we present direct-microscopic experimental evidence that the rate behavior observed on the anthracene Hugoniot is due to chemical interring cross linking of two anthracene molecules, i.e., dimer production. Furthermore, within the sensitivity of our experiments, dimers are the only new chemical species that we observe. Considering the harshness of the physical environment produced by the shock waves this is a remarkably simple result.

The remainder of this article is arranged as follows: Sec. II is a brief review of earlier relevant shock-wave and static high-pressure experimental data and of the previously proposed theoretical explanations of the experimental findings; Sec. III is a discussion of the experimental methods and apparatus used in our experiments; in Sec. IV, we examine and analyze our experimental results; Sec. V contains a summary of what has been found, comments on the generality of the findings, and suggestions on possible future work, and finally, in the Appendix, we propound a simple statistical-

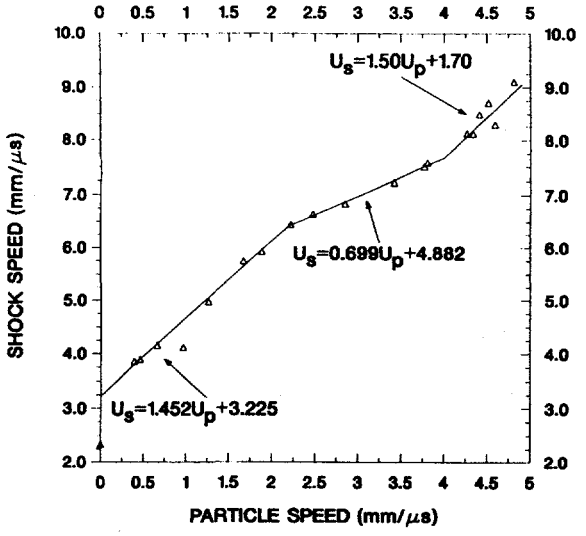

FIG. 1. Warnes' measured $U_s - u_p$ Hugoniot for anthracene. The slope-intercept values shown for the third branch are slightly different from those of Warnes; this change was made to get reasonable behavior in the corresponding region of the P-v plane (see Fig. 2); i.e., v decreases as P increases.

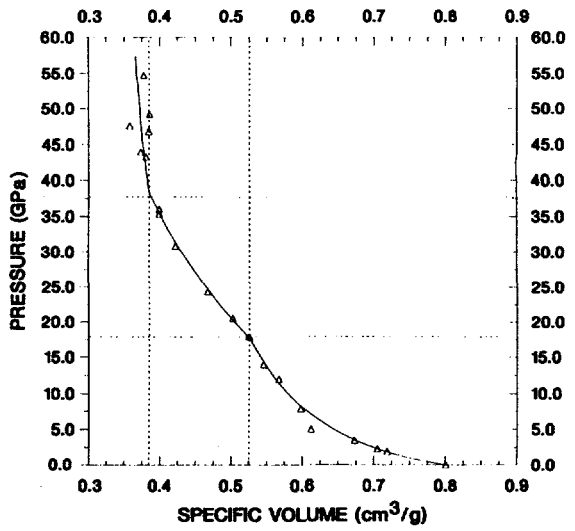

FIG. 2. The pressure/specific-volume (P,v) Hugoniot of anthracene as obtained from Warnes' $U_s - u_p$ data. The points of slope discontinuity are at [P(GPa), v(cm^3/g)] (17.1,0.53) and (38.4,0.38), respectively.

mechanical model of the relative amount of the monomer reactant and dimer product present as a function of pressure. This simple model casts some light on why the shock-wave data show such sharp changes in character as a function of pressure.

II. BACKGROUND

A. Shock-wave studies

Dick[1] and Warnes[2] experimentally obtained the principal shock Hugoniots of the ring structures benzene, toluene, anthracene, phenanthrene, pyrene, 1,3- and 1,4-cyclohexadiene, cyclohexene, and cyclohexane up to pressures of ~40 GPa. Five of these ring structures contain aromatic rings. The principal Hugoniot of a material is the locus of all thermodynamic state points reachable by a single-shock process from ambient conditions.[7,8] In their shock-wave experiments, six of the nine materials were initially in the liquid state; the three exceptions being anthracene, phenanthrene, and pyrene. The latter three materials were initially polycrystalline solids essentially pressed to crystal density. Their shock-wave experiments measured the relationship between the shock speed (U_s) in a material as a function of the particle speed (u_p) behind the shock. Figure 1 shows this measured relationship for anthracene.

Given the values of U_s, u_p, and the initial mass density (ρ_0) of a substance, one can derive the pressure/specific-volume form of its Hugoniot via the conservation of mass and momentum relations.[7,8(a)–8(c)] Figure 2 shows this relationship for anthracene. Note that in both Figs. 1 and 2 there is evidence of two points where the functions have discontinuities in slope. Such discontinuities are evidence that a rate phenomenon is occurring at the microscopic level; see, e.g., Duvall and Graham's review of phase transitions under shock loading.[9]

The observation of Dick and Warnes of primary interest here is that *all* five of the molecular species studied that contain aromatic rings show this discontinuity behavior and that the four other species without aromatic rings do *not*. This points to a common underlying chemical reaction that the aromatic structures are susceptible to, but which does not occur under the same physical conditions in the other ring structures. Dick[1] observed for benzene, on the basis of electrical conductivity measurements, that this rate process equilibrates "instantaneous(ly)"—instantaneously in this context means ≤ 1 μs. The relative mass density change in anthracene due to the rate process is ~20%. Interestingly, the crystal volume of anthracene decreases by ~20% (at ambient pressure) when the material is photodimerized.[10] Warnes[2] recovered anthracene that had been shocked above the first slope discontinuity (see Figs. 1 and 2) and found by mass spectroscopy and chromatography evidence that "seem(ed) to indicate that at least some of the (recovered) material maintains its anthracene bonding." He found some material with mass of 354 amu; an anthracene dimer has mass of 356 amu. He did not rule out cross linking and pointed out that "the chaotic conditions to which the sample was exposed (after shocking) might very well have disturbed initially cross-linked material."

One further point is that Nellis *et al.*[11] have shocked benzene to over 71 GPa and found no further slope discontinuities on its Hugoniot; this indicates there are no further rapid changes in chemical composition in benzene above the second cusp in its Hugoniot (at ~19 GPa)—at least up to 71 GPa.

In contrast to the evidence for a chemical reaction in the aromatics, Dick found no evidence of rate processes in the principal Hugoniots of the nonaromatic ring structures listed above up to pressures of ~43 GPa.

These observations suggest that it is the number and arrangement of the ring pi bonds in the cyclic structures that

determine whether a chemical rate process occurs. A correlated property is the planarity of the aromatic ring systems; this planarity may be sterically helpful in promoting the observed reaction.

B. Static high-pressure studies

Drickamer and his co-workers[6,12,13] studied the behavior of the aromatics pentacene, hexacene, and violanthrene under static high pressure up to ~30 GPa. They found evidence of irreversible reaction at pressures of ~20 GPa and ambient temperature or lower. Optical spectroscopy of their reaction products showed that the absorption peaks due to the lowest energy pi transitions of the reactants (characteristic of the original largest set of connected aromatic rings) were nearly absent, but that the peak at 280 nm (characteristic of all aromatic compounds) was essentially unaffected. They interpreted this as evidence of chemical cross linking between molecules due to intraring pi bonds becoming interring sigma bonds.

Murphy and Libby[14] statically compressed solid polycrystalline anthracene to 5.8 GPa at ambient temperature and below. They found, via mass spectroscopy, evidence of cross-linked dimers, including one at 356 amu. The yields of all the cross-linked species were very low under their experimental conditions. Their most interesting result was that the *rate* of the dimerization reactions had an inverse dependence on temperature. That is, increasing the temperature decreased the reaction rate. They interpreted this to mean that the activation volume of the reaction was sufficiently large (and negative) that the pressure/activation volume product dominated the activation-energy term in the activation enthalpy (see the Appendix).

We do not review high-temperature static high-pressure work here as such conditions seem to lead to a manifold of reaction products; for a discussion of such work see Refs. 4 and 15 and references therein.

C. Theoretical studies

Pucci and March[3] put forward a quantitative theoretical model of the Hugoniot results reviewed above. This model casts some light on the rate process regions on the arene Hugoniots and its absence from those of the other cyclic species. Their model is a quantified form of the idea that, at sufficiently high pressures, the out-of-plane pi bonds on the aromatic rings overlap sufficiently to cause bonding between rings. Using this model, they succeeded in giving fairly quantitative representations of the high-pressure sections of the aromatic Hugoniots.

Engelke and his co-workers[4,5] studied aromatic-ring cross-linking reactions between a pair of benzene rings using semiempirical and *ab initio* quantum-chemical methods. These calculations produced information on the stability, geometries, and energetics of a number of cross-linked benzene dimers. These results are applicable to larger aromatic structures than benzene, provided only one aromatic ring per molecule is involved in the cross-linking reaction. The calculations rule out a number of cross-linked benzene dimer isomers based on the internal energy change that a shock to the first cusp point on the benzene Hugoniot can produce. They suggested that the likely dimer isomer being produced in the high-pressure process is the result of a Diels–Alder reaction; this reaction involves the formation of sigma bonds between the "end" carbons of one benzene ring to the "center" carbons of a second ring. The resultant dimer is a 1,4-cyclohexadiene cross-linked to 1,3-cyclohexadiene.[5(b)] These results suggest that in the present work, we are seeing a dimer that similarly cross links anthracene.

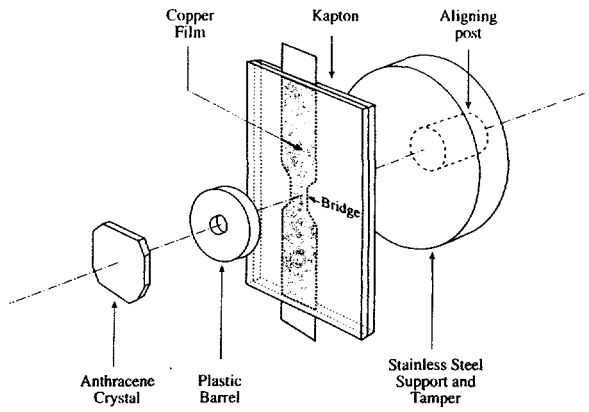

FIG. 3. An exploded schema of a shot assembly showing its various components. The slapper's copper bridge is 3 mm wide, 3 mm high, and has a thickness of 0.7 mils. The barrel hole diameter is 3 mm, and the barrel length (i.e., thickness) is determined by the desired impact pressure as discussed in the text. The kapton "flyer" film is 3 mils thick. Upon discharge of the 12 μf capacitor unit, the typical maximum current through the bridge is 60 kA, about 1/4 μs after being triggered, when the capacitor was charged to 7.5 kV. The voltage drop across the bridge is 9.7 kV.

Ree[16] put forward a theoretical model of the hydrocarbon Hugoniots based in statistical mechanics. The central hypothesis of his work is that hydrocarbons at pressure and temperature greater than 10 GPa and 1000 K "dissociate into carbon in the diamond phase and hydrogen in a condensed molecular phase." The work cited above and what we describe below implies an alternative and simpler mechanism for aromatic materials.

III. EXPERIMENTAL METHODS

A. Pressurization of the anthracene crystals

We used "slapper" detonators[17] to produce the high pressure in the experiments to be discussed in Sec. IV. A slapper detonator is a thin piece of plastic film driven to high speed by electrically vaporizing a thin layer of metal (a "bridge") in contact with the plastic (see Fig. 3).

A slapper detonator is a form of electrical gun in which one can control the flyer's speed by varying the distance of flight before collision with the target (i.e., by controlling the gun's barrel length).

To determine the pressure produced in the anthracene quantitatively we needed to know the functional dependence between the kapton flyer's speed and the barrel length. This relationship was obtained by use of a velocity interferometer system for any reflector ("visar") apparatus.[18] Figure 4 is the measured speed of one of our slapper flyers obtained *from a*

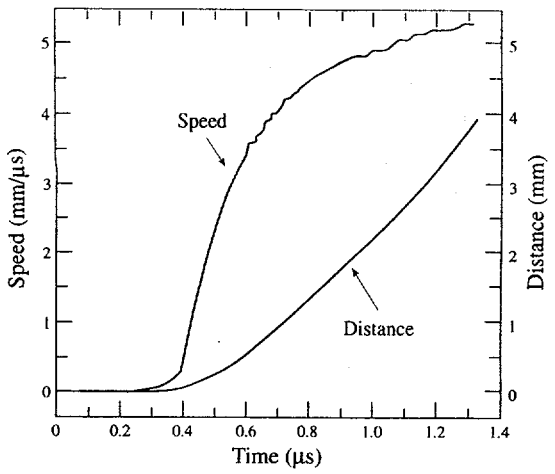

FIG. 4. Experimental visar velocity and trajectory records. The fine structure on the velocity history is reproducible; this structure is due to the compression/rarefaction wave structure in the kapton produced by the high-pressure copper plasma. The reproducibility of this structure is an indication of the precision of the visar experiment and the slapper's acceleration history.

visar experiment; one curve in Fig. 4 is the measured speed and the second curve is the time-integrated speed, i.e., the flyer trajectory. The abscissa of Fig. 4 is the flyer's time of flight referred to an arbitrary time origin. This experiment is very reproducible, e.g., even the small ripples in speed seen on the record in Fig. 4 are reproduced on nominally identical experiments.

Given the speed of the kapton flyer when it impacts the anthracene as obtained from a visar experiment, one can determine the pressure generated by the resultant shock wave propagated into the anthracene. It is possible to do this if the principal Hugoniots of anthracene and kapton and the "reflected" Hugoniot of kapton are known. The principal Hugoniots have been measured with standard shock-wave experiments.[8(a)–8(c)] The shock response of the kapton[8(b),8(c)] due to its collision with the anthracene is defined by its reflected shock Hugoniot(s). The reflected shock Hugoniot of a material can be obtained from its principal Hugoniot by reflecting the principal Hugoniot curve about an axis such that the u_p value of the reflected curve at $P=0$ is equal to the speed of the "flying" material before the collision. The pressure induced by the collision of the kapton with the anthracene can be obtained by requiring equality of particle speed and pressure at the kapton/anthracene contact surface. This is done quantitatively by finding the point where the anthracene principal and appropriate kapton reflected Hugoniot cross. The collision produces two shock waves of this pressure that propagate into the kapton and anthracene. By varying the barrel length, and consequently the kapton flyer speed, we could "dial" in the pressure introduced into the anthracene.

B. The apparatus

The mass spectrometer apparatus used for this work has been described elsewhere.[19(a),19(b)] The main difference between our usage here and that described in Ref. 19(a) is that anthracene crystals replaced the explosive pellets on the slapper. Also, the slappers used in this study were considerably more robust and required over 100 times more energy, i.e., 336 J.

In contrast to the studies for which the apparatus was originally designed, namely examining the products of detonating explosives, no exoergic processes are expected to occur when we shock anthracene crystals. Therefore, the products that result from shocking an anthracene crystal will not have the velocities characteristic of explosive materials. However, we found that a considerable amount of anthracene arrived at the mass spectrometer ionizer with velocities sufficiently high that, as in the detonation studies, we required using dual multichannel plate detectors and ion-deflector voltages to investigate the full time dependence of the mass spectrum as described in Ref. 19(a). The fastest of the anthracene monomers (mass 178) detected have molecular speeds of 9 km/s. Some of the dimers are measured to have speeds of 7 km/s. These high molecular velocities are found when thin crystals are mounted on our longest barrels. At 7 km/s, the dimer molecule has a kinetic energy of almost 90 eV when it enters the ionizer. A summary of the experimental parameters is provided in Table I.

Because anthracene has a complex electron impact cracking pattern in our mass spectrometer, it was advisable to obtain a mass spectrum of the unshocked material for comparison with the shocked spectra. We did this by using a nozzle expansion of anthracene vapor seeded into helium carrier gas. A heated source was installed with a 1/8 mm diam nozzle 1 cm in front of the skimmer. With anthracene vapor at 110 °C and a helium pressure of 7 kPa about 1200 scans produced a low noise spectrum. The mass range 1–200 amu is shown in Fig. 5.

C. Shot assembly details

The copper-bridge/kapton slapper units shown in Fig. 3 were constructed and provided to us by the detonator group (DX-10) at LANL. The slapper and plastic barrel were glued to the stainless-steel support and tamper using jigs to ensure that the center of the bridge and the hole in the barrel are precisely aligned with the indicated center line. Then the crystal was glued onto this assembly.

We grew all the anthracene crystals out of acetone solutions. The materials used were Aldrich 99% pure protonated and 98% pure deuterated anthracene and Baker acetone of 99.7% purity. The resultant crystals were typically irregular quadrahedrons with sides ~3 to 4 mm long and ~10 to 25 mils thick (i.e., platelets). The crystals used in the experiments were carefully selected for optical clarity and uniformity of thickness. When particularly thin crystals were required thick crystals were cleaved with a razor blade. The thickness of the crystals for each shot is listed in Table I.

We had found in our early experiments that a large amount of anthracene monomer was usually observed, but only a small amount of dimer. If we increased the amplifier gain to increase the dimer signal, the monomer signal was off scale. To circumvent this problem we utilized crystals grown from acetone solutions containing 90/10 wt. % H/D

TABLE I. Shot parameters.

Paper number	Shot number	Barrel length (mils)	Crystal thick. (mils)	Mono. appear. scan No.	Dimer appear. scan No.	Number[b] density ratio	Scaled[c] density ratio	Input press. (GPa)
1	101993f	10	13	24	···	0.0	0.0	9.0
2	101993g	10	13	21	···	0.0	0.0	9.0
3	101993h	52	11	14	20	0.015	0.029	18.4
4	101993i	53	10	13	17	0.030	0.057	18.5
5	101993j	74	11	12	18	0.039	0.074	19.8
6	101993k	72	12	12	20	0.140	0.245	19.6
7	101993e	~120	23	15	47	0.135	0.239	~22.1
8	093093c	~120	21	15	45	0.131	0.232	~22.1
9	093093d	~120	19	13	37	0.346	0.515	~22.1
10	101993d	123	19	15	?[d]	?[d]	?[d]	22.2
11	093093e	~120	16	13	16	0.047	0.090	~22.1
12	093093f	~120	15	14	18	0.007	0.015	~22.1
13	101993b	124	14	15	20	0.018	0.036	22.3
14	101993c	124	14	13	18	0.013	0.027	22.3
15	093093g	~120	13	13	17	0.029	0.056	~22.1
16	101993m	123	11	12	16	0.010	0.019	22.2
17	101993l	121	4	13	18	0.020	0.040	22.1

[a]All crystals were 90/10 H/D wt. % anthracene.
[b]Maximum dimer intensity observed.
[c]Scaled maximum dimer intensity observed.
[d]Spectra intensity is very low, including the monomer peak; thus, the dimer may be unobservable due to the low overall intensity.

anthracene. The presence of the 10 wt. % deuterated anthracene monomer spectra allowed us to compute the intensity of the off-scale protonated monomer peak. Thus, we could still quantitatively estimate the dimer/monomer ratio.

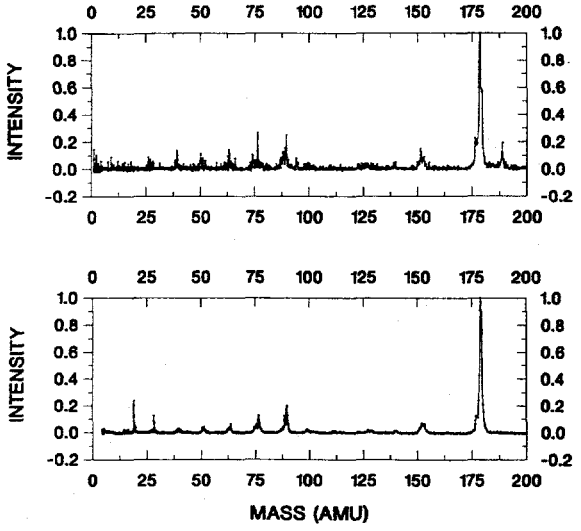

FIG. 5. The lower panel is the mass spectrum of unshocked anthracene in the mass range 1 to 200 amu. It was obtained by (1) thermally evaporating anthracene powder at 110 °C, (2) seeding the vapor into He gas at 7 kPa, and (3) expanding the resultant mixture from a nozzle at 250 °C. The upper panel is the mass spectrum in the same range obtained from a single scan of shocked anthracene (shot No. 101993e scan 61). This shot and scan were selected because of the similarity of the total intensity of signal and because some dimers were also present in the spectrum.

D. Numerical techniques used to analyze the mass spectra

Because of geometrical and electro-optical effects associated with the mass spectrometer, a deconvolution function had to be applied to the raw data in order to compare intensities at different masses and scans within one shot and from shot to shot. The deconvolution function was obtained by calibrating a functional form incorporating the known physical characteristics of the system (e.g., detector shape and size) with experimental data.[19(a)] Division of our raw data by this function produced a new set of intensities that could be compared on an equal footing (see, e.g., Figs. 6 and 7). We believe that this deconvolution function is accurate to ±20% wherever the sensitivity function is greater than 0.5.

The intensities listed in Table I were obtained from the deconvolved intensity spectra by integration. The intensity integrations were carried out for the deuterated monomer using a mass range from 187 to 192 amu and for the protonated dimer using a mass range from 351 to 360 amu. The somewhat larger mass range was used for the dimer because of the instrument's limited mass resolution. The integrals were approximated by using the trapezoidal rule algorithm.

Given the integrated intensities, we wished to define quantities that are a measure of the relative amount of dimer and monomer present. The total monomer intensity (A_{MONO}) is $A_D + 9A_D = 10A_D$, where A_D is the integrated deuterated monomer intensity. We took the integrated protonated dimer intensity (A_{DIMER}) as the total dimer intensity—since the protonated/deuterated hybrid dimer signal was small. Two different measures of the relative amount of dimer to monomer were defined via the equation(s)

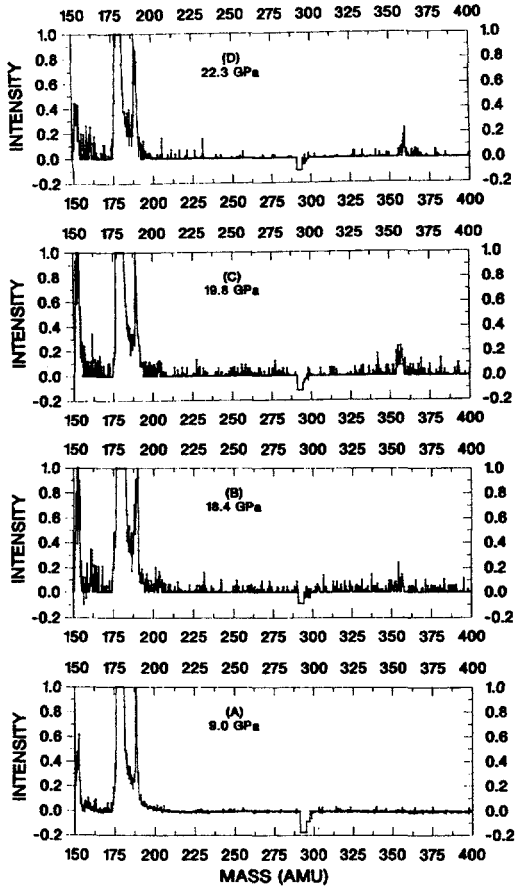

FIG. 6. Spectra obtained from shocked anthracene as a function of the initial shock pressure. The deconvolved spectra have been normalized to the observed maximum intensity of the deuterated anthracene monomer. (a), (b), (c), and (d) show the spectra obtained when the initial shock pressures were 9.0, 18.4, 19.8, and 22.3 GPa, respectively. These spectra are from four separate experiments. The crystals used in these experiments had nearly equal thickness—all being in the interval 11 to 14 mils. Data are from shots 101993g, 101993h, 101993j, and 101993c—see Table I.

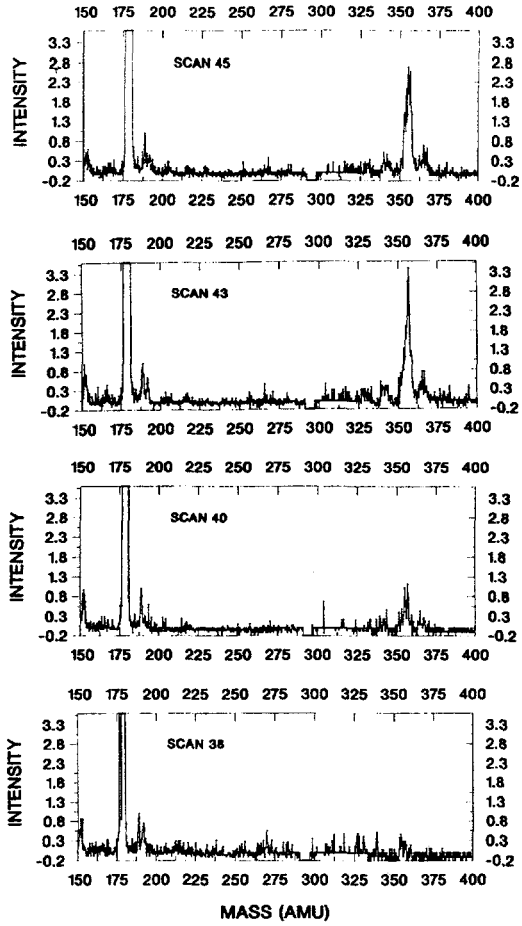

FIG. 7. Spectra obtained from shocked anthracene as a function of scan number. The deconvolved spectra shown are normalized to the observed maximum intensities of the deuterated monomer for each scan. Note that a peak corresponding to the hybrid protonated/deuterated dimer is clearly present on scans 43 and 45. These data are from a single shot (093093d); the crystal used in this experiment was 19 mils thick—see Table I.

$$R_i = \frac{A_{\mathrm{DIMER}}}{A_{\mathrm{DIMER}} + \alpha_i A_{\mathrm{MONO}}},$$

where $\alpha_1 = 1$ and $\alpha_2 = 0.5$. R_1 measures the number of dimer molecules present relative to the total number of molecules observed. R_2 accounts for the fact that it takes two monomers to make one dimer; it is the proportion of the original anthracene that is converted to dimer. R_2 will be useful in the Appendix. R_1 and R_2 values are given in Table I labeled as "number density ratio" and "scaled density ratio," respectively.

E. "Hydrodynamic clocks"

For our kapton/anthracene system, it is the rarefaction waves generated by the shock-wave interaction with the material free surfaces that control the length of time the various material elements within an anthracene crystal are held at high pressure and temperature. Consequently, these rarefaction waves can be thought of as "hydrodynamic clocks;" these clocks allow some insight into the temporal behavior of the anthracene dimerization reaction.

We are in debt to J. Jacobson for the numerical fluid mechanical calculations to be described next. These results were obtained by solving the Euler equations of compressible fluid mechanics with the assumption that our system had cylindrical symmetry. Furthermore, the energetics of the anthracene dimerization reaction were neglected; this is a good approximation—at least for the early stages of the reaction. In the Euler equation model, all dissipative effects in the fluid flow are neglected, other than those produced by the shock waves. One further assumption in the numerical calculations was that none of the materials could support tension.

We break our discussion of the fluid mechanics of the rarefaction wave propagation into two subcases corresponding to an account of the hydrodynamic flow in a 4 mil thick crystal and then a more cursory description of the hydrodynamics that occurs in crystals that are 10 and 22 mils thick.

All the calculations are for the case where the kapton was thrown at 5.15 mm μs; this corresponds to our highest pressure of ~22.0 GPa in the anthracene. In the discussion below all times are measured relative to the time of collision. Also, for all three crystal thicknesses, the slapper-crystal impact produces two shock waves that propagate away from the anthracene/kapton interface. One of these moves back into the kapton and the other forward through the anthracene. The interaction of these two shocks with the kapton back surface and the anthracene front surface generates the rarefaction waves that serve as our "clocks."

1. 4 mil thick crystal

For the 4 mil thick anthracene crystal case (see Table I and Fig. 8), it takes ~15 ns for the two shocks to reach the kapton and anthracene free surfaces and be reflected as strong rarefaction waves. The rarefaction wave from the anthracene crystal face essentially relieves the complete anthracene crystal before the kapton rarefaction wave reaches any of the anthracene. The anthracene near the kapton/anthracene interface is held at ~22 GPa longest (for ~20 ns) and then relieved very rapidly. At 25 ns all the anthracene is at 8 GPa or less. Thus, for a 4 mil thick anthracene crystal, reaction must occur in a time $\leq$~20 ns, if reaction is to be observed. The rarefaction from the anthracene crystal free surface defines the hydrodynamic clock in this geometry.

2. 10 and 22 mil thick crystals

For these two cases we merely summarize the important events depicted by the calculations. For both these crystal thicknesses, the kapton free surface is important, because the rarefaction wave produced at the anthracene free surface occurs later in time than for the 4 mil thick case. The kapton rarefaction reaches the kapton/anthracene contact surface at ~20 ns; i.e., the anthracene at this position has been shocked and held at pressure for this duration. The rarefaction wave now proceeds into the anthracene and catches the shock wave in the anthracene at ~40 ns. During this 40 ns, the shock has propagated ~10 mils into the anthracene. For the 10 mil thick crystal case, this overtake essentially ends the experiment—by 60 ns all the anthracene is at a pressure of ~2.5 GPa or less. For the 22 mil thick crystal, the rarefaction wave proceeds to erode the shock wave as it propagates toward the anthracene free surface. By 70 ns, this erosion has reduced the shock strength to ~18 GPa. This occurs at about 18 mils into the crystal—indicating that crystals thicker than 18 mils cannot reveal anything new about the pressure-driven dimerization reaction in our geometry. By 80 ns, the shock has decayed to ~16 GPa and when it contacts the crystal face its pressure is about 12 GPa.

The above discussion shows we are only interested in times less than 80 ns after collision. This short time and the large lateral extent of our crystals (~1.5 mm) implies that insofar as the pressure-driven chemistry is concerned, all our experiments were one-dimensional; i.e., the fact that our crystals had lateral surfaces is irrelevant to our observations.

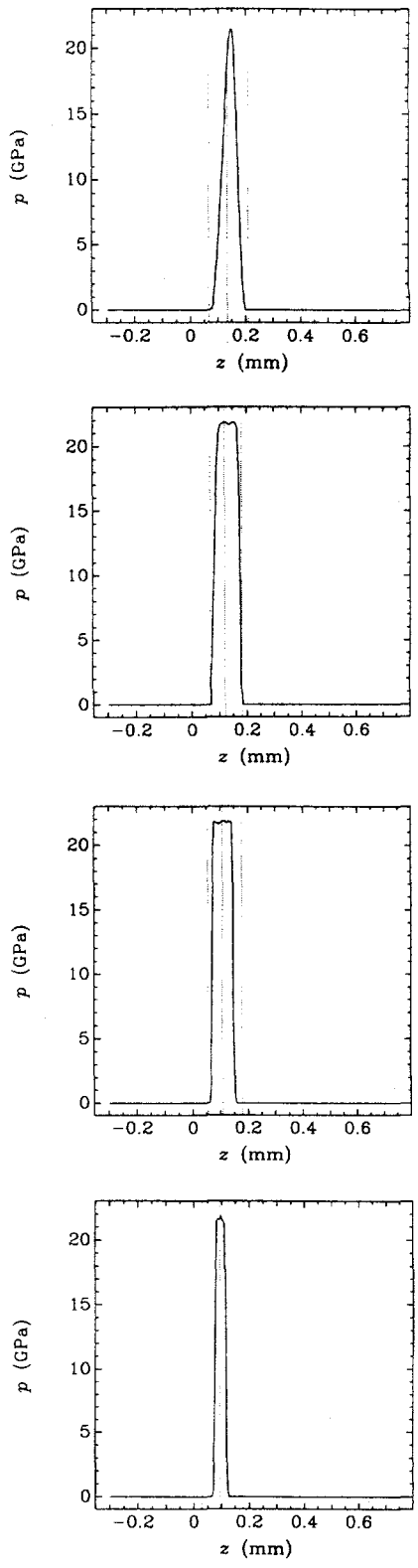

FIG. 8. Pressure vs distance plots obtained from numerical computations of the collision of a 3 mil thick kapton flyer with a 4 mil thick anthracene crystal. In going from the bottom to the top of the figure, one sees the flow history at 5, 10, 15, and 20 ns after the moment of collision. The three dotted lines indicate the surfaces of the kapton and the anthracene. The leftmost line is the rear surface of the kapton, the central line is the impact boundary, and the rightmost line is the anthracene crystal free surface.

IV. RESULTS

Our principal result is that an anthracene dimer is observed in the mass spectrum when the shock pressure is above a threshold value. The threshold pressure required to produce the dimer structure is ~18 GPa. This pressure value correlates well with the pressure at which Warnes[2] found a slope discontinuity in the $U_s - u_p$ Hugoniot of anthracene. In the following, we present the data and analysis that demonstrate these statements. Furthermore, we give arguments that the observed dimer is a chemically bound structure and not a van der Waals bound fragment of the original crystal.

We begin by examining the effect of the initial shock pressure on whether the dimer structure is observed. Figure 6 shows the mass spectra obtained from four different shock experiments. The variable being changed in this sequence of experiments is the initial shock pressure introduced into the anthracene; all other variables in the experiments were held as close to fixed as our abilities allowed. The initial pressures are indicated on each panel of Fig. 6. As outlined in Sec. III A, the initial pressure a crystal was subjected to was controlled by selecting an appropriate slapper barrel length. The mass range on the figure shows both the protonated and deuterated anthracene monomer and the anthracene dimer signals. The particular scan used in Fig. 6 from each shot was the one showing the largest dimer intensity. The intensities shown in the figure are scaled so the deuterated monomer maximum intensity for each shot is one. The short negative pulse at $m = 290$ to 296 amu that appears on all the panels is a fiducial mark that indicates the start of another mass-spectral scan. This fiducial mark appears because the anthracene dimer ion formed during the ionization period of a scan appears at the detectors during the following scan. This occurs because of the large mass of the dimer ion and its concomitant low speed toward the MCP detectors in the mass-spectrometer drift region.

Figure 6 is the central result of this paper; this figure shows that if the pressure introduced into an anthracene crystal is ~9 GPa *no* anthracene dimer is observed. However, if a pressure of ~18.4 GPa or higher occurs in the anthracene, the dimer structure is seen. In 14 experiments where a pressure of ≥18.4 GPa was introduced into anthracene crystals, the anthracene dimer was always observed (see Table I). In two experiments where anthracene crystals were shocked to 9.0 GPa, *no* anthracene dimer was seen. Note that these observations correlate with Warnes[2] observations of a slope discontinuity in the anthracene Hugoniot at ~17.1 GPa (see Figs. 1 and 2). We assert that the microscopic origin of the slope discontinuities observed by Warnes macroscopically are due to the anthracene monomer to dimer reaction.

The experiment in which we used a 4 mil thick crystal (shot No. 1019931) allows us to make a comment on the speed of the chemical kinetic process that produces the anthracene dimer from two monomers. In this shot, the crystal was shocked to ~22.1 GPa. As discussed in Sec. II I, this shock pressure is maintained in the anthracene particle adjacent to the kapton/anthracene interface for ~20 ns. Our data and analysis show a maximum conversion of anthracene monomers to dimer of ~4% in this experiment. Therefore, an observable fraction of the anthracene is converted to an anthracene dimer in a time less than or equal to ~20 ns when the crystal is shocked to ~22 GPa. We do not know whether the monomer–dimer reaction has achieved equilibrium in the 20 ns before the reaction is stopped by the arrival of the rarefaction waves from the kapton/anthracene free surfaces.

The experiment that used sublimation to obtain the cracking pattern of anthracene is useful here for showing that no other new species other than the anthracene dimer is obtained by shocking anthracene above the threshold value for dimer production. For example, in the upper panel of Fig. 5, we show the mass spectrum from 1 to 200 amu obtained by shocking anthracene to ~22 GPa (shot No. 101993c/scan 61). The lower panel shows the analogous mass spectrum obtained by sublimation of anthracene (as described in Sec. III B). The shot and scan number displayed in the upper panel of Fig. 5 was chosen because of the high anthracene monomer intensity observed. Second, there was some dimer intensity visible from the same ionization period—thereby assuring us that the volume element of anthracene being observed has experienced high pressure for a sufficient time for the dimerization reaction to occur. The essential features of the two spectra are identical. The mass range displayed in the figure is limited. However, if any significant ionic signals from heavier masses were present, they would appear in the mass range shown, but at incorrectly labeled (low) mass. The only two differences in the two spectra appear in the sublimated material at mass 19 and 28 amu. We point out that the sublimated spectrum is an average of ions collected over 1200 scans of the mass spectrometer and coadded, while the shocked spectrum is from one scan. The mass 28 peak in the sublimated spectrum is due to background N_2 and CO in the mass spectrometer; this spectral peak has been brought out of the noise by the coadding of 1200 scans. We think the peak at mass 19 is due to CH_3He^+; it arises because of the large amount of He carrier gas needed to obtain the requisite signal intensity in the sublimation experiment. These results show that the shock experiments do not produce any new molecular species not present in the sublimation other than the anthracene dimer.

The sublimation experiment involves a relatively gentle handling of the anthracene—the temperature of the expanding gaseous mixture is less than 523 K because of nozzle cooling, and the pressure is less than 7 kPa, the stagnation pressure. In contrast to this, the shock experiments subject the anthracene to very rigorous conditions—i.e., pressure greater than 18 GPa, temperatures greater than 1350 K, and internal energy changes which in temperature units correspond to tens of thousands of degrees K. Furthermore, an anthracene crystal shocked to the first cusp on the anthracene Hugoniot has undergone a volume reduction of ~35%. That is, the molecules of the crystal have either been compressed from their ambient crystalline separation far up the repulsive wall of the intermolecular potential or new chemical bonds have been formed that allow more efficient mass packing or both. These considerations suggest that van der Waals dimers might be seen in the sublimation experiment, but not in the shock-wave experiments. In contrast to this, we see the converse. That is, dimers are seen in the shock experiments, but not in the sublimation experiment. This is strong evidence

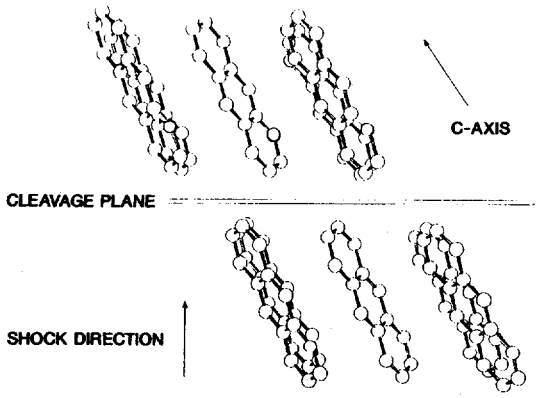

FIG. 9. Schema of the anthracene crystal structure in a direction perpendicular to the shock-wave propagation direction; the cleavage plane direction is also shown.

that a chemical dimerization has occurred in the shock-wave experiments. Warnes[2] observation of a chemically bond structure at 354 amu in his recovery shock-wave experiment is consistent with this interpretation as are the other experimental results from static high-pressure studies outlined in Sec. II B. An ancillary conclusion is that even the relatively gentle conditions in the sublimation experiments appear to be too rough to produce observable amounts of van der Waals dimers in our apparatus.

The next reasonable question to pose is if the observed anthracene dimer is chemically bound, then what is its likely chemical structure. We first note that there is no mass loss in the dimer formation; this implies cross linking with no hydrogen loss. This means that ring *pi* bonds are being converted to interring sigma bonds. The observed reaction is driven primarily by pressure; this is consistent with the smaller volume of the cross-linked dimer relative to two monomers. There is a class of ring-forming reactions that are known to be strongly pressure driven and which have relatively low activation barriers even at ambient pressure. These are the Diels–Alder reactions—the simplest of which is the cross linking of ethylene with butadiene to form cyclohexene. Aromatic ring systems can undergo Diels–Alder reactions.[5(b)] With no other constraints (such as spatial orientation of the molecules), it would be difficult to isolate any subset of the possible cross linkings of two anthracene molecules. However, this is not the case in our experiments since the crystalline forces produce conditions of strong ordering in space of the various molecules as shown in Fig. 9. Furthermore, the initial compression caused by the shock is a *longitudinal* compression of the crystal perpendicular to the crystal cleavage plane. Our thin crystal experiment shows that at least some dimerization can occur quickly (in ~20 ns or less). In view of these considerations, we *speculate* that the dimerization reaction we are observing is a Diels–Alder reaction involving the end benzene rings between molecules on the two sides of a cleavage plane of a crystal (see Fig. 9). The two new sigma bonds formed between the two end rings produce modified rings one of which is 1,3-cyclohexadiene and the other 1,4-cyclohexadiene. All the data discussed in this article are consistent with this interpretation, but do not prove it. See the Appendix for a more quantitative discussion of the energetic and pressure dependence of the anthracene dimerization reactions and consideration of whether it may be a Diels–Alder cross linking.

Next we discuss data from the shock experiments that indicate a time evolution in the amount of dimer observed. Figure 7 shows a succession of scans from shot No. 093093d (see Table I). The mass-spectral intensities on the various panels of this figure are normalized to the maximum intensity of the deuterated monomer signal for each scan. An important implication of this figure is that with certain experimental conditions of crystal thickness and shock pressure a large anthracene dimer intensity is obtained. At the maximum dimer intensity for this shot, about 50% of the anthracene was converted to an anthracene dimer (see Table I). Because we have made no attempts to remove instrumental corrections, such as corrections for the detector efficiencies of the monomer and dimer in the mass spectrometer, or to fragmentation differences upon electron impact ionization, the ratios we quote here and in Table I are apparent ratios. However, there can be no doubt that the dimer signal is substantial compared to the monomer.

The question arises of what is the source of the observed increase in dimer population as scan number increases. At first we thought what was being observed was a time resolution of the dimerization chemical rate process. Two things altered our opinion on this; the first being the observed rapidity of the dimerization rate process for the 4 mil thick crystal. Above we showed that this process occurs in 20 ns or less. Second, the fluid-mechanical calculations for the 22 mil thick crystal indicate that the shock in an anthracene crystal is caught by the kapton rarefaction at about 10 mils into the crystal. Thereafter, the shock is being eroded by the rarefaction; by ~18 mils into the crystal, the shock's strength has been diminished to ~18 GPa. After this point the shock is becoming too weak to drive the dimerization reaction. Therefore, we think that what is being observed in Fig. 7 is not the advance with time of the dimerization rate process, but rather the effects of a weaker and weaker shock progressing towards the anthracene crystal face. For scans earlier than scan 38, the shock has been eroded to less than ~17 GPa. For scans 40 to 45, we are looking deeper into the crystal where the shock had been eroded to a lesser extent and, therefore, the reaction was driven further to completion. If one makes the assumption that the dimerization process equilibrates *instantaneously* on the time scale of a scan, the data in Fig. 7 could be used to determine the equilibrium constant of the dimerization reaction as a function of thermodynamic state. Such a determination would require accurate calculations of the pressure-temperature histories of each anthracene "particle;" these calculations would require inclusion of the energetics of the dimerization reaction.

The discussion above assumes that the expansive flow of particles from the shocked crystal to the mass spectrometer is laminar, i.e., that there is no mixing of the various layers of anthracene. Thus, the number density we obtain in each scan is representative of that of a specific layer of shocked material. This assumption is supported by several experimental

observations. For example, a micron size inclusion of acetone solvent in one of our crystals was seen in one experiment and appeared for only one scan. Another example is an explosives experiment in which isotopically labeled constituents remained clearly separated in the mass spectra.[19(b)] We estimate that each scan samples successively about 17 μm deeper into the crystal.

V. DISCUSSION AND CONCLUSIONS

In this section we briefly review our chief results, discuss some of their implications, and suggest some possible directions for further work.

Our primary results are: (1) a dimerization reaction can be made to occur by subjecting anthracene crystals to transient high pressure ($\geqslant$18 GPa) produced by shock waves; (2) this dimerization reaction can be driven to, at least, partial completion in times as short as 20 ns; (3) the experimental evidence supports the view that the dimer is a chemically bond structure—since sublimation experiments that produce much gentler conditions do not show any evidence of van der Waals dimers in the same apparatus; (4) the appearance/nonappearance of the anthracene dimer can be controlled by regulating the strength of the shock wave introduced into the anthracene crystal; (5) for shock strengths of ~9 GPa no dimer production is observed, while for shock of pressure 18 GPa or greater the dimer is always produced; (6) the previous item (5) correlates with Warnes'[2] mechanical measurements showing a cusp in anthracene's Hugoniot at ~17.1 GPa—thus, our measurements connect Warnes' macroscopic mechanical observations to a microscopic chemical event; (7) the *only* new chemical species we see due to the high-pressure shocking is the dimer structure—this fact points to an interpretation that the second cusp on anthracene's Hugoniot at ~38.4 GPa corresponds to a chemical system in which the conversion to dimer is complete; (8) a heuristic statistical-mechanical model is expounded (in the Appendix) that casts light on why the Hugoniot measurements show such sharp changes (i.e., cusp points)—the origin being a sign change in the free energy of reaction when the pressure is raised above a critical value; (9) since there is no mass loss in the dimerization, the reaction must be a ring cross linking in which intraring *pi* bonds are converted to interring sigma bonds; (10) an obvious candidate for such a cross-linking reaction is a Diels–Alder process—such reactions are known to be strongly pressure driven and to have relatively low activation energies even at ambient pressure; (11) using the known anthracene crystal structure and the angle of attack of the shock on the crystals, we suggest a likely candidate for the specific dimer isomer being formed; (12) when thicker ($\geqslant$19 mils) crystals were shock to ~22 GPa, we were able to produce large conversions of the monomer to the dimer—in one case a greater than 50% conversion was observed (*vide infra*).

It is important to realize that the phenomena being studied in anthracene is *not* a characteristic of anthracene only. The cusp behavior in the Hugoniot has been observed in *all* aromatics that have been studied. The structures studied to data are benzene, toluene, anthracene, phenanthrene, and pyrene.[1,2] The combination of the earlier shock-wave work and the current work suggests that aromatics, when shocked to sufficiently high pressure, undergo a cross-linking dimerization reaction that involves loss of intraring *pi* bonds. Note that the cusp behavior on the Hugoniot is even exhibited to some degree by *polymers* that contain aromatic rings somewhere in their structures.[8(b),8(c)] A further point of some interest is that other nonaromatic ring structures such as 1,3- and 1,4-cyclohexadiene do not show such behavior even up to very high pressures.

A related point concerns the behavior of solid high explosives observed in the mass spectrometer. Dimers of the benzene ring-based explosives TNT (2,4,6-trinitrobenzene) and TATB (1,3,5-triamino-2,4,6-trinitrobenzene) have been observed mass spectrometrically during the initiation and detonation of these materials.[21] These observations suggest an *endothermic* process due to ring cross linking is part of the early chemistry of the detonation process (which is overall highly exothermic) of explosives containing aromatic rings.

There are a number of features in our results that we do not fully understand. Among these is the large production of dimer for the cases where thick crystals are shocked to ~22 GPa—i.e., shots Nos. 093093c and d and 101993e. The results of the numerical calculations, within their assumptions, indicate that crystal thickness should not be of critical importance in the amount of dimer produced, since the anthracene 'particle' at the kapton/anthracene interface is shocked and held longest at high pressure and temperature for the 10 and 22 mil crystal cases. It is our judgment that the defect is in the assumptions we utilized in setting up the numerical model. Probably the two most deficient assumptions are the neglect of the endothermicity of the monomer–dimer reaction and the change in compressibility of the shocked-reacting material, when significant amounts of dimer are produced. The neglect of strength effects in the anthracene may also be important. Inclusion of these factors could produce new shocks, shocks that grow in strength, spalling, etc. Such refined calculations are a research project in themselves that we (Jacobson and the authors) may pursue in the future.

Another point of concern about our experimental data is its somewhat erratic quantitative reproducibility; we note that the qualitative result of whether dimers are observed above 17.1 GPa is well reproduced. The quantitative reproducibility is notably poor for the three thick crystal shots (i.e., shot Nos. 093093c and d and 101993e—see Table I). The shock pressures used in these shots were all ~22.1 GPa and the crystal thicknesses were 21, 19, and 23 mils, respectively. Yet the maximum dimer production seen was 23.2%, 51.5%, and 23.9%, respectively. We can think of two possible reasons for this. First, there are neglected fluid-mechanical effects (some of which were discussed in the last paragraph) that occur in the actual flow and that may be modifying the flow in ways our simple picture does not include (e.g., such that crystal thickness becomes important). Second, there may be instabilities in the fluid-mechanical expansion of the "cloud" before the skimmer is reached. High-speed photographs of the cloud expansion in the case of shocked anthracene (and also for other materials) indicate this part of the flow cannot be reproduced in its details. We

note that the instability cannot be of the Rayleigh–Taylor type. Clarification of the origin of these reproducibility difficulties will take further work. If the difficulties are due to an instability in the cloud expansion it would be difficult to eliminate because the quenching of the chemistry requires this rapid expansion.

There are further experiments on this topic that would be of interest. Perhaps the most straightforward of these would be an extension of the current work to other aromatics that have been studied via macroscopic shock-wave techniques, e.g., pyrene and liquid benzene. Another variation would be to shock an anthracene crystal with the shock wave running parallel to the crystal cleavage plane; such an experiment would look for topotactic effects on the reaction chemistry. One could also modulate the "hydrodynamic" clocks in the system by varying the anthracene and kapton thicknesses. Such experiments would cast light on the time dependence of the monomer to dimer rate process. Finally, one could use multilayer isotopically labeled anthracene crystals to determine in a direct way the relationship between a mass-spectral scan and the original spatial location of the material in the unshocked crystal.

ACKNOWLEDGMENTS

This work was supported by the Department of Energy via a Laboratory Directed Research and Development (LDRD) grant. We also need to thank a number of others for their help on various aspects of this work. Among these are N. R. Greiner and H. A. Fry, co-workers who gave helpful advice and comments and A. S. Murray, C. W. Wilson, and J. J. Romero for their valuable technical assistance. We thank W. F. Hemsing and I. A. Garcia for their efforts in obtaining the visar slapper velocity records; without this work we could not have quantified the pressures being introduced into the anthracene crystals. We are indebted to J. D. Jacobson for his numerical simulations of the fluid mechanics occurring in the shocked crystals—this work allowed us to establish rough time scales for the chemical processes being observed. We are grateful to A. C. Larson for the information he provided concerning the crystal structure of anthracene. Finally, R. E. thanks S. A. Sheffield for his comments on and interest in the experiments.

APPENDIX

In this Appendix, we present a heuristic model of the pressure-driven dimerization reaction being observed; it is included to help the reader understand the effect of very high pressure on the rapid onset with pressure of the anthracene dimer in the products distribution.

Consider the shocked anthracene crystal as a two-level statistical-mechanical system in which n_0 and n_1 are the fractional populations of the two-monomer state and dimer state, respectively. The fractional populations of the two states as a function of ΔE, P, Δv, and T is

$$n_0 = Z^{-1}$$

and

$$n_1 = Z^{-1} \exp(-[\Delta E + P\Delta v]/kT), \qquad \text{(A1)}$$

where $Z = 1 + \exp([\Delta E + P\Delta v]/kT)$ and $n_0 + n_1 = 1$. We assume that our experimental observations are from systems that are fully equilibrated (i.e., thermally, mechanically, and chemically).

Note that $\Delta E > 0$ and $P\Delta v < 0$; i.e., the dimer is energetically metastable to two monomers (at $P = 0$), but it occupies less volume than two monomers. Therefore, the argument of the exponential $\Delta E - P|\Delta v|$ will go through a zero when $P = E/|\Delta v|$. Let us examine the character of the change in the relative population of the two states near this zero, using plausible values of kT, ΔE, and $P|\Delta v|$. Warnes[2] estimated that $T \cong 1350$ K ("or higher") at the first slope discontinuity in the anthracene Hugoniot. The Diels–Alder dimer of benzene is ~30 kcal/mol (i.e., $\Delta E \cong 15\ 100$ K) higher in energy than two benzenes.[5(b)] This value should also apply approximately to the analogous dimer of anthracene, since the additional rings on the anthracene molecules are not involved strongly in the energetics of the reaction. With these values of ΔE and T, we can determine Δv, provided we know the value of n_1 at some pressure. Suppose we take shots Nos. 093093d and 101993e of Table I as characteristic of dimer production when a thick crystal is shocked to ~22.1 GPa; these two shots were chosen because they show reasonable reproducibility. The scaled density ratio (R_2) is the appropriate quantity to use for n_1 in the following calculations and its value for these two shots is ~0.24. That is, roughly 1/4 of the system is in the dimer state. Using $n_1 = 0.24$ in Eq. (A1) gives a value of Δv of -5.22 cm^3/mol. The value of n_1 as a function of pressure is $n_1 = E/(1+E)$, where $E \cong \exp\{-0.45[25 - P(\text{GPa})]\}$. The argument of this exponential has a zero at $P \cong 25$ GPa; at this pressure the free energy ordering of the two-monomer/dimer states reverse. This produces a situation where the free energy favors population of the dimer state. These observations cast light on why the slope changes in Warnes' U_s vs u_p Hugoniot are so rapid; i.e., they are a result of the sign change in the exponential dependence of the dimer/monomer population.

It is noteworthy that Murphy and Libby[14] found evidence of a negative *activation* enthalpy for cross linking of anthracene under high static pressures (~5.8 GPa). That is, a cross-linking reaction *rate* was *increased* by *lowering* the temperature. Our work is consistent with their observation, but note we are considering the relative amount of reactant and products and *not* their rate of formation. These same workers derived a volume of activation for production of a 356 amu dimer from their rate data and obtained a value of -5.2 cm^3/mol. It is known that for Diels–Alder reactions, volumes of reaction and activation have similar values.[22] The similarity of our volume of reaction with their volume of activation suggests that the dimers we observe are the result of a Diels–Alder cross linking of two anthracene molecules.

[1] R. Dick, J. Chem. Phys. **52**, 6021 (1970); **71**, 3203 (1979).
[2] R. H. Warnes, J. Chem. Phys. **53**, 1088 (1970).
[3] R. Pucci and N. H. March, J. Chem. Phys. **74**, 1373 (1981).
[4] R. Engelke, P. J. Hay, D. A. Klier, and W. R. Wadt, J. Chem. Phys. **79**, 4367 (1983).
[5] (a) R. Engelke, P. J. Hay, D. A. Klier, and W. R. Wadt, J. Am. Chem. Soc. **106**, 5439 (1984); (b) R. Engelke, *ibid.* **108**, 5799 (1986).

[6] H. G. Drickamer, Science **156**, 1183 (1967).
[7] R. Engelke and S. A. Sheffield, Encycl. Appl. Phys. **6**, 327 (1993).
[8] (a) M. H. Rice, R. G. McQueen, and J. M. Walsh, *Solid State Physics*, edited by F. Seitz and D. Turnbull (Academic, New York, 1958), Vol. 6, pp. 1–60; (b) J. Carter and S. P. Marsh, Los Alamos Scientific Laboratory Report LA-UR-77-2062; (c) *LASL Shock Hugoniot Data*, edited by S. P. Marsh (University of California, Berkeley, CA, 1980).
[9] G. E. Duvall and R. A. Graham, Rev. Mod. Phys. **49**, 523 (1977).
[10] J. O. Williams and J. M. Thomas, Trans. Faraday Soc. **63**, 1720 (1967).
[11] W. J. Nellis, F. H. Ree, R. J. Trainor, A. C. Mitchell, and M. Boslough, J. Chem. Phys. **80**, 2789 (1984).
[12] G. A. Samara and H. G. Drickamer, J. Chem. Phys. **37**, 474 (1962).
[13] R. B. Aust, W. H. Bentley, and H. G. Drickamer, J. Chem. Phys. **41**, 1856 (1964).
[14] R. B. Murphy and W. F. Libby, J. Am. Chem. Soc. **99**, 39 (1977).
[15] F. Cansell, D. Fabre, and J.-P. Petitet, J. Chem. Phys. **99**, 7300 (1993).
[16] F. H. Ree, J. Chem. Phys. **70**, 974 (1979).
[17] (a) R. C. Weingart, R. S. Lee, R. K. Jackson, and N. L. Parker, in *Sixth Symposium (Intl.) on Detonation*, edited by D. A. Edwards (Office of Naval Research, Washington, D.C., 1976), p. 653; (b) A. C. Schwarz, Sandia Laboratory Report SAND 75-0314 (Dec. 1975).
[18] (a) L. M. Barker and R. E. Hollenbach, J. Appl. Phys. **43**, 4669 (1972); (b) W. F. Hemsing, Rev. Sci. Instrum. **50**, 73 (1979).
[19] (a) N. C. Blais, H. A. Fry, and N. R. Greiner, Rev. Sci. Instrum. **64**, 174 (1993); (b) N. R. Greiner, H. A. Fry, N. C. Blais, and R. Engelke, in preprints of the *Tenth Symposium (Intl.) on Detonation*, edited by J. M. Short (Office of Naval Research, Washington, D.C., 1993), p. 268, proceeding to appear.
[20] W. C. Wiley and I. H. McLaren Rev. Sci. Instrum. **26**, 1150 (1955).
[21] N. R. Greiner (private communication, Sept. 1993).
[22] G. Jenner, *Organic High Pressure Chemistry*, edited by W. J. le Noble (Elsevier, New York, 1980), pp. 143–203.

VII.

JOURNAL OF MATERIALS PROCESSING TECHNOLOGY, 60 (1966)

ELSEVIER

Journal of Materials Processing Technology 60 (1996) 261–267

Journal of Materials Processing Technology

Micromechanics of spall and damage in tantalum

A.K. Zurek[a], W.R. Thissell[a], J.N. Johnson[a], D.L. Tonks[b], R. Hixson[c]
Materials Research and Processing Science
[a]*Mechanics of Materials,* [b]*Applied Theoretical Physics,* [c]*Dynamic Experimentation*
Los Alamos National Laboratory, Los Alamos, NM 87545, USA

Abstract

We conducted a number of plate impact experiments using an 80-mm launcher to study dynamic void initiation, linkup, and spall in tantalum. The tests ranged in shock pressure so that the transition from void initiation, incipient spall, and full spall could be studied. Wave profiles were measured using a velocity interferometry system (VISAR), and targets were recovered using "soft" recovery techniques. We utilized scanning electron microscopy, metallographic cross-sections, and plateau etching to obtain quantitative information concerning damage evolution in tantalum under spall conditions. The data (wave profiles and micrographs) are analyzed in terms of a new theory and model of dynamic damage cluster growth.

Keywords: spall, tantalum, void initiation, damage, impact experiments

1. Introduction

Spallation differs from other metal forming processes in several important respects. Stress waves travel in spallation at speeds great enough to form shock waves. This typically happens at very high strain rates. Typical high rate metal forming occurs at strain rates of 1-10 s^{-1}. Spallation occurs at strain rates of $> 10^5 s^{-1}$.

Spallation is one of a variety of experimental configurations that can produce dynamic fracture for the research purposes. Spallation is defined as a dynamic uniaxial strain experiment. It occurs in a material due to tensile stresses generated by the interaction of two release (rarefaction) waves [1]. The principal stress components differ by the flow stress under conditions of dynamic uniaxial strain. Thus, in the ductile case, voids are subject to nearly isotropic tensile stress fields. Void growth and coalescence dominate all stages of the fracture process. Porosity, void formation, growth, and coalescence serve as variables in descriptions of spallation and therefore the fracture criteria of the material [1-3]. In a spallation plate impact experiment, a flyer is launched at a stationary plate sample. Impact results in loading that induces a shock wave at the impact plane. The shock waves travel from the impact plane to both the flyer plate back surface and the target back surface. Reflection of the waves occur at the free surfaces. The two release shock waves meet inside the sample to produce a plane of tension. The sample will fail at the plane and separate into two pieces if the amplitude of the tensile wave exceeds the spall strength of the material. Otherwise, the sample will develop an incipient deformation zone at a tensile plane with characteristic voids, cracks, and plastic deformation.

The process of deformation and fracture can be investigated by using a soft sample recovery system and microscopic observation of the damage after the impact [1]. VISAR laser interferemetry can be employed to record the back free surface velocity of the target [4, 5]. Both techniques were utilized in this study of spallation properties of high-purity tantalum subjected to pressure just above the spallation threshold and to an impact stress one and one-half times the spallation threshold [6].

2. Material and Experiment Description

In this study we used commercially pure (triple electron beam arc melted) unalloyed tantalum plate with the measured composition (in at. %) of 6 ppm carbon, 24 ppm nitrogen, 56 ppm oxygen, < 1 ppm hydrogen, 19 ppm iron, 25 ppm nickel, 9 ppm chromium, 41 ppm tungsten, 26 ppm niobium, and the balance tantalum. The tantalum plate was in an annealed condition and had an equiaxed grain structure of 68 μm grain size [7]. We performed uniaxial strain spall tests utilizing an 80-mm single-stage launcher and recovery techniques as previously described [1]. VISAR interferemetry was used to record the free surface velocity of the sample [4, 5]. Tantalum samples were spalled at 9.5 and 17 GPa pulse pressure and 1 μs pulse duration under symmetric impact conditions. Recovered spalled samples were analyzed theoretically and using optical and scanning electron microscopy.

2.1. Spall Experiments

A great number of reports describe shock compression and release in metals including tantalum [8-14]. Tantalum's mode of failure and hence spall strength is a function of shock amplitude. Previous recovery and non-recovery spall tests reported a 5.2 GPa spall strength for 6 GPa shock amplitude, 7.3 GPa spall strength for 9.5 GPa shock amplitude, and 3.0 to 4.5 GPa spall strength for 15 GPa shock

PII 0924-0136 (96) 02340-0

amplitude [6, 7, 15]. These compare favorably with our results. Figure 1 shows a typical calculated (using a void growth model without volumetric plasticity [2, 6]) and measured spall VISAR wave profile in high purity tantalum shock loaded to approximately 9.5 GPa. This calculated signal also corresponds to a simple tensile fracture model with a spall strength of 7.3 GPa. One of the peculiar observation associated with the 9.5 GPa spall signal is the sudden deceleration that occurs in the pull-back signal in Figure 1.

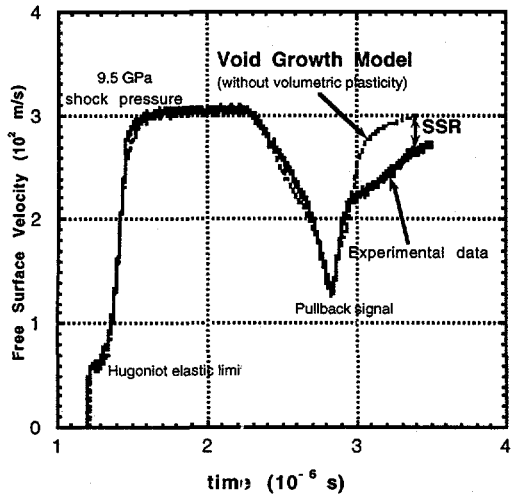

Figure 1. Void-growth model and spall VISAR trace at a shock pressure of 9.5 GPa.

The VISAR signal appearance of a sharp velocity pullback suggests that the material has undergone complete spallation, *i.e.*, separation. However, there remains a restoring force to decelerate the spalled piece. This remained a puzzle until examination of a recovered spall sample disclosed the nature of the actual spall plane. Figure 2 shows the spall region for a 9.5 GPa impact stress.

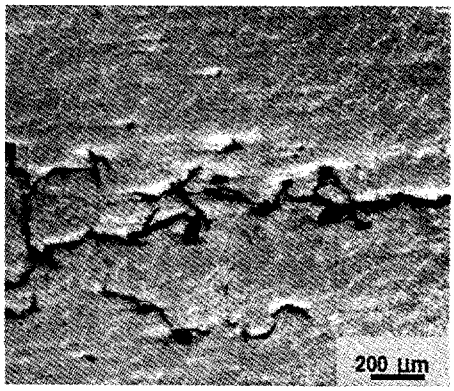

Figure 2. Spalled region for peak impact stress of 9.5 GPa.

Figure 2 shows that the spall plane is not a distinct fracture surface, but it consists of a number of cracks extended over several hundred of microns in the direction of wave propagation (vertical on the

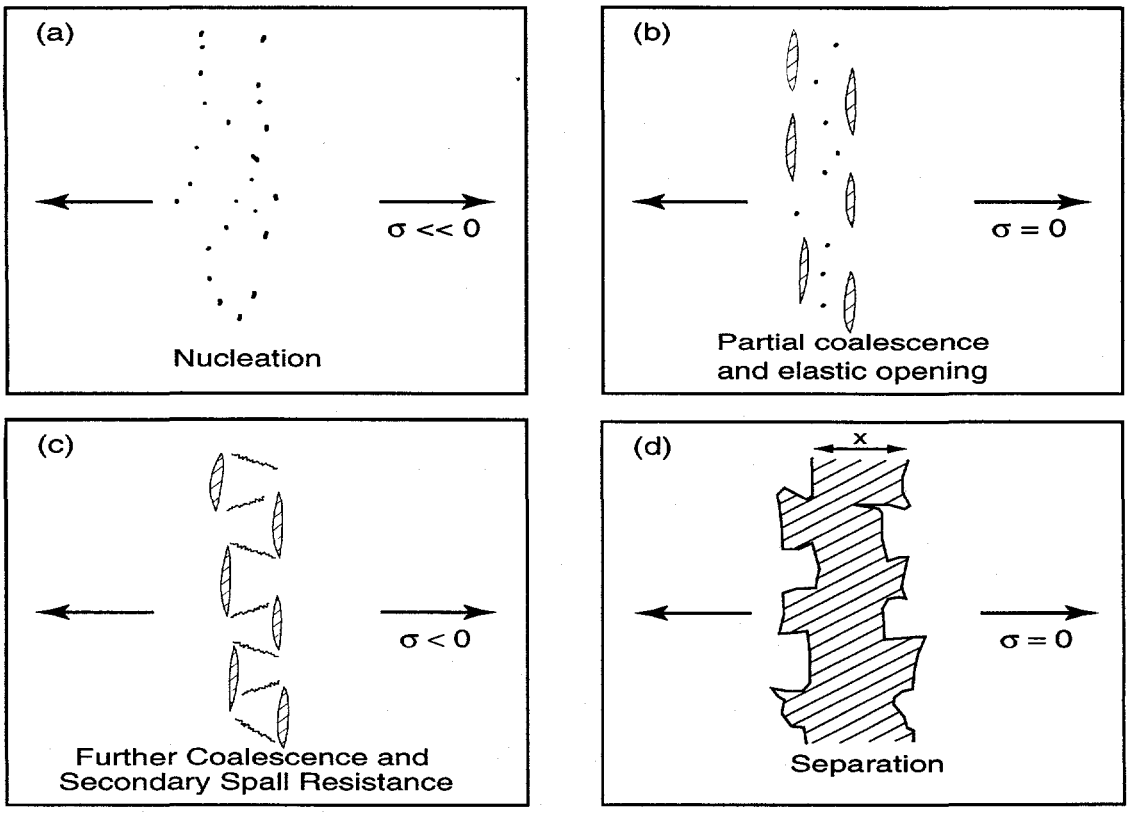

Figure 3. A heuristic picture of a proposed secondary spall mechanism.

micrograph). We suggest that the initial loss of material strength comes from the formation and elastic opening of the cracks and hence the corresponding drop of longitudinal tensile stress. Following this initial loss of tensile strength, the extended spall plane pulls apart and undergoes additional linking of these cracks to eventually form the separated spall plane, but not before developing considerable secondary resistance to separation: this is what we refer to as secondary spall resistance (SSR).

Figure 3 shows a heuristic picture of proposed secondary spall mechanism taking place in tantalum. Nucleation of voids takes place in the spall region when sufficient tensile stress is achieved ($\sigma<<0$, Figure 3a). Partial coalescence occurs in a preferential orientation following nucleation to relieve the longitudinal tensile stress component by the elastic opening of flat cracks parallel to the spall plane (Figure 3b). Further coalescence occurs in the next stage that produces a "jig-saw-puzzle" effect after the flat cracks have opened sufficiently (Figure 3c). This produces the observed secondary spall resistance. The spall plane undergoes complete separation if the impact amplitude is great enough (Figure 3d). We believe that the 9.5 GPa stress amplitude in pure tantalum tested follows the spall process up to the point represented by Figure 3c, while the 17 GPa stress amplitude takes the sample to the point represented by Figure 3d *i. e.*, to complete separation.

The SSR is therefore included in the void growth model in terms of an additional tensile stress that develops following simple tensile fracture. As the separation distance x between the left and right sides of the spall surface increases, the SSR is given by:

$$\sigma_{SSR} = 0 \text{ for } x < a \text{ and } x > b \quad (1)$$

$$\sigma_{SSR} = f\sigma_S\{(x-b)/(b-a)\} \text{ for } a<x<b \quad (2)$$

where, σ_S is the absolute magnitude of the spall strength (here 7.3 GPa) and f is a dimensionless number less than unity. Generally a will be on the order of a few microns (the onset of SSR) and b will be on the order of a hundred microns (the end of SSR). Equations (1) and (2) represent the stress necessary to pull apart the convoluted spall plane shown in Figure 3.

Calculations of the spallation behavior with this model of SSR is shown in Figure 4 for a = 5 microns, b = 200 microns, and f = 0.20, which fit very nicely the observed damage in the pure tantalum spall tests.

2.2. Microscopy

The spall test at 9.5 GPa pulse pressure produced an incipient spall fracture. The cross section of the recovered spall sample showed distinctive cracks running across the entire diameter of the sample with multiple branched and interlocking cracks extending into the sample away from the principal fracture surface. The two halves of the spall sample did not separate from each other, regardless of the fact that the pulse pressure exceeded the expected spall strength of this material (see Figure 2).

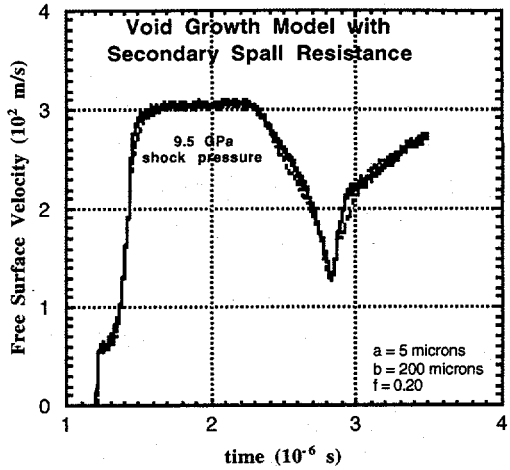

Figure 4. Void growth model with secondary spall resistance terms.

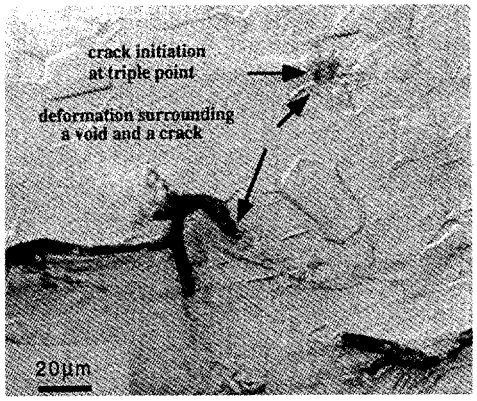

Figure 5. Cross section of tantalum sample spalled at 9.5 GPa showing void initiation at the point of intersection of several grains and propagating cracks with deformation surrounding a void and a crack (optical micrograph).

Figure 5 shows higher magnification of the same spall cross section of the tantalum sample spalled at 9.5 GPa shock pressure.

We have sectioned off part of the spalled sample to allow it to separate the spall surfaces. Figure 6 shows the typical ductile dimple fracture surface characteristic for metals in Group V_A. Multiple impurities on the fracture surface are present, and most likely they are responsible for the void initiation.

The spall was complete and two halves of the spalled sample fully separated to reveal fracture surface under increased loading pulse pressure (17 GPa). The micrograph shows a mixture of cleavage fracture and ductile dimples present on the sample spalled at 17 GPa loading pulse pressure (Figure 7).

This change in the fracture morphology can be induced by significant deformation twinning which

will initiate cleavage [7]. The etched cross section, orthogonal to the spall fracture surface, reveals a significant density of deformation twins and only a few twins in the sample spalled at the lower pulse pressure (Figure 5, Figure 8).

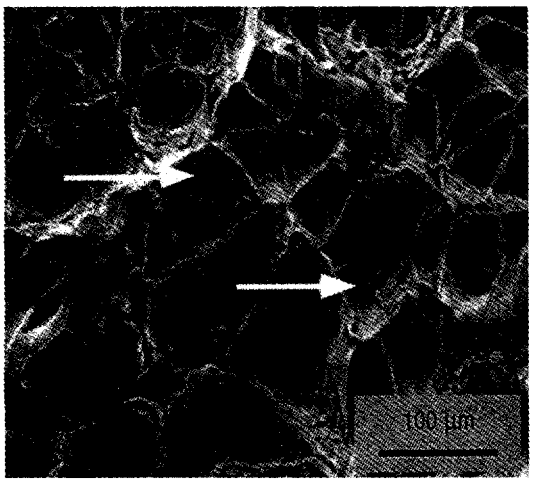

Figure 6. Spall fracture surface of tantalum spalled at 9.5 GPa. Arrows point to the particles which most likely initiated dimples on a ductile fracture surface.

Figure 7. Fracture surface of tantalum spalled at 17 GPa shock pressure.

The sample tested at the higher pulse amplitude did not show crack branching, unlike the sample tested at the lower pulse amplitude. This observation, and the change in mode fracture from ductile to a mixture of ductile and cleavage fracture explains an observed decrease in spall strength with increased applied pulse amplitude in this material [6, 7, 15].

Cleavage fracture is associated with the ductile-to-brittle transition in this material especially under severe loading rates or low temperatures [7, 16]. High hydrostatic tensile stress develops at the spall plane. The ductile-to-brittle transition is pushed to higher temperatures with increases in applied stress. The fracture stress therefore increases because, to a first approximation, it is linearly proportional to the applied stress. The combination of this effect and a significant amount of deformation twinning triggers cleavage fracture.

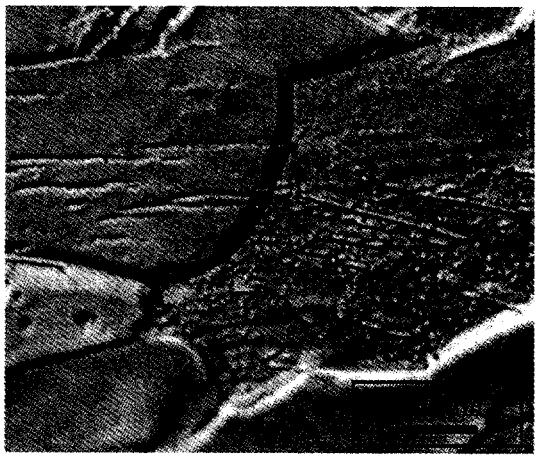

Figure 8. Deformation twins present on the cross section of the tantalum sample spalled at 17 GPa shock pressure.

2.3. The Micromechanical Model of Spall Events in Pure Tantalum

A theoretical program is underway to model the damage evolution observed in materials such as tantalum The void-growth model with secondary spall resistance involves the mechanics of non-interacting spherical voids coupled with an ad hoc description of partial coalescence and elastic opening followed by crack link-up and finally, complete loss of strength [6]. On the other hand, the micromechanical model of spall is a theoretical analysis that attempts to explain, from more fundamental principles [17-20], the microscale interactions of voids to form the observed, complex fracture patterns (*e.g.*, Figures 2 and 5). Quantification of the micromechanical model, in combination with wave-propagation and spall calculations, should lead to an improved explanation of observed spall signals in materials undergoing void nucleation, growth and coalescence under dynamic loading conditions.

The micromechanical model includes damage induced by shear stress as well as damage caused by volumetric tension. Spallation is included in the model as a special case and strain induced damage is also treated. Void nucleation and growth are taken into account and give rise to strain rate effects, which also occur through elastic release wave propagation between damage centers (voids). The underlying physics of the model is the nucleation, growth, and coalescence of voids in a plastically flowing solid. The model is intended for hydrocode based computer simulation. The details of the model are published elsewhere [17-20], but qualitative description of the model is presented below.

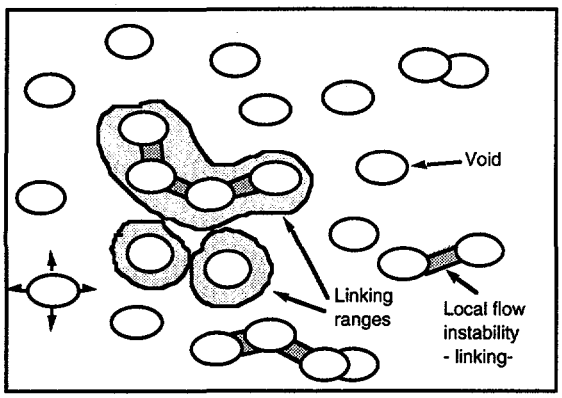

Figure 9. Statistical treatment of voids in a material.

The voids are assumed to exist from time 0 of the deformation time in this micromechanical model, and they are randomly distributed throughout the material. The void may be an impurity, for example. Two voids coalesce when a local flow instability forms in the intervoid ligament, which then thins out. This process is called void linking. Each void is surrounded by a stress and strain linking range. Figure 9 represents the statistical consideration of the voids in any material. Arrows in the figure point to the voids, potential linking ranges (light gray) and local flow instabilities (dark gray).

The coalescence of two damage clusters (voids) requires the fulfillment of two conditions: sufficient stress and sufficient strain in the intervening ligament. An enhanced stress field around the periphery of large damage clusters leads to an enhanced stress link range. Material in the intervening ligament undergoes plastic flow under the applied external stress. The intervening ligament thins out when sufficient plastic flow accumulates. The degree of plastic flow necessary to thin out the ligament between two clusters is approximately inversely proportional with respect to distance between them, because of a local unloading resulting in an elastic region surrounding damage clusters and neighboring voids. This results in the stress and strain concentration at the periphery of damage clusters and voids. Figure 10 represents schematically a mechanism of a single void linking to a damage cluster.

Two modes of fracture can be represented that are functions of the rate of void growth and coalescence, which are in turn a function of tensile pulse amplitude, pulse duration, strain rate, and sound velocity of the material.

The first mode of fracture is dominated by a stress linking enhancement which is an increasing function of cluster size. The stress linking enhancement can occur at rates of void growth and coalescence lower than the second mode of fracture. A limiting condition for the occurrence of the stress linking enhancement is that the loading pulse duration exceeds the damage cluster diameter divided by the sound velocity of the material. This defines the time needed after initial loading for the establishment of the stress enhancement at the damage cluster periphery. The loading occurs *via* sound (release) wave propagation from one end of the damage cluster to the other end (Figure 10).

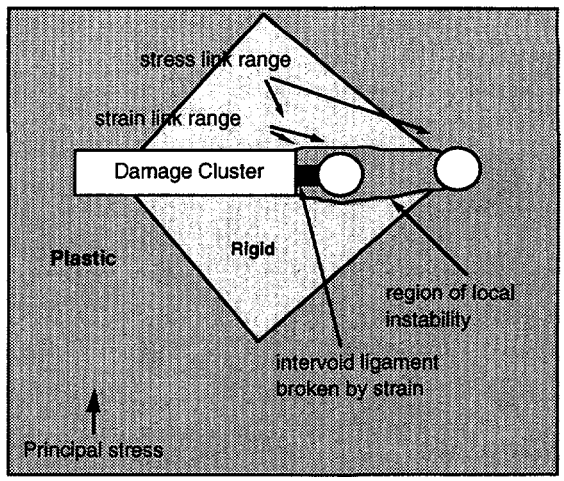

Figure 10. Single void linking to a damage cluster.

This process is highly **deterministic**. Fracture will occur when the largest damage cluster grows much faster than small clusters *via* void coalescence. Figure 11 depicts this process. Due to the nature of this process, this will happen at a lower end of the high strain rate regime of dynamic deformation, *i. e.,* spall tests but not explosive tests.

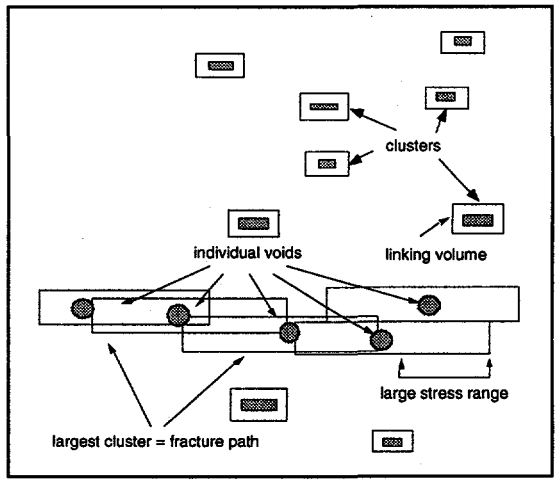

Figure 11. Single crack fracture mechanism.

The stress linking enhancement is inhibited in the second mode of fracture, at higher rate of void growth and coalescence and when the pulse duration does not exceed the typical damage cluster diameter divided by the sound velocity. Failure occurs when the independently growing damage cluster linking ranges happen to overlap, forming a continuous fracture surface. This is a **stochastic** process similar to percolation, hence the name percolation fracture criteria which describes this process.

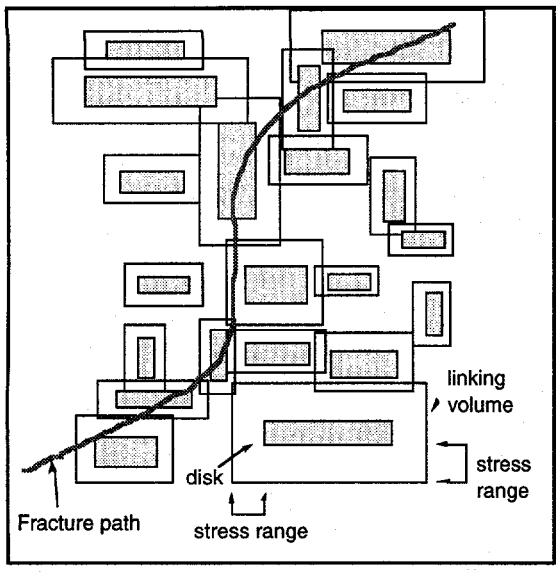

Figure 12. Percolation fracture criteria.

Figure 12 depicts this process and it is expected to happen at higher strain rates (explosive loading). The growth of large clusters is expected to be inhibited by the lack of time to form stress enhancements at a damage cluster (disk) periphery, and damage will form independently everywhere until it is connected into a continuous fracture path. The shallow dimple depth (Figure 6) of the spall plane and the small thickness of the crack nodes of the cross section micrographs (Figure 5, Figure 6) can be interpreted as small voids and failed intervoid ligaments. The plastic flow field surrounding a small void plausibly approximates the void link range (Figure 13). The void link range is very large due to the large tantalum spall strength.

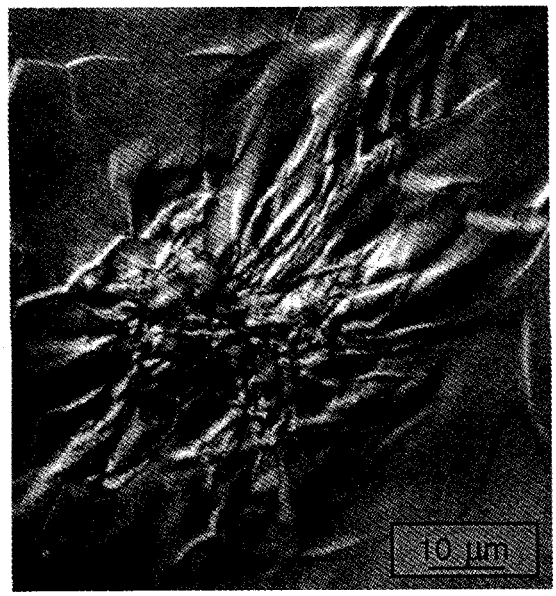

Figure 13. Etched cross section of a plastic field surrounding a void.

The computer calculations show that the loading time was too short for the cluster peripherial stress enhancement to occur [21]. These two occurrences support and favor the percolation process.

Qualitative correlations suggest that spall in high purity tantalum occurs by linking of widely separated voids *via* the percolation process.

3. Summary

Spall experiments on pure tantalum were performed under a range of shock pressures covering the transition from void initiation, incipient void linkup, to full fracture. These experiments have allowed the microstructural mechanisms of spallation to be studied and verified qualitatively. Shock pressures above the spall strength of the pure tantalum studied do not necessary lead to complete fracture. This is explained by a proposed model that incorporates a secondary spall resistance that follows the initial partial coalescence and elastic opening of voids. The secondary spall resistance is included in a proposed micromechanical model. The micromechanical model consists of two representations of fracture mechanisms that depend on the deformation strain rate. The mechanism that occurs at lower strain rates is called the single crack fracture mechanism. This mechanism arises due to an enhanced stress and strain fields around the periphery of large damage clusters. These fields interact in a highly deterministic process of void coalescence. The second fracture mechanism occurs at higher strain rates where void growth occurs rapidly and independently throughout the fracture region. The process is stochastic and is reminiscent of percolation theory. The fracture surface is formed when the growing voids intersect by chance and form a continuous path.

This micromechanical explanation of dynamic fracture suggests that pure tantalum spalls by percolation fracture mechanism due to rather large stress and strain linking ranges between voids and short loading times.

Acknowledgments: We are pleased to acknowledge support from the US Joint DoD/DOE Munitions Technology Development Program and the US DOE. Carl Trujillo is thanked for performing the spall tests. Max Winkler is greatly appreciated for assistance and tutelage in setting up and operating the VISAR apparatus. Sheri Bingert is thanked for annealing the samples. Mike Lopez is appreciated for help in optical microscopy. Ron Ellis is thanked for illustrating assistance.

References

[1] A. K. Zurek, J. N. Johnson, and C. E. Frantz, *Journal de Physique*, *49*, C3, suppl. 9, (1988), 269.

[2] J. N. Johnson, *J. of Applied Physics*, *52*, 4, (1981), 2812.

[3] D. R. Curran, L. Seaman, and D. A. Shockey, *Physics Reports*, *147*, (1987), 253.

[4] L. M. Barker and R. E. Hollenbach, *J. Applied Physics, 43*, 11, (1972), 4669.
[5] R. A. Graham and J. R. Asay, *High Temperature - High Pressure, 10*, (1978), 355.
[6] J. N. Johnson, R. S. Hixson, D. L. Tonks, *et al.*, in *Shock Compression of Condensed Matter*, edited by S. C. Schmidt and W. C. Tao (AIP, New York, 1996), p. in press.
[7] G. T. Gray, III, in *High-Pressure Science and Technology*, edited by S. C. Schmidt, J. W. Shaner, G. A. Samara and M. Ross (AIP, 1994).
[8] J. N. Johnson and P. S. Lomdahl, *J. de Physique, IV*, Collaque C3, (1991), 223.
[9] J. N. Johnson, P. S. Lomdahl, and J. M. Wills, *Acta Metallurgica, 39*, (1991), 3015.
[10] J. N. Johnson, R. S. Hixson, G. T. Gray, III, *et al.*, *J. of Applied Physics, 72*, (1992), 429.
[11] J. N. Johnson, in *High Pressure Shock Compression of Solids*, edited by J. R. Asay and M. Shahinpoor (Springer-Verlag, 1993), p. 217.
[12] J. N. Johnson, *J. of Physica and Chemistry of Solids, 54*, (1993), 691.
[13] J. N. Johnson, R. S. Hixson, D. L. Tonks, *et al.*, in *High Pressure Science and Technology-1993*, edited by S. C. Schmidt, J. W. Shaner, G. A. Samara and M. Ross (American Institute of Physics, 1993), Vol. 309, p. 1095.
[14] J. N. Johnson, in *High Pressure Science and Technology-1993*, edited by S. C. Schmidt, J. W. Shaner, G. A. Samara and M. Ross (American Institute of Physics, 1993), Vol. 309, p. 1145.
[15] G. T. Gray, III and A. D. Rollett, in *High Strain Rate Behavior of Refractory Metals and Alloys*, edited by R. Asfahani, E. Chen and A. Crowson (The Minerals, Metals and Materials Society, 1992), p. 303.
[16] R. W. Armstrong, J. H. Bechtold, and R. T. Begley, in *Refractory Metals and Alloys*, edited by R. Asfahani, E. Chen and A. Crowson (The Minerals, Metals and Materials Society, 1992).
[17] D. L. Tonks, A. K. Zurek, and W. R. Thissell, in *Metallurgical and Materials Applications of Shock-Wave and High-Strain-Rate Phenomena (EXPLOMET'95)*, edited by L. E. Murr, K. P. Staudhammer and M. A. Meyers (Elsevier, New York, 1995), p. 171.
[18] D. L. Tonks, *J. Physique, IV*, C8, 4, (1994), 665.
[19] D. L. Tonks, in *Dynamic Plasticity and Structural Behaviors*, edited by S. Tanimura and A. S. Khan (Gordon and Breach, Luxembourg, 1995), p. 119.
[20] D. L. Tonks, in *Shock Compression of Condensed Matter*, edited by L. Davison, D. E. Grady and M. Shahinpoor, 1995), Vol. IV, p. in press.
[21] D. L. Tonks, *work in progress*, (1996),

*U.S.GOVERNMENT PRINTING OFFICE 1996-0-790-301/27027